Thin film alloys and composites for application of hydrogen storage and oxygen reduction electrocatalysts

by

XueHai Tan

A thesis submitted in partial fulfillment of the requirements for the degree of

Doctor of Philosophy

in

Materials Engineering

Department of Chemical and Materials Engineering

University of Alberta

Abstract

This thesis encompasses aspects of alloy design, fabrication and characterization of thin films, which are employed as model systems to enhance hydrogen storage kinetics and thermodynamics in magnesium hydride and to enhance the catalytic efficacy and corrosion stability of platinum-based electrocatalysts towards oxygen reduction reaction.

Chapter 2 describes the development of various bilayer Pd/X (X = Ti, Nb, Ta) surface catalysts that are used for all Mg-based alloys films in this thesis. The selected interlayer, which forms stable hydride both during absorption and during desorption, reduces the rate of intermetallic formation between Mg and Pd, allowing the Pd to remain catalytically active. The Pd coating is also effective to prevent the underlying alloy from oxidation during the transfer/storage before the hydrogen sorption measurement.

Chapter 3 describes a new bimetallic Nb-V catalyst for enhancing the hydrogen storage kinetics of magnesium hydride. Mg combined with bimetallic Nb-V catalyst displays rapid and stable low temperature (200 °C) sorption kinetics even after 500 cycles. We employed JMA-type kinetic analysis and cryo-stage TEM analysis on fully and partially sorbed materials to provide insight into the rapid Mg to MgH_2 phase transformation. Our results point to the surface catalyst distribution and stability against coarsening as being a key influence on the hydriding kinetics. The cycled Mg-V-Nb structure consists of a dense distribution of catalytic Nb-V nanocrystallites covering the surfaces of larger Mg and MgH_2 particles.

Chapter 4 describes the hydrogen storage properties of ternary Mg-Ni-Cu films using binary Mg-Ni and Mg-Cu as baselines, and aims to elucidate the influences of alloying elements on the hydrogen sorption kinetics, thermodynamics and cycleability. Mg-rich Mg-Ni-(Cu) alloys show two stages during absorption. The first stage due to the absorption of Mg is very quick, but the second one due to the absorption of intermetallic Mg_2Ni and/or Mg_2Cu is significantly slower. The rapid first stage absorption is catalyzed by the intermetallic phase Mg_2Ni. Cu substitution improves the desorption kinetics, but decreases the kinetics of the second absorption stage. From pressure-composition

isotherms, it is found that the Cu substitution has no influence on the plateau pressure of MgH_2 from free-Mg phase, but slightly increases the plateau pressure of LT-Mg_2NiH_4.

Chapter 5 describes a new metastable alloy hydride with promising hydrogen storage properties. Body centered cubic (bcc) $(Mg_{0.75}Nb_{0.25})H_2$ possesses 4.5 wt.% H capacity. The measured enthalpy of hydride formation of -53 kJ mol^{-1} H_2, which indicates a significant thermo-destabilization relative to the baseline -77 kJ mol^{-1} H_2 for rutile MgH_2. The hydrogenation kinetics are remarkable: At room temperature and 1 bar hydrogen it takes 30 minutes to absorb a 1.5 μm thick film at cycle 1, and 1 minute at cycle 5. Using *ab initio* calculations we have examined the thermodynamic stability of metallic alloys with hexagonal close packed (hcp) versus bcc crystal structure. Moreover we have analyzed the formation energies of the alloy hydrides that are bcc, rutile or fluorite.

Chapter 6 describes the support effects of a new highly conductive support that comprises of a 0.5 nm titanium oxynitride film coated by atomic layer deposition onto an array of carbon nanotubes for both pure platinum and platinum–nickel alloy electrocatalysts. Oxynitride induces a downshift in the d-band center for pure Pt and fundamentally changes the Pt particle size and spatial distribution. This results in major enhancements in oxygen reduction reaction electrocatalytic activity and corrosion stability relative to an identically synthesized catalyst without the interlayer. Conversely, oxynitride has a minimal effect on the electronic structure and microstructure, and therefore, on the catalytic performance of Pt-Ni alloy.

Chapter 7 describes the oxygen reduction reaction electrocatalytic activity and the corrosion stability of several ternary Pt-Au-Co and Pt-Ir-Co alloys. The addition of Au fine-tunes the lattice parameter and the surface electronic structure to enable activity and cycling stability that is unachievable in the state-of-the-art binary Pt-Co baseline. Certain Pt-Au-Co ternary alloy shows an activity enhancement that is in fact the most optimum reported for skeleton-type Pt systems. The ternary catalysts exhibit improved corrosion stability with increasing levels of Au or Ir substitution. HRTEM and XPS show that Au alloying promotes the formation of an atomically thin Pt-Au-rich surface layer, which imparts kinetic stabilization against the dissolution of the less noble solute component.

Preface

This thesis is organized into 7 chapters:

Chapter 1 of this thesis provides an overview of the hydrogen-centered energy system, the challenges of hydrogen storage and hydrogen fuel cells technologies, and the research scope of this thesis. The employed thin film deposition method is also introduced in this chapter.

Chapter 2 of this thesis has been published as XueHai Tan, Christopher T. Harrower, Babak Shalchi Amirkhiz, David Mitlin, "Nano-scale bilayer Pd/Ta, Pd/Nb, Pd/Ti and Pd/Fe catalysts for hydrogen sorption in magnesium thin films", International Journal of Hydrogen Energy 2009, vol. 34, 7741-7748.

Chapter 3 of this thesis has been published as XueHai Tan, Beniamin Zahiri, Chris M.B. Holt, Alan Kubis, David Mitlin, "A TEM based study of the microstructure during room temperature and low temperature hydrogen storage cycling in MgH_2 promoted by Nb-V", Acta Materialia 2012, vol. 60, 5646–5661.

Chapter 4 of this thesis has been published as XueHai Tan, Mohsen Danaie, Peter Kalisvaart, David Mitlin, "The influence of Cu substitution on the hydrogen sorption properties of Magnesium rich Mg-Ni films", International Journal of Hydrogen Energy 2011, vol. 36, 2154-2164.

Chapter 5 of this thesis has been published as XueHai Tan, Liya Wang, Chris M. B. Holt, Beniamin Zahiri, Michael H. Eikerling, David Mitlin, "Body Centered Cubic Magnesium Niobium Hydride with Facile Room Temperature Absorption and Four Weight Percent Reversible Capacity", Physical Chemistry Chemical Physics 2012, vol. 14, 10904-10909.

Chapter 6 of this thesis has been published as XueHai Tan, Liya Wang, Beniamin Zahiri, Alireza Kohandehghan, Dimitre Karpuzov, Elmira Memarzadeh Lotfabad, Zhi Li, Michael H. Eikerling, David Mitlin, "The Effect of an Atomic Layer Deposition (ALD)

Titanium Oxynitride Interlayer on the ORR Activity and Corrosion Stability of Pt and Pt-Ni", ChemSusChem 2014, doi:.

Chapter 7 of this thesis has been submitted as XueHai Tan, Sagar Prabhudev, Alireza Kohandehghan, Dimitre Karpuzov, Gianluigi A. Botton, Michael H. Eikerling, David Mitlin, "Pt-Au-Co Alloy Electrocatalysts Demonstrate Enhanced Activity and Durability towards Oxygen Reduction Reaction", ACS Catalysis 2014, doi:.

For each work presented in this thesis, I was involved in the concept formation, and was responsible for the performance of experiments, the data collection and analysis, and the manuscript composition. Dr. David Mitlin was the supervisory author and was involved in the concept formation and the manuscript composition. In chapter 4 and 5, the modeling works based on density functional theory calculations were conducted by Liya Wang and Michael H. Eikerling from Simon Fraser University, as part of research collaboration within the network of Catalysis Research for Polymer Electrolyte Fuel Cells (CaRPE FC). In chapter 6, the atomically-resolved high angle annular dark field (HAADF) and electron energy loss spectroscopy (EELS) analysis were conducted by Sagar Prabhudev and Gianluigi A. Botton from McMaster University, as part of research collaboration within the network of CaRPE FC. The other coauthors, which are not particularly mentioned here, have contributed either to the discussion of research topics, and/or to the operation of scanning electron microscope and photoelectron spectrometer.

This thesis is dedicated to

My loving parents, KaiLin Tan and Yan Zuo

My loving girlfriend, Ran Ma

Acknowledgements

Here I would like to acknowledge everyone who has contributed to the coming together of this thesis. First and foremost, I would like to thank my PhD supervisor, Prof. David Mitlin, for his great support during the course of my research. His scientific inputs, critical reviews on manuscript preparation, and generosity for providing me the resource that I required are invaluable for what I have accomplished. My gratitude also goes to every member of Mitlin Group for his or her unconditional help. It has been wonderful time for me to work with them in the past six years. In particular, I want to thank Dr. Peter Kalisvaart, who gave me precious help during the most difficult time. I have to mention Dr. Beniamin Zahiri, who was my “comrade-in-arms” for both research projects of hydrogen storage and oxygen reduction reaction electrocatalysts. Our endless discussion on various research topics has indeed helped me throughout my PhD thesis. My sincere thanks also go to all the technicians and staff members of Chemical and Materials Engineering Department, National Institute for Nanotechnology, Center for Surface Engineering and Science and Cross-Cancer Institute at University of Alberta. Without the continued training and support from them, this thesis would not be possible. Furthermore, I very appreciate the fruitful collaboration with Liya Wang and Michael H. Eikerling from Simon Fraser University. Their modeling works based on density functional theory calculations have been reflected in chapters 4 and 5 in this thesis. I as well appreciate the fruitful collaboration with Sagar Prabhudev and Gianluigi A. Botton from McMaster University. Their atomically resolved high angle annular dark field (HAADF) and electron energy loss spectroscopy (EELS) analysis have been reflected in chapters 6 in this thesis. Last but not least, my heartfelt thanks go to my parents and my girlfriend for their unconditional love and support through all my graduate studies. This thesis is dedicated to them.

Table of Contents

List of Tables

List of Figures

List of Abbreviations

Abbreviation	Meaning
ALD	Atomic layer deposition
bcc	Body-centered cubic
CV	Cyclic voltammetry
CVD	Chemical vapor deposition
DFT	Density functional theory
ECSA	Electrochemical surface area
EDS	Energy-dispersive x-ray spectroscopy
EELS	Electron energy loss spectroscopy
EIS	Electrochemical impedance spectroscopy
fcc	Face-centered cubic
IBA	Integral breadth analysis
FIB	Focused ion beam
FWHM	Full width half maximum
GADDs	General area 2-dimensional detection system
HAADF	High-angle annular dark field
hcp	Hexagonal close packed
JMA	Johnson-Mehl-Avrami
LSV	Linear sweep voltammetry
LSW	Lifshitz-Slyozov-Wagner
NG	Nucleation and growth
ORR	Oxygen reduction reaction

PCI	Pressure-composites isotherms
PCT	Pressure-composition-temperature
PEMFCs	Proton exchange membrane fuel cell
PVD	Physical vapor deposition
SAD	Selected area electron diffraction
SEM	Scanning electron microscopy
SMSI	Strong metal-support interactions
RDE	Rotating disk electrode
RHE	Reversible hydrogen electrode
SEM	Scanning electron microscopy
STEM	Scanning transmission electron microscopy
TEM	Transmission electron microscopy
XRD	X-ray diffraction
XPS	X-ray photoelectron spectroscopy
upd	Underpotential deposition
UPS	Ultraviolet photoelectron spectroscopy
ZA	Zone axis

Chapter 1

Introduction

1.1 Hydrogen as an energy carrier

Despite the recent discoveries of large shale gas reserves, the concerns of the excessive greenhouse gas emission, national energy security and economic stability still demand the adoption of renewable energy sources. A key hurdle for the large-scale integration of some most important renewable energy resources, for example the solar and wind energies, into our energy system is their intermittent characteristic. Consequently, clean energy carriers that can store the generated energy and also facilitate transportation are necessary to balance the dynamic changing between the energy demand and the intermittent supply. In many ways, hydrogen is the leading candidate as an energy carrier to store the excess energy produced in peak hours. Its chemical energy can be converted to electricity with high-energy efficiency during peak demand time. To realize the future "hydrogen economy", a hydrogen-centered energy system requires both reliable mechanism for storage of the hydrogen and high efficient energy conversion to electricity. Stored hydrogen can be used in two forms: as a gas in e.g. proton exchange membrane fuel cells (PEMFCs) [1] or electrochemically in rechargeable Nickel-Metal Hydride (NiMH) batteries [2], which can be used in portable applications or in Hybrid Electric Vehicles (HEVs) [3]. This thesis concerns the technologies related to the former scenario.

1.2 Overview of hydrogen storage

At present, there are a number of different storage options for hydrogen. It can be stored under very high pressures in containers, as a liquid at cryogenic temperatures, or within a “material-based” hydrogen storage system using the interaction of hydrogen with various materials [4].

Currently, pressurized hydrogen gas and cryogenically liquefied hydrogen are the two main commercially available options for hydrogen storage. These two storage technologies however suffer from high operating pressure safety hazards, non-competitive energy efficiency/cost and their low volumetric densities. The latter deficiency can be a major impediment when volumetric constraints are imposed on the design of storage system, e.g. in transportation applications.

The material-based hydrogen storage has the potential to reach higher volumetric density than that of liquid hydrogen, which has a density of 70 kg m^{-3} [5]. The material-based hydrogen storage systems can be generally categorized into metal hydrides, chemical hydrides and carbon-based large surface area materials [6]. Metal hydrides provide a possibility to reversibly store and extract hydrogen through the hydride formation and decomposition reaction, respectively [7]. Since the discovery of hydrogen absorption by palladium in 1866 [8], metal hydrides have been intensively studied. Metal hydrides can be further classified into three groups depending on the character of the metal-hydrogen bond [9], including covalent hydrides such as SnH_4 and AlH_3, interstitial hydrides such as $PdH_{0.7}$ and $LaNi_5H_6$ and ionic hydrides such as NaH and MgH_2. The latter case of storing hydrogen as MgH_2 is the focus of the present thesis and will be studied in detail in the following chapters. Chemical hydrides are referred to the systems when hydrogen is produced by the chemical reaction of a hydride, generally with water or an alcohol. This reaction is not easily reversible on-board of a vehicle. The spent fuel and the by-products of the hydrogen generation reaction should be removed from the vehicle and regenerated in a plant [10]. The last category, carbon-based high surface area materials, takes advantage of the small surface forces to adsorb hydrogen molecule on large surface area materials, e.g. metal organic frameworks (MOF) or different forms of carbon allotropes. As the magnitudes of these surface interactions are small, these storage techniques usually operate at low temperatures [11].

1.2.1 Magnesium as a hydrogen storage medium

For a hydrogen storage technology to be viable, it must store more than 5.5 wt.% of hydrogen as stated in the U.S. Department of Energy (DoE) target for 2015 [4,12]. Pure Mg has a competitively high reversible hydrogen storage capacity, storing up to 7.6 wt.% H with a volumetric hydrogen density of 110 kg m^{-3} upon transformation to MgH_2. Also, Mg is cheap, safe and non-toxic. These make MgH_2 a very attractive hydrogen storage medium in principle.

The biggest issue of MgH_2 originates from its excessive stability (enthalpy of hydride formation is approximately −77 kJ mol^{-1} H_2) [13], which requires either high temperature or very low pressure for the hydride to decompose. Using the standard Van't Hoff equation:

$$\ln\left(\frac{P_{eq}}{P^0}\right) = \frac{\Delta H^0}{RT} - \frac{\Delta S^0}{R} \qquad \text{(Eq. 1.1)}$$

where P_{eq} is the equilibrium hydrogen partial pressure; ΔH^0 and ΔS^0 indicate the standard enthalpy and entropy of hydride formation, respectively, this would yield an equilibrium hydride decomposition temperature of more than 300°C at 1 bar hydrogen pressure. This temperature-pressure combination is unsuitable for any on-board hydrogen storage application, since the target of operating temperature at 1 bar hydrogen pressure for transportation application is -50 to 150°C [14].

Besides, hydrogen absorption and desorption are kinetically slow, arising both from the sluggish phase transformation, and the high oxidation sensitivity of Mg surface. To break down the kinetic limitations of Mg $\leftrightarrow$ MgH_2 phase transformation into individual possible rate-limiting step, the slow kinetics is due to the high energy barrier for hydrogen dissociation and recombination [15,16], very slow hydrogen diffusion through MgH_2 [17] and through Mg [18], and the difficulty of nucleation of Mg in hydride and vise-versa, given the large volumetric and chemical interfacial energy mismatch between Mg and MgH_2 [19,20].

Numerous studies have aimed to overcome the kinetic limitations by the addition of catalysts to enhance the dissociation rate of hydrogen at the Mg surface and by reducing the particle size to shorten the diffusion length [21-25]. There are also some recent promising studies where researchers have shown thermodynamic destabilization of MgH_2 through selective alloying [26-29] or creation of constrained nanolayered structures [30,31]. Despite great efforts to overcome its limitations, practical application of Mg remains problematic.

1.3 The Hydrogen-driven Fuel cell

The hydrogen stored in Metal Hydrides when released via the gas phase can be used in a PEMFC, which produces electricity from the electrochemical oxidation of hydrogen. A schematic picture of a PEMFC is shown in Figure 1.1.

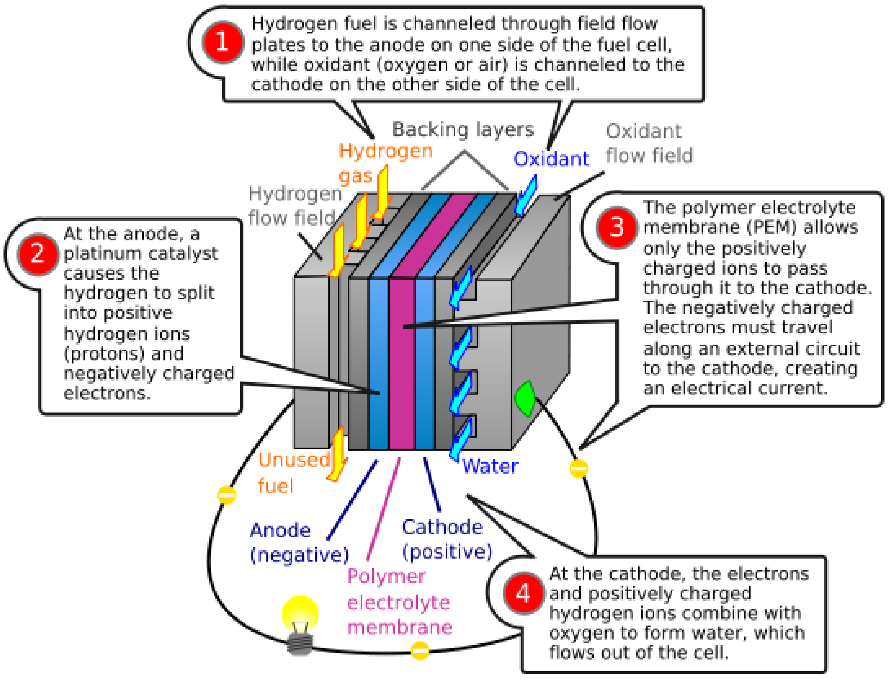

① Hydrogen fuel is channeled through field flow plates to the anode on one side of the fuel cell, while oxidant (oxygen or air) is channeled to the cathode on the other side of the cell.

② At the anode, a platinum catalyst causes the hydrogen to split into positive hydrogen ions (protons) and negatively charged electrons.

③ The polymer electrolyte membrane (PEM) allows only the positively charged ions to pass through it to the cathode. The negatively charged electrons must travel along an external circuit to the cathode, creating an electrical current.

④ At the cathode, the electrons and positively charged hydrogen ions combine with oxygen to form water, which flows out of the cell.

Figure 1.1: Schematic overview of a hydrogen-driven PEM fuel cell [32].

The chemical reactions taking place inside a fuel cell are simple. On the anode, the gaseous hydrogen fuel is oxidized into protons and electrons:

$$H_2(g) \xrightarrow{catalyst} 2H^+ + 2e^- \qquad \text{(Eq. 1.2)}$$

where the protons migrate towards the cathode through a polymer membrane electrolyte, and the electrons travel through an external circuit. On the cathode, the oxygen gas (air) is recombined with the protons and electrons to form water:

$$O_2(g) + 4H^+ + 4e^- \xrightarrow{catalyst} 2H_2O \qquad \text{(Eq. 1.3)}$$

This reaction is referred as the oxygen reduction reaction (ORR) that proceeds with the complete 4-electron reduction mechanism. As a result, the process produces only water and heat as the by-products, and the electrons that are moving through an external circuit could drive e.g. an electric motor in an automobile.

Fuel cell vehicles powered by hydrogen from secure and renewable sources have one of the highest potential for reducing greenhouse gas emission [33]. Over the past decade, extensive research and development on all aspects of this technology has delivered prototype cars with impressive performances; however, taking the step towards the successful commercialization still requires the PEMFCs to meet three major criteria: cost, performance and durability [34]:

1. At present, the PEMFCs require relatively high loading of platinum, because the cathode ORR and anode hydrogen oxidation reaction both occur on the surfaces of Pt-based catalysts. Though substantial gains have been made in the development of low cost non-noble electrocatalysts [35 - 37], Pt-based electrocatalysts continue to remain as the key commercialization target due to their unsurpassed catalytic activities [38-40]. The high price of this scarce precious metal consequently has a decisive impact on the costs of PEMFCs.
2. The performance of fuel cell strongly depends on the catalytic efficacy of the ORR catalysts. The cathode ORR is orders of magnitude slower than the anode hydrogen oxidation reaction, and thus limits the performance of PEMFCs [34].
3. The development criteria for automotive fuel cell electrocatalysts must also meet the durability target of hundreds of thousands of load cycles over the 5000-hour operation lifetime [34]. However, the widely used cathode electrocatalysts

nowadays, such as carbon-supported Pt nanoparticles, degrade during operation. This is due to the tendency for the cathode to reach potentials higher than the onset of Pt dissolution and carbon oxidation [41,42].

Given these technical challenges stated above, most research and development is focusing on improving the cathode catalyst and electrodes. Finding a way to reduce the Pt loading i.e. the cost without the loss of performance and durability is the subject of most ORR electrocatalyst research.

1.4 Scope of this thesis

The present thesis is focused on the design and characterization of various alloys and composites for application of solid state hydrogen storage and of PEMFCs cathode electrocatalysts, aiming to tackle all the technical issues that are stated above. In chapter 2 to 5, the thesis is centered on hydrogen storage in solid state using magnesium-based alloys and composites as the storage medium. The content embodies my research findings of several new catalyst designs for accelerating the hydrogen sorption kinetics, and of the discovery of metastable alloys with favorably altered thermodynamics to lower the required hydriding/dehydriding temperatures. In chapter 6 and 7, the thesis is centered on electrocatalysts for cathode oxygen reduction reaction. The content embodies my research findings of several multicomponent Pt-based alloys with outstanding ORR activity and corrosion stability. Several catalyst supports including different carbon allotropes and metal oxide/nitride are also investigated.

There are several approaches of alloy design that are involved in this thesis. In each chapter, the details of alloy design including the targeting technical issues, the selection of alloy elements and compositions, the wanted crystal structure and microstructural properties, and the resulting hydrogen storage / ORR properties are clearly presented.

1.5 Materials Preparation

In this thesis, alloy design is one essentially coherent topic that is involved in both hydrogen storage and ORR electrocatalyst research. All the materials designed and tested in this thesis were fabricated by co-sputtering technique in the form of thin films or dewetted nanoparticles. Thin film can serve as ideal model system for alloy design to search for promising alloy composition and structure, which may be then translated to bulk material. Thin film deposition by co-sputtering is a high throughput screening method, allowing rapid synthesis and testing of numerous compositions and microstructure. Co-sputtering also has excellent stoichiometry control, and more importantly can repeatably synthesize both metastable or equilibrium structure. Metastable alloys, which are not predicted by equilibrium phase diagram or are not achievable at ambient condition using conventional material synthesis techniques, are expected to possess enhanced performance for both applications of Mg-based hydrogen storage and Pt-based ORR electrocatalysts.

1.5.1 Sputtering

Sputtering is a physical vapor deposition technique that involves using ionized noble gas atoms (typically argon) to kinetically eject atoms from a target surface in a vacuum chamber. The positive charged noble gas ions are accelerated toward the target with sufficient kinetic energy, causing cascade of collisions on the target surface. Part of the target atoms will be ejected out and travel towards a substrate to deposit a thin film with desired composition. Sputtering requires sustained plasma created by ionizing the noble gas, in order to have continuous ions bombardment on the target surface. For better efficiency, powerful magnets are mounted behind the target (*magnetron sputtering*), so that electrons will be trapped by the magnetic fields, which cause a much higher ionization fraction of the sputtering gas near the target surface. As a result, the deposition rate can be increased by an order of magnitude via magnetron sputtering.

In DC sputtering, the entire vacuum chamber and most equipment inside are grounded, with the exception that the deposition target is kept at a large negative potential. In such a way, the positive gas ions will be continuously accelerated towards the target. This method is suited to sputter highly conductive materials such as metals, which are the majority of materials used to fabricate Mg-based or Pt-based alloys. For dielectric materials, i.e. metal oxides, radiofrequency (RF) or pulsed-DC sputtering must be used. The periodic polarity reversal of the target potential prevents the charges build-up on the target surface and allows the deposition of virtually any material, but at much slower rates than that of DC magnetron sputtering.

1.6 Reference

[1] F. Barbir, *PEM fuel cells: theory and practice*, Elsevier Academic Press, London, **2005**.

[2] P. H. L. Notten, *Rechargeable nickel-metal hydride batteries: a successful new concept*, in: F. Grandjean, G. J. Long, K. H. J. Buschow (Editors), *Interstitial Intermetallic Alloys*, NATO ASI Series E, vol. 281, **1995**.

[3] R. F. Nelson, *J. Power Sources,* **2000**, *91*, 2-26.

[4] The US Department of Energy (DOE), Office of Energy Efficiency & Renewable Energy, http://energy.gov/eere/fuelcells/hydrogen-storage-current-technology.

[5] The US Department of Energy (DOE), Office of Energy Efficiency & Renewable Energy, http://energy.gov/eere/fuelcells/gaseous-and-liquid-hydrogen-storage.

[6] The US Department of Energy (DOE), Office of Energy Efficiency & Renewable Energy, http://energy.gov/eere/fuelcells/materials-based-hydrogen-storage.

[7] J. Graetz, *Chem. Soc. Rev.* **2009**, *38*, 73-82.

[8] T. Graham, *Phil. Trans. R. Soc.* **1866**, *156*, 399-439.

[9] W. M. Müller, J. P. Blackledge, J. J. Libowitz, *Metal hydrides*, Academic press, New York, **1968**.

[10] The US Department of Energy (DOE), Office of Energy Efficiency & Renewable Energy, http://energy.gov/eere/fuelcells/chemical-hydrogen-storage.

[11] The US Department of Energy (DOE), Office of Energy Efficiency & Renewable Energy, http://energy.gov/eere/fuelcells/carbon-based-materials-high-surface-area-sorbents-and-new-materials-and-concepts.

[12] D. Pukazhselvan, V. Kumar, S. K. Singh, *Nano Energy* **2012**, *1*, 566-589.

[13] X. Tan, L. Wang, C. M. B. Holt, B. Zahiri, M. H. Eikerling, D. Mitlin, *Phys. Chem. Chem. Phys.* **2012**, *14*, 10904-10909.

[14] P. P. Edwards, V. L. Kuznetsov, W. I. F. David, *Phil. Trans. R. Soc.* A **2007**, *365*, 1043-1056.

[15] A. J. Du, S. C. Smith, X. D. Yao, G. Q. Lu, *J. Phys. Chem. B* **2005**, *109*, 18037-18041.

[16] G. Wu, J. Zhang, Q. Li, Y. Wu, K. Chou, X. Bao, *Comput.Mater.Sci.* **2010**, *49*, S144-S149.

[17] S. Hao, D. S. Sholl, *Appl. Phys. Lett.* **2008**, *93*, 251901.

[18] H. G. Schimmel, G. J. Kearley, J. Huot, F. M. Mulder, *J. Alloy. Compd.* **2005**, 404-406, 235-237.

[19] M. Danaie, S. X. Tao, P. Kalisvaart, D. Mitlin, *Acta Mater.* **2010**, *58*, 3162-3172.

[20] X. Tan, B. Zahiri, C. M. B. Holt, A. Kubis, D Mitlin, *Acta Mater.* **2012**, *60*, 5646-5661

[21] W. P. Kalisvaart, C. T. Harrower, J. Haagsma, B. Zahiri, E. J. Luber, C. Ophus, E. Poirier, H. Fritzsche, D. Mitlin, *Int. J. Hydrogen Energ.* **2010**, *35*, 2091-2103.

[22] W. P. Kalisvaart, A. Kubis, M. Danaie, B. S. Amirkhiz, D. Mitlin, *Acta Mater.* **2011**, *59*, 2083-2095.

[23] A. Borgschulte, R. Gremaud, *Phys. Rev. B* **2008**, *78*, 094106.

[24] M. Dornheim, N. Eigen, G. barkhordarian, T. Klassen, R. Bormann, *Adv. Eng. Mater.* **2006**, *8*, 377-385.

[25] B. Sakintuna, F. Lamari-Darkrim, M. Hirscher, *Int. J. Hydrogen Energm* **2007**, *32*, 1121-1140.

[26] R. Gremaud, C. P. Broedersz, A. Borgschulte, M. J. van Setten, H. Schreuders, M. Slaman, B. Dam, R. Griessen, *Acta Mater.* **2010**, *58*, 658-668.

[27] S. X. Tao, P. H. L. Notten, R. A. van Santen, A. P. J. Jansen, *Phy.s Rev. B* **2010**, *82*, 125448.

[28] M. G. Shelyapina, D. Fruchart, *Solid State Phenom.* **2011**, *170*, 227-231.

[29] M. Dornheim, S. Doppiu, G. Barkhordarian, U. Boesenberg, T. Klassen, O. Gutfleisch, R. Bormann, *Scripta Mater.* **2007**, *56*, 841-846.

[30] A. Baldi, M. Gonzalez-Silveira, V. Palmisano, B. Dam, R. Griessen, *Phys. Rev. Lett.* **2009**, *102*, 226102.

[31] L. P. A. Mooij, A. Baldi, C. Boelsma, K. Shen, M. Wagemaker, Y. Pivak, H. Schreuders, R. Griessen, B. Dam, *Adv. Energy Mater.* **2011**, *1*, 754-758.

[32] http://www.fueleconomy.gov

[33] F. T. Wagner, B. Lakshmanan, M. F. Mathias, *J. Phys. Chem. Lett.* **2010**, *1*, 2204-2219.

[34] M. K. Debe, *Nature* **2012**, *486*, 43-51.

[35] T. Maiyalagan, K. A. Jarvis, S. Therese, P. J. Ferreira, A. Manthiram, *Nature Commun.* **2014**, *5*, 3949.

[36] a) D. Yu, Y. Xue, L. Dai, *J. Phys. Chem. Lett.* **2012**, *3*, 2863-2870; b) I-Y Jeon, H-J Choi, S-M Jung, J-M Seo, M-J Kim, L. Dai, J-B Baek, *J. Am. Chem. Soc.* **2013**, *135*, 1386-1393; c) H. Zhong, H. Zhang, Z. Xu, Y. Tang, J. Mao, *ChemSusChem*, **2012**, *5*, 1698-1702.

[37] a) Y. Liang, H. Wang, P. Diao, W. Chang, G. Hong, Y. Li, M. Gong, L. Xie, J. Zhou, J. Wang, T. Z. Regier, F. Wei, H. Dai, *J. Am. Chem. Soc.* **2012**, *134*, 15849-15857; b) Z. Yang, X. Zhou, Z. Jin, Z. Liu, H. Nie, X. Chen, S. Huang, *Adv. Mater.* **2014**, *26*, 3156-3161.

[38] P. Strasser, S. Koh, T. Anniyev, J. Greeley, K. More, C. Yu, Z. Liu, S. Kaya, D. Nordlund, H. Ogasawara, M. F. Toney, A. Nilsson, *Nature Chem.* **2010**, *2*, 454-460.

[39] U. Martinez, A. Serov, M. Padilla, P. Atanassov, *ChemSusChem* **2014**, *7*, 2351 – 2357.

[40] I. E. L. Stephens, A. S. Bondarenko, U. Gronbjerg, J. Rossmeisl, I. Chorkendorff, *Energy Environ. Sci.* **2012**, *5*, 6744-6762.

[41] J. C. Meier, C. Galeano, I. Katsounaros, A. A. Topalov, A. Kostka, F. Schuth, K. J. J. Mayrhofer, *ACS Catal.* **2012**, *2*, 832-843.

[42] Y. Shao, G. Yin, Y. Gao, *J. Power Sources,* **2007**, *171*, 558-566.

Chapter 2

Nano-scale bilayer Pd/Ta, Pd/Nb, Pd/Ti and Pd/Fe catalysts for hydrogen sorption in magnesium thin films*

2.1 Introduction

Magnesium-based thin films are subject to intense scientific inquiry as they are becoming increasingly more utilized for optical hydrogen sensing, switchable mirrors and solar absorbers, and as model alloys for designing and understanding bulk hydrogen storage materials [1-7]. Magnesium and magnesium oxide are known to have poor activity towards hydrogen dissociation, which is the first step in the absorption process. Because of this, Pd catalyst films are normally deposited on the fresh magnesium surfaces to aid the sorption kinetics. Increasingly, these catalysts consist of bilayers, consisting of Pd on an oxide or a metallic support. This intermediate layer serves the critical role of reducing the highly deleterious interdiffusion between the Pd and the underlying hydrogen storing material [8]. Bilayer catalysts may also exhibit enhanced kinetics due to strong-metal support-interactions (SMSI) [9], though this effect is less explored for two metals as it is for metals on oxide supports.

Remhof et al. was the first to utilize a metallic (Nb) intermediate layer between the catalytically active palladium cap and the hydrogen storing yttrium phase, though not

---

[*] Materials in this chapter has been published in:

- XueHai Tan, Christopher T. Harrower, Babak Shalchi Amirkhiz, David Mitlin, International Journal of Hydrogen Energy 2009, 34, 7741-7748.

providing a comparison of the sorption kinetics without it [10]. An early work on oxide-based intermediate layers for hydrogen storing materials was by researchers who examined nano-scale Y_2O_3 buffer layers for YH_x [11], and nano-scale AlO_x buffer layers for LaH_x and YH_x [12]. In both studies the authors concluded that the presence of an intermediate oxide layer did not impede hydrogen loading. Rather these purposely grown buffer layers had a beneficial role of impeding the interdiffusion of the active base metal and the Pd catalytic cap. The interdiffusion would presumably result in the formation of a discontinuous layer of binary intermetallics, the oxidation of the underlying active metal, and a subsequent loss of hydrogen dissociation catalytic activity. Subsequent studies utilized Ti or Fe underlayers to reduce the interdiffusion of the palladium with the base material and the consequent formation of intermetallics [13-19]. The base materials tested include pure Mg, a range of Mg–Ni alloys, Y and Mg–Al alloys.

It is difficult to provide a systematic comparison of the bilayer scientific literature since in the above studies not only did the materials for the base and the intermediate layers differ, but so did the individual layer thicknesses, as well as the conditions for hydrogen loading (temperature, pressure, volumetric vs. electrochemical). Therefore one cannot establish a systematic trend in the degree of underlayer effectiveness in terms of long-term microstructural stability. That is the goal of this study: To provide a systematic comparison of the sorption cycling behavior for a range of bilayer catalysts using identical sample geometries and sorption conditions for each one. We chose bilayer combinations of Pd/Nb, Pd/Ti and Pd/Fe, Pd/Ta, using pure Pd as a baseline. The elements Nb, Ti and Fe are explored because various researchers have utilized them as intermediate layers for several base materials. Tantalum is chosen because it is well known as an excellent diffusion barrier for metals [20]. It also possesses a very high hydrogen permeability (1.3×10^{-7} mol/ms $Pa^{1/2}$ at 500 °C) [21]. We chose pure magnesium as the base material since it represents the simplest case in terms of the equilibrium phases formed upon hydrogen sorption (α-MgH_2) and has well defined equilibrium binary phase diagrams with both the Pd and the intermediate layers [22].

2.2 Experimental

The samples consisted of 1.5 μm Mg films coated with bilayer 7.5 nm Pd/7.5 nm Fe (or Ti or Nb or Ta) catalysts on both the top and the bottom Mg surfaces. The transition metal served as an intermediate layer between the Mg and the Pd. A 15 nm Pd single-layer film, on both top and bottom, was used as a baseline. The films were sputtered onto a nominally room temperature 4 inch Si (100) substrate that was coated with a hardened (so as not to outgas in the chamber) photoresist. Inside the sputter system the thin films stack had following sequence: vacuum/7.5 nm Pd/7.5 nm transition metal/1.5 μm Mg/7.5 nm transition metal/7.5 nm Pd/photoresist/Si wafer.

After deposition the photoresist was washed away using acetone allowing the films to be fully released from the Si wafer. Release from the substrate allowed the films to be treated as free powders, in turn allowing for both accurate volumetric sorption testing and XRD analysis. During the release step, the films developed cracks perpendicular to their surface, disintegrating into millimeter and micron-scale flakes. The ultimate geometry of the films was that of powder-like flakes that were 1.5 μm thick with the bilayer catalysts coating the top and the bottom flake surfaces. Figure 2.1A shows a SEM micrograph of a cross section of the Pd/Nb catalyzed Mg thin film flake after removal from the wafer and prior to testing. The bilayer catalyst coats the Mg film conformally. Figure 2.1B shows a plan-view SEM micrograph of the top flake surface revealing the morphology of the Mg grains. The Mg is microcrystalline with columnar grain morphology.

Depositions of the catalysts and of the bulk Mg were performed sequentially without any interruption. We used Ar gas with a purity of 99.999% at a sputtering pressure of 5×10^{-3} mbar, with a maximum base pressure of 5×10^{-8} mbar. Deposition was performed using a DC-magnetron co-sputtering system (AJA International). The substrate temperature was maintained near ambient. Deposition was done in a sputter-up configuration with continuous substrate rotation. Film thickness and deposition rates were obtained through the use of crystal deposition rate monitor held at the substrate plane. A separate series of experiments involving ex-situ film thickness measurements versus deposition parameters were used to cross check the thickness/rate accuracies. The deposition rates were the following: Mg 3; Pd 1.7; Ta 0.3; Ti 0.4; Nb 0.4; and Fe 0.7 Å s^{-1}.

Volumetric absorption and desorption measurements were performed on a Sieverts hydrogen sorption analysis system (Hy-Energy LLC. PCTPro 2000). All the measurements were carried out at 250 °C. All specimens were absorbed at a starting pressure near 2.5 bar and desorbed at a starting pressure near 0.05 bar. Samples received up to 8 absorption/desorption cycles.

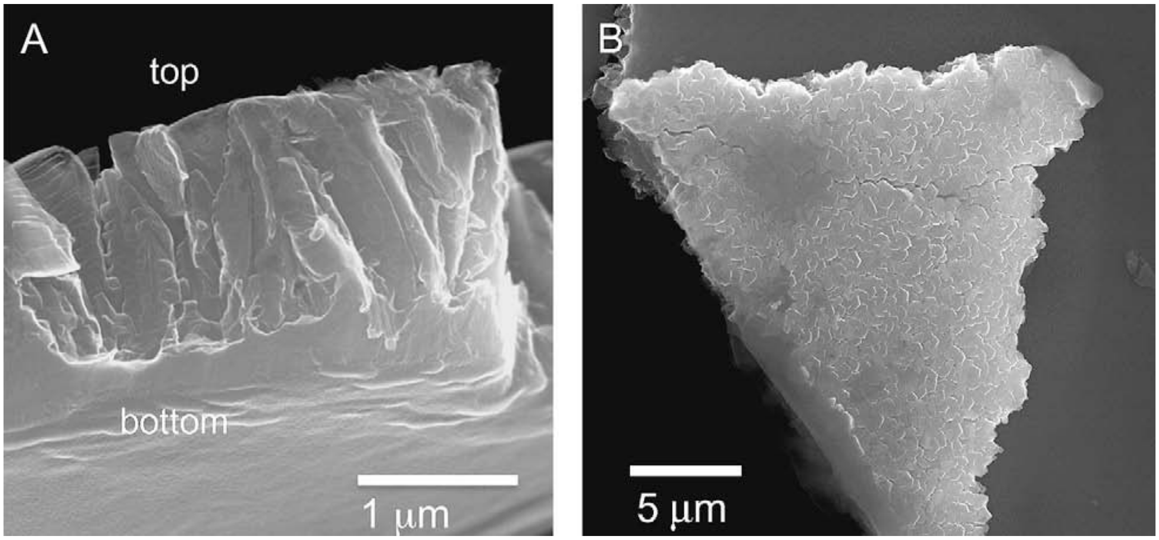

Figure 2.1: (A) SEM micrograph of a cross section of the Pd/Nb catalyzed Mg thin film flake after removal from the wafer and prior to testing. The 7.5 nm Nb/Pd bilayer (present, though not discernable) coats both surfaces, with the Nb being in contact with the Mg. (B) Plan-view SEM micrograph of the top flake surface revealing the morphology of the Mg grains.

We used scanning electron microscopy (SEM) to analyze the morphology of the films. A Hitachi S-4800 SEM was operated at 7 kV accelerating voltage. Imaging was performed in secondary electron mode. The loose film flakes where mounted onto SEM stubs using conductive carbon tape. X-ray diffraction experiments were performed on a Bruker AXS diffractometer (Bruker Discover 8) using a copper Kα radiation source (λ = 0.1541 nm) that was monochromatized using a single Gobel mirror. Geometry of the system was in the Bragg-Brentano Geometry with a general area 2-dimensional detection system (GADDs). The data from the XRD database on EVA^{TM} software were used for peak identification. Additional simulation of the peaks was performed using Desktop Microscopist^{TM} commercial electron and X-ray diffraction simulation package using the well-known crystallographic information of the metals, intermetallics and hydrides. The samples were analyzed by XRD directly after the last sorption cycle shown in the accompanying figure. The samples analyzed by Sieverts and XRD were in powder form after having been removed from the Si wafer by dissolving the photoresist.

2.3 Results

Figure 2.2A shows the absorption and desorption data of the Mg films with the baseline 15 nm Pd capping layers. At 250 °C the kinetics are very slow, agreeing with the commonly reported observation that pure magnesium requires temperatures in excess for 300 °C for appreciable sorption [23,24]. The absorption time for the first cycle was 2.5 h. While the magnesium would have taken on more hydrogen if held for longer times the point was to demonstrate the sluggishness of the baseline reaction. After two and a half hours, less than 1 wt.% hydrogen is absorbed (theoretical capacity of MgH_2 is 7.6 wt.%) and the majority of the magnesium remains metallic. The sample was even slower in desorption, essentially possessing negligible rates at the 0.05 bar hydrogen pressure. Subsequent attempts to absorb and desorb this microstructure were not successful. As we will demonstrate in the rest of the figures, the sorption rates achieved with various bilayer catalysts are orders of magnitude higher at identical pressure/temperature sorption conditions. Figure 2.2B shows that XRD pattern obtained from the sample after the last attempted desorption cycle (desorption data taken from 4.5 to 5 h). As expected the base material microstructure is a mixture of magnesium that displays peaks of the highest intensity and some α-MgH_2. No Pd peaks were detected. Instead clear and relatively intense Mg_6Pd intermetallic peaks were present, indicating almost complete (within the detection limits of the XRD analysis) reaction of the Pd with the Mg at elevated temperatures.

Figures 2.3–2.6 will show the sorption and the XRD data for the Pd/Fe, Pd/Ta, Pd/Nb and Pd/Ti bilayer catalysts. Figure 2.7 will provide a comparison of the absorption and desorption times for each of these systems as a function of sorption cycle number. Figure 2.3A demonstrates that the initial absorption/desorption behavior of Mg with the Pd/Fe bilayer catalysts is markedly different from the case when single-phase Pd was used. In the first sorption cycle the Pd/Fe sample absorbs over 4 wt.% hydrogen in 10 min. The first desorption cycle is also quite encouraging: 12 min to fully desorb. However the subsequent sorption cycle is much less impressive, with the required time to absorb 4 wt.% hydrogen being an hour. Subsequent desorption is not possible, with the sample losing only about 0.5 wt .% before the kinetics become very sluggish.

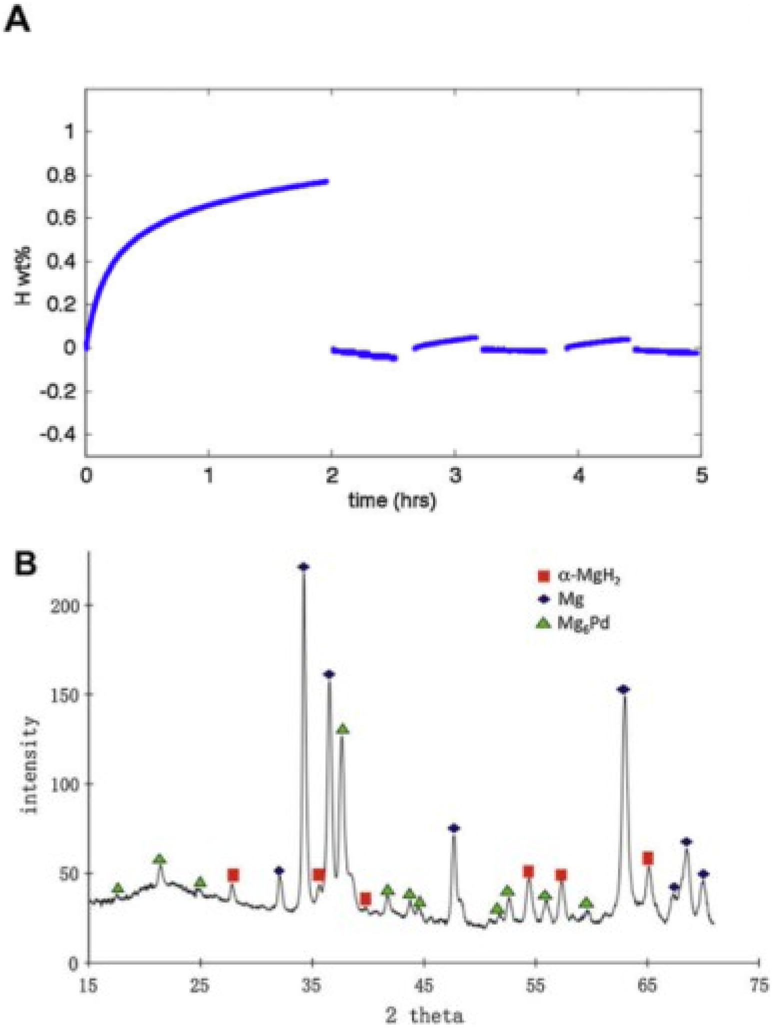

Figure 2.2: Cycled kinetics of magnesium with Pd catalyst layers. The corresponding XRD pattern after the last sorption cycle (partial desorption). For all samples in this study absorption was at 2.5 bar hydrogen and desorption was at 0.05 bar hydrogen. The testing temperature was 250 °C.

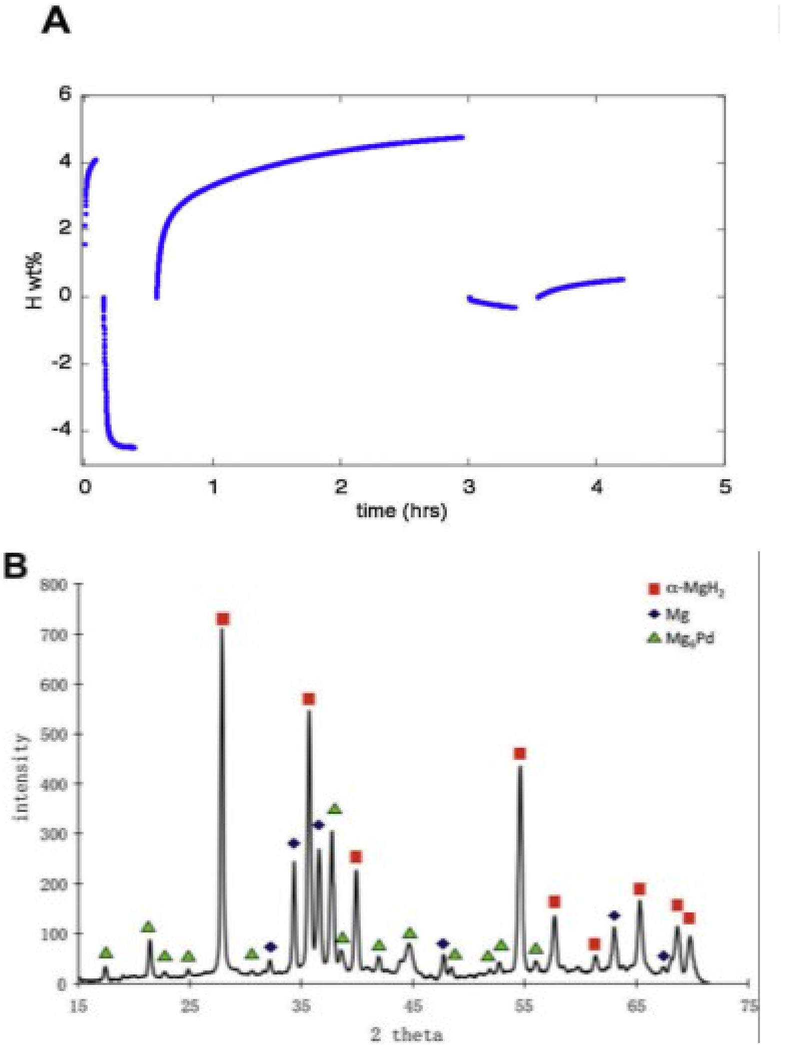

Figure 2.3: Cycled kinetics of magnesium with Pd/Fe bilayer catalysts. The corresponding XRD pattern after the last sorption cycle (absorption).

The XRD pattern shown in the Figure 2.3B is of the specimen after the last sorption cycle. The sample should nominally contain 4 wt.% hydrogen, and hence be only partially sorbed. The theoretical capacity for pure MgH_2 is 7.6 wt.%. The theoretical capacity of the composite should be lower due to the presence of the bilayer catalysts on both film surfaces. As expected the XRD pattern shows the presence of a-MgH_2 as well as unsorbed Mg. Interestingly the other dominant phase that is clearly present in the material is the Mg_6Pd intermetallic. This is somewhat surprising considering that the Mg and the Pd were not in contact in the as-synthesized films. This result can be qualitatively understood by considering the phase diagrams for Mg–Fe, Mg–Pd and Fe–Pd [22].

Magnesium and Fe are virtually immiscible and do not form any intermediate phases. Magnesium and Pd form a series of intermetallics with the Mg_6Pd being the stable phase on the Mg-rich side. The Fe–Pd phase diagram consists of an α-Fe phase, with negligible solubility for Pd at 250 °C, in equilibrium with ordered Fe–Pd having the prototype AuCu structure. At higher Pd compositions the ordered $FePd_3$ phase is formed (prototype $AuCu_3$). This phase is unlikely since at a bilayer film thickness of 7.5 nm/7.5 nm there is not enough Pd to fully react with the Fe. A possible scenario is that at elevated temperatures the Pd and Fe interdiffuse, forming a Fe–Pd alloy that is in contact with the underlying Mg. The formation of Mg_6Pd then ensues with the accompanying loss of catalytic activity for hydrogen dissociation/reassociation.

Figure 2.4 shows the cycling and the XRD data for the Pd/Ta bilayer samples. Figure 2.4A shows the cycling data in its entirety while Figure 2.4B highlights the first and the second desorption cycle. The initial absorption cycle is quite slow, taking 5.5 h to absorb 5 wt.% hydrogen. However the first desorption is extremely fast, where 5 wt.% is released in 6 min. Interestingly, the second absorption cycle becomes faster (2 h) while the second desorption cycle becomes slower (also 2 h). The XRD data from the sorbed specimen indicates that α-MgH2 coexists with remaining Mg and with Mg_6Pd. Since Pd and Ta have appreciable mutual solubility at 250 °C (~ 9 at.% Pd in Ta, and ~ 15 at.% Ta in Pd) the formation of Mg_6Pd is feasible. It is not possible to conclusively identify or negate the presence of $\beta\text{-}TaH_{0.5}$ since its XRD peaks overlap those of Mg_6Pd. For example the most intense peak of $\beta\text{-}TaH_{0.5}$ (111) at $2\theta = 37.5°$, would experimentally overlap with the second most intense peak of Mg_6Pd (066) at $2\theta = 38°$. The (020), (200), (002) and (220) peaks of $\beta\text{-}TaH_{0.5}$ would similarly do that.

Figure 2.5 shows the results for the Pd/Nb system, which behaves similarly to Pd/Ta. The first absorption cycle is slow, taking over slightly over 2 h to reach 5 wt.% hydrogen content. First desorption is very rapid, achieving fully metallic state in just 13 min. As in the case of Pd/Ta, the second desorption cycle is slower while the second absorption cycle becomes faster. The XRD pattern shows the presence of $\alpha\text{-}MgH_2$, Mg, Mg_6Pd and $NbH_{0.5}$ phases. Niobium and Pd have nearly 20 at.% mutual solubility and thus allow for the formation of Mg_6Pd.

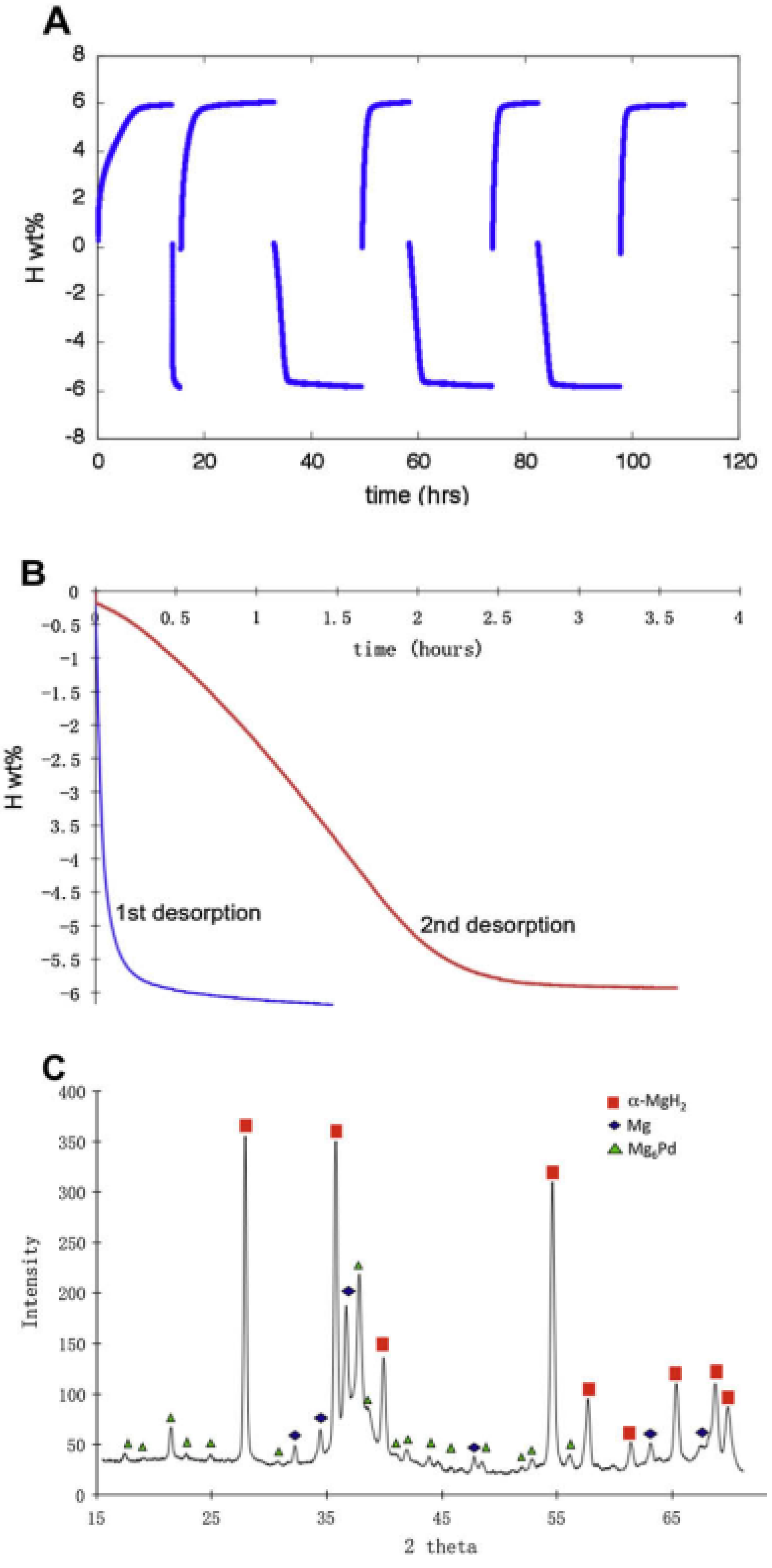

Figure 2.4: Cycled kinetics of magnesium with Pd/Ta bilayer catalysts. The corresponding XRD pattern after the last sorption cycle (absorption).

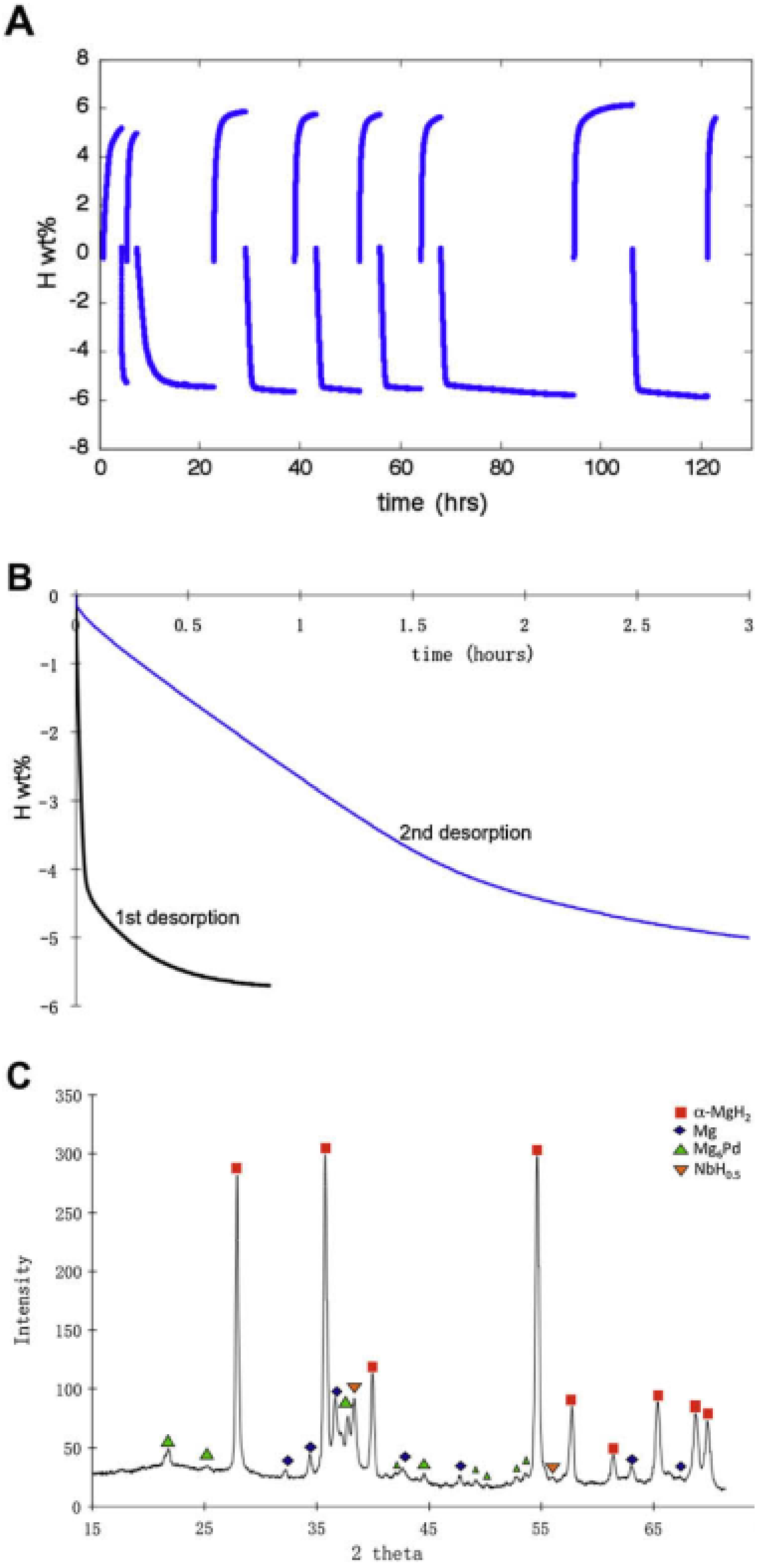

Figure 2.5: Cycled kinetics of magnesium with Pd/Nb bilayer catalysts. The corresponding XRD pattern after the last sorption cycle (absorption).

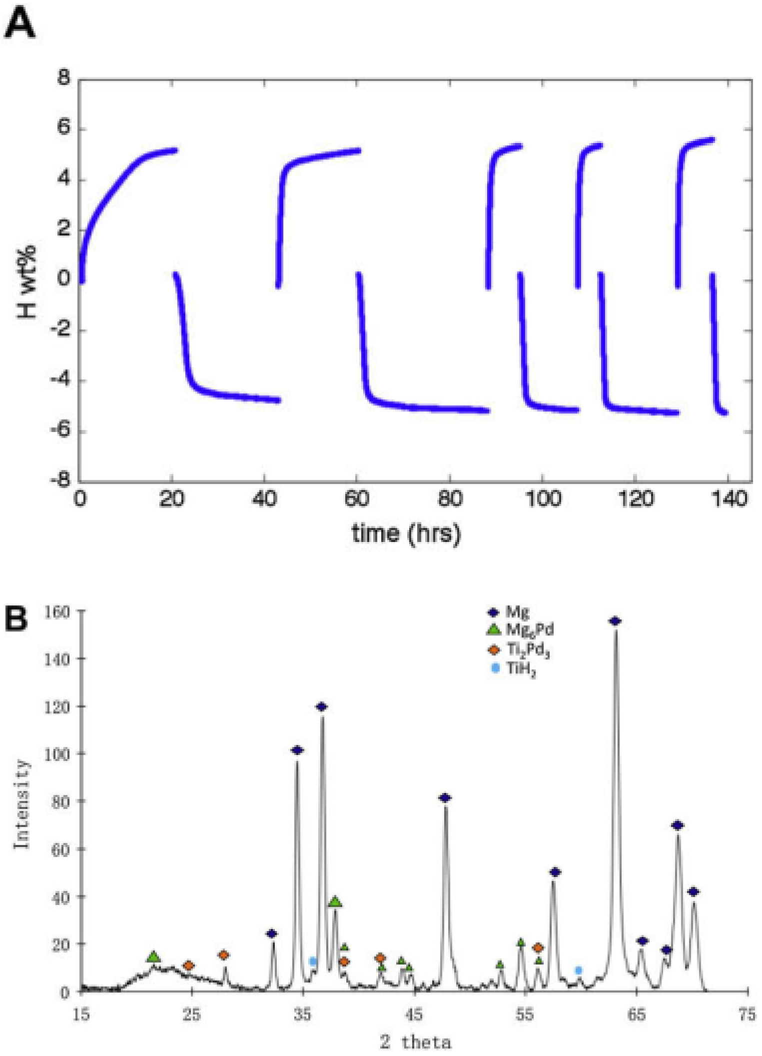

Figure 2.6: Cycled kinetics of magnesium with Pd/Ti bilayer catalysts. The corresponding XRD pattern after the last sorption cycle (desorption).

Figure 2.6 shows the Pd/Ti system. The initial time to absorb 5 wt.% hydrogen is 14 h. The time to desorb is even longer: 16 h. However, with cycling the sorption behavior improves. On the second cycle the time to absorb is 4 h, while the time to desorb is 3 h. With addition cycling the sorption times improve. The XRD pattern obtained after the last desorption cycle indicates the presence of Ti_2Pd_3 intermetallics as well as TiH_2 (really a substoichiometric $TiH_{1.7}$) in addition to metallic Mg.

Figure 2.7 compares the absorption and the desorption behavior of each of the bilayer catalyst systems versus the number of cycles. In the figure ‘‘cycle 1’’ indicates the first absorption cycle, ‘‘cycle 2’’ indicates the second absorption cycle, etc. In all

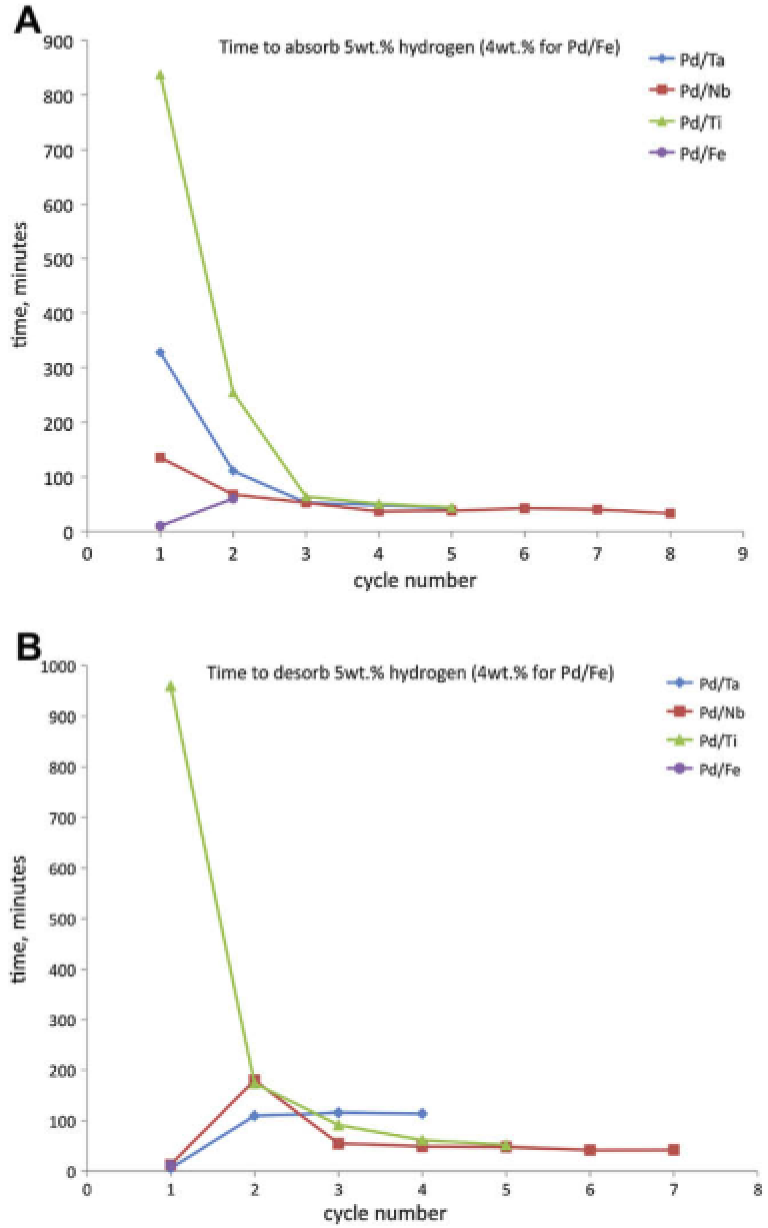

Figure 2.7: Absorption and desorption comparisons of the bilayer catalysts.

cases the bilayer catalyst systems perform better (faster rates, higher stability) than the baseline single-layer Pd. The baseline Pd data is not included in Figure 2.7 because the samples did not sufficiently absorb. Magnesium catalyzed with Pd absorbed less than 1 wt.% hydrogen, versus the bilayer systems that absorbed over 4 wt.% at the identical temperature/pressure conditions.

Interestingly both the absorption data and the desorption data indicate a fundamentally different behavior during the first two cycles versus consequent cycling. For cycle 1 Pd/Fe clearly shows the fastest absorption, followed by Pd/Nb and Pd/Ta. Pd/Ti has the slowest absorption of all the bilayer catalyst combinations. The first cycle desorption for Pd/Fe, Pd/ Nb and Pd/Ta are all similarly fast: 12, 13 and 6 min. However Pd/Ti takes almost two orders of magnitude more time to desorb than the others.

The sorption behavior observed in these composites during the first several cycles is quite complex. Comparing the initial rates of hydrogen sorption of the various bilayers versus the pure Pd there certainly appears to be a strong support effect. This may be understood in terms of the heats of hydride formation and the hydrogen diffusivities through the intermediate layers, using the methodology established by authors in Ref. [19]. It is also perhaps due to a fundamentally different catalytic behavior of the Pd on various supports [9]. However, it is difficult to model or even discuss the root-causes of the observed trends without detailed analysis of the ‘‘early’’ microstructures. We intend to pursue such analysis in future research.

By cycle 3 the Pd/Nb and Pd/Ti catalysts begins to reach a nearly identical steady-state behavior, for both absorption and desorption. The desorption time in Pd/Ta also reaches a steady state though at a higher value; 110 min vs. approximately 50 min for Pd/Nb and Pd/Ti. However the absorption behavior of samples with the Pd/Ta catalytic layers does begin to show slight kinetic degradation with increasing number of cycles. Despite having very rapid initial sorption rates the composite with the Pd/Fe bilayer is not cycleable beyond the first adsorption/desorption.

2.4 Discussion

A fundamental question that arises from the results summarized by Figure 2.7 is why it is possible to cycle Mg with Pd/Nb, Pd/Ta and Pd/Ti catalysts, whereas Mg covered with Pd or Pd/Fe rapidly and irreversibly degrade. One hypothesis is that the bilayers that are stable during sorption preserve some Pd (not Pd based intermetallic) coverage. This, in turn, is a result of having the underlying transition metal transform to a hydride that remains stable during desorption. Unlike its metallic counterpart, these hydrides have negligible solubility for atomic Pd and hence are much more effective in separating the catalyst form the base Mg. An alternative explanation is that the transition metal hydrides are sufficiently active towards hydrogen dissociation/reassociation and transport that the observed stable kinetic behavior is actually due the their presence on the Mg surface, rather than due to any remaining Pd. Similar argument was put forward by Huot et al. for case of MgH_2 – Nb powder composites [25]. In both scenarios, however, the key is the hydride's thermodynamic stability.

If we consider the heats of hydride formation for Pd, Fe, Ta, Nb and Ti [26], the cycling stability trends are relatively consistent with the above hypothesis. The test temperature in this study was 250 °C and the hydrogen desorption pressure was 0.05 bar, while the absorption pressure was 2.5 bar. The standard Van't Hoff equation is used to calculate the plateau pressure with respect to temperature: $In(P/P_0) = \Delta H/RT - \Delta S/R$ where ΔH is the enthalpy of hydride formation, $\Delta S = -130\ J\ K^{-1}\ mol^{-1}\ H_2$, and $P_0 = 1$ bar. Magnesium hydride (α-MgH_2) with a heat of formation equal to -74 kJ mol^{-1} has a plateau pressure of 0.25 bar; an order of magnitude higher than the desorption pressure. $PdH_{0.6}$ has a heat of formation of -40 kJ mol^{-1} and a plateau pressure of 634 bar. This indicates that Pd will be in its metallic state throughout absorption and desorption. $FeH_{0.5}$ has a positive heat of hydride formation of 10 kJ mol^{-1} and will remain metallic throughout the entire test as well. An ordered alloy of Fe and Pd should similarly not form hydrides at the test conditions.

The heat of formation for $NbH_{0.5}$ is -88 kJ mol^{-1}, giving a pressure plateau of 0.01 bar. TiH_2 has an enthalpy of formation of -134 kJ mol^{-1} and a pressure plateau of 2.5×10^{-7} bar. Thus once these hydrides are formed, they will remain for the remainder of the test. The presence of Mg_6Pd intermetallics in the XRD pattern of the Pd/Ti and Pd/Nb samples is likely due to the interdiffusion that has taken place during the initial sorption cycle before the hydrides could form. This may also be the origin of the kinetic variations in the sorption behavior observed during the first few cycles: Once stable hydrides are formed, steady-state sorption behavior is achieved.

Ta is the one outlier. β-$TaH_{0.5}$ has a heat of formation equal to -76 kJ mol^{-1}. Thermodynamically it should be a hydride during sorption and metallic during desorption. However in the case of Ta, the prolonged catalytic activity may be related to its elevated temperature stability. Recent work have shown that metallic Ta may be utilized as a nano-scale barrier for hydrogen storing thin films, minimizing the interdiffusion of Mg and Al with the Pd catalyst [27]. Alternatively the observed relatively stable cycling behavior may actually be due to the catalytic properties of Pd–Ta alloys that form during desorption. A theoretical study has predicted the Ta/Pd system to be very effective for hydrogen catalysis [9].

We intend to further test these scenarios in subsequent studies where we will rely on analytical tools such as TEM and in-situ neutron reflectometry to site-specifically probe the microstructure of each layer.

2.5 Conclusion

This study focused on the elevated temperature (250 °C) hydrogen sorption behavior of magnesium catalyzed by nanoscale bilayers of Pd/Ta, Pd/Nb, Pd/Ti and Pd/Fe. The bilayers, which were 7.5/7.5 nm in thickness, were sputter deposited on each side of 1.5 μm thick pure Mg thin films. For a baseline we also examined a standard single-layer Pd catalyst deposited on each side. Volumetric sorption cycling demonstrated two fundamentally different behaviors: With the pure Pd and the Pd/Fe catalysts, the sorption kinetics of the Mg films rapidly degraded. The samples with Pd failed to appreciably take up hydrogen even in the first absorption cycle, while the samples with Pd/Fe catalyst could only absorb/desorb once before deteriorating. Conversely the Pd/Ta, Pd/Nb and Pd/Ti catalysts remained active throughout multiple sorption cycles, reaching what appeared to be steady-state kinetics. For example, Mg catalyzed by Pd/Nb is able to sorb 5 wt.% hydrogen in approximately 40 min during cycles 5–8. Our hypothesis is that the cycling stability of the Mg film depends on the intermediate metal layer's enthalpy of hydride formation. Palladium and Fe remain metallic throughout sorption. This allows for rapid interdiffusion of the elements and the complete transformation of the Pd catalyst to

Mg_6Pd. Metals with high negative heats of hydride formation, such as Ti and Nb, remain as hydrides during sorption cycling, acting as more effective diffusion barriers to stabilize the Pd catalyst. In addition the $NbH_{0.5}$ and TiH_2 may actively catalyze hydrogen dissociation/reassociation and provide transport paths in and out of the Mg microstructure.

2.6 Reference

[1] A. Baldi, R. Gremaud, D. M. Borsa, C. P. Balde, A. M. J. van der Eerden, G. L. Kruijtzer, et al. *Int. J. Hydrogen Energ.* **2009**, *34*, 1450-1457.

[2] Y. Wang, W. Hua, J. Qu, X. Li, *Int. J. Hydrogen Energ.* **2008**, *33*, 7207-7213.

[3] J. Qu, Y. Wang, L. Xie, J. Zheng, Y. Liu, X. Li, *Int. J. Hydrogen Energ.* **2009**, *34*, 1910-1915.

[4] P. Vermeulen, P. C. J. Graat, H. J. Wondergem, P. H. L. Notten, *Int. J. Hydrogen Energ.* **2008**, *33*, 5646-5650.

[5] H. Fritzsche, M. Saoudi, J. Haagsma, C. Ophus, E. Luber, C. T. Harrower, et al. *Appl. Phys. Lett.* **2008**, *92*, 12917.

[6] A. Baldi, R. Gremaud, D. M. Borsa, C. P. Balde, A. M. J. van der Eerden, G. L. Kruijtzer, et al. *Int. J. Hydrogen Energ.* **2008**, *33*, 3188-3192.

[7] A. Sepulveda, A. F. Lopeandia, R. Domenech-Ferrer, G. Garcia, F. Pi, J. Rodriguez-Viejo, et al. *Int. J. Hydrogen Energ.* **2008**, *33*, 2729-2737.

[8] J. L. Slack, J. C. W. Locke, S. W. Song, J. Ona, T. J. Richardson, *Sol. Energ. Mat. Sol. C* **2006**, *90*, 485-490.

[9] J. Greely, M. Mavrikakis, *Nat. Mater.* **2004**, *3*, 810-815.

[10] A. Remhof, G. Song, K. Theis-Brohl, H. Zabel, *Phys. Rev. B* **1997**, *56*, R2897.

[11] S. J. van der Molen, J. W. J. Kerssemakers, J. H. Rector, N. J. Koeman, B. Dam, R. Griessen, *J Appl. Phys.* **1999**, *86*, 6107.

[12] A. T. M. van Gogh, S. J. van der Molen, J. W. J. Kerssemakers, N. J. Koeman, R. Griessen, *Appl. Phys. Lett.* **2000**, *77*, 815-817.

[13] T. J. Richardson, J. L. Slack, R. D. Armitage, R. Kostecki, B. Farangis, M. D. Rubin, *Appl. Phys. Lett.* **2001**, *78*, 3047-3049.

[14] A. Borgschulte, R. J. Westerwaal, J. H. Rector, B. Dam, R. Griessen, J. Schoenes, *Phys. Rev. B* **2004**, *70*, 155414.

[15] M. Pasturel, M. Slaman, D. M. Borsa, H. Schreuders, B. Dam, R. Griessen, et al. *Appl. Phys. Lett.* **2006**, *89*, 021913.

[16] A. Borgschulte, R. Gremaud, S. de Man, R. J. Westerwaal, J. H. Rector, B. Dam, et al. *Appl. Surf. Sci.* **2006**, *253*, 1417-1423.

[17] D. M. Borsa, A. Baldi, M. Pasturel, H. Schreuders, B. Dam, R. Griessen, et al. *Appl. Phys. Lett.* **2006**, *88*, 241910.

[18] G. Garcia, R. Domenech-Ferrer, F. Pi, J. Santiso, J. Rodriguez-Viejo, *J Comb. Chem.* **2007**, *9*, 230-236.

[19] M. Pasturel, R. J. Wijngaarden, W. Lohstroh, H. Schreuders, M. Slaman, B. Dam, et al. *Chem. Mater.* **2007**, *19*, 624-633.

[20] R. Hoogeveen, M. Moske, H. Geisler, K. Samwer, *Thin Solid Films* **1996**, *275*, 203-206.

[21] N. W. Ockwig, T. M. Nenoff, *Chem. Rev.* **2007**, *107*, 4078-4110.

[22] T. B. Massalski, editor. *Binary alloy phase diagrams*, 2nd ed. Materials Park, Ohio: ASM International; 1990.

[23] B. S. Amirkhiz, M. Danaie, D. Mitlin, *Nanotechnology* **2009**, *20*, 204016.

[24] M. Danaie, D. Mitlin, *J. Alloy. Compd.* **2009**, 476, 590-598.

[25] J. Huot, J. F. Pelletier, G. Liang, M. Sutton, R. Schulz, *J. Alloy. Compd.* **2002**, 330–332, 727-731.

[26] G. Alefeld, J. Volkl, editors. *Hydrogen in metals I (Topics in applied physics)*. Berlin: Springer-Verlag; 1978. p. 266–9.

[27] H. Fritzsche, C. Ophus, C. T. Harrower, E. Luber, D. Mitlin, *Appl. Phys. Lett.* **2009**, *9*4, 241901.

Chapter 3

A TEM based study of the microstructure during room temperature and low temperature hydrogen storage cycling in MgH_2 promoted by Nb-V[*]

3.1 Introduction

Magnesium hydride (MgH_2) based systems are considered promising for solid-state hydrogen storage [1-4]. However practical applications are hindered by the systems' excessive thermodynamic stability and sluggish hydriding/dehydriding kinetics [5,6]. The origins of the slow kinetics have been investigated using a variety of analytical techniques, such as in situ synchrotron X-ray diffraction [7], in-situ or cryo-stage electron microscopy [8-10], first principles calculations [11], and neutron scattering [12-14]. There have been some recent promising studies where researchers have shown thermodynamic destabilization of MgH_2 through selective alloying [15-17] or creation of constrained nanolayered structures [18,19]. Some researchers have demonstrated that the sorption kinetics are significantly accelerated by intimately mixing or alloying proper transition metals with Mg [20-25]. A number of authors have also accelerated the kinetics by synthesizing nanoscale structures so as to reduce diffusion limitations [26-31], or by creating highly deformed structures with high dislocation densities [32-34].

---

[*] Materials in this chapter has been published in:

- XueHai Tan, Beniamin Zahiri, Chris M.B. Holt, Alan Kubis, David Mitlin, Acta Materialia 2012, 60, 5646–5661.

Mg-based alloys, in thin film form, are currently subject to intense scientific inquiry. As a high-throughput screening method, thin film techniques are useful to identify the ideal compositions and amounts of secondary catalytic or destabilizing additives [35-37]. For example, by physical vapor depositing Mg films with suitable elements, such Fe, Ti, V, Cr, it is possible to create materials with rapid sorption kinetics [38-40]. It is known that if the selected elements do not form intermetallic compounds with Mg or have appreciable solubility in Mg at equilibrium, they will segregate from the as-deposited supersaturated solid solutions of Mg and form separate phases [41]. The superb kinetic enhancement of such composite materials has been attributed to the catalytic effect of the secondary phases that are densely dispersed in the Mg matrix. Though the exact role of the secondary phase is yet to be determined, it has been hypothesized that it could serve as hydrogen dissociation/recombination catalysts, heterogeneous nucleation sites and high H diffusivity paths. The secondary phase may also act as pinning points forming a network along the Mg(MgH_2) grain boundaries [41]. This would prevent the growth of Mg grains and the sintering of Mg particles, reducing the diffusion distances. More work is needed in terms of providing direct microstructural evidence to demonstrate these arguments. For example, one unknown regards the systems' microstructural evolution during extended elevated temperature hydriding/dehydriding cycling and its relationship to the universally observed degradation of the kinetics. Another question concerns the microstructural origin of fundamental differences that have been reported in the sorption kinetics of systems catalyzed by single elements versus that of bimetallic catalyst phases [38].

Both V and Nb are known catalysts that promote the hydrogen sorption kinetics in Mg [42-44]. They have body-centered cubic (bcc) structure, with appreciable hydrogen solubility and high hydrogen diffusivity [45]. In addition, both elements form hydrides at the pressures/temperatures utilized for magnesium. The catalytic properties of their respective hydrides, rather than those of the metals, have been suggested to play an equally important role for catalyzing the reactions under certain sorption conditions [46]. Though binary systems of Mg and a single transition metal have been the subject of extensive research, hydrogen storage in Mg-rich ternary Mg-V-Nb has not received any attention.

In the present study the interrelationship between the microstructure and the hydrogen storage cycling behavior of Mg-rich ternary Mg-V-Nb alloys is investigated in detail. As a baseline we also present the properties and the microstructure of Mg-V and Mg-Nb systems. As will be demonstrated, Mg-20V and Mg-10V-10Nb samples possess similarly rapid initial hydrogen sorption kinetics. However the two systems show fundamentally differing trends in the microstructural evolution induced by hydrogen absorption and desorption cycling, with concomitantly disparate rates of kinetics degradation. Though we utilize a variety of analytical techniques along with Avrami-type (Johnson-Mehl-Avrami; JMA) kinetic analysis, our primary tool is cryogenic stage transmission electron microscopy (TEM). Using cryo-stage TEM allowed us to observe the microstructures in the fully hydrided or fully metallic state with minimal beam-induced specimen damage. It also allowed us to examine partially sorbed microstructures containing both Mg and MgH_2, thus allowing for a realistic comparison between the obtained JMA parameters and the actual growth process. Combining these techniques led to a general mechanistic description of the microstructural evolution in these alloys both at 200 °C and at room temperature.

3.2 Experimental

The ternary Mg-V-Nb and binary Mg-V and Mg-Nb alloy films were synthesized by physical vapor deposition (PVD). They were 10 cm in diameter and 1.5 μm thick. The Mg-based alloy films were coated with 7.5 nm Pd/7.5 nm Ta bilayers on the top and bottom of the stack. The Ta interlayer reduced the rate of intermetallic formation between the Mg and the Pd, allowing the Pd to stay active during the first few cycles [47]. Deposition was performed using a DC-magnetron co-sputtering system (AJA International Inc. ATC ORION 8), in a sputter-up configuration with continuous substrate rotation. The substrate temperature was maintained near ambient for all depositions. Argon gas with a purity of 99.999% was used at a working pressure of 5×10^{-3} mbar, with a maximum base pressure of 5×10^{-8} mbar. The Si substrates were first coated with a layer of hardened photoresist to enable post deposition lift-off of the films using acetone. The deposition rates were the following: Mg 2.3 Å s^{-1}, Pd 1.6 Å s^{-1}, Ta 0.3 Å s^{-1}. The deposition rates of V and Nb varied accordingly to adjust for different stoichiometries. The levels of secondary additions were kept the same for both ternary and binary samples, namely 20 at.%. For simplicity, we denote samples as Mg-xV-yNb, which indicates stoichiometry of 80 at.% Mg – x at.% V – y at.% Nb.

Volumetric absorption and desorption kinetic measurements and the desorption pressure-compositions isotherms (PCT-desorption) were performed on an automated Sieverts type hydrogen sorption analysis system (Hy-Energy LLC. PCTPro 2000). The typical sample amount used for each measurement was ~15 mg. Cycling kinetics measurements were performed at 200 °C and at 20 °C. For cycling tests at 200 °C, the hydrogen pressures at the beginning of absorption and desorption steps were ~2.3 and 0.007 bar, respectively. The absorption and desorption steps were reversed when the average sorption rate fell below 0.005 wt.% min^{-1} over a period of 3 minutes. Room temperature hydrogen uptake was performed with a sample that first underwent 50 full sorption cycles at 200 °C. The sample was then cooled to 20 °C and absorbed at 1 bar. After absorption, the sample was again heated to 200 °C to desorb at a starting hydrogen pressure of 0.005 bar. Partially absorbed/desorbed samples were prepared by interrupting the sorption process at a predetermined reaction wt.% fraction.

X-ray diffraction (XRD) analysis was performed on a Bruker AXS diffractometer (Bruker Discover 8) using a Cu-Kα radiation source (λ = 1.5406 Å) that was monochromatized using a single Gobel mirror. The diffractometer was equipped with a HiStar general area 2-dimensional detection system (GADDs) with a sample-detector distance of 15 cm. Powder diffraction patterns from both simulated results and the XRD database of DIFFRAC^{plus} EVA^{TM} software were used for peak identifications. Grain size (D) analyses were performed by using the well-known Scherrer equation:

$$D = \frac{k\lambda}{\beta \cos\theta_0} \qquad \text{(Eq. 3.1)}$$

where k is a constant taken as 0.9, λ is the x-ray wavelength, β is the full width half maximum of the peak (FWHM) in radians with the instrumental broadening effect corrected, and θ_0 is the position of the peak maximum. For each testing condition, the grain size was reported as the average value from the best-resolved peaks. The deviation of the mean from the maximum and minimum calculated values are reported as the error bars. The peak fitting using Voigt function and necessary deconvolution of overlapping peaks were performed on Fityk commercial software [48]. The instrumental broadening was carefully determined by using a LaB_6 standard material and subtracted from the measured line broadening.

Scanning electron microscopy (SEM) analysis was performed on a Zeiss NV vision 400 equipped with a gallium liquid metal ion source. The cross-section sample of internal film structure was prepared using focused ion beam (FIB) lift-out. The FIB was operated at 30 kV and down to a lowest probe current of 80 pA to polish the surface of the cross-section sample. Imaging and selected area electron diffraction (SAD) analysis was performed on JEOL 2100 transmission electron microscope operated at 200 kV, using a liquid nitrogen cooled sample holder. At 93 K the beam-induced decomposition of hydride phases occurred relatively slowly, allowing for proper analysis of the hydride [49]. The TEM powder samples were prepared by dry dispersion of the powders onto an ultrathin carbon film supported by a lacey carbon film on a copper grid. Commercial software Desktop Microscopist^{TM} and Crystal Maker^{TM} are used to simulate electron diffraction patterns.

3.3 Results

3.3.1 Hydrogen sorption at 200 °C and at room temperature

Figure 3.1 compares the hydrogen cycling sorption behavior of the binary (Mg-20V and Mg-20Nb), as well as the ternary (Mg-7V-13Nb, Mg-10V-10Nb, Mg-13V-7Nb) systems. The measured hydrogen absorption/desorption capacities, and the time to absorb/desorb 80% of the average capacity for each composition, as a function of cycle number, are depicted in Figure 3.1A-D respectively. Mg-20V exhibits rapid sorption kinetics at early stages of cycling. However, after ~90 sorption cycles, the system

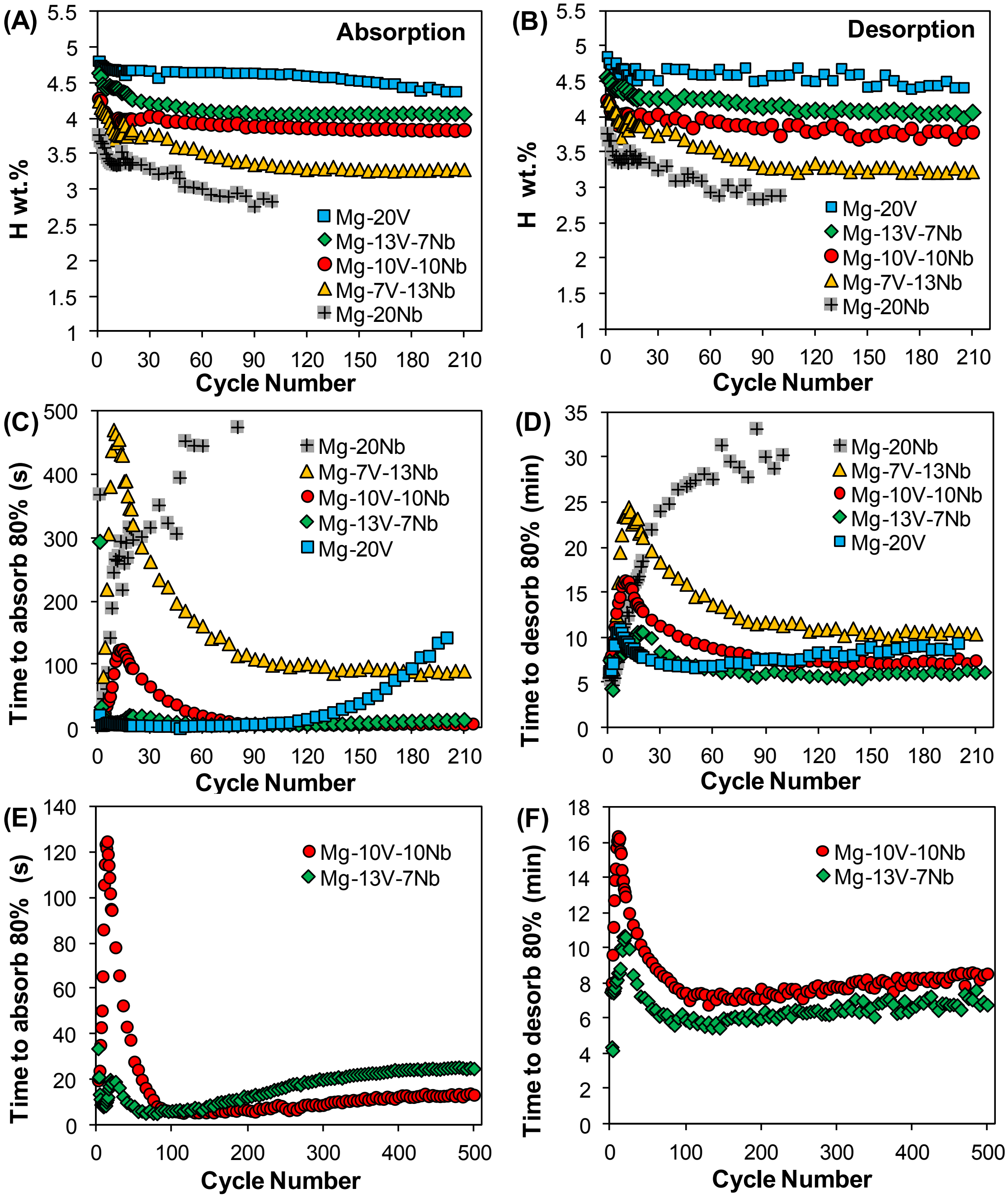

Figure 3.1: Hydrogen cycling sorption behaviors of the binary (Mg-20V and Mg-20Nb), as well as the ternary (Mg-7V-13Nb, Mg-10V-10Nb, Mg-13V-7Nb) systems at 200°C. (A, B) The measured hydrogen absorption and desorption capacities for each composition as a function of sorption cycle number. (C, D) The time to absorb and desorb 80% of the average measured capacity for each composition as a function of sorption cycle number up to 210 cycles. (E, F) The time to absorb and desorb 80% of the average measured capacity for Mg-10V-10Nb and Mg-13V-7Nb up to 500 cycles.

begins to display obvious kinetic degradation, which is especially manifested during absorption. For example, it takes 40 times longer to absorb 80% of the average capacity at the 200th cycle, as compared to the 45th cycle. Since the sorption step was reversed when the rate fell below 0.005 wt.% min^{-1}, the kinetic slowdown also led to a decrease in the reversible capacity with cycling. Since the kinetics of binary Mg-20Nb rapidly degraded during the early stages of cycling, testing for that system was ceased after 100 cycles. The ternary Mg-V-Nb alloys exhibit much more favorable hydrogen storage cycling properties. All three ternary compositions show almost no kinetic degradation even at over 200 cycles. Since the sorption kinetics of both Mg-10V-10Nb and Mg-13V-7Nb were extremely rapid, the two compositions were cycled 500 times, and these results are shown in Figure 3.1E and F, respectively. Overall the Mg-10V-10Nb system displays the least cycling-induced kinetics degradation though the difference with Mg-13V-7Nb is fairly minor. The sorption kinetics of Mg-7V-13Nb is not as rapid, indicating that a minimum amount of V is required before the kinetics reaching optimum. This may highlight the superior catalytic properties of V over Nb. The fact that all five alloys begin with essentially the same sorption kinetics seems to suggest that the selection of secondary catalytic phases becomes more important during later stages of cycling.

It is evident that the hydrogen cycling sorption behaviors of the ternary Mg-V-Nb alloys and the binary Mg-V alloy possess a common characteristic: the presence of an "activation period" before the sorption kinetics reaching the fully activated state. Though to a varying extent, both the absorption and the desorption kinetics progressively worsen during the first 10-20 cycles. The sorption rates subsequently improve and reach the fully activated state at which they remain stable for a duration that depends on the sample's composition. The length of the activation period varies with the sample compositions. While the binary Mg-20V required less than 20 cycles to be fully activated, the ternary Mg-V-Nb films required significantly more cycles. Also, the kinetic slowdown during the activation period became more severe with increasing Nb doping. In all cases, the first cycle absorption times were much longer than those in the subsequent cycles. For example, the first cycle absorption times of Mg-10V-10Nb and Mg-7V-13Nb samples were so long that the data could not be practically plotted on the same graphs. This behavior is not representative of the materials' general hydriding performance. The as-synthesized microstructures were supersaturated solid solutions without a secondary V, Nb or V-Nb catalytic phase, but with the bilayer Ta/Pd surface coatings still intact. It is known that decomposition of as-deposited supersaturated Mg solid solution mainly occurs during the first hydrogenation [41,50].

Pressure composition temperature (PCT) tests were utilized for Mg-10V-10Nb to ascertain its thermodynamic properties. The plateaus were obtained from specimens that have undergone 100 plus sorption cycles, so as to analyze the "steady-state" microstructure. The desorption plateaus at 190 °C, 210 °C and 230 °C are shown in Figure 3.2. The measured equilibrium pressures are 0.031, 0.072 and 0.153 bar, yielding the enthalpy and entropy of hydride decomposition of 76.8 kJ mol^{-1} H_2 and 136.9 J K^{-1} mol^{-1} H_2, respectively. Both are in good agreement with literature-reported values for the equilibrium α-MgH_2 phase, e.g. [27]. It is thus confirmed that the rapid sorption behavior of the alloys is a kinetic effect.

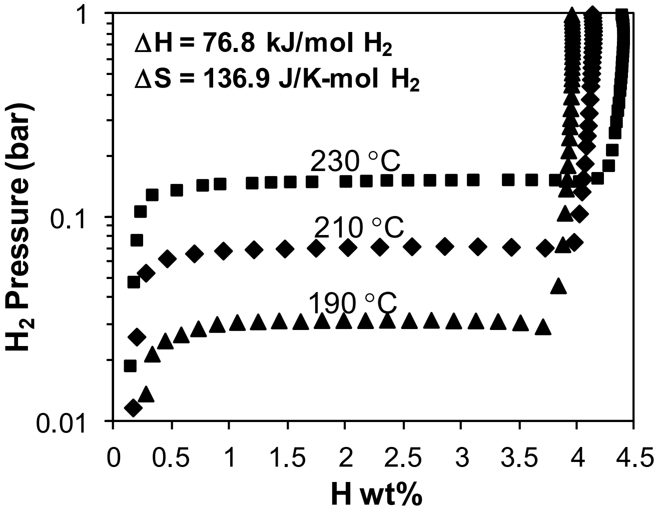

Figure 3.2: Desorption pressure-composition-temperature (PCT) at 190, 210 and 230 °C of Mg-10V-10Nb.

Among the five compositions examined above, binary Mg-20V and ternary Mg-10V-10Nb and Mg-13V-7Nb are the most interesting candidates for further investigation. The former represents a material with rapid kinetics but lacking in kinetic stability for extended cycling; the latter two represent materials showing significantly improved cycling stability without compromising the sorption kinetics. These materials also exhibit different lengths of activation. Figure 3.3A and B show the selected absorption and desorption cycles of Mg-20V at 200 °C. From the 45th to the 200th cycle, the amount of H that can be absorbed within 10 seconds significantly decreases from 4.5 to only 2.3 wt.%. The kinetics of desorption on the other hand degrades only slightly. Figure 3.3C and D show the selected absorption and desorption cycles of Mg-10V-10Nb. The sorption curves of Mg-13V-7Nb are analogous, and are thus not shown here. In the ternary cases, even at 500 cycles, both absorption and desorption kinetics show negligible degradation.

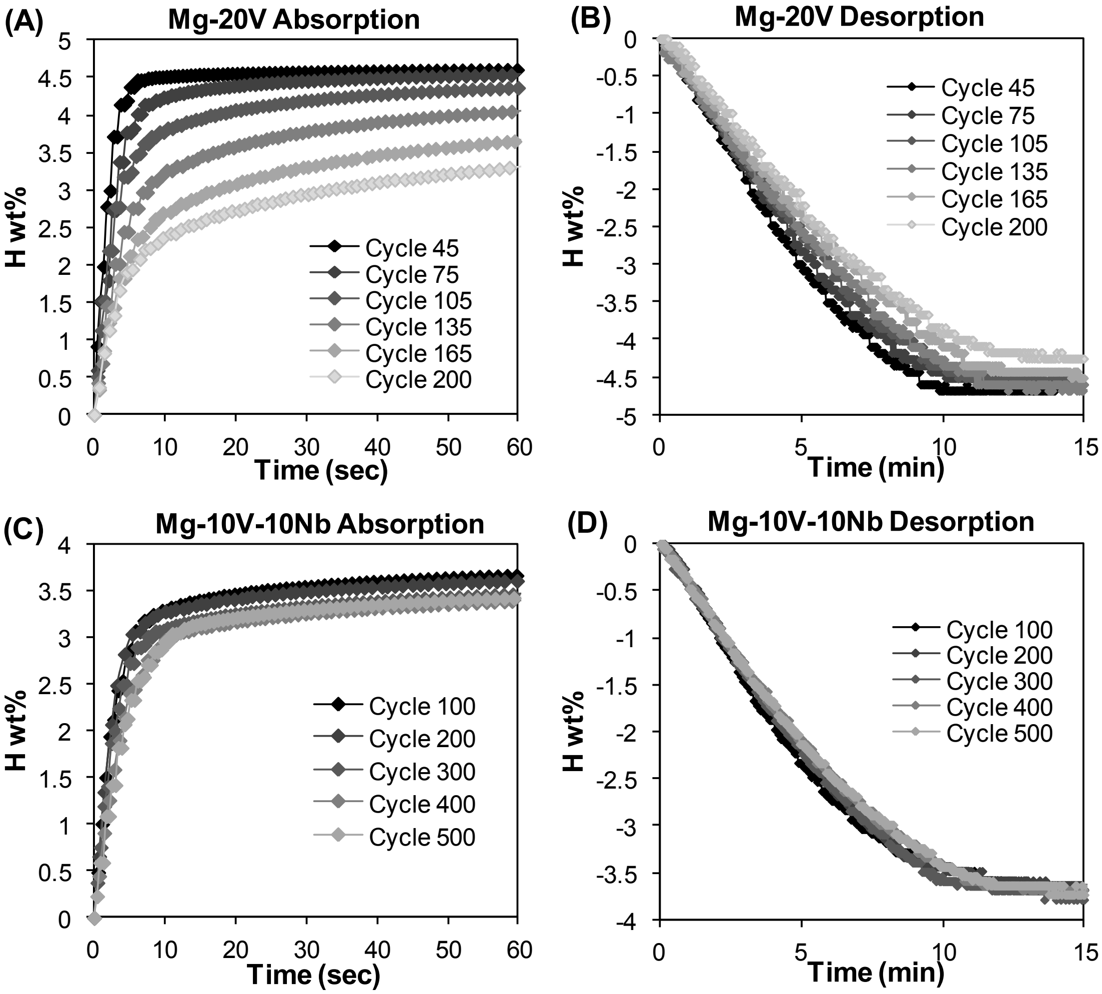

Figure 3.3: Comparison of the hydrogen sorption cycling behaviors between Mg-20V and Mg-10V-10Nb at 200 °C. (A) Selected absorption cycles and (B) selected desorption cycles of Mg-20V. (C) Selected absorption cycles and (D) selected desorption cycles of Mg-10V-10Nb.

To obtain further insights into the cycling induced kinetic degradation mechanism, in particular as manifested in the hydriding kinetics, we first fit the experimental absorption data (first 90% of the transformed fraction) of Mg-20V and Mg-10V-10Nb at various cycling stages with the Johnson-Mehl-Avrami (JMA) kinetic model [51]. The JMA model is a well-known analytical description of transformation kinetics based on homogeneous nucleation and growth (NA) process and is expressed as

$$f = 1 - \exp(-kt)^n \qquad \text{(Eq. 3.2)}$$

where f is the transformed fraction, k is the kinetic rate constant and t is the reaction time. The value of the Avrami exponent n, which depends on the type of nucleation, dimensionality of growth and the rate-limiting step of growth, can be obtained from the slope of the straight line when plotting $\ln[\ln(1/(1-f))]$ vs. $\ln(t)$.

The best fits to the experimental absorption data are obtained with two JMA functions. In Figure 3.4A and B, the experimental data (reported as open diamonds) for Mg-20V (45th and 200th cycles) and Mg-10V-10Nb (100th and 500th cycles) are plotted as both $\ln[\ln(1/(1-f))]$ vs. $\ln(t)$ and as f vs. t. Two stages with different slopes are observed for all cases. The JMA fits are superimposed onto the experimental data, with solid and dashed lines fitting stages I and II, respectively. Such two-stage behavior is known, having been covered by Christian [52]. The onset of stage II has been attributed to site saturation [52], which would lead to impingement of the growing hydride nuclei and a corresponding significant reduction of the transformation rate. In the case of Mg-20V, with increasing cycling there was progressively less material transformed to the hydride at the conclusion of stage I (indicated as f_t). For example, f_t decreased from 0.95 at the 45th cycle to 0.45 at the 200th cycle. Conversely for Mg-10V-10Nb, f_t decreased only slightly from 0.81 at 100th cycle to 0.78 at 500th cycle. Since stage II is significantly slower than stage I, the fraction of material that can be transformed to hydride before the onset of the stage II would directly impact on the overall absorption kinetics. It should be noted that the n values of the absorption stage I, for both samples, remain close to 1 throughout cycling. This strongly suggests that the nucleation and growth mechanism during stage I is similar for both systems and does not evolve with cycling. According to

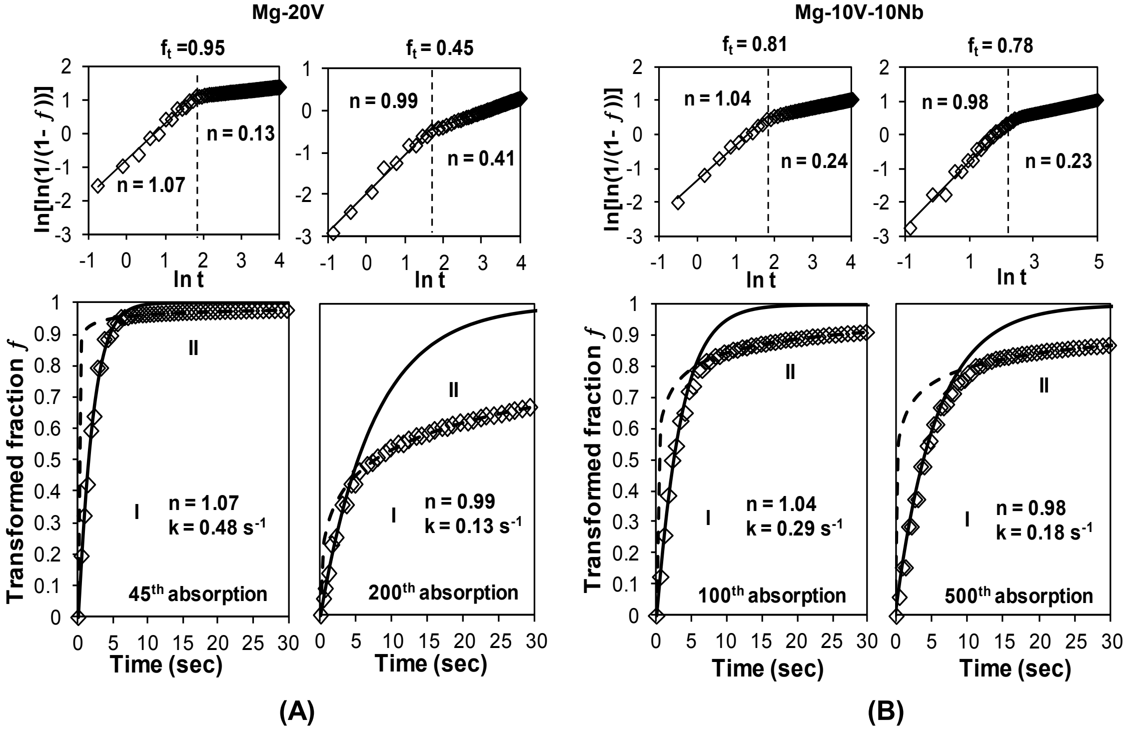

Figure 3.4: Kinetic analyses on the absorption curves of Mg-20V and Mg-10V-10Nb at selected sorption cycles. Top figures: the evaluation of the experimental data (open diamonds) using Eq. 3.2; two stages with different slopes (n) are clearly observed. Bottom figures: the experimental data (open diamonds) plotted as transformed fraction *f* vs. time in seconds; the JMA models fits for the stages I and II are superimposed in the transformed fraction graphs as solid and dashed lines respectively. (A) The 45th and the 200th absorption cycle for Mg-20V. (B) The 100th and the 500th absorption cycle for Mg-10V-10Nb.

Christian [52], $n = 1$ could describe several phenomena, such as grain boundary nucleation or diffusion controlled growth of various geometries.

The superb absorption kinetics during stage I can be further characterized by calculating the apparent activation energy of the hydriding reaction (Q_A), according to the Arrhenius-type ln(k) vs. $1/T$ formulation. The rate constant k was obtained by fitting the sorption data with the JMA model. To minimize any influence on sorption kinetics due to cycling degradation, the data was acquired on a fully activated Mg-10V-10Nb sample, which is kinetically more stable than Mg-20V. In addition, only the initial 60% of the transformed fraction was fitted. This ensures that the obtained apparent activation energy could truly represent the stage I hydrogenation reaction. The pressure-temperature combinations used for activation energy measurements were specified, so that the reaction driving forces were kept as close as possible to the one used during hydrogen cycling sorption. Based on the results from Zahiri's work [53], the driving force formula $T(1-(P_{eq}/P)^{0.5})$ was selected in this study. This expression was originally derived by Rudman [54], assuming that diffusion is the rate-limiting step. Figure 3.5 shows the Arrhenius plot of rate constants k of the absorption stage I at five different temperatures (190, 200, 210, 220 and 230 °C). An apparent activation energy (Q_A) of 14.6 ± 1.1 kJ mol^{-1} is obtained. Such a low energy barrier is consistent with the sorption kinetics during absorption, stage I being extremely rapid.

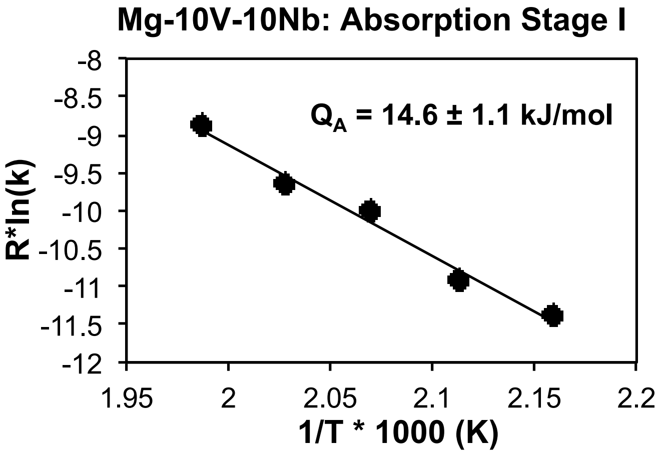

Figure 3.5: Measured activation energy of the stage I absorption.

The ternary samples are also able to relatively quickly absorb hydrogen at room temperature at a pressure of 1 bar and over 20 sorption cycles. The selected hydrogen uptake curves of the activated Mg-13V-7Nb sample are shown in Figure 3.6. Since the enthalpy of hydride decomposition is not altered compared to bulk MgH_2, after each absorption step, the sample was heated to 200 °C to release the hydrogen under a rough vacuum. Analogous to the absorption curves at 200 °C, two-stage behavior also presents in the hydrogenation curves at room temperature. However, the onset of stage II occurs at a lower transformed fraction. The hydriding kinetics during stage II becomes substantially slower as well.

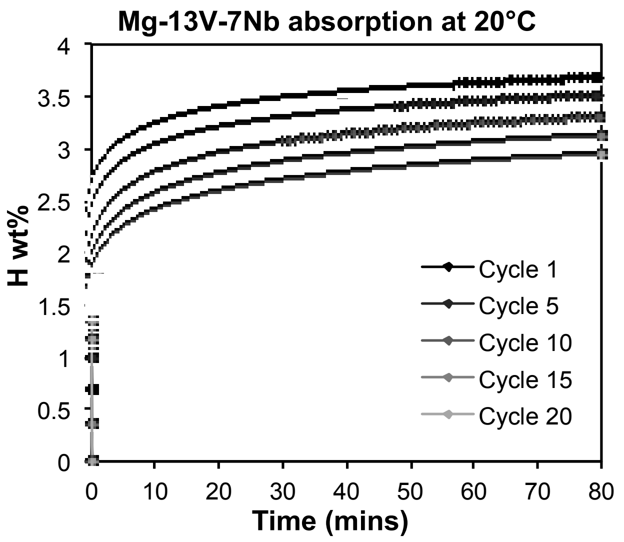

Figure 3.6: Room temperature absorption cycling of Mg-13V-7Nb at 1 bar hydrogen pressure. After each absorption step, hydrogen is released at 200 °C.

3.3.2 Microstructural analysis

Figure 3.7A shows the XRD patterns of Mg-20V in the as-deposited state, in the post-cycled desorbed state, and in the post-cycled absorbed state. In the as-deposited state, the film has a strong Mg [0001] fiber texture. The Mg (0002) reflection shifts to higher angle (2θ = 35.5°) as compared to the equilibrium value of 34.4° for pure Mg. The lattice parameter of V (a = 3.04Å) is smaller than that of Mg (a = 3.21 and c = 5.21Å), so a shift to higher 2θ values is expected. Conversely there is no evidence of the equilibrium V Bragg peaks. This indicates that the as-deposited alloy microstructure consists of supersaturated solid solution of V in Mg. After cycling, the most prominent peaks can be unambiguously indexed to Mg and MgH_2. Since there is no detectable variation of the lattice parameters from the literature-reported values, the previously dissolved V has almost entirely segregated out of the Mg/MgH_2 lattice. Despite the Ta underlayer, the Mg–Pd intermetallics are still formed during cycling. Mg_6Pd is detected in the desorbed state, while Mg_5Pd_2 is detected in the absorbed state. In the diffraction patterns of Mg-20V after 200 sorption cycles, body-centered tetragonal $VH_{0.5}$ (I4/mmm (139)) is found in the fully absorbed state, and a mixture of $VH_{0.5}$ and metallic V (Im-3m (229)) is found

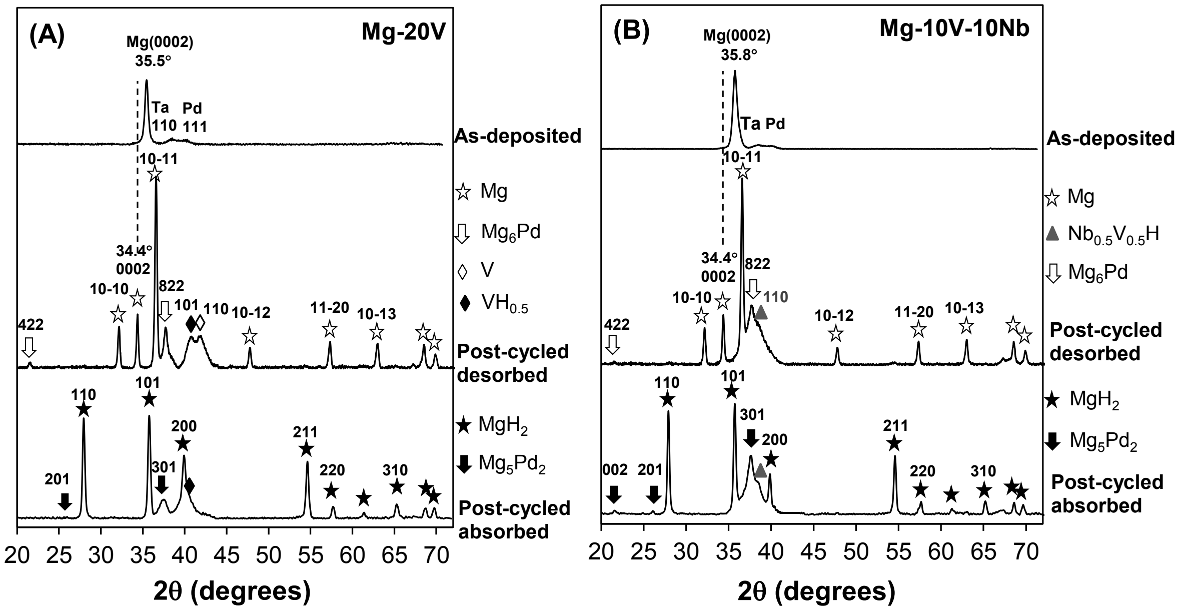

Figure 3.7: XRD patterns of (A) Mg-20V and (B) Mg-10V-10Nb in the as-deposited state, the post-cycled desorbed state and the post-cycled absorbed state, respectively.

in the desorbed state. The reported values of the enthalpy of formation for $VH_{0.5}$ range from -70 to -84 kJ mol^{-1} H_2 [50,55]. Assuming an entropy of -130 J mol^{-1} K^{-1}, the equilibrium pressure would range from 0.1 bar to 0.003 bar. The partially desorbed microstructure of $VH_{0.5}$ indicates that the plateau pressure at 200 °C should be slightly higher than 0.007 bar that is used for desorption. The vanadium dihydride VH_2 is not observed, agreeing with the reported enthalpy of formation of -40.25 kJ mol^{-1} H_2 [56].

Figure 3.7B shows the XRD patterns of Mg-10V-10Nb. In the as-deposited state, the Mg (0002) peak in this case is located at $2\theta = 35.8°$. After 500 cycles, the reflections of Mg and MgH_2 are at their theoretical positions. For the post-cycled Mg-10V-10Nb, a broad reflection is observed, partially overlapping with the strongest peak of the Mg-Pd intermetallic. Since Nb and V possess a small but negative enthalpy of mixing (-5 kJ mol^{-1}), and are negligibly soluble in Mg, the formation of a bcc Nb-V solid solution is expected. The position of this broad reflection, centered at $2\theta = 38.5°$, does not change between the desorbed and the absorbed state. Authors have reported that the monohydrides of Nb-V possess a bcc lattice, with $a = 3.32$ Å for the $Nb_{0.5}V_{0.5}H$ stoichiometry [57]. This unit cell yields the observed 2θ position for the (110) reflection.

Conversely, a strict "Vegard's law" lattice parameter for metallic $Nb_{0.5}V_{0.5}$ would give the position of the (110) reflection at $2\theta = 40.2°$, which is significantly outside the measured position.

Figure 3.8A shows the average grain size of metallic Mg in the desorbed state, as a function of cycle number. For the binary Mg-20V, the Mg grain size is 35 nm after 45 cycles, which increases to 57 and 84 nm after 90 and 200 cycles, respectively. For the ternary Mg-10V-10Nb, an increasing trend for Mg grain size is also observed, but the rate of increase is markedly lower. After 45 cycles, the Mg grain size is 29 nm. This value increases to 33 and 43 nm after 90 and 200 cycles, respectively. Eventually, the Mg grain size increases to 60 nm after 500 cycles. This value is still smaller than that of binary sample after 200 cycles. Figure 3.8B shows the average grain size of MgH_2 in the absorbed state after selected cycling stages. The ternary sample again shows a markedly lower rate of grain growth. The grain size of MgH_2 increases almost synchronously compared to the metallic counterpart. After prolonged sorption cycling, the mean grain size of MgH_2 becomes slightly smaller than that of Mg. However, since the differences are still within the range of error bars, this discrepancy in grain size cannot be conclusively argued. Figure 3.8C shows the crystallite size of the catalysts during various stages of cycling. For Mg-20V, the catalyst is denoted as $VH_{0.5}/V$. The size of $VH_{0.5}/V$ increases from 4 nm after 45 cycles, to 7 nm after 200 cycles. For Mg-10V-10Nb, the size of $Nb_{0.5}V_{0.5}H$ stays essentially the same; it is 3 nm after 45 cycles and 4 nm after 500 cycles.

Figure 3.9 shows the SEM micrographs of Mg-20V and Mg-10V-10Nb samples after selected cycling stages. The microstructures of Mg-20V are presented after 45, 90 and 200 cycles. The microstructures of Mg-10V-10Nb are presented after 45, 90 and 500 cycles. With increasing cycle number, the film structures of both materials show progressive disintegration. This is due to the repeated volume expansion/contraction (24.5% volume mismatch, with respect to the hydride phase, between the metal and the hydride phase) during hydrogen absorption/desorption cycling. The low magnification images highlight one important difference between the two systems: the film structure of binary sample disintegrated faster. For example, after 90 cycles the Mg-10V-10Nb film

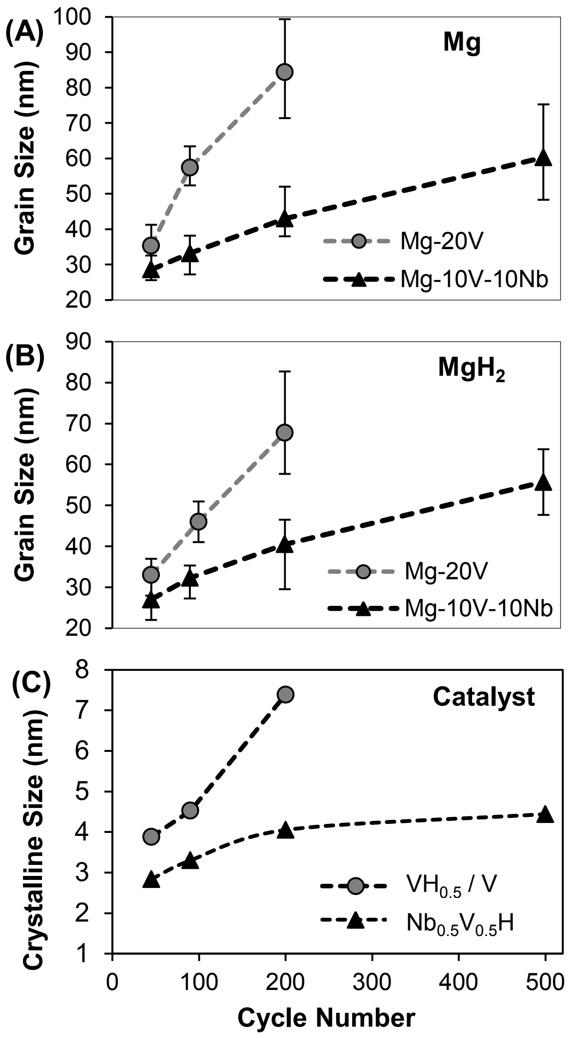

Figure 3.8: During-cycle grain size analysis for Mg-20V and Mg-10V-10Nb. (A) Grain size of metallic Mg in the desorbed state. (B) Grain size of MgH_2 in the absorbed state. (C) Crystalline size of catalyst.

(Figure 3.9H) still consisted of large flakes in the size of 100 or more µm. However, after the same number of cycles the Mg-20V film (Figure 3.9B) was finer, with the size of vast majority of the flakes being 10 µm or less.

The higher magnification micrographs reveal the edge and the surface morphologies of the flakes. For Mg-20V, a high density of surface cracks is visible after 45 cycles (Figure 3.9D). Some of the cracks develop into large fractures through the entire flake thickness after 90 cycles (Figure 3.9E). The Mg-10V-10Nb sample is similarly rough at the surface after 45 cycles (Figure 3.9J). However, the middle section of the flake holds its structural integrity relatively well. After 90 cycles, the original dense film structure has cracked into particles that are held together in the planar film geometry (Figure 3.9K). The absence of large fracture through the thickness may account for the larger flake size of ternary samples at macroscopic view. After extended cycling, both Mg-20V and Mg-10V-10Nb specimens disintegrate into loose powders, though flake edges several micrometers long can still be found (Figures 3.9F and L).

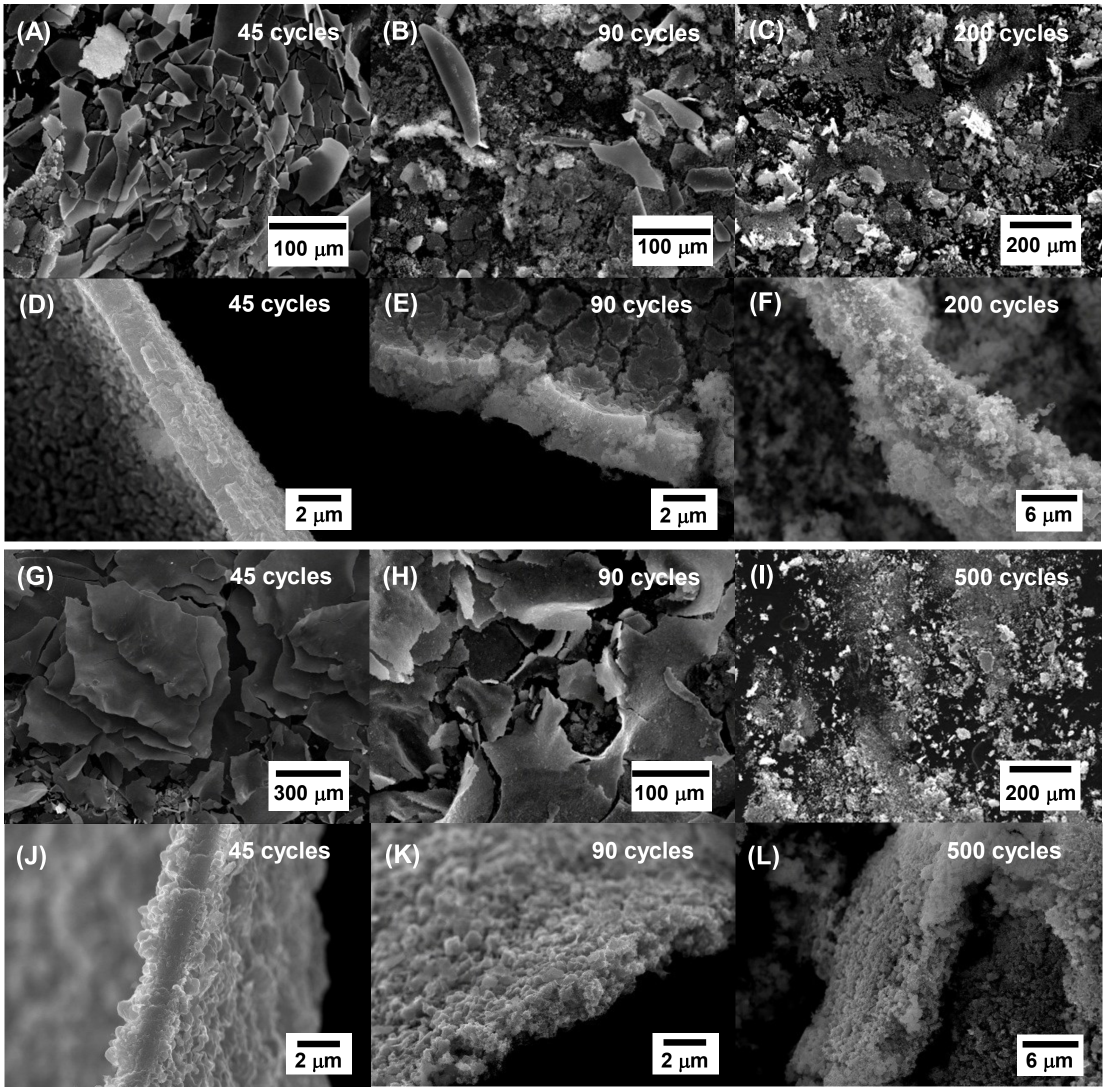

Figure 3.9: SEM micrographs of Mg-20V and Mg-10V-10Nb after various stages of cycling. (A-C) Low magnification images of Mg-20V flakes after 45, 90, and 200 cycles, respectively. (D-F) High magnification images of Mg-20V flakes after 45, 90, and 200 cycles, respectively. (G-I) Low magnification images of Mg-10V-10Nb after 45, 90, and 500 cycles, respectively. (J-L) High magnification images of Mg-10V-10Nb flakes after 45, 90, and 500 cycles, respectively.

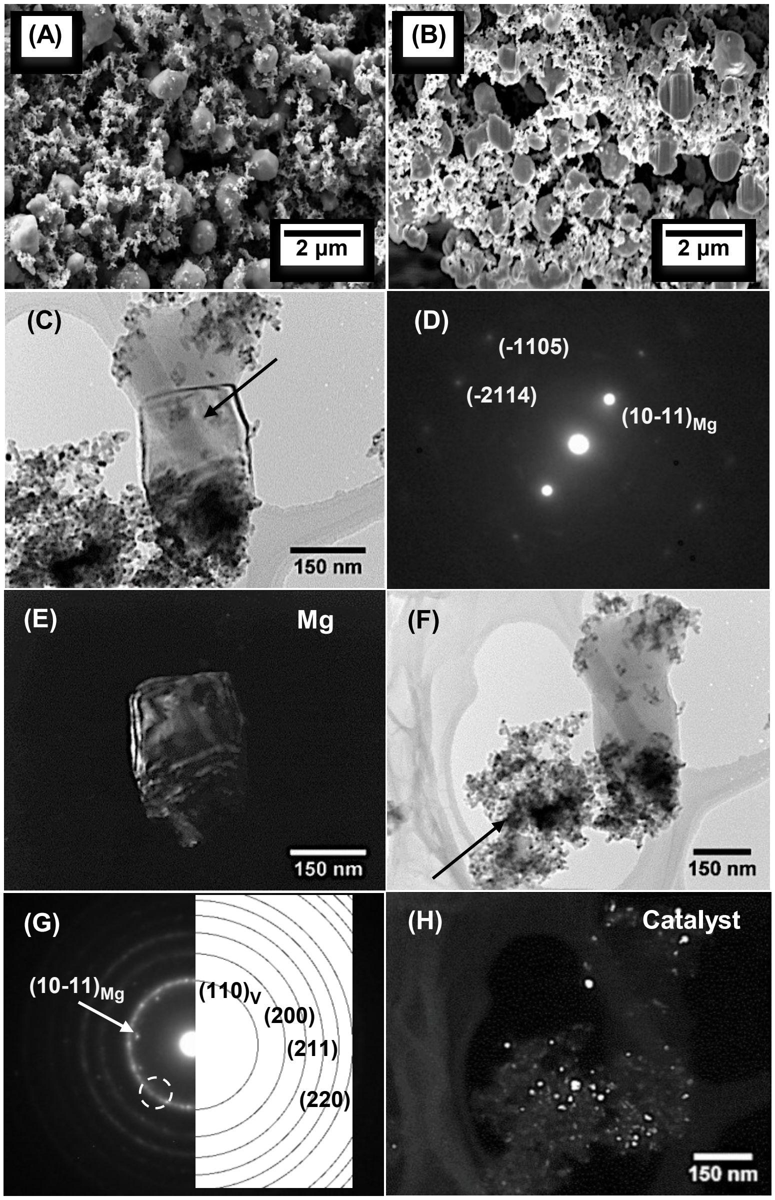

Figure 3.10: SEM and TEM micrographs of Mg-20V, in the desorbed state, after 200 cycles. SEM micrographs of (A) representative post-cycled powder agglomerate and (B) a cross section through the powder agglomerate achieved via FIB sectioning. (C) Bright field TEM micrograph of a representative sample region. (D) Indexed selected area diffraction (SAD) pattern acquired from the Mg particle marked by an arrow in (C). (E) Dark field micrograph of the Mg, obtained using g = $(10\text{-}11)_{Mg}$ reflection. (F) Bright field TEM micrograph of a region adjacent to the same Mg particle, showing a cluster of fine crystallites. (G) SAD pattern acquired from the crystallite cluster, indexed as belonging to $V/VH_{0.5}$; isolated Mg spot reflections are also marked in the SAD (arrowed). Dark field micrograph of the catalyst obtained using a portion of the (110) ring that is marked by a dashed circle.

Figure 3.10 shows the results of SEM and TEM analysis of Mg-20V, in the desorbed state, after 200 cycles. A bimodal powder distribution can be identified in the SEM micrographs (Figure 3.10A). The large 500+ nm particles are magnesium. Though these particles are an obvious feature of the SEM images, much smaller Mg particles are also detected using TEM. A cross section through the representative powder agglomerate, achieved via FIB sectioning, is shown in Figure 3.10B. The image reveals the extensive porosity of the post-cycled sample. The specimens appear to disintegrate into powders that are weakly held in the original film geometry. Figure 3.10C shows a bright field TEM micrograph of a representative sample region. Figure 3.10D shows the indexed selected area diffraction (SAD) pattern acquired from the Mg particle (arrowed). In the corresponding dark field micrograph (Figure 3.10E), obtained using the g = $10\text{-}11_{\text{Mg}}$ reflection, one section of the particle displays strong Bragg contrast. The grain is large enough to show thickness contours along its edges. It also displays Pendellosung contrast of several threading dislocations (top left and bottom right). Figure 3.10F shows a bright field image of the same region, but now with the Mg grain tilted away from strong Bragg contrast. Figure 3.10G shows the indexed SAD pattern acquired from the cluster of fine crystallites (arrowed). The simulation indicates that the observed rings have a bcc-type periodicity, which could be associated with either metallic V or $VH_{0.5}$ (the hydrogen superlattice reflections would not show in an electron diffraction pattern). Isolated Mg spot reflections are also marked in the SAD. Figure 3.10H shows a dark field micrograph of the V catalyst crystallites, obtained using a portion of the (110) ring that is marked by a dashed circle.

Figure 3.11 shows the SEM and TEM micrographs of Mg-10V-10Nb in the desorbed state, after 500 cycles. Figures 3.11A and B highlight the structure of the powder agglomerate, which shows somewhat different morphology compared to Mg-20V. Overall there are fewer 500+ nm large magnesium particles. High levels of porosity are similarly present in the ternary system, though qualitatively the pores appear more uniform. The bright field image (Figure 3.11C), SAD (Figure 3.11D) and dark field micrograph of Mg (Figure 3.11E) all appear relatively similar to Mg-V. However, as evidenced by the dark field micrograph of catalyst particles (Figure 3.11F), the major difference between the two systems is in the size and distribution of the surface catalyst particles. Judging from the image contrast and the appearance of the SAD patterns, the regions shown in Figures 3.10 and 3.11 are of similar thickness. It can be then stated that the catalyst crystallites shown in the ternary Mg-V-Nb are both finer and more densely distributed than those in Mg-V.

To seek direct evidence demonstrating the interrelationship between microstructure and the observed two-stage absorption behavior, we used cryo-stage TEM to examine a binary Mg-20V sample that was partially absorbed. The material was previously cycled

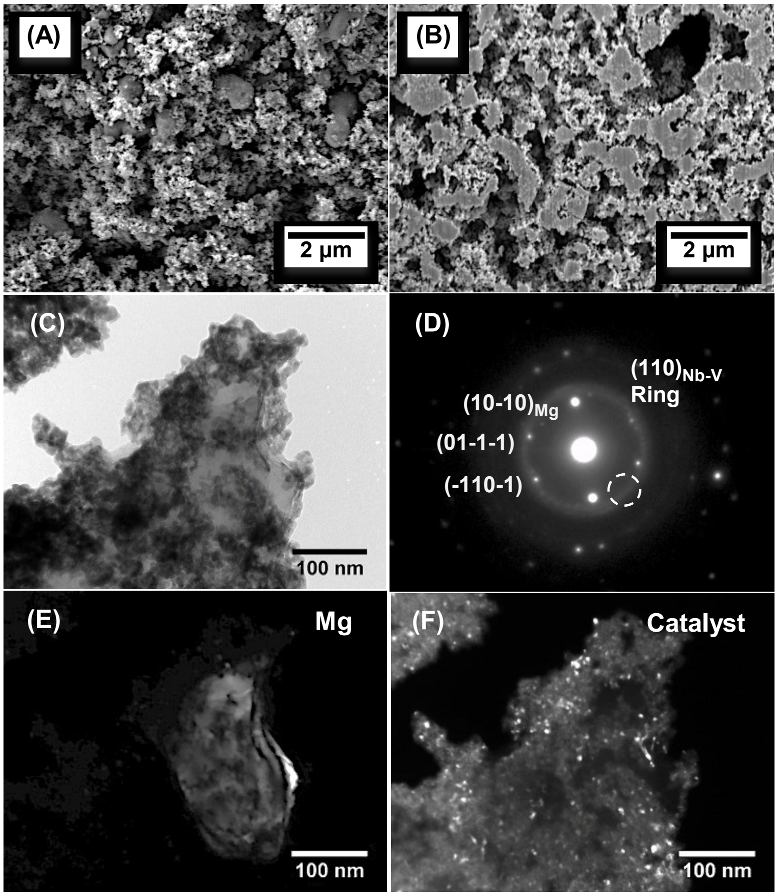

Figure 3.11: SEM and TEM micrographs of Mg-10V-10Nb, in the desorbed state, after 500 cycles. SEM micrographs of (A) representative post-cycled powder agglomerate and (B) FIB cross section through the agglomerate. (C) Bright field TEM micrograph of a representative electron transparent region. (D) The corresponding SAD pattern, indexed as a single crystal Mg. (E) Dark field TEM micrograph of Mg, obtained using g = $(10\text{-}10)_{Mg}$ reflection. (F) Dark field micrograph of catalyst particles, obtained using a portion of the $(110)_{Nb-V}$ ring that is marked by a dashed circle.

200 times at 200 °C, and the final absorption procedure was interrupted right after the rapid stage I (~ 50% reaction fraction). In this way, we were able to identify the type of microstructure that would absorb hydrogen rapidly during stage I. The material remaining as metallic Mg would thus absorb hydrogen slowly during stage II. The partially absorbed sample contains 2 wt.% hydrogen, corresponding to an overall H/Mg ~ 1. However, as been previously reported using in situ neutron scattering, H (D) solubility in

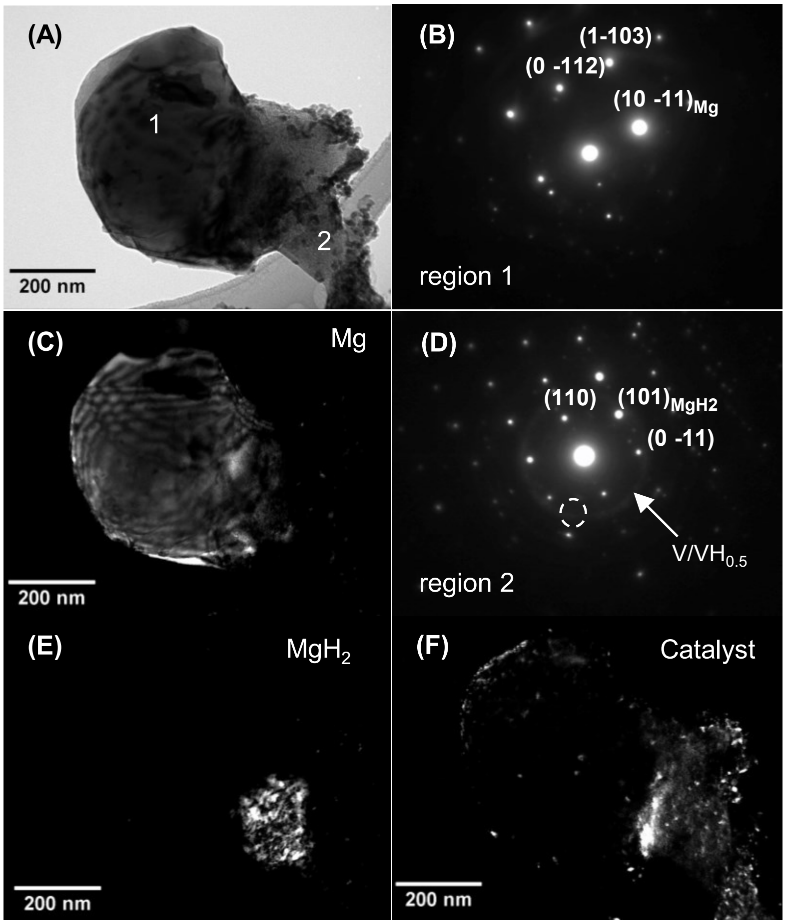

Figure 3.12: Cryo-stage TEM analysis of partially absorbed (~ 50% reaction fraction) Mg-20V, after 200 full sorption cycles at 200 ˚C. (A) A bright field micrograph of a representative region. (B) SAD pattern acquired from the region marked 1, indexed as single crystal Mg. (C) A dark field micrograph of the Mg grain obtained using g = $(10\text{-}11)_{Mg}$ reflection. (D) SAD pattern acquired from the region marked 2, indexed as a single crystal MgH_2, along with rings associated with the $V/VH_{0.5}$ catalyst crystallites. (E) A dark field micrograph of MgH_2 obtained using g = $(101)_{MgH2}$ reflection. (F) A dark field micrograph of $V/VH_{0.5}$ catalyst crystallites obtained using a portion of the (110) ring that is marked by a dashed circle.

the Nb- and V-catalyzed Mg α-phase is very low even at an elevated temperature of 320 °C [46]. This implies that the H-absorbed microstructure is β-MgH_2. The results of cryo-stage TEM analysis are shown in Figure 3.12. Examining region marked 1 in the bright field micrograph (Figure 3.12A), it is apparent from the dark field micrograph (Figure 3.12C) that the grain remains entirely metallic. Conversely, the region marked 2 in the bright field micrograph, has transformed to a relatively large MgH_2 grain that can be imaged using the $g = (101)_{MgH2}$ reflection. The dark field micrograph of the MgH_2 grain shown in Figure 3.12E has the characteristic mottled contrast related to ionic materials [49]. As shown in the dark field micrograph of catalyst crystallites (Figure 3.12F), the catalyst number density in region 2 is higher than that in region 1. What is evident from the microstructure is that the hydride preferentially formed in the region with a denser catalyst distribution. The regions of microstructure where few catalyst particles were observed remained untransformed.

We examined a partially absorbed ternary Mg-13V-7Nb sample that was previously cycled for 500 times at 200 °C. The hydriding procedure was interrupted ~60 to 70% reaction fraction, which also corresponds to stage I absorption. The results of cryo-stage TEM analysis are shown in Figure 3.13. For sample regions with non-uniform catalysts distribution (see Figure 3.13A–F), the hydrides again show clear spatial correlation with the Nb-V catalyst particles distributed on the surface, agreeing very well with what was observed in the binary Mg-20V sample. This mechanistic picture of hydride formation is also encountered at room temperature. Figure 3.14 shows the results of the ternary Mg-13V-7Nb sample that is partially absorbed (~35% reaction fraction) at room temperature.

It should be noted that the non-uniform catalyst distribution is not the representative microstructure of the ternary systems. For a representative region of ternary Mg-13V-7Nb sample (see Figure 3.13G-L), the particle with uniform catalyst distribution has completely transformed to a single grain of MgH_2, though its size is as large as the ones shown in Figures 3.12A and 3.13A. The presence of growth twins of MgH_2 is consistent to what has been previously reported by Zahiri et al. [53]. The fast hydrogenation process and the presence of trace-level Nb and V impurities in the hydride promote the twinning that would compensate for the internal stress buildup during the Mg to MgH_2 phase transformation. What needs to be emphasized is that regardless of the surface catalyst distribution, there is no evidence of any “core-shell” or “contracting volume” type of hydride growth mechanism, where many small MgH_2 nuclei would form covering the Mg surfaces. Rather the formation of isolated MgH_2 nuclei and their subsequent growth into the magnesium grain is always the hydriding mechanism in both the binary and the ternary systems.

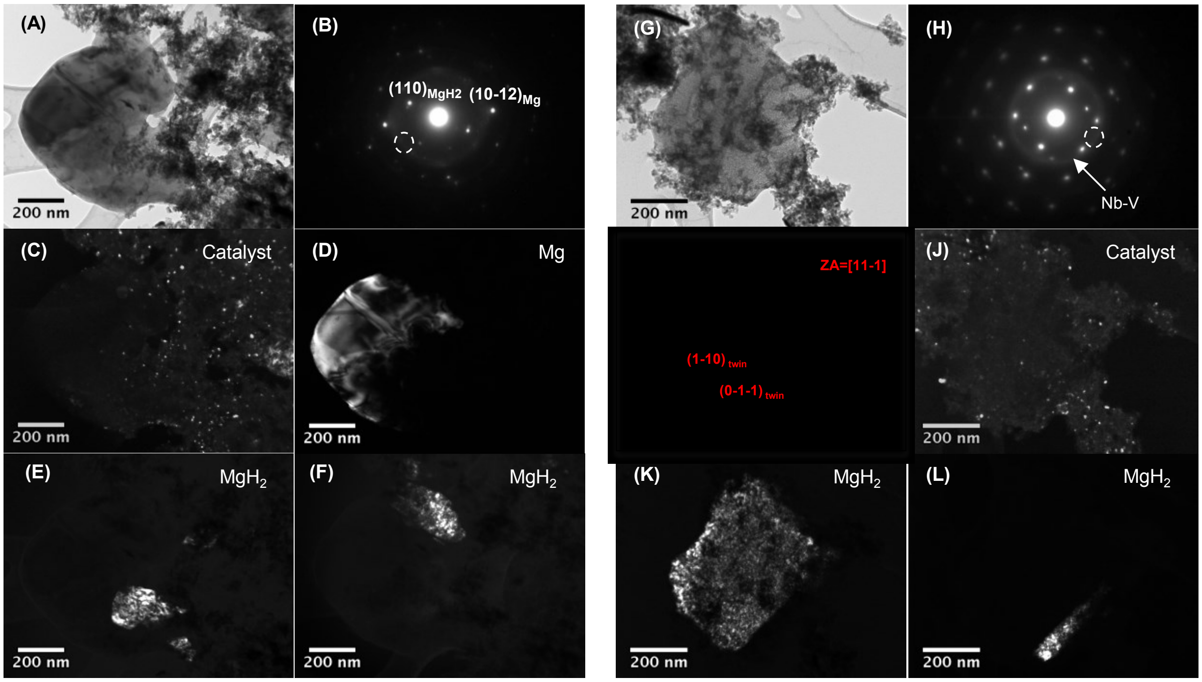

Figure 3.13: Cryo-stage TEM analysis of partially absorbed (60-70% reaction fraction) Mg-7Nb-13V, after 500 full sorption cycles at 200˚C. (A) Bright field micrograph of a representative region with non-uniform catalysts distribution. (B) The corresponding SAD pattern. (C) Dark field micrograph of Nb-V catalyst crystallites (C) Dark field micrograph of the Mg grain obtained using g = $(10\text{-}12)_{Mg}$ reflection. (D) Dark field micrograph of MgH_2 obtained using g = $(110)_{MgH2}$ reflection. (E) Dark field micrograph of another MgH_2 grain obtained by tilting the sample. (G) Bright field micrograph of a representative region with uniform catalysts distribution. (H) The corresponding SAD pattern. (I) Simulation of the diffraction pattern which shows that Matrix ZA is close to [-1-11], and the observed twinning plane is (101). (J) Dark field micrograph of Nb-V catalyst crystallites obtained using a portion of the (110) ring that is marked by a dashed circle. (K) Dark field micrograph of MgH_2 obtained using the matrix spot g = $(101)_{MgH2}$ reflection. (L) Dark field micrograph of the twinned MgH_2 obtained from g = $(101)_{twin}$ reflection.

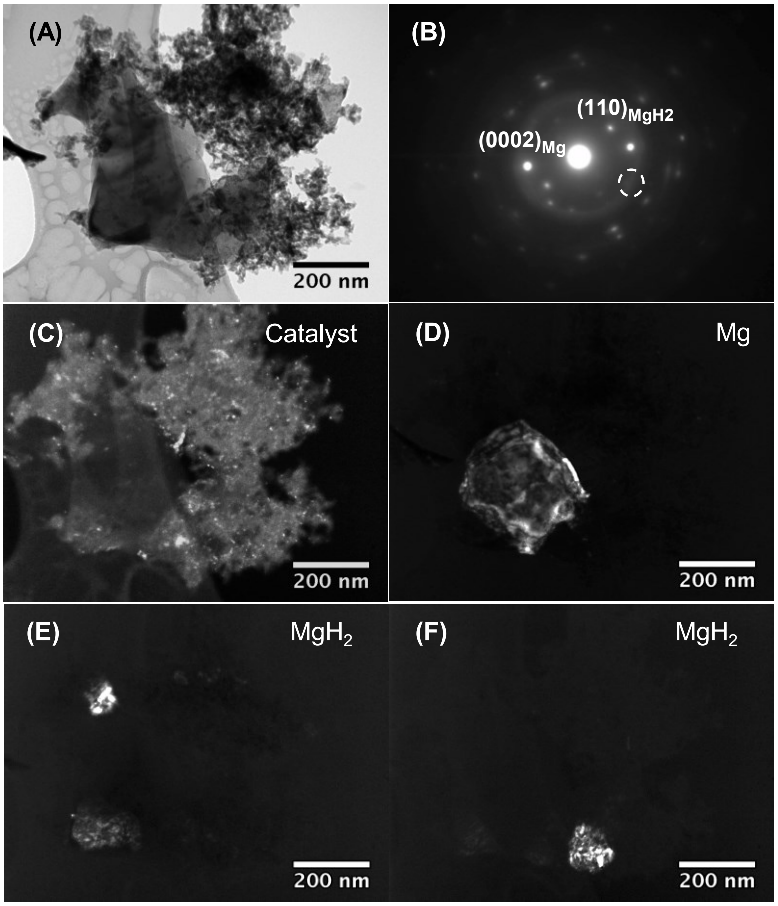

Figure 3.14: Cryo-stage TEM analysis of partially absorbed (35% reaction fraction) Mg-7Nb-13V at room temperature. (A) Bright field micrograph of a representative region with non-uniform catalysts distribution. (B) The corresponding SAD pattern. (C) Dark field micrograph of Nb-V catalyst crystallites. (D) Dark field micrograph of Mg obtained using g = $(0002)_{Mg}$ reflection. (E) Dark field micrograph of MgH_2 obtained from g = $(110)_{MgH2}$ reflection. (F) Dark field micrograph of another MgH_2 grain obtained by tilting the sample.

3.4 Discussion

The results of X-ray diffraction analysis showed that the initial co-deposited alloy materials decompose into composites of magnesium with separate catalytic phases. However, the effectiveness of secondary catalysts dispersed in the composites should be strongly affected by the actual surface area of these catalysts in contact with hydrogen molecules. During the early cycling stages, the films are largely intact and do not contain an extensive network of cracks running throughout the bulk. At that stage, the surface Pd layer also has not yet fully reacted with the underlying Mg [47]. Therefore the primary regions that are catalytically active towards hydrogen dissociation/recombination are the Pd layers on top and bottom. The dissociated hydrogen atoms have to diffuse into the bulk. For pure Mg films with a catalyst layer on the surface, it has been observed that the migration of hydrogen atoms into or out from the bulk would be impeded by the blocking effect of a continuous MgH_2 layer [58,59]. However in systems alloyed with elements such as Cr-V [41] or Al [60], hydriding proceeds quite uniformly throughout the bulk of the film, indicating enhanced hydrogen diffusion.

From Figure 3.1, an initial progressive kinetic worsening has been observed in both absorption and desorption kinetics. This occurs for a set number of cycles, after which the sorption kinetics slowly improves again. The activation behavior in sorption kinetics may be viewed as the interplay between the progressive degradation of the surface Pd/Ta catalyst and the progressive formation of V or Nb-V exposed catalytic surface. As demonstrated in Figure 3.9, the progressive film disintegration that exposes more secondary catalysts to hydrogen molecules has occurred in both binary and ternary systems. Once the amount of V or Nb-V exposed catalytic surface is sufficient to overcome the loss of Pd, both the absorption and desorption rates begin to improve.

It is evident that the behaviors of activation depend on the sample compositions. Since all the films contain initially the same amount of Pd/Ta catalyst and the degradation rate of Pd/Ta layer should be roughly the same, the difference in activation behavior is most likely due to the variation in film disintegration rates (see Figure 3.9). It is expected that the internal stress buildup, induced by repeated volume expansion/contraction during hydrogen absorption/desorption cycling, would result in cracking at Mg-MgH_2 interfaces [61]. From the fracture mechanism, it is known that the distance that a crack will advance per cycle will scale with the material’s grain size [62]. It can be therefore argued that the variation in grain sizes is the microstructural cause for the observed discrepancy in film disintegration rates. As shown in Figure 3.8A, the Mg grain size in the binary Mg-20V is consistently larger than that in the ternary Mg-10V-10Nb. Therefore, the former film would disintegrate faster with deeper cracks. This provides the binary system with a kinetic advantage during activation due to more dissociation/recombination sites and reduced diffusion distance.

As shown in Figure 3.8C, the bimetallic $Nb_{0.5}V_{0.5}H$ crystallites exhibit improved resistance towards cycling-induced coarsening as compared to $VH_{0.5}/V$ crystallites. The microstructural stability of secondary catalytic nanoparticles plays a role in stabilizing the grain size and particle size of Mg/MgH_2. From the dark field micrographs of both binary and ternary systems (see Figures 3.10E, 3.11E, 3.12C, 3.12E, 3.13D-F, 3.13K and 3.14D-F), there is no evidence of Ashby-Brown type strain contrast [63,64] that would be expected if the nanoparticles were actually embedded in the bulk of the grains. Rather the catalyst particles remain at grain boundaries and/or surfaces throughout cycling sorption. In the following paragraphs, we will discuss the possible mechanisms through which the V or Nb-V catalysts at grain boundaries and/or the surface result in the observed differences in magnesium (hydride) grain size and particle size between the binary and the ternary systems.

It is known that the precipitates at grain boundaries can act as pinning points retarding the grain growth of the matrix material. The pinning force P (Zener Drag effect) that a particle exerts on the boundary is expressed by [65]:

$$P = \frac{3f\gamma}{2r} \qquad \text{(Eq. 3.3)}$$

where f is the volume fraction of precipitates, γ is the grain boundary energy and r is the radius of the precipitates. The pinning effect is reduced as the size of precipitates increases. Therefore, one would expect to see more substantial coarsening of the Mg grains in the binary Mg-V sample, since the crystallite size of $VH_{0.5}/V$ is consistently larger than that of $Nb_{0.5}V_{0.5}H$. It must be kept in mind that if the precipitated particles coarsen above a certain critical size, grain growth of the matrix phase would still occur [66]. Moreover, as is evident from Figures 3.10 and 3.11, the majority of catalyst crystallites wind up distributing on the external surface of relatively large Mg particles (which may or may not be a single crystal) after extended sorption cycling. These facts suggest that the precipitates' pinning effect will diminish with cycling.

Considering the possibility that every V or Nb-V catalyst/Mg interface is a potential nucleation center for hydride to grow, the distance between the catalyst particles will then primarily determine the hydride grain size. It has been recently demonstrated that the finely dispersed MgF_2 nanocrystals, serving as nucleation centers for MgH_2, have remarkable effect on refining the grain size of hydride throughout cycling [67]. From Figure 3.10 and 3.11, it is clear that the ternary Mg-V-Nb systems consist of an overall denser distribution of catalysts on the surface of Mg particles. Herein, one would expect a higher density of MgH_2 nuclei in the ternary systems. The shorter distance between the hydride nuclei would result in an earlier impingement of growing hydride crystallites, and thus a smaller grain size of MgH_2 in the ternary systems. This agrees well with the result shown in Figure 3.8B. The ternary Mg-V-Nb system with a denser surface catalyst distribution has a consistently smaller grain size of MgH_2 than the binary Mg-V one.

Though not being characterized quantitatively, the particle size of Mg/MgH_2 also increases with sorption cycling, due to the sintering and the agglomeration of "loose" particles. However, as shown in Figures 3.10 and 3.11, the overall Mg particle size in the ternary Mg-V-Nb system is smaller than that in the binary Mg-V system. It has been recently demonstrated that Fe (which does not hydride) is much less effective than Ti (which forms a very stable hydride), in preventing sintering/agglomeration of the hydrogen cycling magnesium microstructure [68]. This is in line with our results. As demonstrated in Figure 3.7, Nb-V nanoparticles remain as hydride throughout the cycling, whereas the V particles are at least partially desorbed. Since a diffusional flux of metal atoms away (or towards) the hydride would upset the exact stoichiometry, it would be more difficult for a hydride to undergo some form of Ostwald Ripening.

On the basis of the above-mentioned discussion, a mechanistic description is provided for the hydrogen cycling-induced microstructural evolution at elevated temperature, as shown in the schematic in Figure 3.15. In the period of activation, the films continuously transform from fully dense structures, with hydrogen ingress being possible only at surfaces, to powders with progressively more exposed catalysts. After extended cycling, the sample structure becomes analogous to that of a weakly held together nanocomposite powder, with a distribution of catalytic nanoparticles on the surfaces of larger Mg/MgH$_2$ particles. The schematic illustrates the cracking during activation. It also illustrates the interrelationship between the size of catalyst particles and the grain size, particle size of Mg, as well as the surface catalyst distribution. The schematic highlights the difference in microstructure between Mg-V and Mg-V-Nb during hydrogen cycling.

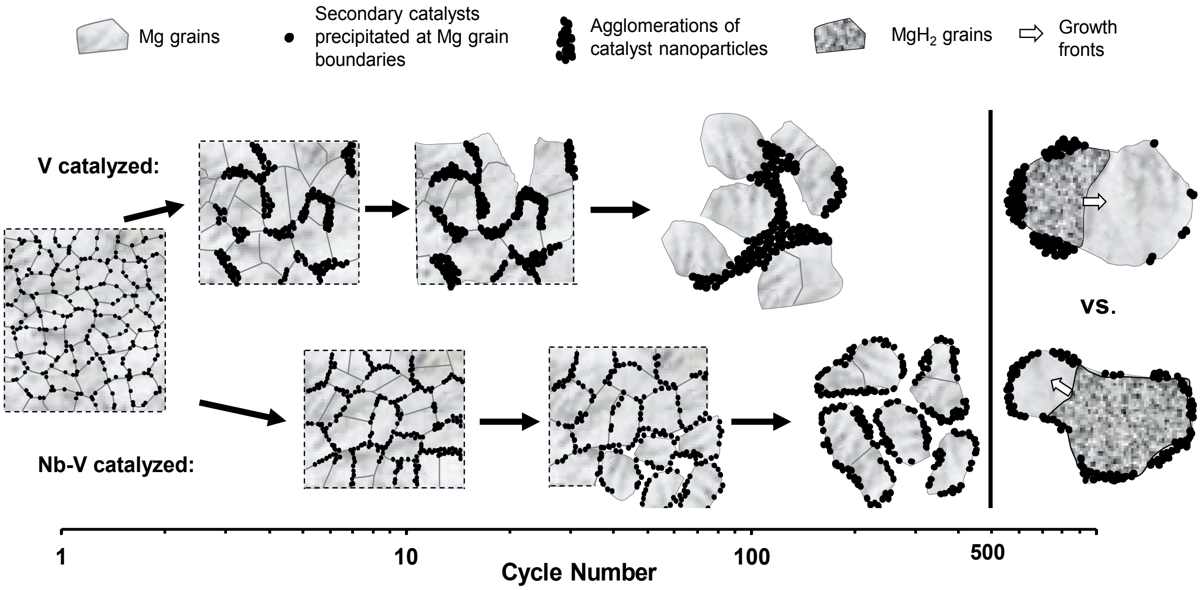

Figure 3.15: Schematic representation of the mechanistic description for the cycling-induced microstructural evolution of initial Magnesium alloy film. Dashed lines indicate non-physical boundaries. The microstructures and the absorption behaviors between the elemental V catalyzed and the bimetallic Nb-V catalyzed MgH$_2$ are compared in parallel with respect to the cycle numbers.

The ultimate outcome of the disparity in the coarsening rates of the V versus Nb-V catalysts is that the kinetics of the binary system degrades much more rapidly than that of the ternary system. Generally speaking, the kinetic degradation could be due to several microstructural factors. The decreased availability of the surface catalysts with increasing cycle number, the progressive increase in the Mg grain size and particle size, which increases the hydrogen diffusion distance, or a combination of both are all plausible explanations. However, as observed from the Avrami plots in Figure 3.4, it is the magnitude of a two-stage hydriding behavior, namely the conclusion point of the rapid stage I with respect to reaction fraction, that defines the disparate rates of kinetics degradation between the binary and the ternary systems. Therefore, any insight regarding the microstructural origin for the two-stage hydriding behavior would be the key for understanding the degradation mechanism and the enhanced cycling stability of ternary systems.

The cryo-stage TEM analysis, prepared by interrupting the reaction right after or within the stage I absorption, reveals direct microstructural evidence for the rapid absorption in stage I. Figures 3.12-3.14 demonstrate a key feature of Mg to MgH_2 phase transformation: The hydriding during stage I only occurs in the regions with a denser distribution of surface catalysts. The regions with few catalyst particles remain untransformed. Therefore, our hypothesis is that it is the surface catalyst distribution and its stability that dictate the magnitude of the two-stage hydriding kinetics. This hypothesis is in accord with the results shown by Anastasopol et al. [31], where the heterogeneity in the reaction rates within one sample is due to the different configurations (e.g. particle size in their case) of the reacting particles.

As indicated by the cryo-stage TEM analysis, hydride nucleates on the surface in close proximity to the catalyst particles. In a previous study, we have also demonstrated that the hydride to metal phase transformation occurs entirely on the particle surface, in that case on pre-existing MgH_2 with the right crystallographic orientation [69]. This makes sense in terms of the difficulty of nucleating one phase in the bulk of the other, due to the immense volumetric and chemical interfacial energy mismatches between the metal and the hydride. One plausible interpretation for the spatial correlation is that the catalyst particles facilitate the nucleation of hydride by serving as heterogeneous nucleation sites or nucleation centers for MgH_2 [39,67,70]. If the nucleation density of MgH_2 scales with the surface catalyst distribution, the different magnitudes of two-stage hydriding behaviors between binary Mg-V and ternary Mg-V-Nb systems can be rationalized by arguing that there are more hydride nuclei formed in the ternary samples.

The comparison between the two microstructures in Figure 3.13 suggests another mechanistic picture regarding the influence of surface catalyst distribution on hydriding kinetics. Compared to the hydride grains in the region with non-uniform catalyst distribution (see Figures 3.13E and F), the hydride grain in Figure 3.13K grew up to at least five times larger (measured by projected area) within the same period of time. This fact indicates that the denser distribution of surface catalysts dramatically increased the growth rate of the hydride phase. To explain the influence on growth rate, we have to consider the fact that the effectiveness of secondary catalytic phases is also strongly affected by the actual distribution of catalyst on Mg surface. Hydrogen dissociation would primarily take place on the exposed surface of V or Nb-V catalysts, rather than on the pure Mg surface. Thus, the distribution of catalyst on Mg would strongly affect the surface concentration of hydrogen atoms and the flux of hydrogen atoms diffusing towards the growth front of the hydride phase. Overall, since ternary Mg-V-Nb samples have a larger proportion of Mg with a denser surface catalyst distribution than the binary Mg-V sample, a larger fraction of Mg can be transformed to hydride during the rapid stage I absorption.

The measured apparent activation energy (see Figure 3.5) shed light on the hydride growth mechanism during the stage I absorption. One may argue that the measured activation energy (Q_A = 14.6 kJ mol^{-1}) agrees quite well with hydrogen diffusion in magnesium, as the reported values for hydrogen diffusion in magnesium range from 24 to 40 kJ mol^{-1} [71,72]. A variety of experimental and theoretical studies yielded activation energies, ranging from 96 to 166 kJ mol^{-1}, for hydrogen diffusion in MgH_2 [73-75]. Therefore, we could rule out the possibility that diffusion of hydrogen through a product layer of hydride is the rate-limiting step here. Rather, hydrogen atoms transport towards the hydride growth front through the surrounding magnesium matrix. This mechanistic picture of hydride growth is consistent with the results of cryo-stage TEM analysis, where little evidence for any “core-shell” structure was observed.

3.5 Conclusion

Magnesium hydride catalyzed by new nano-scale bimetallic Nb-V catalysts exhibits significantly enhanced cycling kinetic stability without compromising the sorption kinetics even after 500 hydrogen sorption cycles. By studying a binary Mg-V system as the baseline, we observed clear trends of the cycling-induced microstructural evolution and the concomitant change in sorption kinetics. Using a combination of several analytical techniques, we elucidated the major differences in microstructure between the ternary Mg-V-Nb and the binary Mg-V systems. By employing cryo-stage TEM characterization on partially absorbed material, we demonstrated that it is the surface catalyst distribution and its stability that dictate the magnitude of a two-stage hydriding behavior, which in turn determines the cycling-stability of the materials. We provided a mechanistic description of the cycling-induced microstructural evolution, which serves to systematically explain the interrelationship between the microstructure and the observed kinetic trends for both the binary and the ternary systems during the activation period and after prolonged sorption cycling.

3.6 Reference

[1] K. F. Aguey-Zinsou, J. R. Ares-Fernandez, *Energ. Environ. Sci.* **2010**, *3*, 526-543.

[2] T. K. Nielsen, F. Besenbacher, T. R. Jensen, *Nanoscale* **2011**, *3*, 2086-2098.

[3] R. Bardhan, A. M. Ruminski, A. Brand, J. J. Urban, *Energ. Environ. Sci.* **2011**, *4*, 4882-4895.

[4] H. Shao, G. Xin, J. Zheng, X. Li, E. Akiba, *Nano Energy* **2012**, *1*, 590-601.

[5] I. P. Jain, C. Lal, A. Jain, *Int. J. Hydrogen Energ.* **2010**, *35*, 5133-5144.

[6] R. Gosalawit-Utke, T. K. Nielsen, I. Saldan, D. Laipple, Y. Cerenius, T. R. Jensen, T. Klassen, M. Dornheim, *J. Phys. Chem. C* **2011**, *115*, 10903-10910.

[7] R. V. Denys, A. B. Riabov, J. P. Maehlen, M. V. Lototsky, J. K. Solberg, V. A. Yartys, *Acta Mater.* **2009**, *57*, 3989-4000.

[8] S. D. Beattie, U. Setthanan, G. S. McGrady, *Int. J. Hydrogen Energ.* **2011**, *36*, 6014-6021.

[9] D. L. Croston, D. M. Grant, G. S. Walker, *J. Alloy. Compd.* **2010**, *492*, 251-258.

[10] B. S. Amirkhiz, M. Danaie, D. Mitlin, *Nanotechnology* **2009**, *20,* 204016.

[11] S. X. Tao, W. P. Kalisvaart, M. Danaie, D. Mitlin, P. H. L. Notten, R. A. Van Santen, A. P. J. Jansen, *Int. J. Hydrogen Energ.* **2011**, *36*, 11802-11809.

[12] P. K. Pranzas, U. Bosenberg, F. Karimi, M. Munning, O. Metz, C. B. Minella, H. W. Schmitz, F. Beckmann, U. Vainio, D. Zajac, E. Welter, T. R. Jensen, Y. Cerenius, R. Bormann, T. Klassen, M. Dornheim, A. Schreyer, *Adv. Eng. Mater.* **2011**, *13*, 730-736.

[13] H. Fritzsche, C. Ophus, C. T. Harrower, E. Luber, D. Mitlin, *Appl. Phys. Lett.* **2009**, *9*4, 241901.

[14] T. E. C. Price, D. M. Grant, V. Legrand, G. S. Walker, *Int. J. Hydrogen Energ.* **2010**, *35*, 4154-4161.

[15] R. Gremaud, C. P. Broedersz, A. Borgschulte, M. J. van Setten, H. Schreuders, M. Slaman, B. Dam, R. Griessen, *Acta Mater.* **2010**, *58*, 658-668.

[16] S. X. Tao, P. H. L. Notten, R. A. van Santen, A. P. J. Jansen, *Phy.s Rev. B* **2010**, *82*, 125448.

[17] M. G. Shelyapina, D. Fruchart, *Solid State Phenom.* **2011**, *170*, 227-231.

[18] A. Baldi, M. Gonzalez-Silveira, V. Palmisano, B. Dam, R. Griessen, *Phys. Rev. Lett.* **2009**, *102*, 226102.

[19] L. P. A. Mooij, A. Baldi, C. Boelsma, K. Shen, M. Wagemaker, Y. Pivak, H. Schreuders, R. Griessen, B. Dam, *Adv. Energy Mater.* **2011**, *1*, 754-758.

[20] X. F. Liu, G. S. McGrady, H. W. Langmi, C. M. Jensen, *J. Am. Chem. Soc.* **2009**, *131*, 5032-5033.

[21] W. P. Kalisvaart, C. T. Harrower, J. Haagsma, B. Zahiri, E. J. Luber, C. Ophus, E. Poirier, H. Fritzsche, D. Mitlin, *Int. J. Hydrogen Energ.* **2010**, *35*, 2091-2103.

[22] H. Shao, M. Felderhoff, F. Schuth, C. Weidenthaler, *Nanotechnology* **2011**, *22*, 235401.

[23] A. Fernandez, E. Deprez, O. Friedrichs, *Int. J. Hydrogen Energ.* **2011**, *36*, 3932-3940.

[24] Z. Zlatanova, T. Spassov, G. Eggeler, M. Spassova, *Int. J. Hydrogen Energ.* **2011**, *36*, 7559-7566.

[25] H. W. Langmi, G. S. McGrady, X. F. Liu, C. M. Jensen, *J. Phys. Chem. C* **2010**, *114*, 10666-10669.

[26] K. J. Jeon, H. R. Moon, A. M. Ruminski, B. Jiang, C. Kisielowski, R. Bardhan, J. J. Urban, *Nat. Mater.* **2011**, *10*, 286-290.

[27] W. P. Kalisvaart, A. Kubis, M. Danaie, B. S. Amirkhiz, D. Mitlin, *Acta Mater.* **2011**, *59*, 2083-2095.

[28] V. A. Vons, A. Anastasopol, W. J. Legerstee, F. M. Mulder, S. W. H. Eijt, A. Schmidt-Ott, *Acta Mater.* **2011**, *59*, 3070-3080.

[29] Y. Liu, G. C. Wang, *Nanotechnology* **2012**, *23*, 025401.

[30] C. Zlotea, C. Chevalier-Cesar, E. Leonel, E. Leroy, F. Cuevas, P. Dibandjo, C. Vix-Guterl, T. Martens, M. Latroche, *Faraday Discuss* **2011**, *151*, 117-131.

[31] A. Anastasopol, T. V. Pfeiffer, A. Schmidt-Ott F. M. Mulder, S. W. H. Eijt, *Appl. Phys. Lett.* **2011**, *99*, 194103.

[32] M. Danaie, C. Mauer, D. Mitlin, J. Huot, *Int. J. Hydrogen Energ.* **2011**, *36*, 3022-3036.

[33] J. Lang, J. Huot, *J. Alloy. Compd.* **2011**, *509*, L18-L22.

[34] A. Revesz, A. Kis-Toth, L. K. Varga, E. Schafler, I. Bakonyi, T. Spassov, *Int. J. Hydrogen Energ.* **2012**, *37*, 5769.

[35] A. Baldi, B. Dam, *J. Mater. Chem.* **2011**, *21*, 4021-4026.

[36] Z. P. Tan, C. Chiu, E. J. Heilweil, L. A. Bendersky, *Int. J. Hydrogen Energ.* **2011**, *36*, 9702-9713..

[37] H. Oguchi, Z. Tan, E. J. Heilweil, L. A. Bendersky, *Int. J. Hydrogen Energ.* **2010**, *35*, 1296-1299.

[38] B. Zahiri, B. S. Amirkhiz, M. Danaie, D. Mitlin, *Appl. Phys. Lett.* **2010**, *96*, 013108.

[39] B. Zahiri, B. S. Amirkhiz, D. Mitlin, *Appl. Phys. Lett.* **2010**, *97*, 083106.

[40] H. Fritzsche, W. P. Kalisvaart, B. Zahiri, R. Flacau, D. Mitlin, *Int. J. Hydrogen Energ.* **2012**, *37*, 3540-3547.

[41] P. Kalisvaart, E. Luber, H. Fritzsche, D. Mitlin, *Chem Commun* **2011**, *47*, 4294-4296.

[42] J. F. Pelletier, J. Huot, M. Sutton, R. Schulz, A. R. Sandy, L. B. Lurio, S. G. J. Mochrie, *Phys. Rev. B* **2001**, *63*, 052103.

[43] G. Liang, J. Huot, S. Boily, A. Van Neste, R. Schulz, *J. Alloy. Compd.* **1999**, *291*, 295-299.

[44] S. A. Jin, J. H. Shim, J. P. Ahn, Y. W. Cho, K .W. Yi, *Acta Mater* **2007**, *55*, 5073-5079.

[45] H. Wipf, R. G. Barnes, *Hydrogen in metals III*; Springer: Berlin ; New York, 1997.

[46] H. G. Schimmel, J. Huot, L. C. Chapon, F. D. Tichelaar, F. M. Mulder, *J. Am. Chem. Soc.* **2005**, *127*, 14348-14354.

[47] X. H. Tan, C. T. Harrower, B. S. Amirkhiz, D. Mitlin, *Int. J. Hydrogen Energ.* **2009**, *34*, 7741-7748.

[48] M. Wojdyr, *J. Appl. Crystallogr.* **2010**, *43*, 1126-1128.

[49] M. Danaie, D. Mitlin, *J. Alloy. Compd.* **2009**, 476, 590-598.

[50] M. Gonzalez-Silveira, R. Gremaud, A. Baldi, H. Schreuders, B. Dam, R. Griessen, *Int. J. Hydrogen Energ.* **2010**, *35*, 6959-6979.

[51] M. Avrami, *J. Chem. Phys.* **1941**, *9*, 177-184.

[52] J. W. Christian, *The theory of transformations in metals and alloys;* 2nd ed.; Pergamon Press: Oxford ; New York, 1975.

[53] B. Zahiri, M. Danaie, X. Tan, B. S. Amirkhiz, G. A. Botton, D. Mitlin, *J. Phys. Chem. C* **2012**, *116*, 3188-3199.

[54] P. S. Rudman, *J. Appl. Phys.* **1979**, *50*, 7195-7199.

[55] R. Griessen, T. Riesterer, *Hydrogen in Intermetallic Compounds I*; Springer-Verlag: Berlin Heidelberg NewYork London Paris Tokyo, 1988.

[56] T. Schober, *Hydrogen Metal Systems I;* Zurich: Trans Tech Publications, Ltd., 1996.

[57] H. Muller, K. Weymann, *J. Less-Common Met.* **1986**, *119*, 115-126.

[58] P. Vermeulen, A. Ledovskikh, D. Danilov, P. H. L Notten, *Acta Mater.* **2009**, *57*, 4967-4973.

[59] M. S. Conradi, M. P. Mendenhall, T. M. Ivancic, E. A. Carl, C. D. Browning, P. H. L. Notten, W. P. Kalisvaart, P. C. M. M. Magusin, R. C. Bowman, S. J. Hwang, N. L. Adolphi, *J. Alloy. Compd.* **2007**, *446*, 499-503.

[60] H. Fritzsche, M. Saoudi, J. Haagsma, C. Ophus, E. Luber, C. T. Harrower, et al. *Appl. Phys. Lett.* **2008**, *92*, 12917.

[61] T. Schober, *Metallurgical Transactions A* **1981**, *12A*, 951

[62] R. W. Hertzberg, *Deformation and fracture mechanics of engineering materials*; 4th ed.; J. Wiley & Sons: New York, 1996

[63] M. F. Ashby, L. M. Brown, *Philos Mag* **1963**, *8*, 1083-1103.

[64] M. F. Ashby, L. M. Brown, *Philos Mag* **1963**, *8*, 1649-1676.

[65] C. Zener, *Tran. Amer. Inst. Min. Metall. Engrs.* **175**, 15.

[66] T. Gladman, *Proc R Soc Lon Ser-A* **1966**, *294*, 298-309.

[67] F. M. Mulder, S. Singh, S. Bolhuis, S. W. H. Eijt, *J. Phys. Chem. C* **2012**, *116*, 2001-2012.

[68] B. S. Amirkhiz, B. Zahiri, P. Kalisvaart, D. Mitlin, *Int. J. Hydrogen Energ.* **2011**, *36*, 6711-6722.

[69] M. Danaie, S. X. Tao, P. Kalisvaart, D. Mitlin, *Acta Mater.* **2010**, *58*, 3162-3172.

[70] M. Vittori Antisari, A. Aurora, D. Mirabile Gattia, A. Montone, *Scripta Materialia* **2009**, *61*, 1064-1067.

[71] C. Nishimura, M. Komaki, M. Amano, *J. Alloy. Compd.* **1999**, *293*, 329-333.

[72] H. G. Schimmel, G. J. Kearley, J. Huot, F. M. Mulder, *J. Alloy. Compd.* **2005**, *404*, 235-237.

[73] R. L. Corey, T. M. Ivancic, D. T. Shane, E. A. Carl, R. C. Bowman, J. M. B. von Colbe, M. Dornheim, R. Bormann, J. Huot, R. Zidan, A. C. Stowe, M. S. Conradi, *J. Phys. Chem. C* **2008**, *112*, 19784-19790.

[74] S. Q. Hao, D. S. Sholl, *Appl. Phys. Lett.* **2008**, *93*, 251901.

[75] J. Cermak, L. Kral, *Acta Mater.* **2008**, *56*, 2677-2686.

Chapter 4

The influence of Cu substitution on the hydrogen sorption properties of Magnesium rich Mg-Ni films[*]

4.1 Introduction

Magnesium is one of the most promising candidates for solid state hydrogen storage due to its high storage capacity and low cost. It reacts with hydrogen to form MgH_2, according to reaction:

$$\mathrm{Mg} + \mathrm{H_2} \leftrightarrow \mathrm{MgH_2} \qquad \text{Eq. 4.1}$$

with a calculated hydrogen capacity of 7.6 wt.%. However, the thermodynamic and kinetic limitations are major obstacles preventing the use of MgH_2 in mobile applications. Recent results showed that, by alloying Mg with secondary catalyst phases such as Fe-Ti, Fe-V, Al-Ti, the kinetic barriers of MgH_2 can be overcome [1-3]. These ternary systems display very fast sorption kinetics and excellent cycling stability at 200 °C. However, since the active hydrogen storage medium in these systems is pure MgH_2, the thermodynamic barrier still exists. Therefore it is necessary to destabilize MgH_2 or use less stable hydrides.

---

[*] Materials in this chapter has been published in:

- XueHai Tan, Mohsen Danaie, Peter Kalisvaart, David Mitlin, International Journal of Hydrogen Energy 2011, 36, 2154-2164.

Alloying Mg with Ni, Cu or both of them may be an effective way to achieve this goal. It is reported that the destabilization effect on MgH_2 increases in the order: Ti, Nb, Al, Fe, Ni and Cu according to first-principles simulation assuming that all the alloying elements were in solid solution in the MgH_2 phase [4]. It is also known that Mg reacts with Ni to form Mg_2Ni, which can react with hydrogen to form Mg_2NiH_4, according to reaction:

$$\mathrm{Mg_2Ni + 2H_2 \leftrightarrow Mg_2NiH_4} \qquad \mathrm{Eq. 4.2}$$

with a calculated hydrogen capacity 3.6 wt.% [5]. Two forms of Mg_2NiH_4 exist. Mg_2NiH_4 transforms from a high temperature (HT) cubic structure to a low temperature (LT) monoclinic structure at about 235°C, but LT-Mg_2NiH_4 is more stable than HT-Mg_2NiH_4, shown in both theoretical simulations and experimental results [6-8]. The hydride formation enthalpy for the two Mg_2NiH_4 phases is experimentally determined only for the HT form, which sits in a range from -64.3 to -69.3 kJ mol^{-1} H_2 [5, 9-10]. There is lack of experimentally determined thermodynamic results for LT-Mg_2NiH_4 and deep disagreements still remain for this value, ranging from -68.6 to -81.0 kJ mol^{-1} H_2 [8, 11]. Mg will also react with Cu to form Mg_2Cu, and it has been reported that Mg_2Cu will disproportionate under H_2 to form MgH_2 and $MgCu_2$ according to reaction:

$$\mathrm{2Mg_2Cu + 3H_2 \leftrightarrow 3MgH_2 + MgCu_2} \qquad \mathrm{Eq. 4.3}$$

with a calculated hydrogen capacity of 2.62 wt.% [12]. The hydride formation enthalpy for the above reaction has been experimentally determined before as -70 or -71.9 kJ mol^{-1} H_2 [12,13].

If the amount of Mg in the alloy is in excess of the composition needed for the formation of Mg_2Ni or Mg_2Cu, Mg and Mg_2Ni or Mg_2Cu intermetallics will coexist. Possible synergetic effects on hydrogen sorption have been actively discussed. Reilly et al. first pointed out that the presence of Mg_2Ni or Mg_2Cu has catalytic effect on $Mg + H_2 \leftrightarrow MgH_2$ reaction [5,12]. Zaluska et al. presented the hypothesis about synergetic effects in hydrogen desorption of MgH_2/Mg_2NiH_4 systems: Mg_2NiH_4 undergoes significant contraction (~32%) upon hydrogen desorption, and this contraction applies strain to the attached MgH_2 neighbor, which locally triggers the desorption from MgH_2 [14]. In short, Mg-rich ternary Mg-Ni-Cu alloys have high potential for solid state hydrogen storage systems and have attracted many research interests.

Despite having been subject to extensive research, the precise mechanisms by which Cu-substitution affects the hydrogen desorption properties in ternary Mg-Ni-Cu systems are still unclear. Hao Gu et al. [15] studied the effect of Cu-doping on the hydrogen storage properties of Mg-rich $Mg_{95}Ni_5Cu_x$ (x = 0, 0.5, 1, 2) prepared by hydriding combustion synthesis and mechanical milling, concluding that Cu has an obvious catalytic effect on the dehydriding properties, decreasing the dehydriding temperature onset from 450K for $Mg_{95}Ni_5$ to 420K for $Mg_{95}Ni_5Cu_2$. Milanese et al. [16,17] systematically studied a large range of Mg-Ni-Cu compositions prepared by reactive mechanical grinding, focusing on the compositions with excess Mg. However, they pointed out that Ni is more effective than Cu in catalyzing the desorption reactions, because for mixtures with identical Mg content, the desorption rate is better for higher Ni content. Most of the kinetic and thermodynamic results for Mg-rich ternary Mg-Ni-Cu systems from literature were obtained at temperatures higher than 250 °C. Moreover, not much attention has been paid to the cycling hydrogen sorption behavior of ternary Mg-Ni-Cu systems at elevated temperatures.

The present study investigates the hydrogen storage properties of sputter-deposited Mg-rich ternary Mg-Ni-Cu films. As an ultrafast cooling-rate technique, sputtering enables the synthesis of metastable alloys and solid solution with well-controlled surface area and reproducible defect density and grain size by using similar deposition parameters. The sorption kinetics, cycling stability and thermodynamic properties of the ternary alloys are investigated and compared with binary Mg-Ni and Mg-Cu alloys which are included as baseline cases. In such way, the individual role of alloying elements Cu or Ni in the ternary systems can be clarified. The present phases and microstructures of the alloys are characterized by XRD and TEM, and their relation with the observed sorption behaviors will be discussed. A Van't Hoff plot for LT-Mg_2NiH_4 will be constructed by using PCT-desorption in the temperature range below 235 °C. Whether Cu has an effect on the thermodynamic stability of Mg hydride or Mg_2NiH_4 will be investigated by comparison of isotherms.

4.2 Experimental

The samples consist of 1.5 μm Mg-based alloy layer coated with 7.5 nm Pd/7.5 nm Ta bilayer catalysts on top and bottom of the stack. Deposition was performed using a DC-magnetron co-sputtering system (AJA International). Ar gas with a purity of 99.999% was used at a sputtering pressure of 5×10^{-3} mbar, and the maximum base pressure was 5×10^{-8} mbar. The detailed deposition methods and conditions are very similar to those described by Kalisvaart et al [1]. The use of Pd/Ta bilayer as surface catalyst and oxidation prevention and the process to produce free-standing film were described in detail in a previous paper [18]. The deposition rates were the following: Mg 2.3-3.3 Å s^{-1}, Pd 1.6 Å s^{-1}, Ta 0.3 Å s^{-1}; Ni and Cu rates varied with Mg rate to adjust for different stoichiometry.

Volumetric absorption and desorption measurements and the PCT-desorption were performed on a Sieverts type hydrogen sorption analysis system (Hy-Energy LLC. PCTPro 2000). Cycling kinetics measurements were performed at 200 °C. The absorption reservoir was 11.8 ml, and the desorption reservoir was 1178 ml volume. The pressure in the absorption reservoir was set to 3 bar; for desorption, the reservoir was initially put under primary vacuum. The absorption and desorption steps were terminated when an average rate lower than 0.0001 wt.% min^{-1} was measured over a period of 6 minutes.

X-ray diffraction experiments were performed on a Bruker AXS diffractometer (Bruker Discover 8) using a Cu-Kα radiation source ($\lambda = 1.5406$ Å). The details of XRD instrumentation are similar to those described in previous chapters. Grain size and lattice strain analyses were performed. Integral breadth analysis (IBA) was used to deconvolute the broadening effects of grain size and lattice strain by using the following relation [19]:

$$\frac{(\delta 2\theta)^2}{(tan\theta_0)^2} = \frac{k\lambda}{D}\left(\frac{\delta 2\theta}{tan\theta_0 sin\theta_0}\right) + 16e^2 \qquad \text{Eq. 4.4}$$

and plotting $(\delta 2\theta)^2/(\tan\theta_0)^2$ versus $(\delta 2\theta/\tan\theta_0\sin\theta_0)$, where $\delta 2\theta$ is integral breadth of the peaks, and θ_0 is the peak maximum position. The grain size (*D*) and microstrain (*e*) can be obtained from the fitted linear line slope and ordinate intercept respectively. For each analysis, 5 best resolved peaks were used to generate the linear graph. Peak fitting was performed on EVA™ commercial software, and deconvolution of overlapping peaks was performed on Origin 8, if it was necessary. The instrumental broadening was determined by using standard LaB_6 material and subtracted from the measured line broadening.

4.3 Results

4.3.1 Thermodynamic properties of Mg-15at.%Ni

PCTs-desorption were measured for Mg-15at.%Ni, in order to characterize the thermodynamic properties of Mg-rich binary Mg-Ni alloys. The testing temperatures were kept below 230 °C so that the LT-Mg_2NiH_4 to HT-Mg_2NiH_4 transition would not occur. The PCTs-desorption results for Mg-15at.%Ni at three different temperatures i.e. 175, 200 and 225 °C with the corresponding Van't Hoff plots for the enthalpy and entropy of hydride formation are shown in Figure 4.1. For Mg-15at.%Ni, without considering the bilayer Pd/Ta catalyst, the theoretical H capacities in the form of MgH_2 or Mg_2NiH_4 are 3.5 wt.% and 1.9 wt.% respectively. The observed lower plateau with about 3 wt.% H capacity is apparently due to MgH_2, with calculated enthalpy of hydride formation to be -79.6 kJ mol^{-1} H_2, in good agreement with previously found values of ΔH for α-MgH_2, range from -72 to -79 kJ mol^{-1} H_2, so Ni addition does not have a tangible effect on the stability of MgH_2 from the free-Mg phase. Here, free-Mg denotes the Mg that is not alloyed in the form of Mg_2Ni and Mg_2Cu. The higher plateau is thus due to LT-Mg_2NiH_4, with calculated enthalpy and entropy of hydride formation to be -78.6 kJ mol^{-1} H_2 and -147.83 J K^{-1} mol^{-1} H_2, respectively. To author's best knowledge, this is the first time that the thermodynamic properties of Mg_2NiH_4 restricted in the low temperature form are experimentally determined. Also, the relative hydride stabilities of MgH_2 from free-Mg phase and LT- Mg_2NiH_4 are determined.

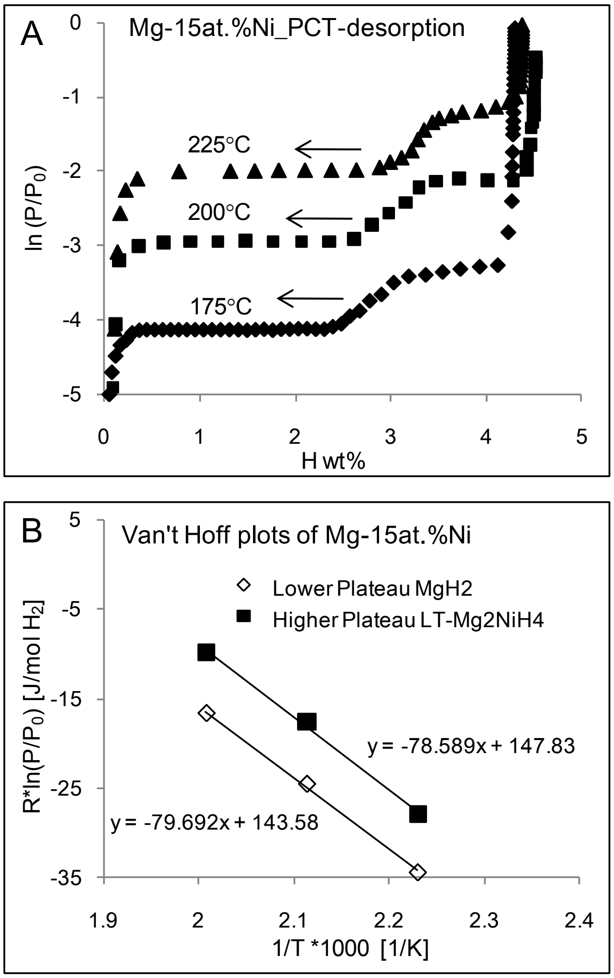

Figure 4.1: (A) Pressure-composition isotherm (PCT) of desorption of post-cycling 1.5 μm Mg-15at.%Ni film capped with Pd/Ta bilayer catalyst at 175 °C, 200 °C and 225 °C. (B) The corresponding Van't Hoff plots for enthalpy and entropy of hydride formation of Mg-15at.%Ni.

4.3.2 Kinetic properties, cycleability and microstructures

Figure 4.2A-F show the cycling absorption and desorption behaviors of 1.5 μm Mg-15at.%Ni, Mg-15at.%Cu and Mg-10at.%Ni-5Cu films capped with Pd/Ta bilayer catalyst at 200 °C, with the former two as the binary baselines. The hydriding process was carried out with initial hydrogen pressure of 2 bar, and the dehydriding process was carried out with initial hydrogen pressure of 5 mbar. Mg-15at.%Ni and Mg-10at.%Ni-5Cu have been tested for 9 hydrogen absorption and desorption cycles at 200 °C for more than 50 hours.

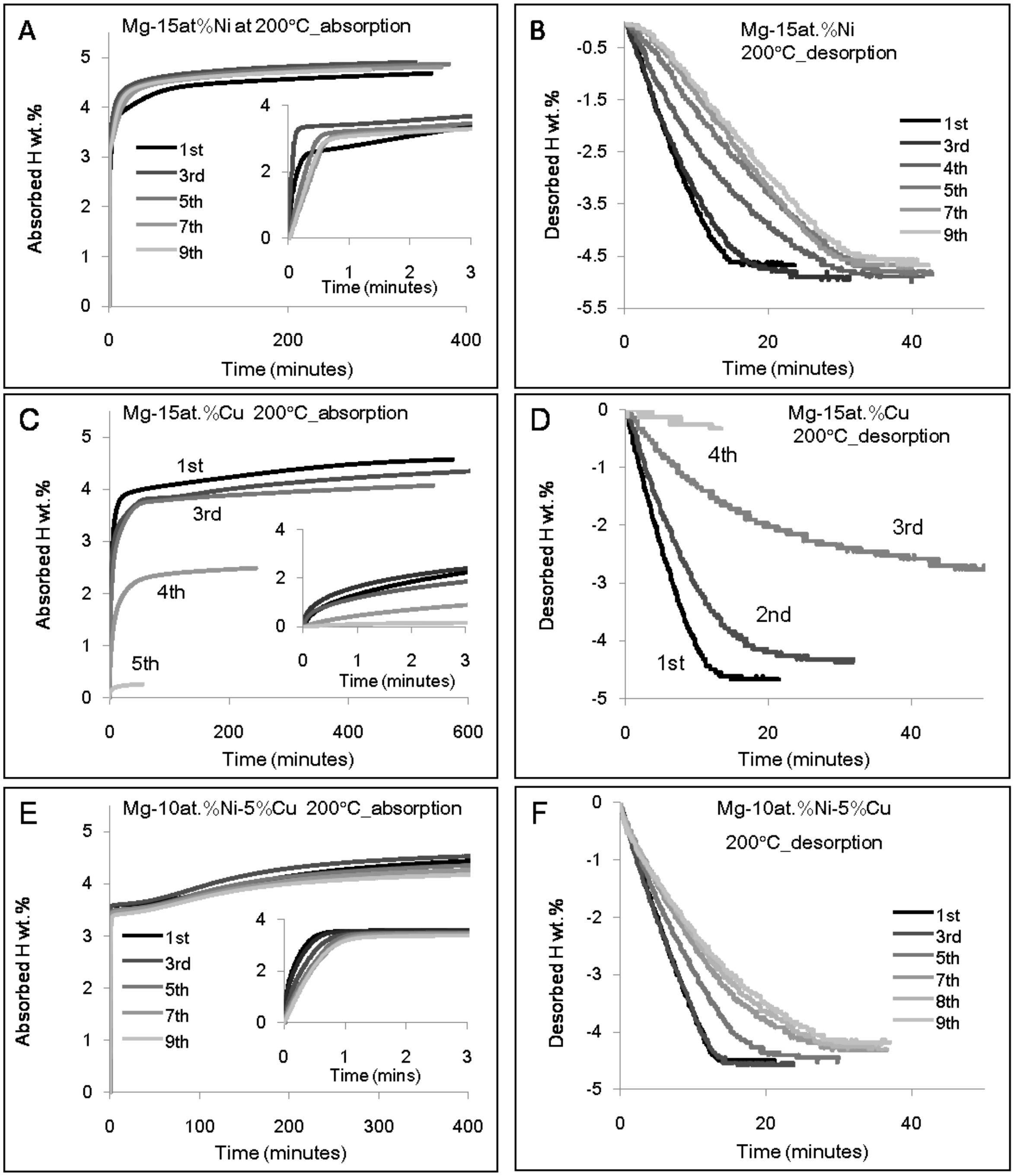

Figure 4.2: Hydrogen cycling absorption and desorption behaviors of (A-B) 1.5 µm Mg-15at.%Ni, (C-D) Mg-15at.%Cu, and (E-F) Mg-10at.%Ni-5Cu films capped with Ta/Pd bilayer catalyst at 200 °C.

Over the 9 cycles, similar hydrogen cycling behaviors were observed: the active hydrogen capacities are initially more than 4 wt.% and degrade slightly during cycling. While the absorption kinetics were quite stable, the desorption kinetics at the ninth cycle became two folds slower compared to the first cycle,.

On the other hand, the sorption behavior of Mg-15at.%Cu deteriorated very quickly. In the first cycle the initial 3.8 wt.% of hydrogen is absorbed relatively quickly compared to the final ~0.7 wt.%. In the second cycle the amount of hydrogen absorbed in this second stage is already significantly decreased, and in the third cycle it is almost zero. There is a big decrease in the desorption rate: only about 2.7 wt.% hydrogen could be desorbed in the third cycle, with the active hydrogen capacity being completely lost after the fourth cycle.

As can be seen, two absorption stages are clearly differentiated for Mg-15at.%Ni and Mg-10at.%Ni-5Cu. The first stage can absorb 3 wt.% of hydrogen in less than 1 minute as shown in the inserts of Figures 4.2A and E, but the second stage takes several hours to absorb only 1-2 wt.% of hydrogen. For Mg-15at.%Cu, two absorption stages can still be differentiated before its severe cycling degradation, but as shown in the inserts of Figure 4.2C, the first absorption stage is slow comparing with the other two cases, and its second stage takes as long as 10 hours to absorb an additional fraction of hydrogen. The results strongly suggest that the superior first absorption stage in Mg-rich Mg-Ni-Cu ternary system is due to the Ni related phases rather than the Cu related phases.

In order to elucidate the possible factors contributing to the different sorption behaviors discussed above, XRD characterizations have been performed. In the as-deposited state (see Figure 4.3A), Mg-15at.%Ni film has amorphous or nanocrystalline structure, but Mg-15at.%Cu film has a strong Mg [0001] texture with Mg (0002) peak being clearly observed. Mg-10at.%Ni-5Cu film exhibits an intermediate structure, in which a small Mg (0002) peak is observed. The Mg (0002) reflection is shifted to $2\theta = 34.5°$, a slightly higher angle compared to the value of 34.4° for pure Mg. In equilibrium, both Ni and Cu have no appreciable solubility in Mg at room temperature, which means the as-deposited films are metastable supersaturated solid solutions of Ni, Cu or both in Mg. Since both Ni and Cu have smaller molar volume than Mg, Mg (0002) reflection shifts to higher angles. Since the shift is very minor, the amount of Ni or Cu dissolved in Mg is probably low. The hump near 2θ = 40° is attributed to the Pd/Ta bilayer catalyst.

The distinct microstructures of the as-deposited films, however, do not represent the films' structures at the moment that the cycling hydrogen sorption begins. In the Sieverts apparatus, the sample is heated to 200 °C under helium before being exposed to hydrogen. The XRD patterns of the three films after one hour equivalent heat treatment at temperature ramping to 200 °C under helium are shown in Figure 4.3B. The as-deposited metastable alloys decompose to Mg and a variety of intermetallic phases. All three films have similar microstructure with strong Mg [0001] texture and their Mg (0002) peaks are shifted back to 2θ = 34.4°. For Mg-15at.%Ni, Mg_2Ni reflections are now clearly visible after annealing, and the same is true for Mg-15at.%Cu where Mg_2Cu reflections are now visible. At 2θ = 38.0°, a sharp reflection appears after annealing. The peak position is very close to the (822) reflection of Mg_6Pd ($F\bar{4}3m$ (NO. 216)) formed by Mg/Pd interdiffusion [18], pseudo-binary $Mg_6(Ni,Pd)$ as described by Cuevas et al. [20] and a metastable Mg_6Ni phase that was found by Kempen et al. during recrystallization of melt-spun Mg-Ni ribbon with composition very close to that of our Mg-Ni film [21]. Since the products of further crystallization of the ribbon, Mg and Mg_2Ni [21] are also observed here, it is most likely the metastable Mg_6Ni phase that is present in our annealed sample. For the ternary alloy, Mg_2Ni reflections appear, the same as for Mg-15at.%Ni, but contrary to Mg-15at.%Cu, no crystalline Mg_2Cu is observed. The hump near 20~25° is attributed to the background signals from the carbon tape that was used to mount the sample in the XRD diffractometer.

The post-cycling X-ray powder diffraction patterns of Mg-15at.%Ni in its ninth absorbed state and Mg-15at.%Cu after the fifth absorption are shown in Figure 4.4. Tetragonal MgH_2 ($P4_2/mnm$ (No. 136)) and monoclinic LT-Mg_2NiH_4 (C2/c (No. 15)) with some trace of un-sorbed hexagonal Mg_2Ni ($P6_222$ (No.180)) are found in Mg-15at.%Ni in absorbed state. The fact that no Mg_6Pd is detected in cycled Mg-15at.%Ni lends further support to the assumption that metastable Mg_6Ni was present in the annealed sample (see Figure 4.3).

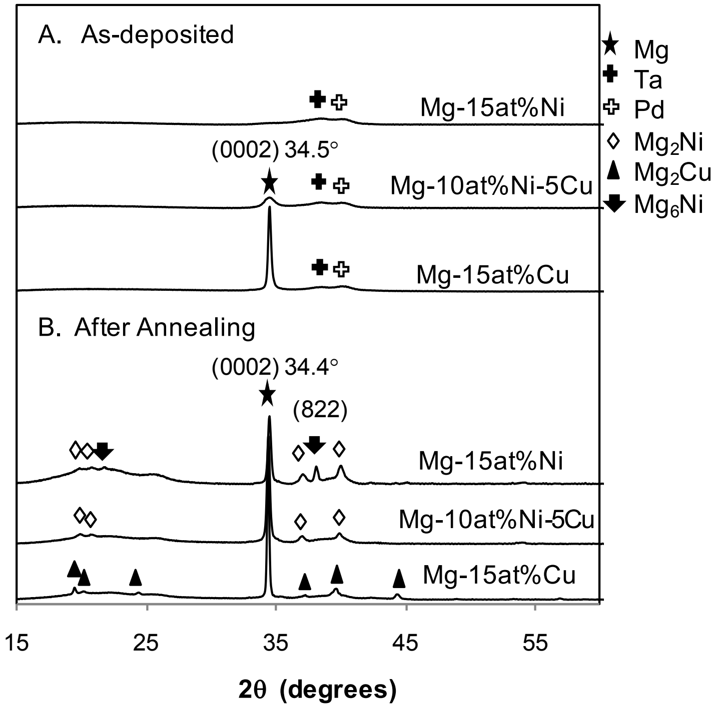

Figure 4.3: XRD characterizations of (A) the as-deposited; (B) the post-annealing (200 °C, 1 hour in helium) state of Mg-15at.%Ni, Mg-10at.%Ni-5Cu and Mg-15at.%Cu films.

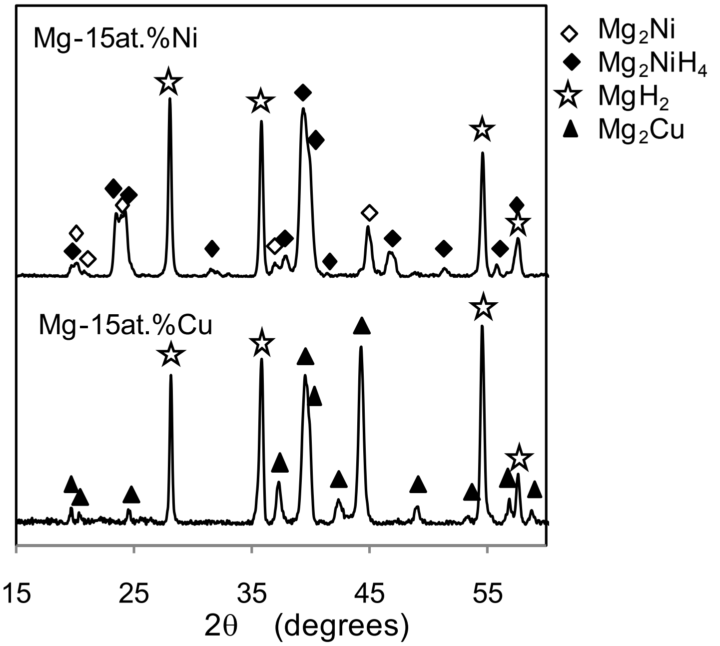

Figure 4.4: X-ray powder diffractions of (A) Mg-15at.%Ni in its ninth absorbed state, and (B) Mg-15at.%Cu in its completely deteriorated state after the fifth absorption.

For Mg-15at.%Cu film in its completely deteriorated state, no metallic Mg is found. Instead, MgH_2 is unambiguously observed. Therefore, the deterioration of hydrogen cycling performances in Mg-15at.%Cu is due to the inability of hydrogen to desorb from MgH_2 upon cycling. This conclusion agrees with the cycling sorption behaviors shown above, such that the active absorption capacity is determined by the amount of hydrogen desorbed out in the previous dehydrogenation step.

IBA analysis has been conducted on the MgH_2 peaks for both Mg-15at.%Ni and Mg-15at.%Cu, in order to clarify the possible microstructure factors. The following five MgH_2 peaks were used for the analyses: (110) (101) (211) (310) and (112). The average grain size of MgH_2 in Mg-15at.%Ni is 27.7 ± 0.4 nm in its absorbed state after the ninth cycle; the average grain size of MgH_2 in Mg-15at.%Cu is 37.9 ± 1.1 nm in its post-cycled state. The larger grain size means longer diffusion distance of hydrogen to the MgH_2 grain boundaries and smaller number of high diffusivity paths for hydrogen to diffuse in and out of the microstructures. However, since the average grain size of Mg-15at.%Cu after the first absorption is 32.6 ± 1.8 nm, the grain size discrepancy here is rather small and hardly significant, which may not be large enough to explain the completely different cycling behaviors observed between Mg-15at.%Ni and Mg-15at.%Cu and the severe deterioration of the sorption kinetics for Mg-15at.%Cu.

TEM analysis was performed on post-cycled Mg-15at.%Cu for direct site-specific microstructure characterizations. Figure 4.5A-B show the bright field and its corresponding High-Angle Annular Dark Field (HAADF) TEM images of one typical sample region. Spherical grains with grain size around 40 nm are observed (indicated by arrows), which is similar to the average grain size of MgH_2 obtained from IBA analysis. These spherical grains show high Z-contrast in the HAADF image, indicating that they are probably MgH_2 with a shell of Cu-rich phase.

Figure 4.6A-B show the bright field and HAADF TEM images of another typical sample region. In the upper part of the image, spherical grains with size about 40nm are visible again, similar to Figure 4.5. For these large, spherical grains, a shell with high Z-contrast is observed. A HAADF TEM image with higher magnification focused on this

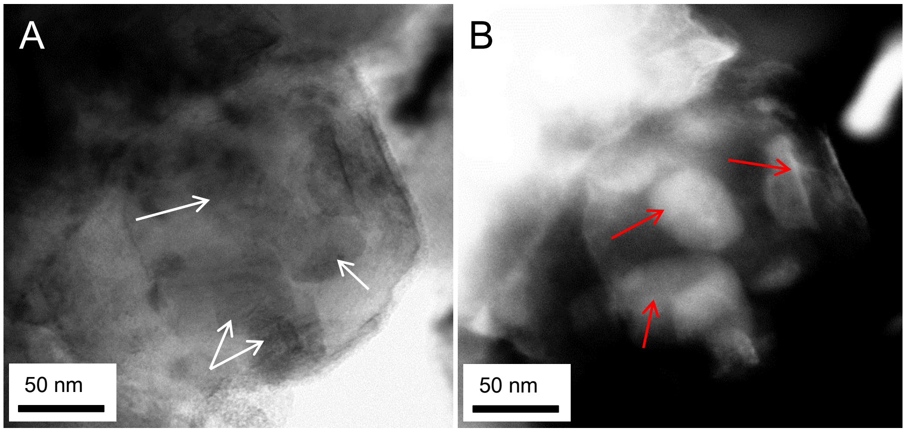

Figure 4.5: (A) Bright field and (B) High-Angle Annular Dark Field (HAADF) TEM images of a typical sample region of post-cycled Mg-15at.%Cu. Regions with spherical grains with grain size about 40nm are indicated by arrows.

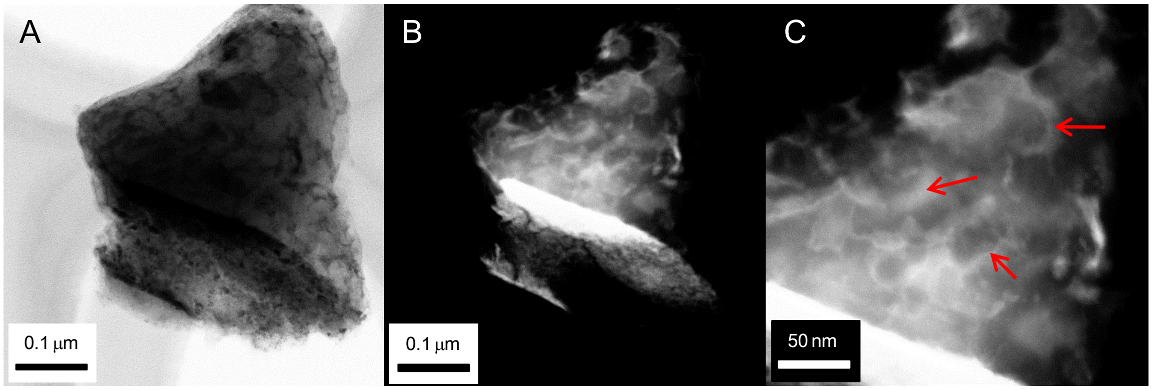

Figure 4.6: Bright field, (B) High-Angle Annular Dark Field (HAADF) and (C) HAADF TEM images with higher magnification of a typical sample region of post-cycled Mg-15at.%Cu. Regions with spherical grains with core-sell structure are indicated by arrows .

core-shell structure (indicated by arrows) is presented in Figure 4.6C. Based on the phases and average grain size found by XRD, the spherical grains observed in the TEM images are most likely MgH_2 grains covered by Mg_2Cu, where Figure 4.5 represents a top-down view of this structure and Figure 4.6A-C a cross-sectional view. Since the size of these large, spherical MgH_2 grains corresponds very well with the average grain size derived from IBA analysis, this is assumed to be the predominant microstructure, and not the much finer-grained structure observed in the bottom part of the image. In the middle of Figure 4.6B, a remnant of the Pd/Ta bilayer catalyst can be seen as a region with very bright Z-contrast.

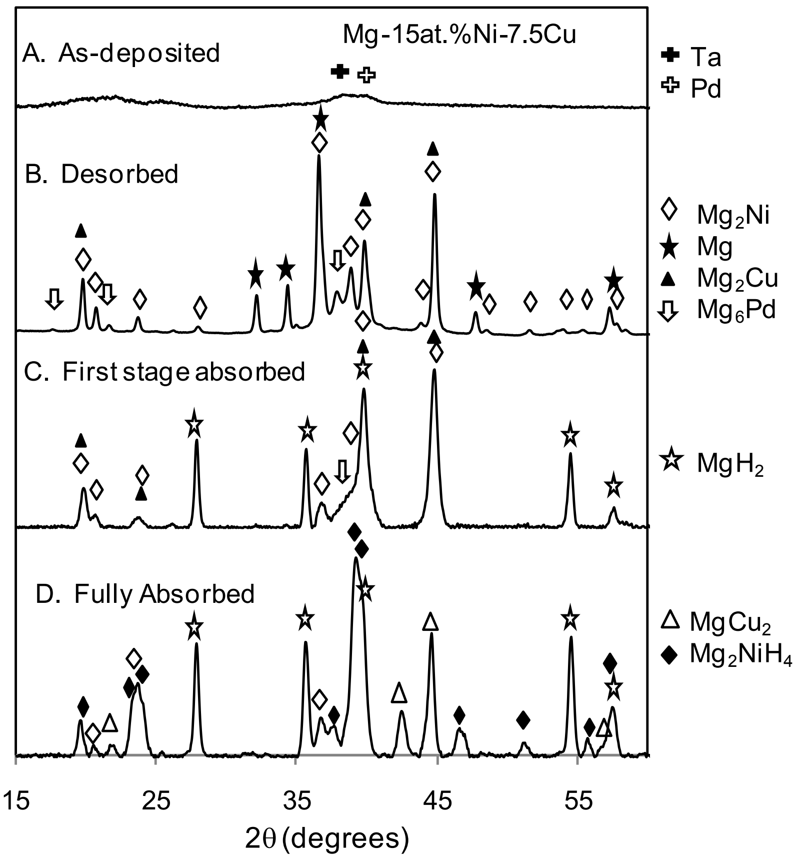

Figure 4.7: XRD characterizations of Mg-15at.%Ni-7.5Cu at (A) as-deposited state; (B) desorbed state; (C) partial absorbed state after the first stage; (D) fully absorbed state. These XRD characterizations emphasizes that the first stage absorption is mainly contributed by the absorption of free-Mg part.

Similar observations of the two-stage absorption in Mg-rich ternary Mg-Ni-Cu systems have been reported by Milanese et al. [17]. They concluded that the first stage corresponds to the absorption of free-Mg and the second stage corresponds to the absorption of intermetallic Mg_2Ni and Mg_2Cu phases. Here, by using direct XRD characterizations at different absorption stages and desorbed stage, the phases at each stage have been identified, so that the hydrogen absorption sequence is confirmed. In order to have clear signals from all phases, XRD characterizations have been performed on Mg-15at.%Ni-7.5Cu. The cycling kinetics of Mg-15at.%Ni-7.5Cu has also been measured, which has very similar two-stage absorption as Mg-10at.%Ni-5Cu, with measured first stage hydrogen capacity of ~2 wt.%. The XRD results, including (A) as-deposited state, (B) desorbed state, (C) absorbed after the first stage, and (D) fully absorbed state, are shown in Figure 4.7. The as-deposited state of this film has amorphous or nanocrystalline structure. During the hydrogen cycling at 200 °C, the as-deposited metastable alloy decomposes. The post-cycling alloy consists of part free Mg and part Mg_2Ni and Mg_2Cu. Reflections from Mg_6Pd-type structure also present, with the (822) reflection at $2\theta = 37.9°$, which corresponds to a calculated lattice parameter of 20.13 Å. It is therefore safe to conclude the formation of Mg_6Pd [20], which agrees with the earlier observation that the Mg/Pd interdiffusion reaction occurs despite the presence of a Ta underlayer [18]. In pattern Figure 4.7C, strong MgH_2 peaks are observed, with very little evidence of LT-Mg_2NiH_4 and $MgCu_2$, but they are all clearly observed in Figure 4.7D. Therefore, it is confirmed now that the superior fast first stage absorption is mainly contributed by the absorption of free-Mg phase according to reaction 4.1, and the slow second stage absorption is due to the absorption of intermetallic Mg_2Ni and Mg_2Cu phases according to reactions 4.2 and 4.3. Since no metallic Ni but intermetallic phase Mg_2Ni is detected in XRD patterns, it is safe to conclude now that the rapid hydrogen absorption of free-Mg phase is mainly attributed to the strong catalytic effect from the intermetallic phase Mg_2Ni. Also with knowledge of the relative hydride stability of free MgH_2 and LT-Mg_2NiH_4 obtained from the PCT isotherms in Figure 4.1, it is actually not surprising to observe this absorption sequence. Mg_2Ni with relatively less stable hydride promotes the rapid uptake of hydrogen in free-Mg phase, which has a more stable hydride.

By taking the advantage of the superior fast first stage absorption and discarding the sluggish second absorption stage, both Mg-10at.%Ni-5Cu and Mg-15at.%Ni films were cycled at 200 °C for more than 100 cycles. Specifically by using a rate limit of 0.005 wt.% min^{-1}, the absorption procedure of Mg-10at.%Ni-5Cu will be cut off after the completion of first stage absorption, because the initial kinetics of its second stage absorption is slower than this rate. For Mg-15at.%Ni, the absorption time was adjusted, so that the absorption procedure will be cut off right after the completion of first absorption stage. In both ways, cycling hydrogen sorption was specifically performed on the free-Mg part with theoretical hydrogen capacity of ~3.5 wt.%. However, by doing this, only about 65% of their full theoretical hydrogen capacities are utilized.

Figure 4.8 A and B show the measured H sorption capacity and the time to absorb/desorb 90% of the average H capacity (3.1 wt.% H for both cases), respectively, as a function of cycle numbers. Upon absorbing and desorbing for more than 100 cycles, both systems showed minor capacity degradation of less than 0.4 wt.% H. The absorption

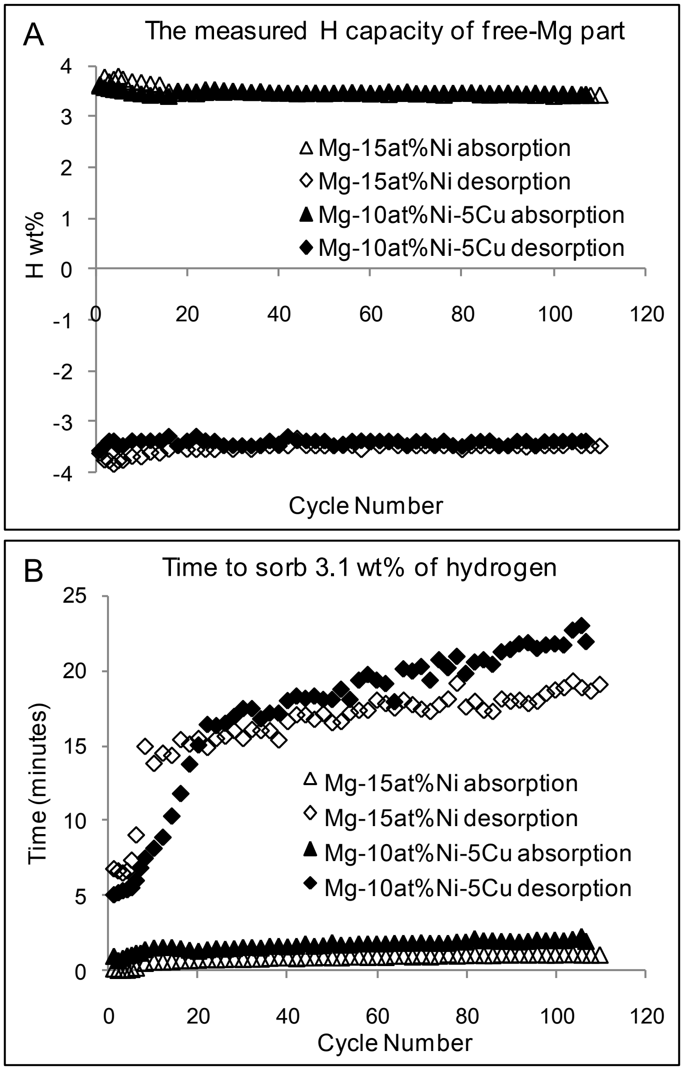

Figure 4.8: Hydrogen cycling performances of 1.5 μm Mg-15at.%Ni film and Mg-10at.%Ni-5Cu film, both capped with Ta/Pd bi-layer catalyst at 200 °C for 100 plus cycles. Specifically, only the first stage capacity (the free-Mg part) is cycled, by cutting off the absorption procedure at the end of the first absorption stage. (A) The measured hydrogen sorption capacity vs. cycle number. (B) The time to absorb and desorb 90% of the average measured capacity (3.1 H wt.%) vs. cycle number.

kinetics of the first stage remained rapid, taking ~2 minutes for Mg-10at.%Ni-5Cu and about 1 minute for Mg-15at.%Ni to absorb 3.1 wt.% of hydrogen at the 100th cycle. On the other hand, their desorption kinetics showed significant degradation. For the first 5 cycles, the systems only took 5-6 minutes to desorb 3.1 wt.% of hydrogen, but their desorption kinetics quickly degraded after that. It took 16 minutes for Mg-10at.%Ni-5Cu at 22nd cycle, and 15 minutes for Mg-15at.%Ni at 8th cycle. Then, their desorption kinetics degraded slowly and at similar rates, to 22 minutes for Mg-10at.%Ni-5Cu and 19 minutes for Mg-15at.%Ni respectively at the 100th cycle.

Figure 4.9 compares the hydrogen sorption kinetics between Mg-15at.%Ni and Mg-10at.%Ni-5Cu, including the test conditions of both full capacity cycling and free-Mg part cycling. For the former test condition, the kinetic data at ninth cycle is used. For the latter, the kinetic data at 110th cycle for Mg-15at.%Ni and at 100th cycle for Mg-10at.%Ni-5Cu are used. In this way, the overall cycling time is about the same for all 4 cases (~78 hours). As shown in Figure 4.9A, the second absorption stage of ternary Mg-10at.%Ni-5Cu behaves quite differently comparing to binary Mg-15at.%Ni. At the beginning of the second absorption stage, there is a kinetic bottle-neck for the ternary sample, similar to what was observed for binary Mg-15at.%Cu. This result suggests that the addition of Cu or the formation of Mg_2Cu has a strong negative effect on the second stage absorption kinetics for ternary Mg-Ni-Cu systems. This agrees with the general understanding that if the absorption or desorption step involves the formation or decomposition of intermetallic phases, the kinetics is much slower [1]. During the absorption, MgH_2 and $MgCu_2$ must nucleate from the intermetallic phase Mg_2Cu, which involves long-range atom diffusion.

Figure 4.9B compares the desorption kinetics of Mg-15at.%Ni and Mg-15at.%Ni-5Cu. Cu substitution does not show positive influence on the desorption of free-Mg hydride only. However, if the alloy's full hydrogen capacity is cycled, such that the (de)hydrogenation of the intermetallic Mg_2Ni and Mg_2Cu phases are involved, the Cu substitution apparently improves the desorption kinetics, particularly for the initial part of desorption.

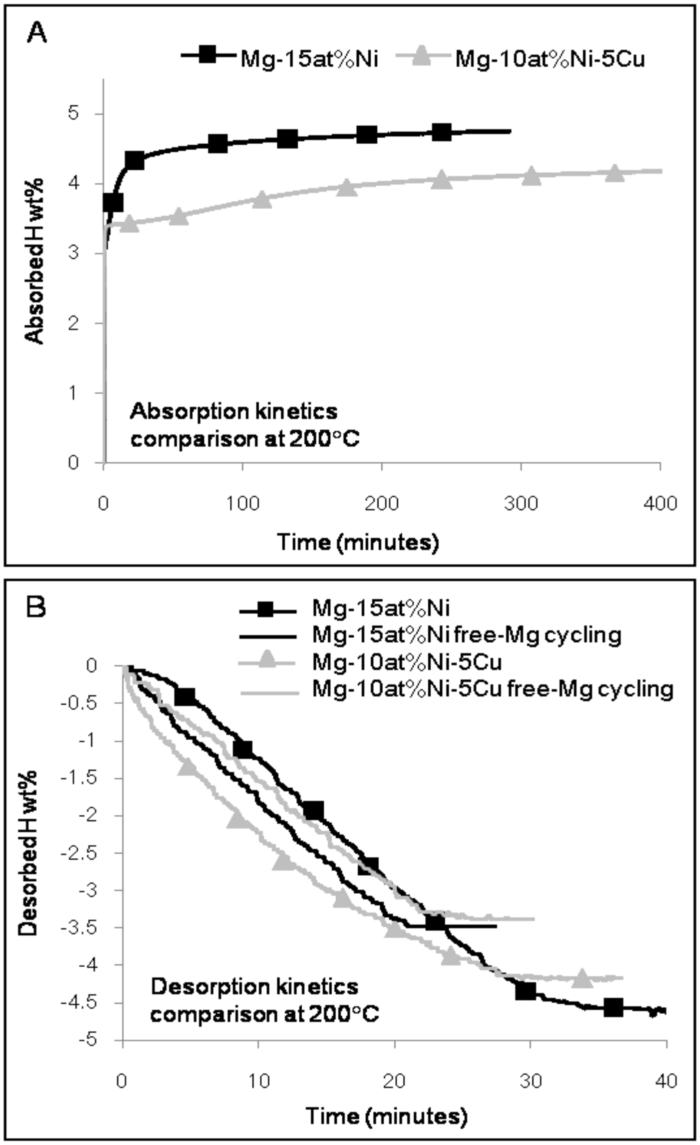

Figure 4.9: The kinetics comparisons of (A) absorption and (B) desorption between Mg-15at.%Ni and Mg-10at.%Ni-5Cu at 200 °C. Both full capacity hydrogen cycling and free-Mg part only hydrogen cycling are included.

4.3.3 Thermodynamic effects of Cu-substitution

To clarify the mechanisms through which Cu-substitution affects the desorption kinetics, we compare the post-cycling PCTs-desorption of Mg-15at.%Ni, Mg-10at.%Ni-5Cu and Mg-15at.%Ni-7.5Cu at 225 °C, shown in Figure 4.10. Three plateaus can be identified in the ternary systems. The lowest plateau obviously corresponds to free-MgH_2. As can be seen, the good coincidence of the free-MgH_2 plateaus for all three alloys confirm that the PCT measurements are consistent. It is then feasible to compare and discuss the relative heights of the higher plateaus. Based on the PCT desorption of binary Mg-15at.%Ni, the middle plateau in the ternary alloys should correspond to the desorption of LT-Mg_2NiH_4. From this indirect way, the highest plateau in the ternary system should thus correspond to the desorption of MgH_2-$MgCu_2$ pair. Therefore, one can safely conclude now that the three plateaus, which can be clearly identified in ternary Mg-15at.%Ni-7.5Cu, correspond to the dehydrogenations according to reactions 4.1, 4.2 and 4.3, with the equilibrium pressures increasing in the same order. Given the lower level of Ni and Cu in Mg-10at.%Ni-5Cu, it is more difficult to discern the upper two plateaus. Though each plateau's middle point matches quite well with the middle point of corresponding plateau in Mg-15at.%Ni-7.5Cu, as indicated by the dash lines AB and CD. Finally, it is important to note that, by adding Cu into the systems the lowest plateau of free-MgH_2 is unaffected. However, the LT-Mg_2NiH_4 plateau in the ternary alloys is ~80 mbar higher than that in the binary alloy, denoted by ΔP.

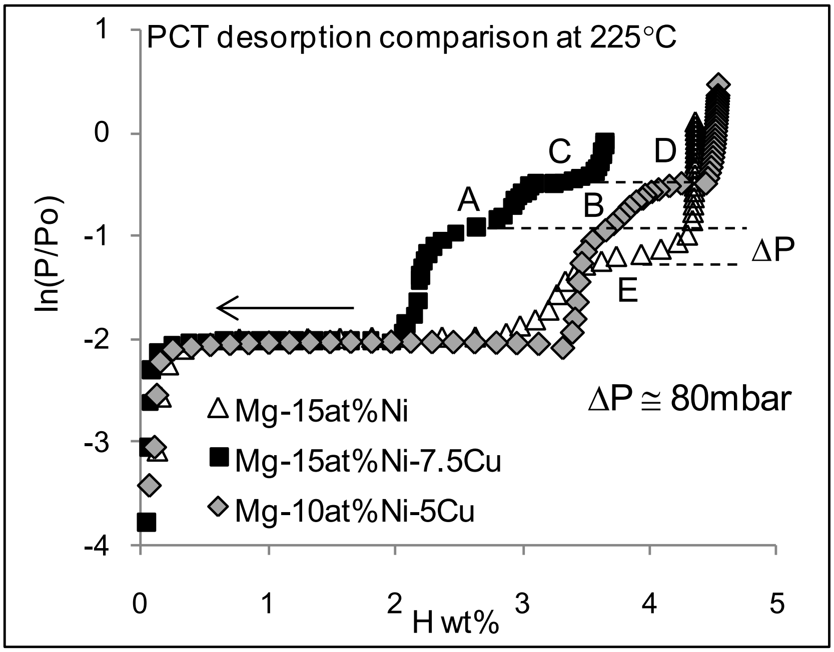

Figure 4.10: The comparison between the post-cycling PCTs-desorption of Mg-15at.%Ni, Mg-15at.%Ni-7.5Cu and Mg-10at.%Ni-5Cu.

4.4 Discussion

As shown in the comparisons of PCTs-desorption of different alloys, the Cu-substitution only increases the plateau pressure of LT-Mg_2NiH_4, with the plateau pressure of free-Mg hydride unaffected. Similar results about increasing plateau pressure in Mg_2Ni-Cu type alloys have been reported before by Zaluski et al. and Woo et al. [22,23]. The change of plateau pressure in PCT measurements may be attributed to both thermodynamic and kinetic factors. It must be kept in mind that each ΔP step during isotherm is stopped when the sorption rate falls below a threshold. This practical kinetic factor causes an apparent change in the measured equilibrium pressure. As shown in this study, the Cu substitution actually significantly retards the absorption kinetics, so any increasing plateau pressure measured during PCT-absorption may be actually attributed to this sluggish absorption kinetics. However, since the desorption kinetics for ternary Mg-Ni-Cu alloys are similar or almost equally fast, compared to the binary Mg-Ni, the source of error during desorption isotherm from kinetics factors is definitely minimized and the higher equilibrium pressures found for LT- Mg_2NiH_4 are real. Therefore, by using PCT-desorption results, the interplay between the higher LT-Mg_2NiH_4 plateau pressures and the faster desorption kinetics in the ternary Mg-Ni-Cu alloys can be established. Since the initial absorption and desorption pressure were kept the same for all measurements, the higher equilibrium pressures for LT-Mg_2NiH_4 and Mg-Cu hydride in the ternary Mg-Ni-Cu alloys contribute to the larger ΔP for desorption. The faster desorption kinetics observed during the full capacity cycling, especially for the initial part, is attributed to this larger desorption driving force. Since the plateau pressure of free-Mg hydride is unaffected, no positive effects on desorption kinetics is observed during free-Mg part only hydrogen cycling.

For Cu-substitution's different influences on the plateau pressures of free-Mg hydride and Mg_2NiH_4, it is important to consider the stability of the as-synthesized metastable microstructure at elevated temperatures. The simulation results of the alloying destabilization effects are based on the fact that the alloying elements are in solid solution in MgH_2 or Mg_2NiH_4 [4,24]. However, at elevated temperatures, this is not necessarily the case. At equilibrium, Ni or Cu has no appreciable solubility in free-Mg phase. As shown in Figure 4.3, after one hour annealing at 200 °C, Ni and Cu precipitate out from the as-deposited supersaturated solid solution, and react with Mg respectively to form binary intermetallics Mg_2Ni, Mg_2Cu and etc. After heat treatment, the Mg (0002) peaks are shifted back to the same position as pure Mg at $2\theta = 34.4°$, indicating that no more alloying elements are in solid solution in Mg. This maybe the reason that plateau pressure of free-MgH_2 is not affected. On the other hand, it is known that the substitutional solubility of Cu in Mg_2Ni phase is up to 25 at.% at 400 °C [25], so at lower temperatures, the solubility may be still significant. As shown in the XRD patterns of thin films after annealing in Figure 4.3, no clear Mg_2Cu reflections are actually observed in ternary Mg-15at.%Ni-5Cu, contrary to the case of annealed binary Mg-15at.%Cu. Significant amount of Cu may still dissolve in the matrix of Mg_2Ni. Since Cu has slightly larger molar volume than Ni, the partial substitution of Ni by Cu in the LT-Mg_2NiH_4 matrix will induce minor lattice expansion, which may account for the higher equilibrium pressure and improve desorption kinetics. Simulation result has shown before that, by alloying with other elements, the cubic HT-Mg_2NiH_4 becomes unstable with increasing unit cell volume, and the destabilization effect is maximized by alloying with Cu [23]. However, similar simulation of the alloying effects on LT-Mg_2NiH_4 is not available. Here, the destabilization effect of Cu-substitution on LT-Mg_2NiH_4 is experimentally observed.

Despite the fact that improved hydrogen desorption behaviors of Mg-rich Mg-Cu alloys have been reported before compared to pure Mg, both for Mg + Mg_2Cu and Mg + $MgCu_2$ mixtures [12,13,26], the behavior at temperatures higher than 300 °C is not representative of the cycling sorption behavior of binary Mg-Cu alloys at 200 °C. It is clear now from Figure 4.9 that the Cu-substitution only enhances the hydrogen desorption kinetics when the material is fully absorbed to $MgCu_2$ + MgH_2 + Mg_2NiH_4 and not when absorption is stopped after reaction of the free Mg is complete. Without the presence of Ni, binary Mg-Cu alloys are not even cycleable at all at 200 °C. IBA analysis has suggested that the grain size discrepancy of MgH_2 between Mg-15%Ni and Mg-15%Cu is not significant enough to justify the poor cycling stability of binary Mg-15at.%Cu. Since all the samples investigated here are in the same form of thin films, another important factor for sorption kinetics, i.e. the surface-to-volume ratio, does not account for it either. As shown in the XRD profile of Mg-15at.%Cu after the fifth absorption, no cubic $MgCu_2$ (Fd3m (No. 227)) but orthorhombic Mg_2Cu (*Fddd* (No. 70)) is detected. This agrees with the observed cycling sorption behaviors shown in Figure 4.2, because upon cycling, the hydrogenation reaction according to reactions 4.3, the second absorption stage in Mg-15at.%Cu is no longer observed. Apparently, due to microstructural evolution of intermetallic $Mg_2Cu/MgCu_2$, the hydrogenation of Mg_2Cu becomes very slow.

Based on the TEM analysis results shown in Figure 4.5 and Figure 4.6, our hypothesis for the progressive deterioration in Mg-15at.%Cu is attributed to grain boundary segregation, i.e. for an enrichment of intermetallic Mg-Cu phases at the grain boundaries of MgH_2. With knowledge of the relative hydride stabilities, see Figure 4.10, MgH_2 in the vicinity near $MgCu_2$ desorbs first according to reaction 4.3. The desorbed metallic Mg will then react with nearby $MgCu_2$ to reform Mg_2Cu. Because MgH_2 and $MgCu_2$ evolve from the same phase (Mg_2Cu) upon hydrogenation, the Mg-Cu intermetallics will always be present at $Mg(H_2)$ grain boundaries. As can be seen from IBA analysis, upon cycling, the grain size of MgH_2 slightly grows, diminishing the grain boundary area. Even though the decrease was small, it appears to be big enough for the Mg_2Cu to form a closed shell around the $Mg(H_2)$ grains This is supported by the core-shell structure observed in TEM images. This coarsening may be the reason why hydrogenation of Mg_2Cu becomes extremely slow. Models for hydriding and dehydriding processes of Mg_2Cu-catalyzed Mg have been proposed before by Karty et al. [26]. In such models, Mg_2Cu serves as a pathway for hydrogen to diffuse into or out from $Mg(H_2)$. However, as they also pointed out, this model may only work for specific condition, such as the sorption temperatures being higher than 300 °C. However, given the relative hydride stabilities derived from Figure 4.10, it is unlikely that hydrogen will diffuse *through* Mg_2Cu phase during desorption, as the chemical potential of hydrogen in Mg_2Cu will be higher than that in Mg or MgH_2. It is therefore more likely that hydrogen diffuses along grain boundaries between $Mg(H_2)$ and Mg_2Cu towards a catalytic site on the surface. Hence, a *closed shell* of Mg_2Cu, as observed in the TEM micrographs, will trap the hydrogen in MgH_2, decreasing the active capacity of Mg-15at.%Cu. This progressive degradation process is depicted schematically in Figure 4.11. Our observations agree quite well with earlier studies such as the one by Pasturel et al. who found that for Mg_2Ni films with Transition Metal/Pd bilayer catalysts, TM layers that form highly unstable hydrides such as Mn, Ni and Cr are poor catalysts for desorption and relatively good catalysts for absorption [27].

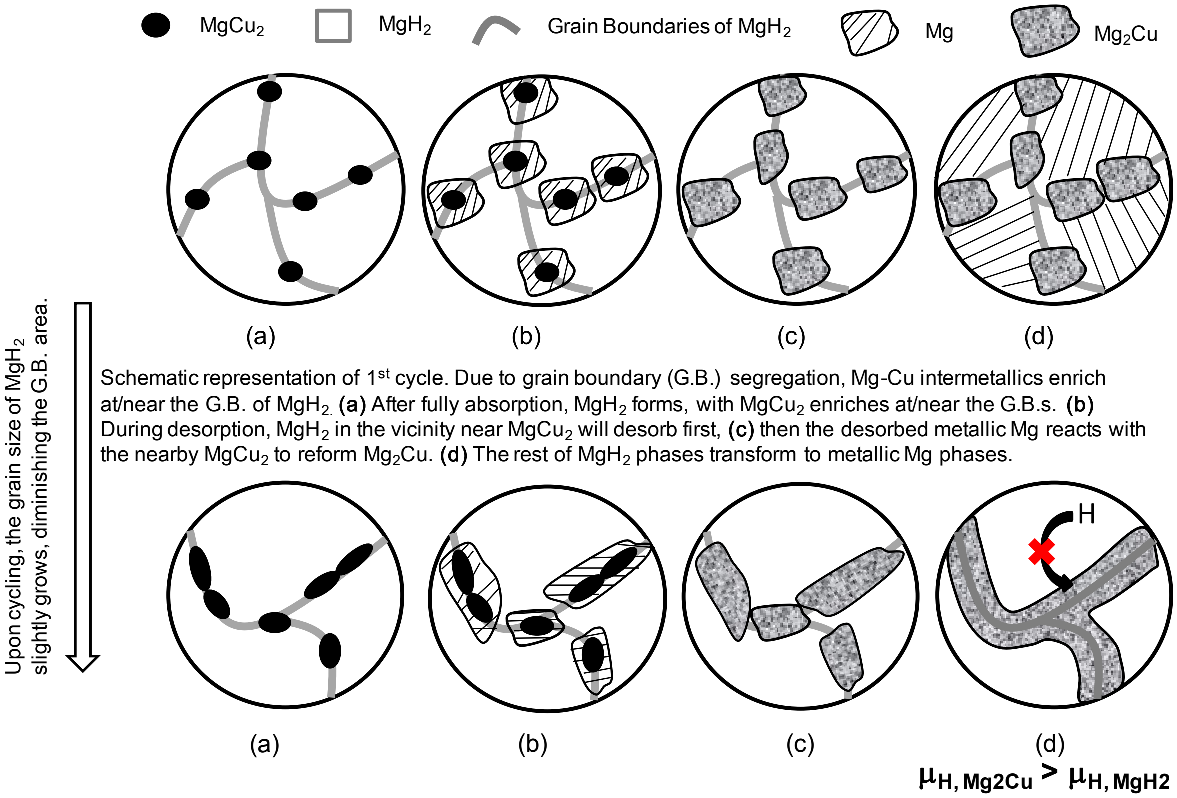

Schematic representation of 1st cycle. Due to grain boundary (G.B.) segregation, Mg-Cu intermetallics enrich at/near the G.B. of MgH_2. **(a)** After fully absorption, MgH_2 forms, with $MgCu_2$ enriches at/near the G.B.s. **(b)** During desorption, MgH_2 in the vicinity near $MgCu_2$ will desorb first, **(c)** then the desorbed metallic Mg reacts with the nearby $MgCu_2$ to reform Mg_2Cu. **(d)** The rest of MgH_2 phases transform to metallic Mg phases.

Schematic representation of the degradation mechanism. **(a)** Due to the diminishing MgH_2 G.B. area, continuous islands of $MgCu_2$ forms at/near the G.B. **(b)&(c)** During desorption, larger blocks of Mg_2Cu phase form at/near the G.B. **(d)** Eventually, a closed shell of Mg_2Cu forms around MgH_2 grain. Because it is unlikely that hydrogen will diffuse through Mg_2Cu phase during desorption, a closed shell of Mg_2Cu thus traps H within MgH_2.

Figure 4.11: The schematic representation of the progressive degradation process of Mg-15at.%Cu upon hydrogen cycling at 200 °C.

Compared to binary Mg-Cu systems, ternary Mg-Ni-Cu systems have much better cycling stability. This is likely due to the fact that the intermetallic catalytic phase Mg_2Ni can serves as high diffusivity path for hydrogen and act as pinning-points at the grain boundaries of MgH_2. This prevents the coarsening and growth of Mg_2Cu shell and may also explain why Mg_2Cu disproportionation does occur in the ternary systems such that $MgCu_2$ phase is found in the fully absorbed state of ternary Mg-Ni-Cu systems (see

Figure 4.7). It is known that for Mg_2NiH_x (x=0~0.3), hydrogen dissolves in the interstitial sites of Mg_2Ni host lattice, forming a solid solution [28]. This strongly suggests that the hydrogen diffusivity in Mg_2Ni is fast for low hydrogen concentration, which is the case for desorption, especially when only the free-Mg is cycled.

In a fully absorbed material, Mg_2NiH_4 will desorb before MgH_2. However, we found no evidence for a 'synergetic effect' of Mg_2NiH_4 on desorption of MgH_2 as suggested by Zaluska et al. [14]. On the contrary, when only free-Mg was cycled, desorption was consistently *faster* compared to complete cycling in binary Mg-15%Ni (see Figure 4.9). A synergetic effect was found only for a combination of $MgCu_2$ and Mg_2NiH_4 since the fastest desorption kinetics were Mg-10%Ni-5%Cu.

4.5 Conclusion

In this study, we investigate the cycling hydrogen sorption behaviors of Mg-rich ternary Mg-Ni-Cu thin films, using binary Mg-Ni and Mg-Cu as the baselines.

1. For Mg-rich ternary Mg-Ni-Cu alloys, two absorption stages are observed. The first stage corresponding to the absorption of free-Mg is very fast, catalyzed by intermetallic Mg_2Ni; the second stage corresponding to the absorption of intermetallic Mg_2Ni and Mg_2Cu is much slower. This absorption sequence is clearly confirmed by XRD characterizations at different sorption stages. The Cu-substitution shows positive effects on desorption kinetics during full capacity hydrogen cycling, but shows strongly negative effects on absorption kinetics, particularly for the second absorption stage. The positive effects on desorption are also clearly observed from PCTs-desorption. The plateau pressure of LT-Mg_2NiH_4 is slightly increased in the ternary Mg-Ni-Cu alloys compared to the binary Mg-Ni alloys, but the plateau pressure of free-MgH_2 is unaffected.
2. The cycling hydrogen sorption behaviors of Mg-15at.%Cu quickly deteriorates upon cycling at 200 °C. Using bright field with HAADF TEM imaging, core-shell structured

spherical MgH_2 grains with Mg_2Cu shell are observed in the cycling-ceased state. The Mg_2Cu shell acts as a barrier for hydrogen desorption from MgH_2 and deteriorates the reversible hydrogen capacity.

3. The as-deposited metastable Mg-rich ternary Mg-Ni-Cu alloys decomposes at elevated temperatures, consisting of free Mg and intermetallic Mg_2Ni and Mg_2Cu. At equilibrium, Ni and Cu have no appreciable solubility in Mg, contributing to the fact that no thermo-destabilization is observed for free-Mg hydrides. On the other hand, significant amount of Cu can still dissolve in Mg_2Ni even at elevated temperatures, so minor thermo-destabilization of Mg_2NiH_4 and better desorption kinetics are observed.

4.6 Reference

[1] W. P. Kalisvaart, C. T. Harrower, J. Haagsma, B. Zahiri, E. J. Luber, C. Ophus, E. Poirier, H. Fritzsche, D. Mitlin, *Int. J. Hydrogen Energ.* **2010**, *35*, 2091-2103.

[2] B. Zahiri, B. S. Amirkhiz, M. Danaie, D. Mitlin, *Appl. Phys. Lett.* **2010**, *96*, 013108.

[3] B. Zahiri, C. T. Harrower, B. S. Amirkhiz, D. Mitlin, *Appl. Phys. Lett.* **2009**, *95*, 013114.

[4] C. X. Shang, M. Bououdina, Y. Song, Z. X. Guo, *Int. J. Hydrogen Energ.* **2004**, *29*, 73-80.

[5] J. J. Reilly, R. H. Wiswall, *Inorg. Chem.* **1968**, *7*, 2254-2256.

[6] W. R. Myers, L. W. Wang, T. J. Richardson, M. D. Rubin, *J. Appl. Phys.* **2002**, *91*, 4879-4885.

[7] H. Y. Shao, K. Asano, H. Enoki, E. Akiba, *J. Alloys Compd.* **2009**, *477*, 301-306.

[8] J. Zhang, D. W. Zhou, L. P. He, P. Peng, J. S. Liu, *J. Phys. Chem. Solid*s **2009**, *70*, 32-39.

[9] G. Liang, S. Boily, J. Huot, A. Van Neste, R. Schulz, *J. Alloys Compd.* **1998**, *267*, 302-306.

[10] K. Tanaka, Y. Kanda, M. Furuhashi, K. Saito, K. Kuroda, H. Saka, *J. Alloys Compd.* **1999**, *295*, 521-525.

[11] S. E. Guthrie, G. J. Thomas, D. Noreus, E. Ronnebro, *Mat. Res. Soc. Symp. Proc. Materials Research Society*, **1998**

[12] J. J. Reilly, R. H. Wiswall, *Inorg. Chem.* **1967**, *6*, 2220-2223.

[13] A. Andreasen, M. B. Sorensen, R. Burkarl, B. Moller, A. M. Molenbroek, A. S. Pedersen, T. Vegge, T. R. Jensen, *Appl. Phys. A-Mater.* **2006**, *82*, 515-521.

[14] A. Zaluska, L. Zaluski, J. O. Strom-Olsen, *J. Alloys Compd.* **1999**, *289*, 197-206.

[15] H. Gu, Y. F. Zhu, L. Q. Li, *Int. J. Hydrogen Energ.* **2009**, *34*, 2654-2660.

[16] C. Milanese, A. Girella, G. Bruni, P. Cofrancesco, V. Berbenni, M. Villa, P. Matteazzi, A. Marini, *Int. J. Hydrogen Energ.* **2008**, *33*, 4593-4606.

[17] C. Milanese, A. Girella, G. Bruni, P. Cofrancesco, V. Berbenni, P. Matteazzi, A. Marini, *Intermetallics* **2010**, *18*, 203-211.

[18] X. H. Tan, C. T. Harrower, B. S. Amirkhiz, D. Mitlin, *Int. J. Hydrogen Energ.* **2009**, *34*, 7741-7748.

[19] H. P. Klug, L. E. Alexander, *X-ray Diffraction Procedures;* John Wiley and Sons, New York, 1974.

[20] A. T. W. Kempen, H. Nitsche, F. Sommer, E. J. Mittemeijer, *Metal Mater. Trans. A* **2002**, *33*, 1041-1050.

[21] F. Cuevas, J. F. Fernandez, J. R. Ares, F. Leardini, C. Sanchez, *J. Phys. Chem. Solids* **2010**, *71*, 1259-1263.

[22] L. Zaluski, A. Zaluska, J. O. Stromolsen, *J. Alloys Compd.* **1995**, *217*, 245-249.

[23] J. H. Woo, K. S. Lee, *J. Electrochem. Soc.* **1999**, *146*, 819-823.

[24] Y. Takahashi, H. Yukawa, M. Morinaga, *J. Alloys Compd.* **1996**, *242*, 98-107.

[25] S. Gorsse, G. J. Shiflet, *Calphad-Computer Coupling of Phase Diagrams and Thermochemistry* **2002**, *26*, 63-83.

[26] A. Karty, J. Grunzweiggenossar, P. S. Rudman, *J. Appl. Phys.* **1979**, *50*, 7200-7209.

[27] M. Pasturel, R. J. Wijngaarden, W. Lohstroh, H. Schreuders, M. Slaman, B. Dam, R. Griessen, *Chem. Mater.* **2007**, 19, 624-633.

[28] D. Noreus, P. E. Werner, *Acta Chem Scand A* **1982**, *36*, 847-851.

Chapter 5

Body Centered Cubic Magnesium Niobium Hydride with Facile Room Temperature Absorption and Four Weight Percent Reversible Capacity [*]

5.1 Introduction

Hydrogen storage in metal hydrides provides the advantage of higher volumetric density over the storage of molecular hydrogen in gaseous and liquid state. Magnesium hydride (MgH_2), which has high gravimetric capacity of 7.6 weight % hydrogen and low cost, is considered a promising material [1]. However, the hydride's high thermodynamic stability (approximately -77 kJ mol^{-1} H_2) necessitates operating temperatures above 300 °C for 1 atmospheric hydrogen desorption pressure. The large heat release upon hydrogenation would also require a substantial cooling load during hydrogen refilling [2]. In addition, due to the low hydrogen diffusivity through the bulk of the hydride [3], elevated temperatures are also normally required to achieve reasonable hydrogen absorption rates. Researchers have demonstrated that the hydrogenation kinetics are significantly accelerated by one or a combination of nanodispersing magnesium with a suitable catalyst, via nanostructuring, or via nanoconfinement [4-11]. Another promising approach is to synthesize nano-scale MgH_2 particles in an air-impermeable but hydrogen permeable polymer matrix [12].

---

[*] Materials in this chapter has been published in:

- XueHai Tan, Liya Wang, Chris M. B. Holt, Beniamin Zahiri, Michael H. Eikerling, David Mitlin, Physical Chemistry Chemical Physics 2012, 14, 10904-10909.

Many efforts are directed toward modifying the thermodynamics of Mg-H system. Researchers have induced thermodynamic destabilization of MgH_2 via a new application of the classic rule of reverse stability [13], or by utilizing nanolayered structures to achieve elastic clamping [14], interfacial intermetallic formation [15], or increased interface energy [16,17]. Theoretical studies also demonstrated the possibilities of weakening the Mg-H bonding through selective alloying [18]. When alloying magnesium with immiscible elements such as Ti and Zr, a fluorite face centered cubic (fcc) structure has been reported [19, 20]. A key observation is that such structure may be reversibly cycled if not fully desorbed. Calculations based on density functional theory (DFT) suggest that the remaining hydrogen, which is more strongly bonded to the transition alloying elements than magnesium, prevents large scale of segregation [21,22]. High temperature ultra high-pressure techniques (600 °C, 4GPa anvil cell) have been used to synthesize fluorite Mg_7NbH_x as well [23]. This ternary hydride was reported to desorb hydrogen at significant rates at 300 °C. In general these metastable fluorite hydrides possess improved kinetics relative to the rutile MgH_2, but only a small thermodynamic destabilization that is on the order of a few kJ mol^{-1}.

In this study we discovered that by physically co-depositing Mg and Nb of a specific stoichiometry (3:1 Mg:Nb), we are able to create a body centered cubic (bcc) alloy with its hydride possessing both kinetic and thermodynamic properties markedly superior to MgH_2. This ternary hydride that is also bcc has never been reported in the literature, though hydrogen sorption kinetics of co-deposited Mg-Nb alloy films have been previously reported [24].

5.2 Experimental

The binary Mg-Nb alloy films, with 150 nm or 1.5 μm thickness, were synthesized by physical vapor deposition (PVD). The alloy film was coated with 7.5 nm Pd/7.5 nm Nb bi-layers on the top and bottom of the stack. The Nb interlayer reduced the rate of intermetallic formation between the Mg and the Pd, allowing the Pd to stay catalytically active during the first few cycles [25]. The Pd coating is also effective to prevent the underlying alloy film from oxidation during the transfer/storage before the hydrogen sorption measurement. Deposition was performed at room temperature using a DC-magnetron co-sputtering system. The details of deposition condition and the process to produce free-standing film are similar to those described in Chapter 2. For co-deposition, the Mg sputtering rate was kept at 0.23 nm s^{-1} (100 W power). The Nb sputtering rate was adjusted to create the desired stoichiometry.

Volumetric absorption and desorption kinetic measurements and the desorption pressure-compositions isotherms (PCT-desorption) were performed on an automated Sieverts type hydrogen sorption analysis system (Hy-Energy LLC. PCTPro 2000). The typical sample amount used for each measurement was about 15 milligrams. Absorption was performed at 1 bar hydrogen and room temperature, while desorption was performed at 175 °C and 5 mbar.

X-ray diffraction experiments were performed on a Bruker AXS diffractometer (Bruker Discover 8) using a Cu-Kα radiation source (λ = 1.5406 Å). The details of XRD instrumentation are similar to those described in previous chapters. Scanning electron microscopy (SEM) analysis was performed using a Hitachi field emission microscope. Imaging and selected area electron diffraction (SAD) analysis was performed on JEOL 2100 transmission electron microscope (TEM) operated at 200 kV. This TEM is also equipped with a Gatan imaging filter. The TEM samples were prepared by directly depositing Mg-Nb alloy films onto ultrathin carbon film supported by a lacey carbon film on a copper grid

The ground state energy calculations were performed for a 2x2x2 unit cell with Density functional theory (DFT) by using the Vienna ab initio simulation package (VASP) [26]. The core−valence electron interactions were treated using Blöchl's projector-augmented wave (PAW) formalism with a cutoff energy of 300 eV. The optimization of the structural parameters is performed until the forces on the atoms are < 0.01 eV $Å^{-1}$. The nonlocal exchange and correlation energies were calculated with the Perdew−Wang (PW91) functional within generalized gradient approximation (GGA). The linear tetrahedron method with Blöchl correction is used [27]. Brillouin zone integrations were performed using a Monkhorst−Pack 9 × 9 × 9 *k*-points mesh for best convergence and relaxation to zero strains.

5.3 Results and Discussion

Figure 5.1A shows the X-ray diffraction patterns of the as-deposited Mg-Nb films, displayed as a function of increasing Nb alloying. The stoichiometries are listed in atomic percent, e.g. $Mg_{0.75}Nb_{0.25}$ is 75 at.% Mg and 25 at.% Nb. For compositions low in Nb, e.g. $Mg_{0.87}Nb_{0.13}$, the as-deposited films have a strong Mg [0001] fiber texture as indicated by the predominant (0002) hexagonal close packed (hcp) reflection. In $Mg_{0.87}Nb_{0.13}$ there is no evidence of bcc reflections. This indicates that the microstructure is a supersaturated solid solution of Nb in Mg lattice. With Nb alloying, the Mg (0002) reflection shifts to higher angles as compared to $2\theta = 34.4°$ of pure Mg. This is expected since the effective atomic radius of Nb ($r = 1.429$Å) is smaller than that of Mg ($r = 1.605$Å). At 20 at.% Nb a reflection from the {110} bcc family of planes is also present, indicating the formation of a new phase. With further additions of Nb the relative intensity of the Mg (0002) reflection progressively diminishes. For the $Mg_{0.75}Nb_{0.25}$ alloy, Mg (0002) can be no longer detected. Instead three Bragg peaks, located at $2\theta = 36.51°$, 52.53° and 65.62°, are unambiguously indexed as (110), (200) and (211) reflections of bcc lattice. Using all three bcc reflections we obtained a lattice parameter of 3.48Å, which is larger than $a =$ 3.30Å for pure Nb. The texture also changed with Nb alloying. The $Mg_{0.75}Nb_{0.25}$ and $Mg_{0.69}Nb_{0.31}$ films have to be tilted around χ by 35° as to obtain strong Bragg peaks.

The microstructure of the $Mg_{0.75}Nb_{0.25}$ sample is further investigated via TEM analysis. Figure 5.1B shows a representative selected area electron diffraction (SAD) pattern obtained from a 50 nm thick as-deposited $Mg_{0.75}Nb_{0.25}$ film. By comparing the experimental SAD pattern with a bcc ring pattern simulation (insert), the exclusive presence of the bcc phase is confirmed. A diffuse (200) MgO ring is also identifiable in the diffraction pattern, as would be expected due to the formation of single nm-scale oxide on the surface. The MgO structure is explained by the much higher enthalpy of formation of MgO (-602 kJ mol^{-1}) versus Nb_2O_5 (-440 kJ mol^{-1}). Figure 5.1C shows a HRTEM micrograph of a representative region in the same film. Continuous lattice fringes are observed, with no evidence of an amorphous phase or of secondary precipitates. The interplanar distance of 2.5Å (obtained from FFT) matches the XRD determined d-spacing of the {110} planes.

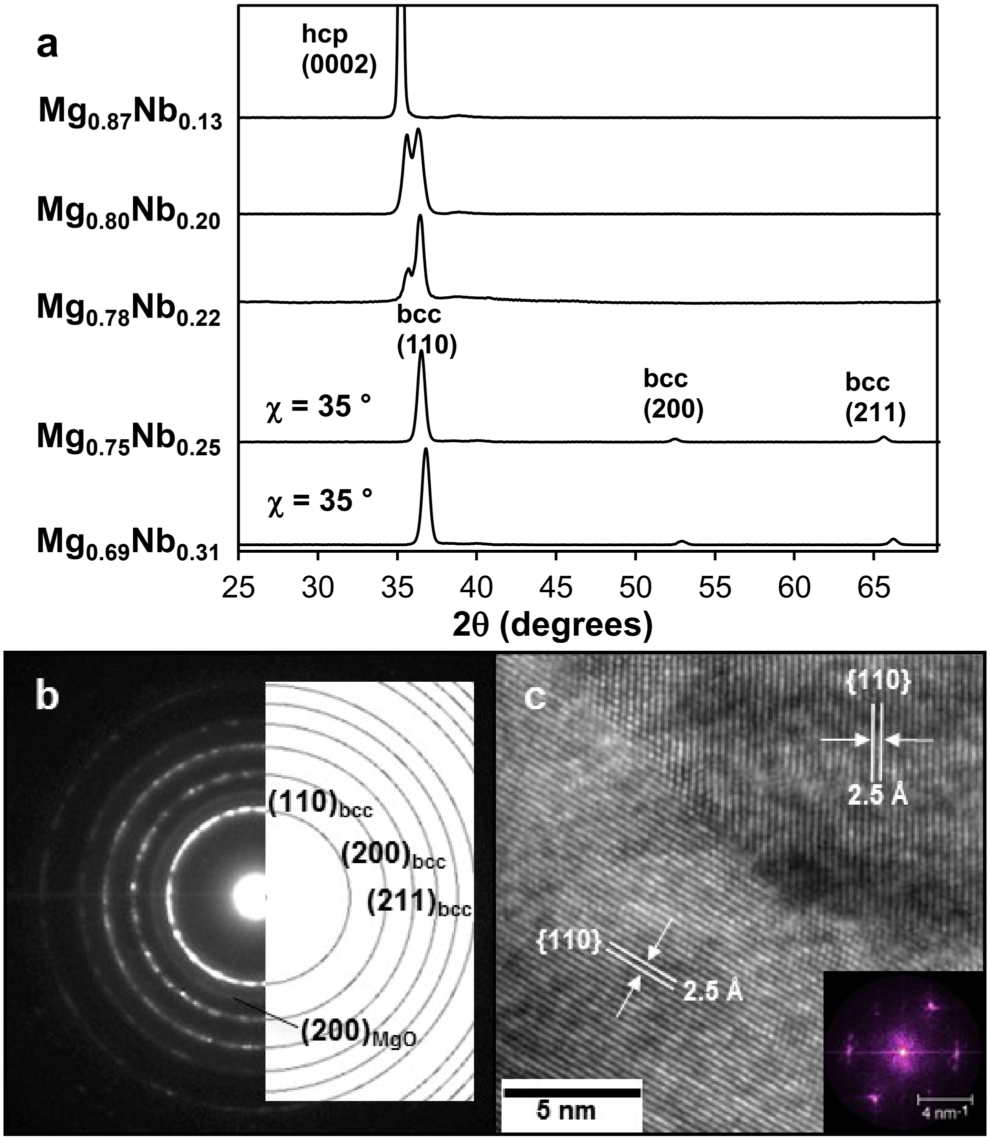

Figure 5.1: (a) X-ray diffraction patterns of the as-deposited $Mg_{0.87}Nb_{0.13}$, $Mg_{0.80}Nb_{0.20}$, $Mg_{0.78}Nb_{0.22}$, $Mg_{0.75}Nb_{0.25}$ and $Mg_{0.69}Nb_{0.31}$ films. (b) TEM selected area diffraction pattern obtained from a 50 nm thick $Mg_{0.75}Nb_{0.25}$ film. (c) High-resolution TEM micrograph of a representative region in the same sample.

To understand the thermodynamic origins of the hexagonal to cubic transition in the Mg-Nb system, we have performed density functional theory (DFT) calculations. The formation energy, E_f, of $Mg_{1-x}Nb_x$ per unit cell is defined as

$$E_f = E(Mg_{1-x}Nb_x) - (1-x)E(Mg) - xE(Nb) \qquad \text{Eq. 5.1}$$

where $E(Mg_{1-x}Nb_x)$, $E(Mg)$ and $E(Nb)$ denote the ground state energy of Mg-Nb alloys, of free Mg atoms and of free Nb atoms, respectively. The lattice constants are determined by geometry optimization of hcp, fcc and bcc structures for $Mg_{1-x}Nb_x$ with x = 0, 0.13, 0.25 and 0.31. Within a unit cell, we considered perfectly homogeneous or atomic-scale segregated distributions of Mg and Nb atoms. The latter may be considered to mimic the precursor stage to phase segregation. Preliminary calculations of E_f demonstrate that unit cells with the segregated atomic configurations are more stable. Moreover the formation of Mg-Nb random solid solution is highly unlikely given their large positive enthalpy of mixing [28]. Subsequent results thus refer exclusively to unit cells with an atomic-scale segregated distribution of Nb atoms.

Figure 5.2 displays values of E_f for hcp, fcc and bcc structures of $Mg_{1-x}Nb_x$ with different compositions, i.e. varying x, as a function of the lattice constant. Lattice constants of the optimized structure and the corresponding values of E_f are listed in Table 5.1. For x = 0 and x = 0.13, the hcp structure is the most stable lattice configuration. For x = 0.25 and x = 0.31, the bcc structure is the most stable structure. The calculated lattice constant of the optimized bcc $Mg_{0.75}Nb_{0.25}$ is 3.5Å, which is in good agreement with the experimental value. The computational results shown in Figure 5.2 confirm that Mg and Nb atoms in $Mg_{0.75}Nb_{0.25}$ alloy spontaneously form a coherent crystalline structure with body centered cubic symmetry, even though Nb atoms are not homogeneously distributed. Interestingly, recent modeling work for atomic layers of (0001)Mg:(110)Nb with stoichiometry 3:1 and 1:1 also identified the bcc lattice structure as the most stable configuration [29].

Our DFT-based structural optimization calculations at 0 K show that the differences in formation energies between the stable lattice configurations are < 5 kJ mol^{-1}. Given such low energetic differences, the transition from hcp to bcc phases could be further facilitated by entropy contributions. The lower coordination number of the bcc structure induces the excess entropy of the bcc phase at higher temperatures. This would thus lead to a further lowering of the free energy in comparison to hcp and fcc phases, favoring the bcc phase upon increasing temperature.

Figure 5.3A shows the hydrogen absorption Pressure-Composites Isotherms (PCI) for freestanding 1.5 µm thick $Mg_{0.75}Nb_{0.25}$ alloy films. The isotherms are measured for the first hydrogenation at 20, 60, 100 and 140 °C. The equilibrium pressures at these four different temperatures are 0.0004, 0.0043, 0.0511, and 0.2390 bar, respectively. Based on the Van't Hoff plot (Figure 5.3B), the standard enthalpy and entropy of hydride

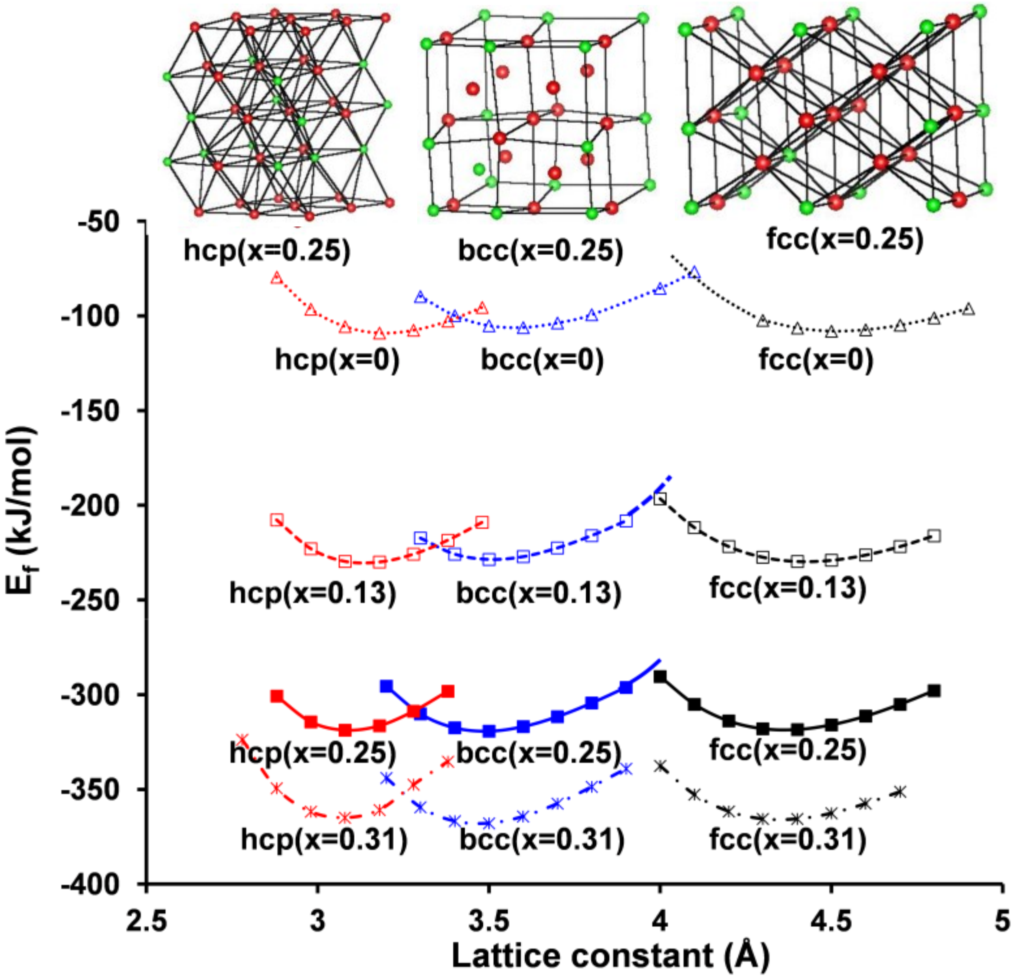

Figure 5.2: Formation energies of $Mg_{1-x}Nb_x$ (x = 0, 0.13, 0.25 and 0.31) with various structures as a function of lattice constant. The hcp, bcc and fcc unit cells for $Mg_{0.75}Nb_{0.25}$ are shown, with Nb atoms being the green spheres.

Table 5.1: Lattice constants and formation energies of Mg and $Mg_{1-x}Nb_x$ with hcp, bcc or fcc structure at various x.

x	structure	Lattice constant Å	E_f (kJ mol^{-1})
0	hcp	3.2	-113.1
	bcc	3.6	-110.2
	fcc	4.5	-112.4
0.13	hcp	3.2	-239
	bcc	3.5	-237.8
	fcc	4.4	-238.7
0.25	hcp	3.1	-323.8
	bcc	3.5	-328.8
	fcc	4.4	-328
0.31	hcp	3.1	-379.9
	bcc	3.5	-381
	fcc	4.4	-378.7

formation are -53 kJ mol^{-1} H_2 and -117 J K^{-1} mol^{-1} H_2, respectively. Compared to the well-known enthalpy for thin film or bulk MgH_2 (approximately -77 kJ mol^{-1} H_2), there is a significant thermodynamic destabilization. The measured maximum hydrogen capacity of 4.5 wt.% corresponds to a hydrogen concentration very close to hydrogen to metal atom ratio (H/M) of 2. However the formed hydride does not possess the rutile structure associated with MgH_2. Figure 5.3C shows the X-ray diffraction pattern of the alloy that is fully absorbed at room temperature. The structure remains bcc. The (110) reflection is centered at $2\theta = 35.86°$ indicating an expansion of the lattice parameter to $a = 3.54$Å. This confirms the presence of interstitial hydrogen.

Although it is not obvious in logarithmic scale, the absorption PCIs actually present two plateaus. The higher equilibrium pressure plateau extends from 0.5 to 4.5 wt.% H, while the lower plateau extends from 0 to 0.5 wt.%. X-ray analysis after the alloy being absorbed to 0.5 wt.% H shows that there is no evidence of rutile MgH_2 formation. Rather the partially absorbed microstructure is still bcc, with the lattice constant being also distinct from the interstitial hydride (α-NbH_x) of Nb. The corresponding lattice parameter (a = 3.50 Å) is intermediate between the as-deposited (a = 3.48 Å) and the fully absorbed one (a = 3.54 Å), though the dilation does not appear to scale linearly with the hydrogen content. Therefore, it is feasible to attribute the lower plateau to the occupation of the hydrogen atoms in certain preferred bcc interstitial locations, which possess the highest binding energy. One could speculate that these sites would be higher in Nb nearest neighbors rather than in Mg. However neutron scattering experiments on the deuterated alloy would be required to identify the site occupancy distribution.

As shown in Figure 5.3D, the experimentally determined equilibrium pressures at 175 and 200 °C (blue and black crosses) are significantly lower than the extrapolations based on $\Delta H^0 = -53\ \mathrm{kJ\ mol^{-1}}\ H_2$ and $\Delta S^0 = -117\ \mathrm{J\ K^{-1}\ mol^{-1}}\ H_2$ (blue and black lines). The deviation increases as the temperature increases. This indicates the decomposition of the

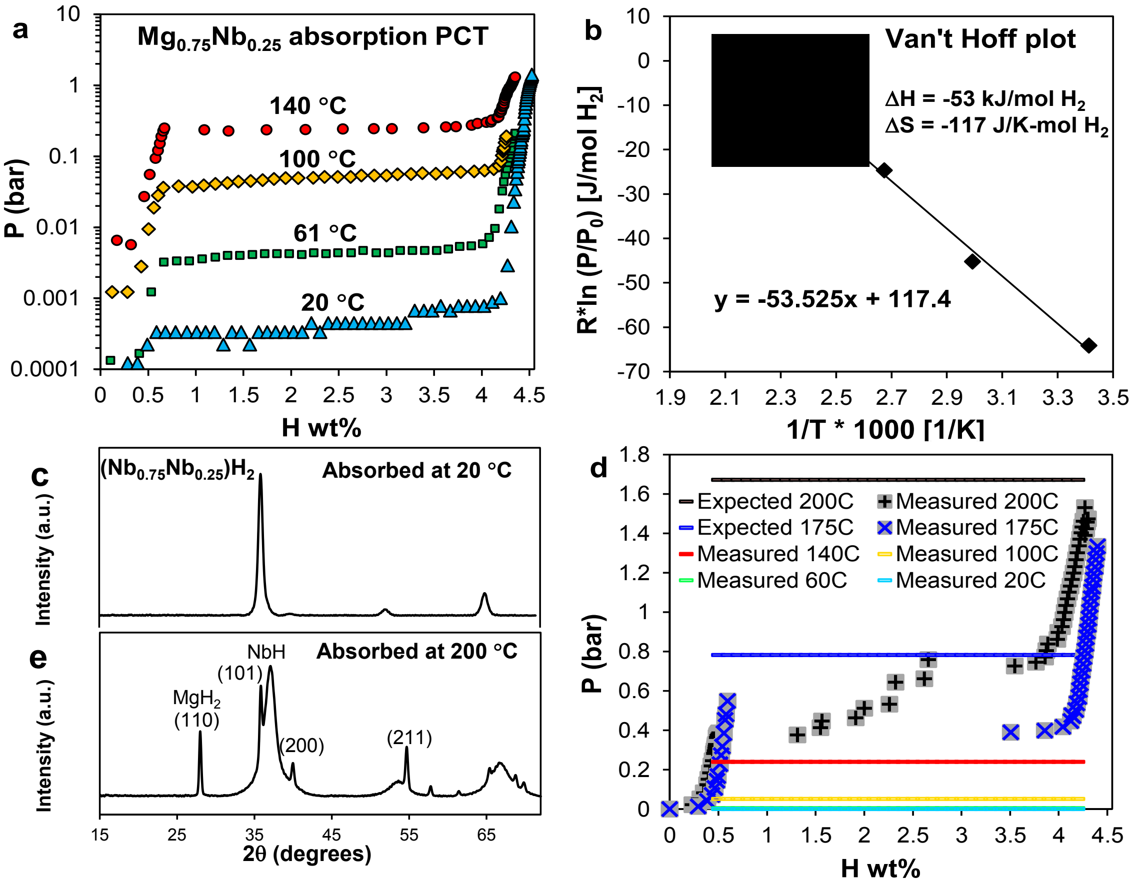

Figure 5.3: (a) Hydrogen absorption Pressure-Composites Isotherms of $Mg_{0.75}Nb_{0.25}$ alloy for the first hydrogenation at 20, 60, 100, and 140 °C. (b) Corresponding Van't Hoff plot. (c) XRD pattern of $Mg_{0.75}Nb_{0.25}$ after being fully absorbed at 20 °C. (d) Absorption isotherm measured at 175 and 200 °C; the expected equilibrium pressures extrapolated from Van't Hoff plot in (b) are depicted as lines. (e) XRD pattern of $Mg_{0.75}Nb_{0.25}$ after being fully absorbed at 200 °C.

Mg-Nb bcc alloy structure. Figure 5.3E shows the X-ray analysis performed on the sample that is fully absorbed at 200 °C. The prominent peaks can be unambiguously indexed as the rutile MgH_2 and the face-centered orthorhombic β-NbH_x with an effective composition of approximately NbH. X-ray analysis was conducted at room temperature. The α-NbH_x containing hydrogen with x ~ 1 formed under the sorption condition (200 °C, 1 bar H_2) transforms to β-NbH. The hydride of niobium with higher hydrogen content is not observed here. This is consistent with the fact that equilibrium pressure of fcc NbH_2 at 200 °C is significantly higher than the applied hydrogen pressure (1 bar).

Using DFT calculations, we also evaluated the hydride formation energy E_{ab} of $(Mg_{0.75}Nb_{0.25})H_2$ at 0 K, using:

$$E_{ab} = E(Mg_{1-x}Nb_xH_2) - E(H_2) - E(Mg_{1-x}Nb_x) \qquad \text{Eq. 5.2}$$

The binding energy of a hydrogen molecule, $E(H_2)$, was calculated using a cubic unit cell with size 10Å×10Å×10Å. We calculated E_{ab} as a function of the lattice constant a, and compared hydride formation energies for $(Mg_{0.75}Nb_{0.25})H_2$ that are bcc, rutile and fluorite. For bcc structure, we placed hydrogen atoms at tetrahedral sites in the unit cell, which are known as preferential H occupation sites in bcc metals [30]. Within a bcc lattice, six tetrahedral sites are available for each metal atom, corresponding to 96 tetrahedral sites for a 2x2x2 unit cell. In order to fix the H/M ratio at 2, the hydrogen atoms are placed into the 32 tetrahedral sites corresponding to maximal H-H separation distances. The thus generated "initial structures" are shown in Figure 5.4. For rutile structure, the ratio of the lattice constants was fixed at $a/c = 1.5$.

As shown in Figure 5.4, fluorite $(Mg_{0.75}Nb_{0.25})H_2$ possesses the lowest E_{ab} value for $a > 4.5$Å. For 3.5Å $< a <$ 4.3Å, rutile $(Mg_{0.75}Nb_{0.25})H_2$ exhibits the lowest E_{ab} value. These results agree with the experimental observation that the bcc hydride is metastable. In principle, the crystal structure of metastable bcc $(Mg_{0.75}Nb_{0.25})H_2$ would transform to a more stable structure. This propensity of transformation is evident from the significant displacement of H atoms from regular tetrahedral sites, and of metal atoms from regular bcc sites, shown in the "relaxed structures". At the experimentally measured lattice constant $a = 3.54$Å, the calculated value of E_{ab} for bcc $(Mg_{0.75}Nb_{0.25})H_2$ is -52 kJ mol^{-1} H_2.

The nearly exact agreement between the computational result and the experimentally determined bcc hydride formation enthalpy (-53 kJ mol^{-1} H_2) may be in part fortuitous. Our calculated value of E_{ab} for rutile MgH_2, with the known lattice constants a = 4.5Å and c = 3.0Å, is –69 kJ mol^{-1}. This value is consistent with the previously reported results of computational studies [31], but underestimates the experimentally measured formation energy of MgH_2 by roughly 10%. This deviation could be attributed to the finite size of the unit cell and the limited number of K points used in the simulation. To justify why such discrepancy is not observed in bcc $(Mg_{0.75}Nb_{0.25})H_2$, it would be worthwhile doing simulation with a larger unit cell. What is important though is that both theory and experiment demonstrate a significant thermodynamic destabilization of the metastable bcc Mg-Nb hydride relative to the equilibrium rutile magnesium hydride.

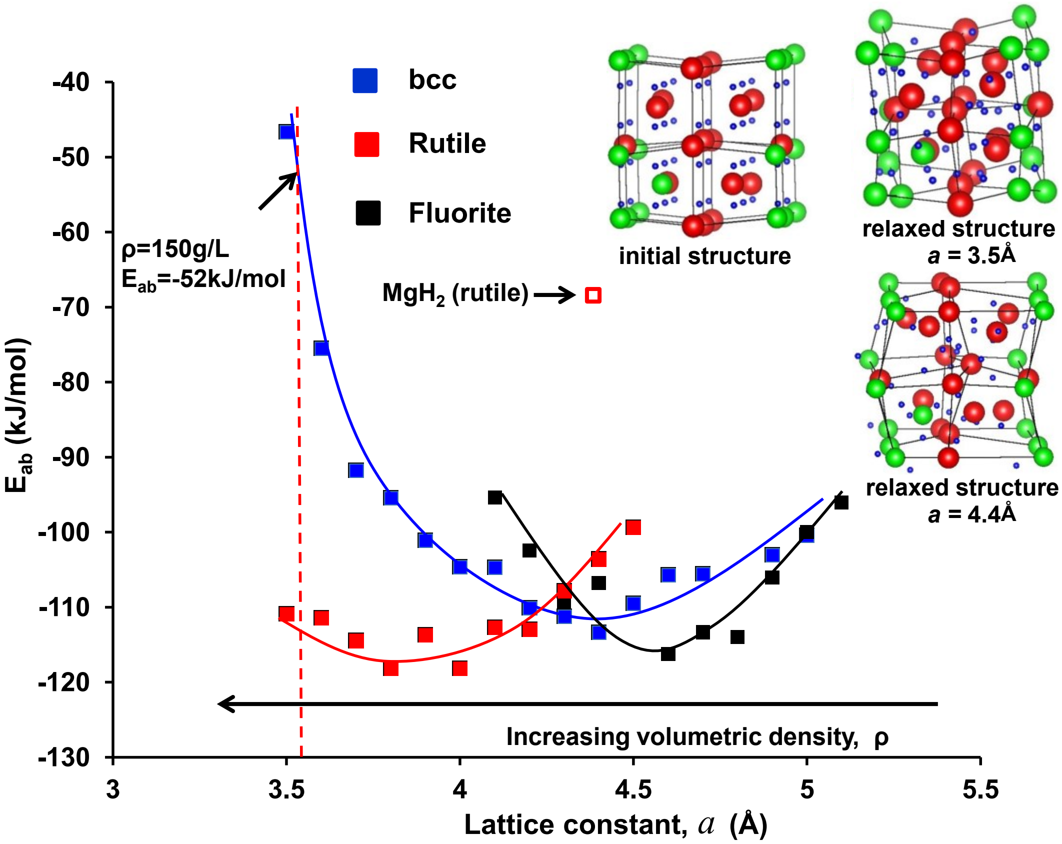

Figure 5.4: Hydride formation energy E_{ab} of $Mg_{0.75}Nb_{0.25}H_2$ with bcc, rutile and fluorite structures as a function of lattice constant a. The H atoms are occupying the tetrahedral sites in the bcc unit cell. The atomic configurations illustrate the initial and relaxed structure of a 2x2x2 bcc unit cell.

Figure 5.5A shows the hydrogenation curves of the bcc $Mg_{0.75}Nb_{0.25}$ alloy at room temperature under hydrogen pressure of 1 bar. Even at such a relatively low hydrogen pressure the absorption kinetics are extraordinarily fast. On the first hydrogen loading, a freestanding 1.5 µm thick film could absorb 4 wt.% H (90% of the total capacity) within 30 minutes. Reducing the film thickness can further increase the absorption kinetics. For a 100 nm thick $Mg_{0.75}Nb_{0.25}$ film, 4 wt.% H could be absorbed within 30 seconds. To our knowledge this is one of the most rapid ambient absorption ever reported for Mg-based alloys. Our hypothesis is that this uniquely rapid hydriding kinetics is attributed to the rapid hydrogen diffusivity within the bcc alloy lattice [30]. Furthermore since the hydride appears to be interstitial, there is no kinetic impediment associated with the heterogeneous nucleation of a crystallographically dissimilar hydride phase as is there for Mg to MgH_2 transition [32].

The hydrogen cycling sorption kinetics of a freestanding 1.5 µm thick $Mg_{0.75}Nb_{0.25}$ alloy film were measured according to the following procedure: Hydrogenation was performed at room temperature under a hydrogen pressure of 1 bar. After each absorption step, the sample was heated to 175 °C as to be able to quickly desorb at rough vacuum (P initial ~ 5 mbar). The selected absorption and desorption curves up to 40 sorption cycles are shown in Figures 5.5B and C, respectively. Initially the alloy absorbs 4.5 wt.% H. However, only 4 wt.% is reversible at this pressure - temperature combination. The irreversible capacity (0.5 wt.%) after the first cycle is likely to be related to the lower plateau discussed earlier. Upon further cycling, the reversible capacity slowly degrades to 3.2 wt.% by cycle 40. X-ray analysis shown in Figure 5.5D will demonstrate that this deterioration in the reversible capacity is most likely due to the cycling-induced partial decomposition of the bcc Mg-Nb phase into the equilibrium structures.

We performed X-ray analysis to characterize the post-cycled microstructure of $(Mg_{0.75}Nb_{0.25})H_2$. The diffraction patterns of the hydrided samples after 1, 10 and 40 sorption cycles are shown in Figure 5.5D. After the initial absorption, XRD identifies the microstructure to be entirely bcc. After 10 sorption cycles, the equilibrium (110) MgH_2 reflections possess a trivial if not negligible relative intensity. However, after 40 sorption cycles the equilibrium (100) and (211) MgH_2 reflections are unambiguously present.

Additional MgH_2 and NbH_2 reflections are probably present too (marked in the Figure), though the overlap with the majority bcc $(Mg_{0.75}Nb_{0.25})H_2$ phase makes unambiguous identification difficult. Compared to the x-ray diffraction shown in Figure 5.3E, large-scale phase segregation however can be ruled out.

The overall sorption kinetics actually improves during the first few cycles. By cycle 5, a total of 3.5 wt.% H can be absorbed within a minute. This initial kinetic improvement could be attributed to the progressive formation of surface cracks in the films during cycling. This would provide an increased surface area for hydrogen dissociation and

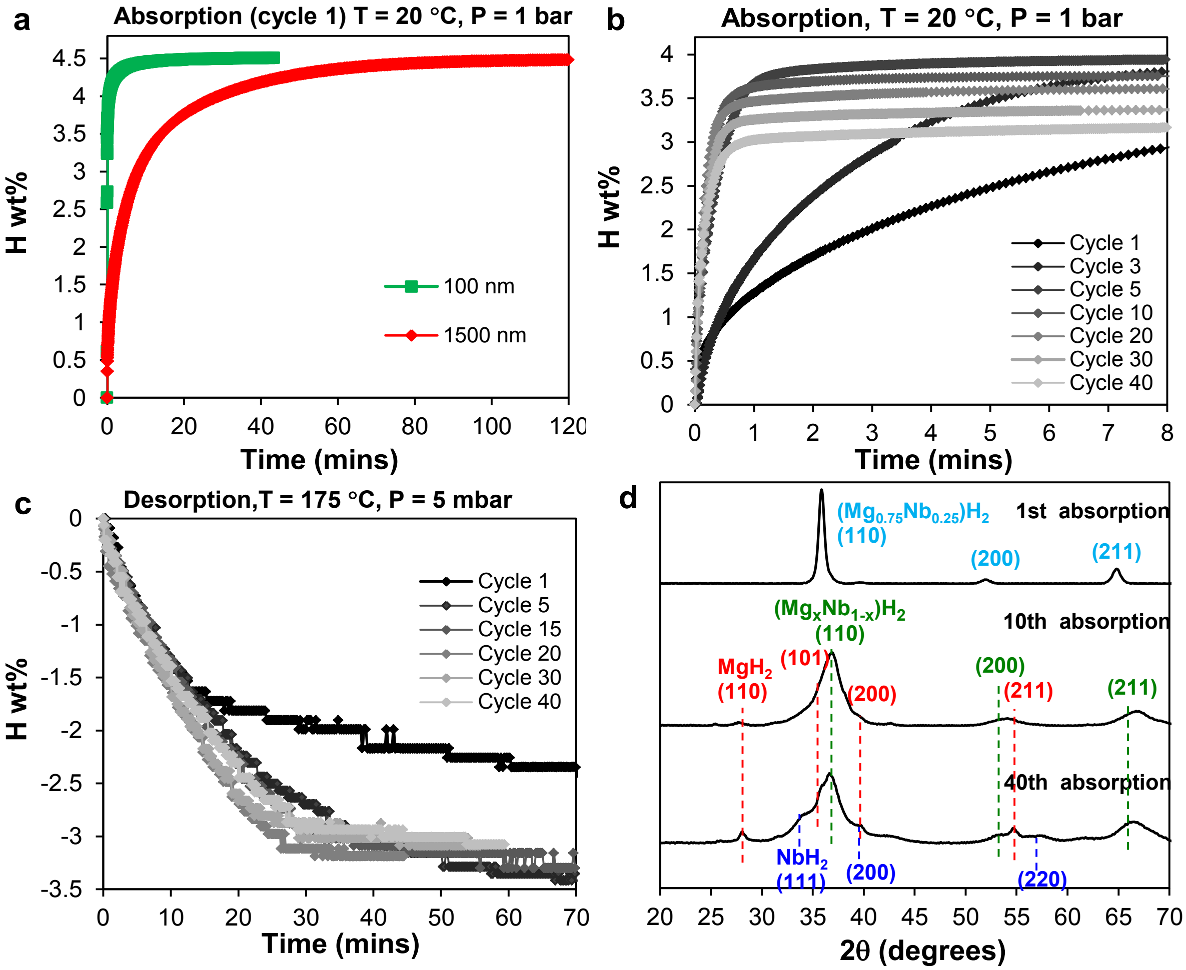

Figure 5.5: (a) Initial hydrogenation curves of 100 nm and 1.5 μm thick $Mg_{0.75}Nb_{0.25}$ alloy films at 20 °C, under hydrogen pressure of 1 bar. The selected (b) absorption and (c) desorption curves of hydrogen cycling sorption of 1.5 μm thick $Mg_{0.75}Nb_{0.25}$ films. (d) XRD patterns of $Mg_{0.75}Nb_{0.25}$ in the absorbed state, measured after 1st, 10th and 40th cycle.

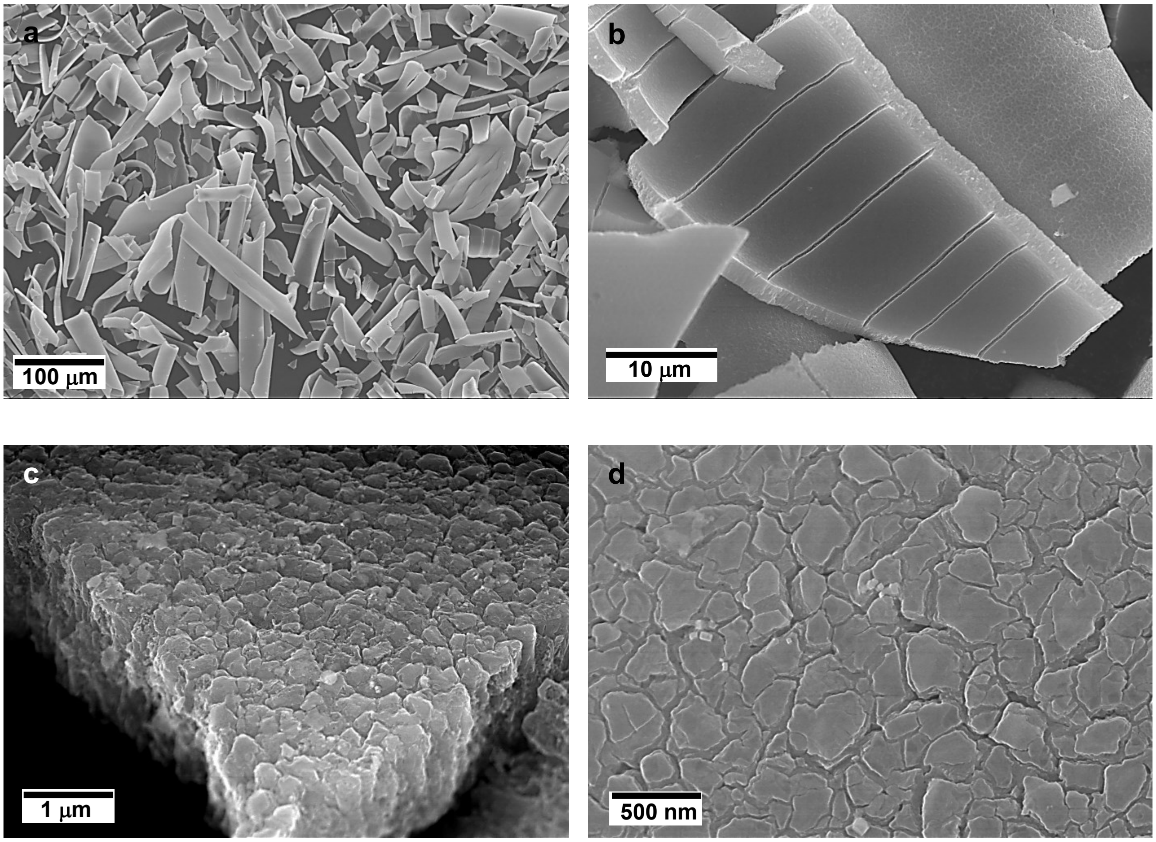

Figure 5.6: Scanning electron microscopy (SEM) micrographs of 1.5 μm thick $Mg_{0.75}Nb_{0.25}$ alloy film after 10 sorption cycles, shown in order of increasing magnification.

recombination, and lower the diffusion distances [33]. SEM micrographs of the films taken after 10 sorption cycles confirm this scenario, as shown in Figure 5.6.

Finally, it is important to discuss from a practical viewpoint that physical co-deposition has analogues in inexpensive bulk manufacturing methods such as rapid solidification techniques and high energy powder co-milling. As the co-deposited materials represent the idealized case, our bcc Mg-Nb alloy microstructure could be alternatively achieved via the methods mentioned above. High energy powder co-milling has already been used to successfully synthesize bcc Mg-Co alloy [34,35]. The bulk manufacturing procedures need to be carried out in an inert atmosphere. It has been confirmed that (results not shown here) our material after 40 sorption cycles cannot further desorb any hydrogen after exposure to air/moisture.

5.4 Conclusion

In summary, we have shown experimentally that physically co-depositing $Mg_{1-x}Nb_x$ alloys over certain composition range ($0.25 \leq x \leq 0.31$) results in a coherent crystalline structure with body centered cubic symmetry. Using DFT based calculations the structural transformation of the Mg-Nb alloys from hexagonal to cubic has been confirmed. The bcc $Mg_{0.75}Nb_{0.25}$ alloy rapidly transforms to a new metastable bcc magnesium niobium hydride $(Mg_{0.75}Nb_{0.25})H_2$ upon exposure to hydrogen at room temperature. This metal-hydrogen system has kinetic and thermodynamic properties markedly superior to that of rutile MgH_2. We envision that with additional alloy design and further nanostructuring, improvements in the thermodynamics and capacity will be possible. The resulted materials could be potentially used for stationary or portable storage applications.

5.5 Reference

[1] K-F Aguey-Zinsou, J-R Ares-Fernandez, *Energy Environ. Sci.* **2010**, *3*, 526-543.

[2] C. Weidenthaler, M. Felderhoff, *Energy Environ. Sci.* **2011**, *4*, 2495-2502.

[3] S. X. Tao, W. P. Kalisvaart, M. Danaie, D. Mitlin, P. H. L. Notten, R. A. van Santen, A. P. J. Jansen, *Int. J. Hydrogen Energ.* **2011**, *36*, 11802-11809.

[4] B. Zahiri, M. Danaie, X. H. Tan, B. S. Amirkhiz, G. A. Botton, D. Mitlin, *J. Phys. Chem. C* **2012**, *116*, 3188–3199.

[5] F. M. Mulder, S. Singh, S. Bolhuis, S. W. H. Eijt, *J. Phys. Chem. C* **2012**, *116* 2001–2012.

[6] R. Bardhan, A. M. Ruminski, A. Brand, J. J. Urban, *Energy Environ. Sci.* **2011**, *4*, 4882-4895.

[7] T. K. Nielsen, F. Besenbacher, T. R. Jensen, *Nanoscale* **2011**, *3*, 2086-2098.

[8] W. P. Kalisvaart, E. J. Luber, E. Poirier, C. T. Harrower, A. Teichert, D. Wallacher, N. Grimm, R. Steitz, H. Fritzsche, D. Mitlin, *J. Phys. Chem. C* **2012**, *116*, 5868−5880.

[9] V.A. Vons, A. Anastasopol, W.J. Legerstee, F.M. Mulder, S.W.H. Eijt, A. Schmidt-Ott, *Acta Mater.*, **2011**, *59*, 3070-3080.

[10] F. Cuevas, D. Korablov, M. Latroche, *Phys. Chem. Chem. Phys.* **2012**, *14*, 1200-1211.

[11] H. Reardon, J. M. Hanlon, R. W. Hughes, A. Godula-Jopek, T. K. Mandal, D. H. Gregory, *Energy Environ. Sci.* **2012**, *5*, 5951-5979

[12] KJ Jeon, H. R. Moon, A. M. Ruminski, B. Jiang, C. Kisielowski, R. Bardhan, J. J. Urban, *Nat. Mater.* **2011**, *10*, 286-290.

[13] G. S. Walker, M. Abbas, D. M. Grant, C. Udeh, *Chem. Commun.* **2011**, *47*, 8001-8003.

[14] A. Baldi, M. Gonzalez-Silveira, V. Palmisano, B. Dam, R. Griessen, *Phys. Rev. Lett.* **2009**, *102*, 226102.

[15] C-J Chung, S-C Lee, J. R. Groves, E. N. Brower, R. Sinclair, B. M. Clemens, *Phys. Rev. Lett.* **2012**, *108*, 106102.

[16] S. X. Tao, P. H. L. Notten, R. A. van Santen, A. P. J. Jansen, *Phys. Rev. B* **2010**, *82*, 125448.

[17] L. P. A. Mooij, A. Baldi, C. Boelsma, K. Shen, M. Wagemaker, Y. Pivak, H. Schreuders, R. Griessen, B. Dam, *Adv. Energy Mater.* **2011**, *1*, 754-758.

[18] M. G. Shelyapina, D. Fruchart, *Solid state Phenom.* **2011**, *170*, 227-231.

[19] D. M. Borsa, R. Gremaud, A. Baldi, H. Schreuders, J. H. Rector, B. Kooi, P. Vermeulen, P. H. L. Notten, B. Dam, R. Griessen, *Phys. Rev. B* **2007**, *75*, 205408.

[20] T. Takasaki, D. Kyoi, N. Kitamura, S. Tanase, T. Sakai, *J. Phys. Chem. B* **2007**, *111*, 14102-14106.

[21] D. Moser, D. J. Bull, T. Sato, D. Noreus, D. Kyoi, T. Sakai, N. Kitamura, H. Yusa, T. Taniguchi, W. P. Kalisvaart, P. H. L. Notten, *J. Mater. Chem.* **2009**, *19*, 8150-8161.

[22] S. X. Tao, P. H. L. Notten, R. A. van Santen, A. P. J. Jansen, *J. Alloy. Compd.* **2011**, *509*, 210-216.

[23] D. Kyoi, N. Kitamura, H. Tanaka, A. Ueda, S. Tanase, T. Sakai, *J. Alloy. Compd.* **2007**, *428*, 268-273.

[24] S. Bao, Y. Yamada, K.Tajima, M. Okada, K. Yoshimura, *Japanese J. Appl. Phys.* **2007**, *46,* L13-L15.

[25] X. H. Tan, C. T. Harrower, B. S. Amirkhiz, D. Mitlin, *Int. J. Hydrogen Energ.* **2009**, *34*, 7741-7748.

[26] G. Kresse, D. Joubert, *Phys. Rev. B* **1999**, *59*, 1758–1775.

[27] P. E. Blöchl, O. Jepsen, O. K. Andersen, *Phys. Rev. B* **1994**, *49*, 16223–16233.

[28] F. R. de Boer, R. Boom, W. C. M. Mattens, A. R. Miedema, A. K. Niessen, *Cohesion in metals: Transition metal alloys*, Elsevier Science Publishers B.V., North-Holland, Amsterdam, 1988.

[29] K. Klyukin, M. G. Shelyapina, D. Fruchart, *Solid State Phenom.* **2011**, *170*, 298-301.

[30] Y. Fukai, *The Metal-Hydrogen System*, Springer Series in Materials Science, 2nd Ed., vol. 21, Springer Verlag, Berln, **2005**.

[31] N. Novakovic, L Matovic, J. G. Novakovic, M. Manasijevic and N. Ivanovic, *Mater. Sci. Eng.* B. *Solid.*, **2009**, *165*, 235-238.

[32] M. Danaie, S.X. Tao, W.P. Kalisvaart and D. Mitlin, *Acta Mater.* **2010**, *58*, 3162-3172.

[33] R. Zahiri, B. Zahiri, A. kubis, W. P. Kalisvaart, B. S. Amirkhiz, D. Mitlin, *Int. J. Hydrogen Energ.* **2012**, *37*, 4215-4226.

[34] J. Matsuda, H. Shao, Y. Nakamura, E. Akiba, *Nanotechnology* **2009**, *20*, 204015.

[35] H. Kim, J. Nakamura, H. Shao, Y. Nakamura, E. Akiba, K. W. Chapman, P. J. Chupas, T. Proffen, *J. Phys. Chem. C* **2011**, *115*, 20335-20341.

Chapter 6

The Effect of an Atomic Layer Deposition (ALD) Titanium Oxynitride Interlayer on the ORR Activity and Corrosion Stability of Pt and Pt-Ni*

6.1 Introduction

There are great expectations for energy conversion technologies such as proton exchange membrane fuel cells (PEMFCs) that are environmentally benign and energetically efficient. Yet despite the tremendous progress, successful wide-scale commercialization will require the development of even more active and durable oxygen reduction reaction (ORR) catalysts that are also lower in cost [1-3]. Though substantial gains have been made in the development of low cost non-noble electrocatalysts [4-9], platinum and other noble metal based electrocatalysts continue to remain the key commercialization target due to their unsurpassed catalytic activities [10-19]. Many efforts have been devoted to the development of advanced supports for platinum electrocatalysts [20-23]. Generally, an ideal catalyst support should have: i) a high surface area for optimum metal dispersion, ii) high electrical conductivity, iii) electrochemical stability under the relevant conditions, and iv) a chemical interaction with the electrocatalyst that enhances its activity and electrochemical stability. Presently,

---

* Materials in this chapter has been published in:

- ➢ XueHai Tan, Liya Wang, Beniamin Zahiri, Alireza Kohandehghan, Dimitre Karpuzov, Elmira Memarzadeh Lotfabad, Zhi Li, Michael H. Eikerling, David Mitlin, ChemSusChem 2014, DOI: 10.1002/cssc.201402704 conductive carbon allotropes with high surface area are the most widely used catalyst supports. However, severe corrosion of such supports is observed, being associated with the tendency for the cathode to reach potentials above the onset of carbon oxidation [24]. Platinum nanoparticles, which are weakly held in place, are also observed to agglomerate [25] and to detach from the carbon supports [26].

Transition metal oxides such as TiO_2 [27-29], NbO_2 [30-33], WO_2 [34], ITO [35], Y_2O_3/Gd_2O_3 [36] and nitrides e.g. TiN [37,38], NiN [39], VN [40] have been investigated as alternative support materials. The metal oxide and nitride supports are electrochemically more stable than carbon and have been found to impart enhanced activity and durability to the Pt catalyst due to the advantageous catalyst - support chemical interactions. These interactions have been proposed to manifest by several mechanisms, including modification of the electronic structure of platinum that shifts the formation of Pt-OH to higher potentials, a lateral repulsion between Pt-OH and oxide surface, and/or a spillover of -OH onto the oxophilic centers of the support surface. One adverse feature of many oxide supports is their unsatisfactory electrical conductivity. For instance, platinum electrocatalysts deposited on niobium oxides show lower specific activity than their carbon-supported counterparts [32]. The resultant ohmic losses may actually outweigh the activity gains from any beneficial changes in the Pt electronic structure. Thus in an ideal case one would minimize the losses due to increased resistance, in order to retain the enhancements in activity and the corrosion resistance. For the case of TiO_2, doping with metal ions (e.g. Nb^{5+} [41]) or incorporating nitrogen [42] is partially effective in increasing the support's electrical conductivity. Highly N-rich TiO_2, also termed titanium oxynitride, may be prepared by either heavy nitridation of TiO_2 in an ammonia atmosphere [43] or partial oxidation of TiN [44]. According to XPS studies of TiN surface [45], oxidation of TiN also proceeds spontaneously at ambient conditions. The reaction front initiates at the air-terminating surface and proceeds slowly through the material.

Alloying platinum with less expensive transition metals has been demonstrated highly effective for increasing ORR activity [46-52]. Among various types of Pt-based alloy catalysts, a Pt-Ni alloy with atomic ratio of 1:1 has been found to exhibit one of the best catalytic activities towards the ORR [53-55]. A number of studies in diverse fields such as the catalytic oxidation of carbon monoxide [56], and catalytic hydrogenation and reformation reactions [57] have highlighted a possible additional synergy of combining an advantageous oxide/nitride support with a binary or a ternary alloy catalyst. Although the general working assumption by researchers and engineers is that the two effects, i.e. alloy catalyst and an advantageous oxide-based support, should work in unison, the effectiveness of combining these two strategies have been found to strongly depend on the type of catalytic reactions [57]. For ORR, Pt-based alloy catalysts supported on TiO_2 have been previously reported [58], However, without a proper baseline, the authors did not investigate whether there is a synergy of combining metal oxide support and a Pt-based alloy catalyst.

The present work is thus intended to address the aforementioned gap in understanding, while presenting a new type of a hybrid catalyst support based on a 0.5 nm layer of titanium oxynitride that is inserted between the carbon (here we employ carbon nanotube arrays CNTs) and the electrocatalyst. Such an atomically thin (effectively a monolayer) interlayer will possess an electrical conductance far superior to a "conventional" oxide support, which may be up to 10's of nanometers in thickness. We hypothesized that this may achieve the greatly desired catalyst - oxide/nitride support synergy without incurring a significant ohmic loss penalty. We demonstrate that the presence of the oxynitride interlayer does offer a remarkable improvement in both the activity and the durability for pure Pt, but provides minimal effect for the Pt-50at.%Ni alloy. Using first-principles modeling we show that this difference may be related to the metal - support chemical interactions and to the compositional segregation occurring at the alloy catalyst - support interface. A general implication to emerge is that while tuning the metal - support chemical interaction is highly effective for improving oxygen reduction reaction (ORR) performance, the results do not necessarily transfer from one electrocatalyst system to another even if the support is identical.

6.2 Experimental

Synthesis. The CNTs array was synthesized using a commercial chemical vapor deposition (CVD) reactor (Tystar Inc.). Polished Inconel 600 disks with 11.32 mm diameter (a geometrical area of 1 cm^2) and 2 mm thickness were utilized as the substrates for CNT growth and as electrodes for electrochemical measurements. A typical top-view of the as-synthesized CNTs array is shown in Figure 6.1. A 0.5 nm Titanium nitride (TiN) film was conformally coated onto the CNTs array using the Oxford FlexAL Atomic Layer Deposition (ALD) instrument. The deposition was performed at 300 °C using $TiCl_4$ and H_2/N_2 as precursor and plasma gas, respectively. To convert the surface of the nitride to an oxynitride, exposed supports were stored at ambient for approximately 24 hours prior to the deposition of the catalysts. Thus a coaxial oxynitride coated CNTs array (termed "/TiO_xN_y/CNTs") support was obtained, with the uncoated CNTs (termed "/CNTs") also employed as a baseline.

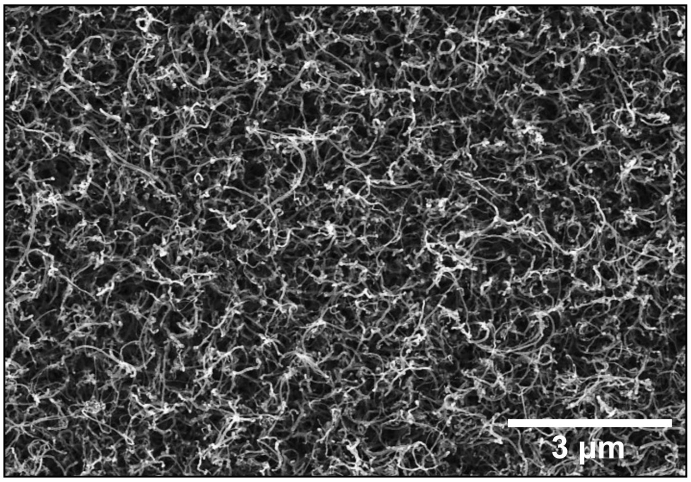

Figure 6.1: Low-magnification SEM micrograph of the as-synthesized CNTs/Inconel electrode from a top view.

Pt and Pt-50at.%Ni catalyst depositions onto the support surfaces were carried out using magnetron co-sputtering from 99.95% pure Pt and Ni targets. A substrate temperature of 700 °C was used for all depositions in order to obtain good crystallization of the catalyst film. The sputtering rate was accurately measured *in-situ* using a crystal monitor at the substrate plane. The deposition rate of Pt was kept at 0.4 Å s^{-1}. The deposition rate of Ni was kept at 0.29 Å s^{-1}, which resulted in 1:1 atomic ratio of Pt:Ni. Composition was confirmed using XPS and EDS. After sputtering, the catalysts were further annealed at 700 ^{o}C for 1 hour under ultrahigh vacuum.

We employed both "low" and "high" mass loadings for each type of catalyst. The high mass loaded sample consists of a 75 nm thick (geometrical) film of either Pt or PtNi deposited onto the array. Given the surface area enhancement of the CNTs is about 18, the average film thickness would be 4 nm. However due to sputter flux shadowing and non-uniform wetting, the actual sizes of the crystallites would vary (discussed in detail in the Results). The 75 nm geometrical thickness corresponds to a total mass loading of 0.15 mg cm^{-2}_{geo} for pure Pt. Since the PtNi film has a different density than pure Pt, 75 nm corresponds to a total mass loading of 0.11 mg cm^{-2}_{geo} for PtNi alloy, which in turn is equivalent to 0.085 mg cm^{-2}_{geo} of Pt. The low mass loaded sample consists of a catalyst film with a 10 nm geometrical thickness. This corresponds to a total mass loading of 0.02 and 0.015 mg cm^{-2}_{geo} for Pt and PtNi, respectively. The total loading of 0.015 mg cm^{-2}_{geo} PtNi alloy is equivalent to 0.0116 mg cm^{-2}_{geo} of Pt. The labeling sequence in the text provides the total mass loading. For example, "PtNi(0.015mg)/TiO_xN_y/CNTs" denotes a low mass loaded PtNi alloy catalyst on an oxynitride support.

Electrochemical characterization: Electrochemical measurements were carried out using a standard rotating disk electrode (RDE) system (Princeton applied research model 616 RDE), a potentiostat (Versa STAT 3) and a three-electrode electrochemical cell. A helical Pt wire and a Cl^- free Hg/Hg_2SO_4 with taper joint (Princeton Applied Research model G0093) were used as the counter electrode and reference electrode, respectively. Perchloric acid ($HClO_4$ optima grade, Fisher Scientific) diluted with Milli-Q water to 0.1M was the electrolyte solution in all cases. All electrochemical measurements were carried out at room temperature using research grade gases (99.999%, Praxair). The reported potentials hereafter are specified relative to the reversible hydrogen electrode (RHE) scale.

The cyclic voltammetry (CV) was recorded in Ar-saturated electrolyte between 0 V and 1.2 V with a scan rate of 50 mV s^{-1}. The electrochemical surface area (ECSA) of the catalysts was estimated by averaging the integral charge of the hydrogen adsorption and desorption areas of the CV profile, including a correction for double layer charging. To avoid the underestimation of the ECSA owing to a possible suppression of hydrogen adsorption, the ECSA was confirmed using CO-stripping. Before CO-stripping, the electrode was immersed in a CO saturated electrolyte for 10 minutes. After that, the electrolyte was purged with Ar and the CO stripping voltammetry was then recorded. Anodic linear sweep voltammetry (LSV) from 0.03 V to 1.05 V was conducted in oxygen-saturated electrolyte to measure the ORR at 1600 rpm with a scan rate of 10 mV s^{-1}. Polarization curves at other rotational speeds (400, 625, 900, 1225, 2025, 2500 and 3600 rpm) were taken using the same potential range and scan rate. The kinetic current was extracted from the measured ORR polarization curve according to the Koutecky-Levich equation:

$$\frac{1}{I}=\frac{1}{I_k}+\frac{1}{I_L}=\frac{1}{I_k}+\frac{1}{B\omega^{1/2}}=\frac{1}{I_k}+\frac{1}{0.62nFA_{geo}D^{2/3}\omega^{1/2}v^{-1/6}C_{O_2}} \qquad \text{Eq. 6.1}$$

where I is the measured ORR current, I_k and I_L are the kinetic and the diffusion limited currents, respectively, B is the Levich slope, F is the Faraday constant, n is the number of electrons transferred per O_2 molecules, D is the diffusion coefficient of oxygen, C_{O2} is the concentration of oxygen in the bulk solution, ω is the angular velocity and ν is the kinematic viscosity of the solution. The durability test of the catalysts was performed in oxygen-saturated electrolyte between 0.6 V and 1.1 V at a sweep rate of 50 mV s^{-1} for 10,000 potential cycles at room temperature. Prior to analyzing the post-cycling ECSA and ORR activities, the electrolyte was replaced with fresh solution. Electrochemical impedance spectroscopy (EIS) measurements were carried out using a Solartron 1470 electrochemical test station. We applied an alternating current in the frequency range from 10 kHz to 0.1 Hz with 25 mV amplitude at 0 V vs. open circuit potential.

Microstructural characterization: X-ray photoelectron spectroscopy (XPS) measurements were performed on an ULTRA (Kratos Analytical) spectrometer under ultrahigh vacuum (10^{-9} Torr), using monochromatic Al-K_α radiation ($h\nu$ = 1486.6 eV) operated at 210 W. All XPS spectra were calibrated using the universal hydrocarbon contamination C1s peak at 284.8 eV. The XPS data were analyzed using CasaXPS software. X-ray diffraction (XRD) analysis was performed on a Bruker AXS diffractometer (Bruker Discover 8) using a Cu-Kα radiation source (λ = 1.5406 Å) that was monochromatized using a single Gobel mirror. The diffractometer was equipped with a Histar general area two-dimensional detection system (GADDs) with a sample-detector distance of 15 cm. Grain size (D) analyses were performed by using the well-known Scherrer equation: $D = k\lambda/\beta\cos\theta_0$ where k is a constant taken as 0.9, λ is the x-ray wavelength, β is the full width half maximum of the peak (FWHM) in radians with the instrumental broadening effect corrected, and θ_0 is the position of the peak maximum. The grain size was reported as the average value from the best-resolved peaks. The peak fitting using Voigt function was performed on Fityk commercial software [59]. The instrumental broadening was determined by using a LaB_6 standard material and subtracted from the measured line broadening. High magnification scanning electron microscopy (SEM) analysis was performed on a Hitachi S-4800 field emission SEM operated at 15 kV accelerating voltage. Bright-field and dark-field imaging and selected area electron diffraction (SAD) analysis were performed on a JEOL 2100 transmission electron microscope (TEM) operated at 200 kV accelerating voltage. The TEM specimens were mechanically removed from the electrodes and dry dispersed onto the grids. Commercial software Crystal Maker ™ and TEM diffraction ring profiler [60] were used to simulate electron diffraction patterns. Based on bright-field TEM images, we determined the catalyst particle size distributions. For each sample, a total of 450 particles have been measured. Based on dark-field TEM images, we determined the catalyst crystallite size distribution. A total of 220 crystallites that displayed strong Bragg contrast have been measured for each sample.

Model and Computational methods: We performed density functional theory (DFT) calculations with the Vienna ab initio Simulation Package (VASP) [61,62]. The core and valence electrons were treated using Blöchl's projector-augmented wave (PAW) formalism with a cutoff energy of 400 eV [63]. The nonlocal exchange and correlation energies were calculated with the Perdew-Wang (PW91) functional within generalized gradient approximation (GGA) [64,65]. For various doping structures, we performed calculations for titanium oxynitride slabs, consisting of four layers and a vacuum distance of 15Å between periodically repeated slabs. For the most stable doping structure of Ti oxynitride, we performed calculations of total energies of two, three and four layer slabs with unit cell size 2x2 and 2x3. The K-mesh points used in calculating 2x2 and 2x3 unit cells are 9x1x9 and 3x1x3, respectively. Based on the total energy per atom for different configurations as the benchmark calculations, we used the four layer slab with a 2x2 unit cell to study the stability of Ti oxynitride with various doping structures, and evaluate atomic adsorption of Pt or Ni on the surface. We used a two layer slab of oxynitride with a 2x2 unit cell to study support effects on metal layers. The electronic structures of Pt atoms are investigated by calculating the projected d-band center, ε_d, of surface Pt atoms:

$$\varepsilon_d = \frac{\sum_m \int_{-\infty}^{+\infty} \epsilon n_{l=2,m}(\varepsilon) d\varepsilon}{\sum_m \int_{-\infty}^{+\infty} n_{l=2,m}(\varepsilon) d\varepsilon} \qquad \text{Eq. 6.2}$$

where l and m are quantum numbers for angular momentum and z-projection of angular momentum; $n_{l=2,m}(\varepsilon)$, is defined as the DOS projected onto one of five localized d-orbitals.

6.3 Results and Discussion

6.3.1 Support and Catalyst Microstructure

Figure 6.2 depicts the Ti2p, O1s and N1s XPS spectra of a native-oxidized 0.5 nm TiN film. The XPS spectra of a 10 nm TiO_2 film, also synthesized by ALD at the same temperature, are included for reference (the spectra have been rescaled to a similar maximum peak intensity for comparison). Oxidation of TiN occurs when TiN surface is exposed to air at ambient, as evidenced by the Ti2p and O1s spectra. The partial coincidence of the XPS spectra of the native-oxidized TiN film with those of TiO_2 reference indicates the existence of Ti^{4+} in an octahedral coordination. The presence of Ti2p doublets at lower binding energies compared to those of TiO_2 reference indicates that Ti at lower valence states also exists. A large shoulder peak, centered at ~ 531.8 eV, is present in the O1s spectrum. Quantitative analysis of the XPS results yields a film chemical composition of 37 at.% Ti, 56 at.% O and 7 at.% N. These values will be used in the computational section for modeling the structure of the titanium oxynitride slab. Based on the above arguments, the 0.5 nm TiN coating, which will be exposed to air before catalysts deposition, can be generally described as titanium oxynitride with the notation "TiO_xN_y".

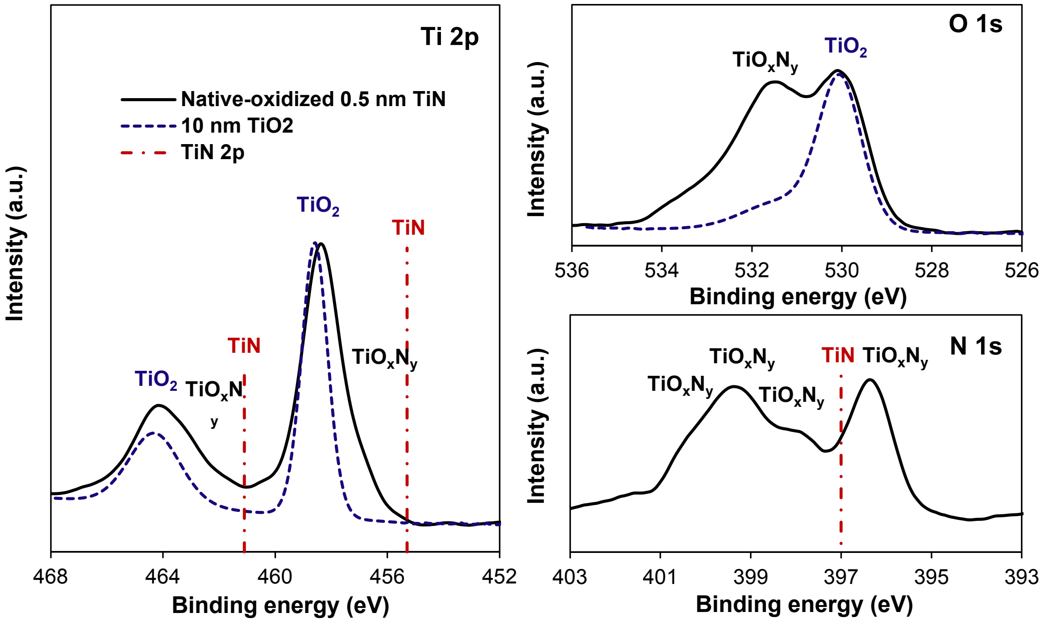

Figure 6.2: Ti2p, O1s, N1s XPS spectra of a native-oxidized 0.5 nm TiN film that was deposited on a mirror polished, plasma treated glassy carbon substrate at ALD deposition temperature of 300°C. The XPS spectra of a 10 nm TiO_2 film, synthesized at the same ALD deposition temperature, are included for reference. The results suggest that upon exposure to air at ambient the 0.5 nm TiN has entirely transformed to a chemical state that can be generally described as TiO_xN_y.

As shown in Figure 6.3A the Pt $4f_{7/2}$ XPS spectrum of Pt(0.02mg)/TiO_xN_y/CNTs shifts to higher binding energies as compared to that of Pt(0.02mg)/CNTs baseline. This is a direct evidence of chemical interaction at the TiO_xN_y-Pt interface. According to the works of Wakisaka et al. [66,67], the positive core level (CL) shift indicates a downshift in d-band center with respect to the Fermi level. From the XPS results of the high mass loaded Pt sample, shown in Figure 6.3B, the Pt $4f_{7/2}$ CL of Pt(0.15mg)/TiO_xN_y/CNTs remains identical as compared to that of Pt(0.15mg)/CNTs. This indicates that at higher mass loading (i.e. higher catalyst thickness) the Pt electronic structure away from the metal-support interface is relaxed to its equilibrium electronic state. The electronic structure of Pt near the oxynitride interface is very likely to still be affected. This is however would not be detected by XPS, which samples the Pt at and near its vacuum terminating surface. In the high Pt mass loaded samples the oxynitride-induced electronic structure modification effects would not be manifested in the ORR activity results (ORR is of course a surface process). However they still would show up in the durability test performance if considerable Pt corrosion occurs at the Pt-support interface. As Figures 6.3A and B demonstrate, the presence of the oxynitride underlayer does not influence the electronic structure of PtNi at either loading. This will be discussed later in the manuscript. The d-band center of PtNi turns out to be lower than that of pure Pt. This is supported by the measured positive Pt $4f_{7/2}$ CL shift of PtNi relative to Pt.

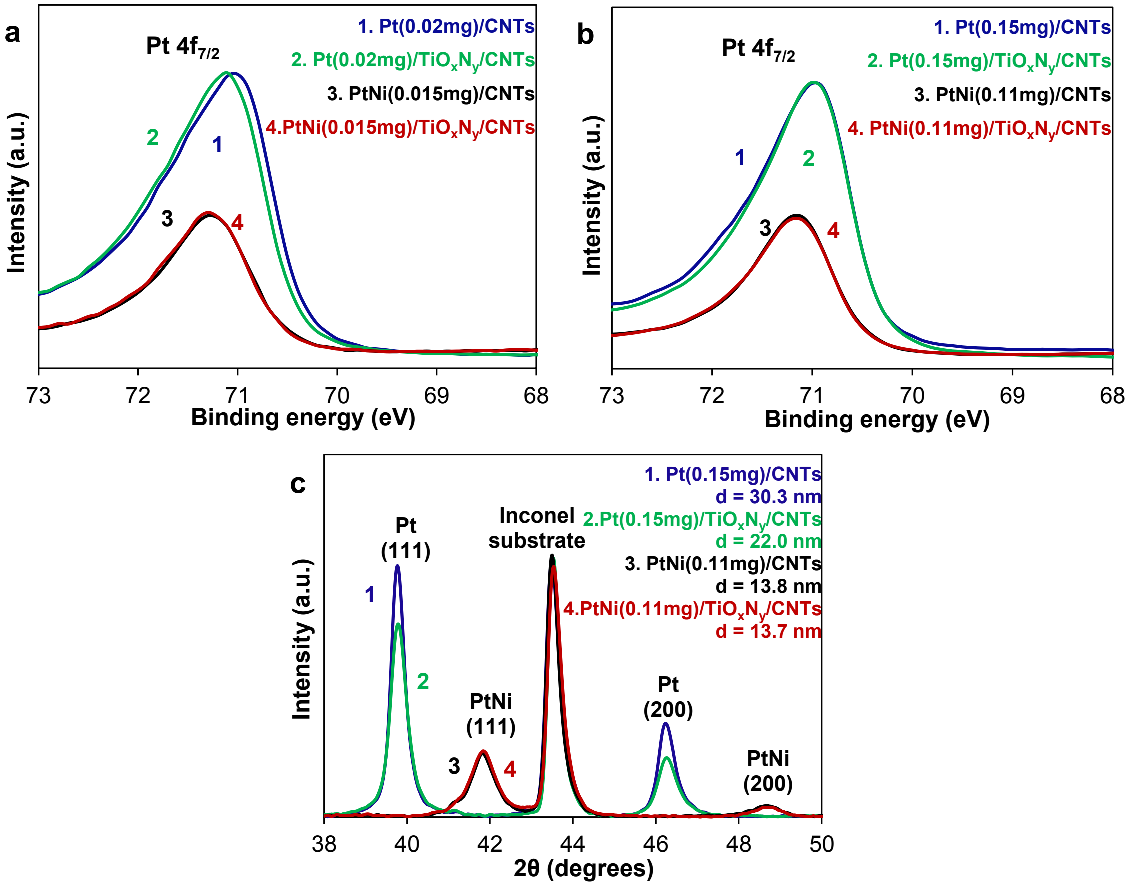

Figure 6.3: Pt $4f_{7/2}$ XPS spectra of as-synthesized Pt/CNTs, Pt/TiO_xN_y/CNTs, PtNi/CNTs and PtNi/TiO_xN_y/CNTs for (a) the low and (b) the high mass loaded samples. (c) X-ray diffraction patterns of high mass loaded samples, with the mean crystallite diameters estimated using the Scherrer equation.

X-ray diffraction patterns of the high mass loaded samples are shown in Figure 6.3C (the low mass loaded samples were too thin to be accurately analyzed by XRD). The pattern confirms the formation of PtNi alloy with a face-centered cubic (fcc) lattice. From the positions of (111) and (200) reflections, a lattice parameter of 3.73 Å is obtained for PtNi. This value obeys quite well to Vegard's law, representing a 4.8% contraction in lattice parameter compared to pure Pt. The results of the Scherrer analysis demonstrate that the TiO_xN_y refines the crystallite size of Pt catalysts. The mean crystallite diameter of Pt decreases from 30.3 nm in the case of Pt(0.15mg)/CNTs to 22.0 nm in the case of Pt(0.15mg)/TiO_xN_y/CNTs. On the other hand, the TiO_xN_y support has negligible influence on the crystallite size of PtNi alloy catalyst, with the mean crystallite diameters of PtNi alloy being 13.8 nm and 13.7 nm for PtNi(0.11mg)/CNTs and PtNi(0.11mg)/TiO_xN_y/CNTs, respectively.

Figures 6.4A-H show representative TEM and SEM micrographs of Pt(0.02mg)/CNTs and Pt(0.02mg)/TiO_xN_y/CNTs. The results of TEM and SEM analyses provide valuable information regarding the morphology and distribution of the wetted catalyst particles. At the low mass loading, rather than continuous film, the pure Pt particles are isolated or only partially interconnected. In the case of Pt on a bare CNT support, the microstructure consists of a bimodal size distribution of Pt particles. Some of the crystallites, such as those imaged in Figure 6.4A, are approximately 50 nm in width, while others are on the order of only several nanometers. The bimodal Pt particle size distribution is quantified in Figure 6.4K, which is statistically determined from multiple bright-field TEM micrographs. For Pt(0.02mg)/CNTs, the ratio N_I/N_{II} is taken to indicate the ratio of the number of particles found in the distribution I (mean diameter = 6.7 nm) versus in distribution II (mean diameter = 26.9 nm). Figure 6.4M shows the mean Pt crystallite size that is statistically determined from multiple dark-field TEM micrographs. Since the particle size results in distribution II yield sufficiently larger values than the crystallite sizes, it may be concluded that many of the larger Pt particles are in-fact polycrystalline. The CNT shown in Figure 6.4A appears to receive higher Pt catalyst loading near its “top” than near its “bottom”. Such a microstructure may be expected due to the directional non-conformal nature of the sputter flux.

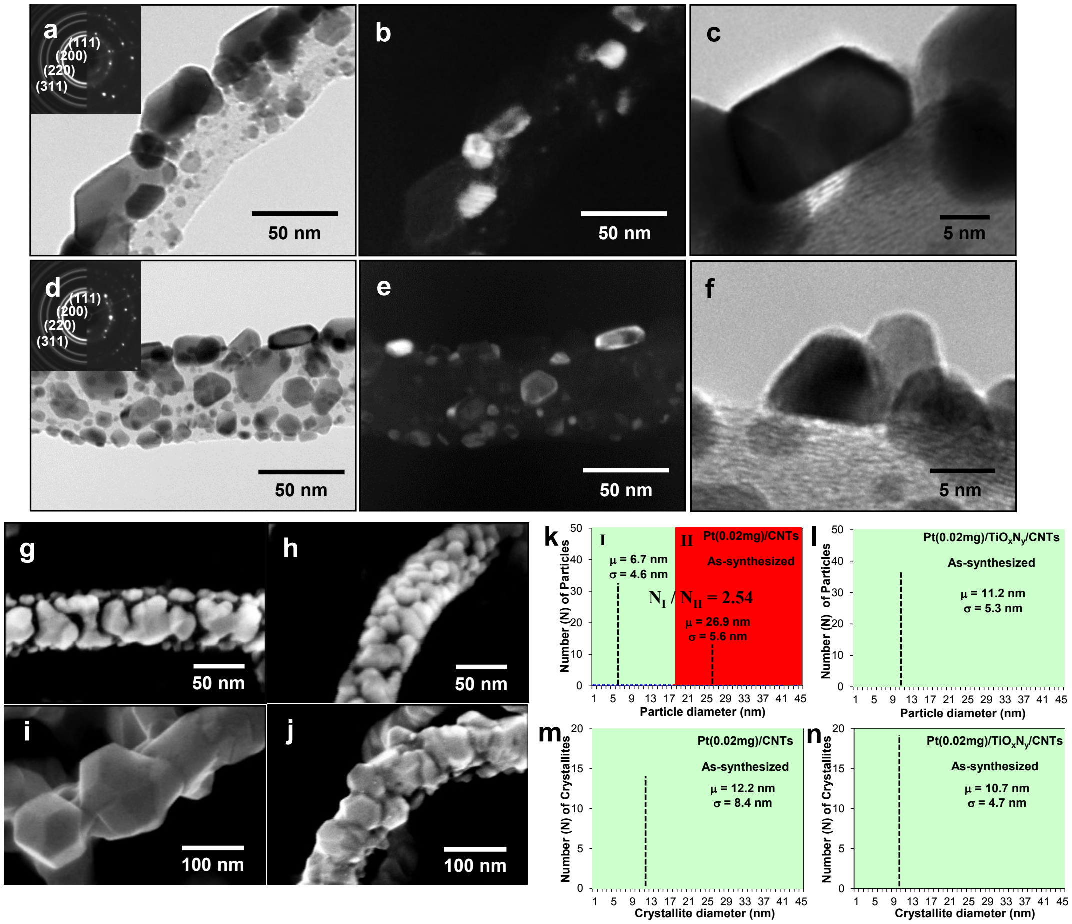

Figure 6.4: TEM analysis of as-synthesized (a)-(c) Pt(0.02mg)/CNTs, and (d)-(f) Pt(0.02mg)/TiO_xN_y/CNTs. SEM analysis of as-synthesized (g) Pt(0.02mg)/CNTs, (h) Pt(0.02mg)/TiO_xN_y/CNT, (i) Pt(0.15mg)/CNTs, and (j) Pt(0.15mg)/TiO_xN_y/CNTs. (k)-(l) The Pt particle size distributions and (m)-(n) the Pt crystallite size distributions for Pt(0.02mg)/CNTs and Pt(0.02mg)/TiO_xN_y/CNTs. In each distribution the symbol μ denotes the mean Pt particle or crystallite diameter and σ denotes the associated standard deviation.

The TiO_xN_y support appears to have a profound influence on the size and the spatial distribution of the pure Pt particles/crystallites. As shown in Figure 6.4L, the Pt particle size distribution in Pt(0.02mg)/TiO_xN_y/CNTs is both narrower and monomodal, being centered at 11.2 nm. A TiO_xN_y induced refinement of Pt crystallite size is also observed at low mass loading. The mean Pt crystallite diameter decreases from 12.2 nm for Pt(0.02mg)/CNTs to 10.7 nm for Pt(0.02mg)/TiO_xN_y/CNTs (Figure 6.4N). Thus, despite being identically sputtered, the Pt crystallites on the oxynitride are much more uniformly spread out than they are on the bare CNT surface. One could hypothesize that the wide size distribution of the Pt on CNTs is a direct manifestation of surface Oswald ripening. Pt atomic diffusion, which is the essential processes that allows optimally oriented particles to grow at the expense of ones with higher surface energy, will occur more rapidly on the chemically inert CNT surface versus on the TiO_xN_y surface, the latter being shown by XPS to have a strong interaction with the Pt. Alternatively or in parallel, for the case of uncoated CNTs the Pt crystallites may preferentially form and grow on the intrinsic tube defects and any remaining heteroatom moieties. Were such defects to be irregularly distributed on the CNT surfaces, a patchy template of Pt surface anchoring sites would result. Conversely the TiO_xN_y interlayer provides a uniform chemically active environment for Pt crystallite nucleation, refining the size distribution and decreasing the average interparticle spacing. Considering that competitive van der Drift type crystallite growth occurs during film deposition [68], a higher density of Pt nuclei on TiO_xN_y surface would lead to earlier impingement of the growing grains. This results in smaller Pt crystallites for Pt(0.15mg)/TiO_xN_y/CNTs relative to Pt(0.15mg)/CNTs, which is consistent with the results of Scherrer analysis (Figure 6.3C) and the SEM analysis of high mass loaded samples shown in Figure 6.4I and J.

Figures 6.5A-H show representative TEM and SEM micrographs of PtNi(0.015mg)/CNTs and PtNi(0.015mg)/TiO_xN_y/CNTs. The representative SEM micrographs of high mass loaded PtNi samples are shown in Figure 6.5I-J. The PtNi particles appear to wet both CNTs and TiO_xN_y surfaces quite well. This is highlighted by the HRTEM micrographs of typical CNTs-PtNi and TiO_xN_y-PtNi interfaces (see Figure 6.5C and F), respectively, where PtNi crystallites form a uniform and continuous layer on the support surface. Overall, the TiO_xN_y interlayer has negligible influence on the morphology and distribution of the PtNi alloy catalyst particles. In the modeling section of this manuscript we will discuss the potential reasons for the morphological similarity of the PtNi catalysts on either support. With a stronger interactions at the support-catalyst interface, one would expect less microstructural coarsening, i.e. smaller crystallite size of PtNi alloy catalyst, due to lower surface diffusion. However, the continuous nature of the PtNi film promotes the formation of large crystallite domains in-plane of the support surface during high temperature film growth. Some crystallite, such as those imaged in Figure 6.5B and E, are 20 ~ 30 nm in width. As shown in Figure 6.5K and L, the mean

PtNi crystallite diameters, based on dark-field TEM analysis, are 12.5 nm and 13.0 nm for PtNi(0.015mg)/CNTs and PtNi(0.015mg)/TiO_xN_y/CNTs, respectively.

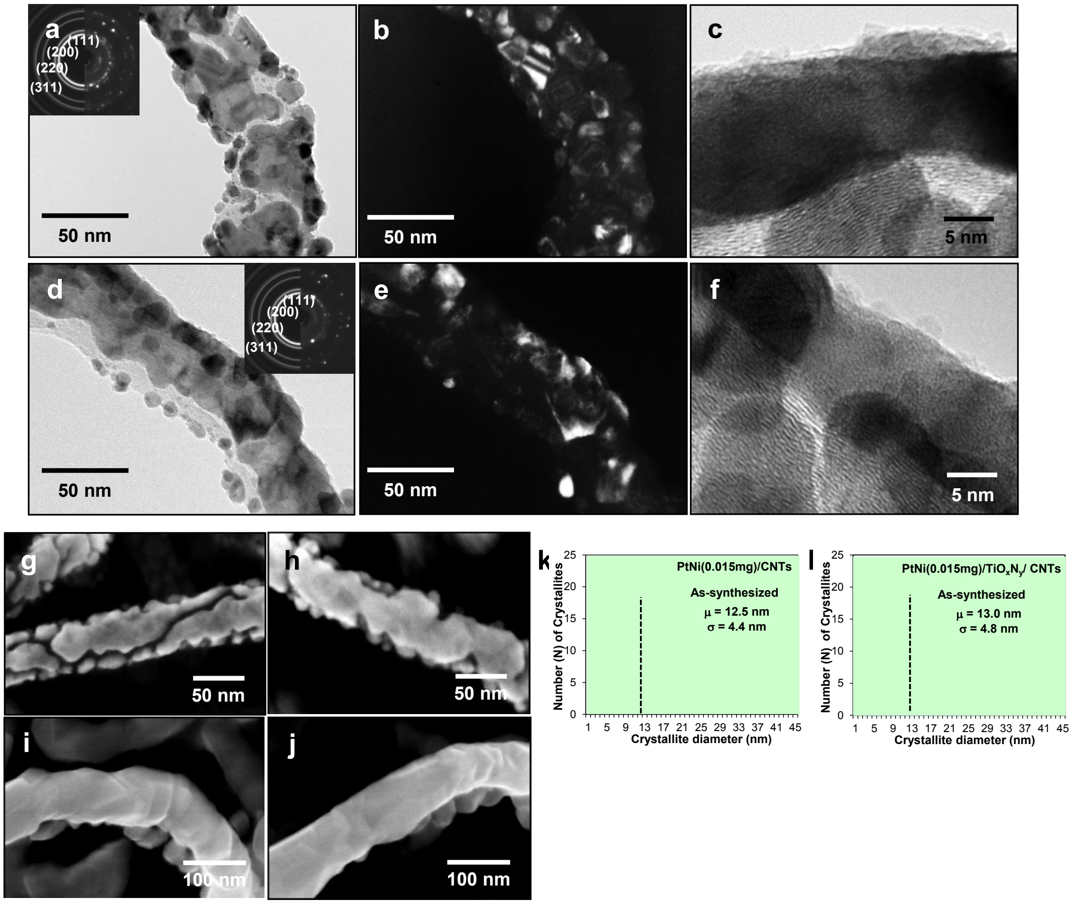

Figure 6.5: TEM analysis of as-synthesized (a)-(c) PtNi(0.015mg)/CNTs, and (d)-(f) PtNi(0.015mg)/TiO_xN_y/CNTs. SEM analysis of as-synthesized (g) PtNi(0.015mg)/CNTs, (h) PtNi(0.015mg)/TiO_xN_y/CNTs, (i) PtNi(0.11mg)/CNTs, and (j) PtNi(0.11mg)/TiO_xN_y/CNTs. (k)-(l) The PtNi crystallite size distributions for PtNi(0.015mg)/CNTs and PtNi(0.015mg)/TiO_xN_y/CNTs.

6.3.2 Oxygen Reduction Reaction Activity

Before embarking on the description of the electrochemical performance of these materials we offer a brief clarification of the primary aim of this study: We are interested in examining the role of the oxynitride support on the performance of each catalyst system *per se*, without making broader inferences regarding the intrinsic performance of

Pt vs. PtNi. Contrasts of the intrinsic activity/stability of Pt versus PtNi have been previously published in literature [53-55]. Rather here we provide a more focused comparison of Pt on CNTs vs. Pt on TiO_xN_y, with the catalyst mass loading in each case being held identical. Specifically, we compare the electrochemical performance of Pt(0.02mg)/CNTs vs. Pt(0.02mg)/TiO_xN_y/CNTs, or Pt(0.15mg)/CNTs vs. Pt(0.15mg)/TiO_xN_y/CNTs. Such independent evaluations on support effect, concerning both low and high mass loading electrodes, allow us to qualitatively deconvolve the role of the oxynitride interlayer. We do the same thing for PtNi on CNTs vs. PtNi on TiO_xN_y, i.e. comparison of PtNi(0.015mg)/CNTs vs. PtNi(0.015mg)/TiO_xN_y/CNTs, or PtNi(0.11mg)/CNTs vs. PtNi(0.11mg)/TiO_xN_y/CNTs. One cannot directly compare the activity or the durability of Pt to PtNi both due to the differences in the Pt mass loadings, and due to the differences in the particle/crystallite sizes and distributions documented in the previous section. The initial particle/crystallite size has been experimentally and theoretically demonstrated to profoundly affect the activity and the durability of Pt ORR catalysts [69-71]. Moreover during electrochemical cycling the PtNi system is expected to undergo dealloying, which will drive very different geometrical evolution in the remaining crystallites as compared to pure catalyst tested identically [72]. As the TiO_xN_y is demonstrated to have a major influence on the geometry of pure Pt and little influence on PtNi, our discussion of the resulting electrochemical properties incorporates these essential size/distribution considerations.

Cyclic Voltammetry (CV) and rotating-disk electrode (RDE) Linear Sweep Voltammetry (LSV) were used to investigate the electrochemical performance of the electrodes. Figure 6.6A and B compares the CV profiles for Pt/CNTs, Pt/TiO_xN_y/CNTs, PtNi/CNTs and PtNi/TiO_xN_y/CNTs. These CV tests were performed in argon-saturated 0.1M $HClO_4$ using a scan rate of 50 mV s^{-1}. For both low and high mass loading there is a clear difference in the shape of the hydrogen adsorption/desorption (H_{ads} and H_{des}) regions between the Pt and PtNi. While H_{upd} and H_{des} peaks at the characteristic positions associated with well-defined (110), (111) and (100) facets exposed to electrolyte [73] can be clearly discerned for pure Pt, they are not resolved for PtNi. This is a typical result for Pt-Ni alloys, which do not contain as well ordered low index crystal terminations as do pure Pt electrocatalysts [54,74-75].

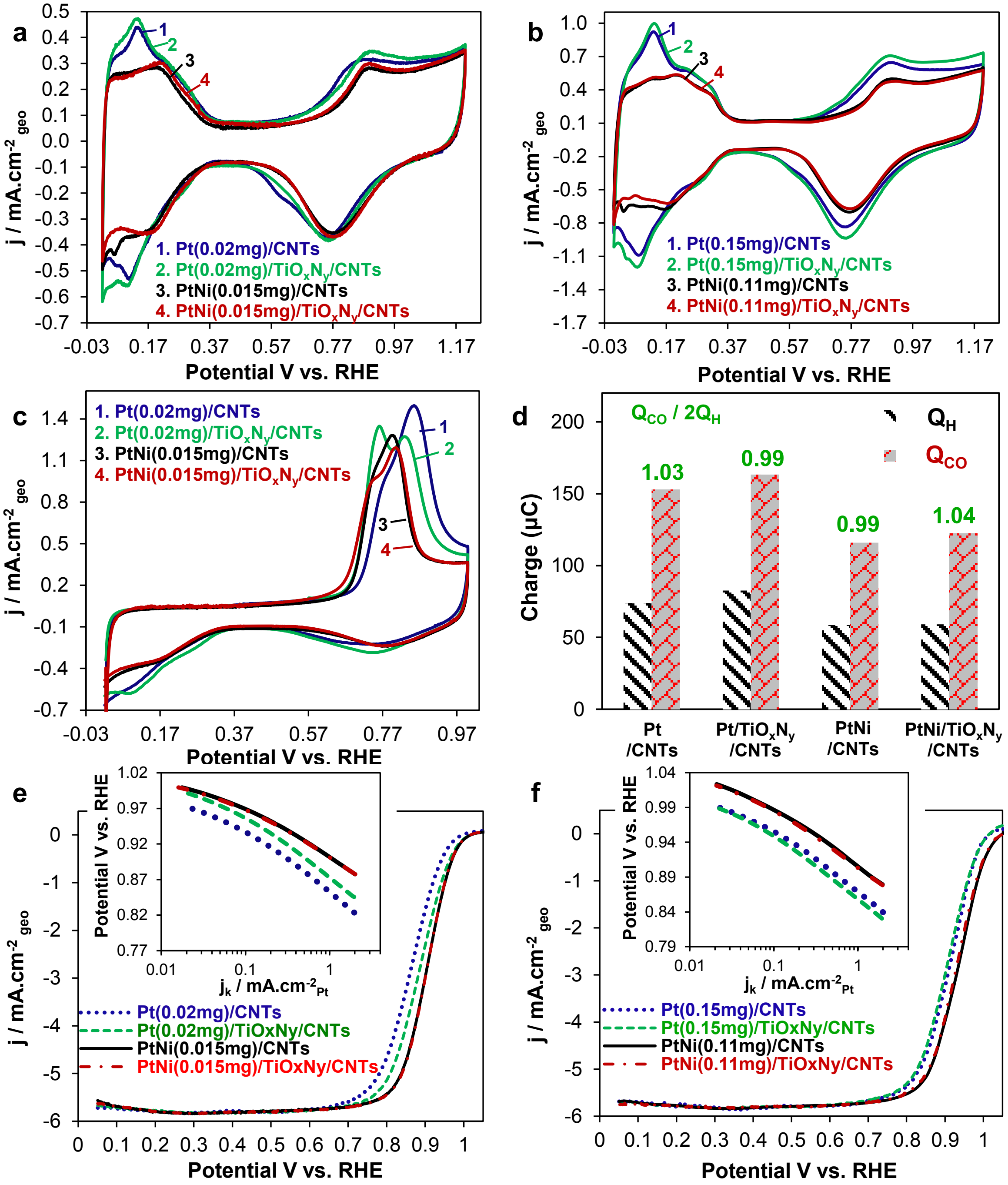

Figure 6.6: (a)-(b) CV of Pt/CNTs, Pt/TiO_xN_y/CNTs, PtNi/CNTs and PtNi/TiO_xN_y/CNTs in argon-saturated 0.1M $HClO_4$ using scan rate of 50 mV s^{-1} (c) CO-stripping curves on low mass loaded samples. (d) Integral charges for H_{upd} (Q_H) and CO stripping (Q_{CO}) obtained from CV of low mass loaded samples; the ratio of Q_{CO} / $2Q_H$ is labeled above the histogram bars. (e)-(f) Master plots comparing ORR polarization curves at 1600 rpm in oxygen-saturated 0.1M $HClO_4$ using scan rate of 10 mV s^{-1}. Inserts show the corresponding Tafel plots.

We estimated the electrochemical surface area (ECSA) by both integral charges of underpotentially deposited hydrogen (Q_H) and CO electro-oxidation (Q_{CO}). Figure 6.6C shows the CO stripping curves for the low mass loaded samples, using a scan rate of 50 mV s^{-1}. There is no discrepancy between the ECSA estimations based on H_{upd} and CO stripping, as the ratio between Q_{CO} and $2Q_H$ remains at 1 for both pure Pt and PtNi alloy samples (Figure 6.6D). This result rules out the formation of a thermally segregated Pt-skin structure with its characteristic ratio of 1.5. [76] Table 6.1 provides the ECSA obtained from H_{upd}. For pure Pt, the incorporation of the TiO_xN_y interlayer led to a minor increase of the Pt ECSA in comparison to the baseline. For the low Pt mass loaded samples the ECSA increased from 7 to 7.5 cm^2, i.e. 7%; for the high mass loading the increase was from 15.7 to 17 cm^2, i.e. 8%. In the case of PtNi the effect of TiO_xN_y on ECSA was very minor: For the low mass loaded PtNi samples the ECSA increased from 5.8 to 6 cm^2, while for the high mass loading there was a decrease from 11.2 to 10.9 cm^2. The reduction of ECSA going from Pt to PtNi is roughly in accordance with the alloy composition present at the surface, as underpotentially deposited hydrogen is known not adsorb on Ni atoms [77].

Table 6.1: Electrochemical surface area (ECSA), ORR half-wave potentials ($E_{1/2}$), specific activities and Pt mass activities at 0.9 V for Pt/CNTs, Pt/TiO_xN_y/CNTs, PtNi/CNTs and PtNi/TiO_xN_y/CNTs in the precycling state.

Precycling Sample	ECSA cm^2	 $m^2.g^{-1}_{Pt}$	$E_{1/2}$ V	Specific activity (0.9V) $mA.cm^{-2}_{Pt}$	Mass activity (0.9V) $A.mg_{Pt}^{-1}$
Pt(0.02mg)/CNTs	7.0	34.9	0.861	0.314	0.110
Pt(0.02mg)/TiO_xN_y/CNTs	7.5	37.3	0.884	0.522	0.195
Pt(0.15mg)/CNTs	15.7	10.4	0.910	0.474	0.050
Pt(0.15mg)/TiO_xN_y/CNTs	17.0	11.3	0.903	0.371	0.042
PtNi(0.015mg)/CNTs	5.8	50.3	0.902	1.068	0.543
PtNi(0.015mg)/TiO_xN_y/CNTs	6.0	51.6	0.903	1.057	0.550
PtNi(0.11mg)/CNTs	11.2	13.2	0.933	1.154	0.153
PtNi(0.11mg)/TiO_xN_y/CNTs	10.9	12.8	0.928	1.097	0.141

Figures 6.6E and F provide the master plots of ORR polarization curves at 1600 rpm, for the low mass loaded and the high mass loaded samples, respectively. The initial ORR activities of both electrocatalysts, at both mass loadings, are quite good. This is indicated

by their high onset potentials of oxygen reduction (ca. ~ 1.0 V) as well as the high half-wave potentials ($E_{1/2}$). The RDE data was further analyzed with the Koutecky-Levich (K-L) approach to extract the kinetic currents from the polarization curves. The Tafel plots, shown in the inserts, highlight the specific activities at different electrode potentials. The K-L plots for each sample with the corresponding ORR curves at different rotation speeds (tested between 400 to 3600 rpm) are shown in Figure 6.7. For all investigated systems, the number of electrons transferred (n) per O_2 molecule calculated from the slope of K-L plot supports the 4-electron pathway of oxygen reduction. Table 6.1 provides the list of the $E_{1/2}$, specific and mass activities for all samples.

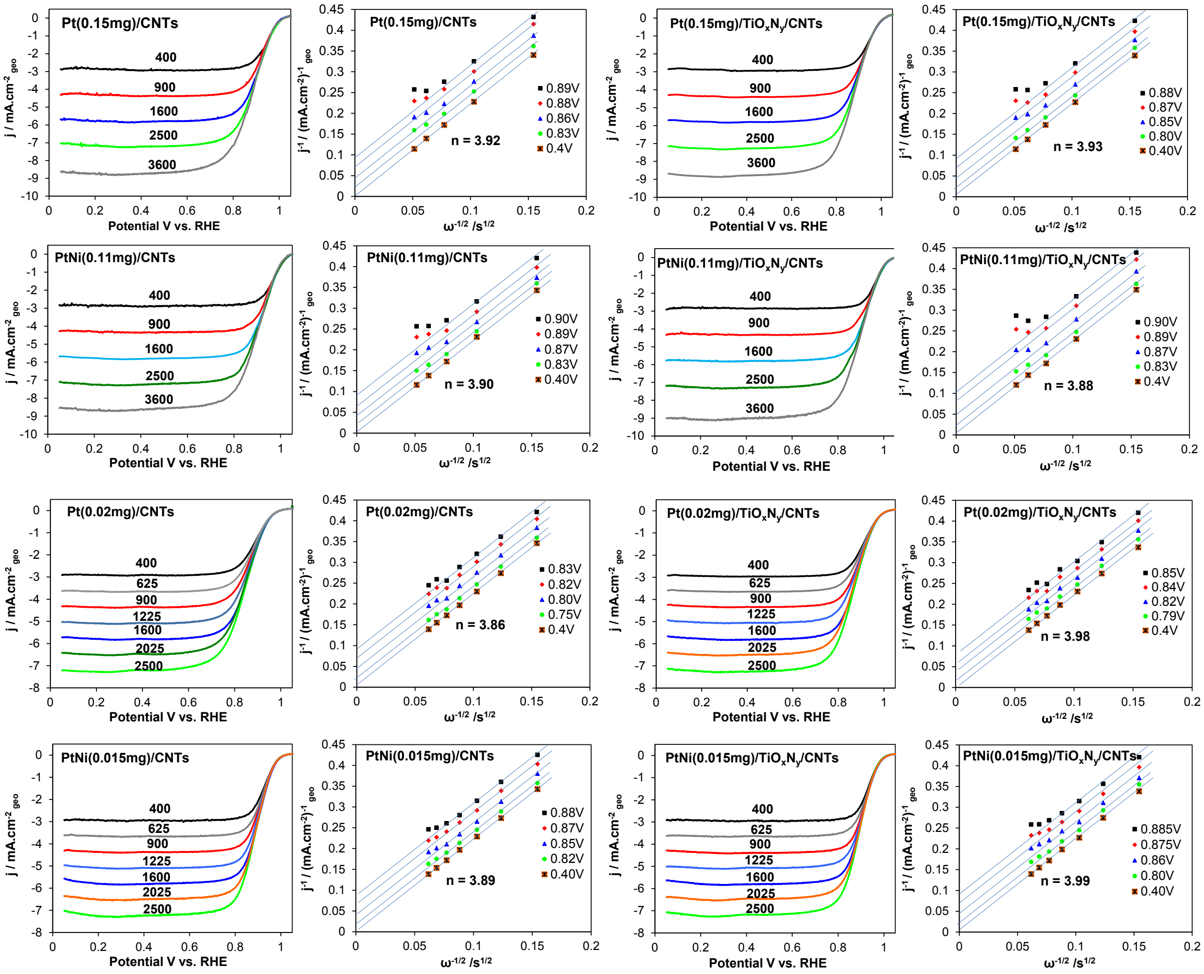

Figure 6.7: Rotating disk electrode (RDE) measurements of the oxygen reduction reaction (ORR) for different electrocatalysts in a 0.1M $HClO_4$ solution saturated with O_2 at different rotation speeds. Scan rate = 10 mV s^{-1}. Electrode Area = 1 cm^2.

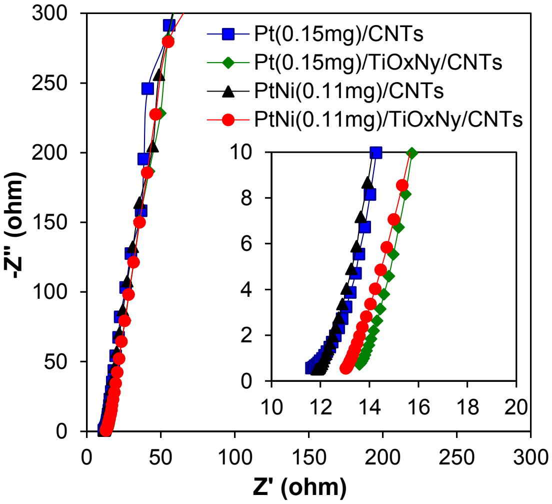

Figure 6.8: Nyquist plots of Pt(0.15mg)/CNTs, Pt(0.15mg)/TiO_xN_y/CNTs, PtNi(0.11mg)/CNTs and PtNi(0.11mg)/TiO_xN_y/CNTs

Figure 6.8 presents the results of electrochemical impedance spectroscopy (EIS) measurements for high mass loaded samples. From the real component value of the impedance at the minimum of Nyquist plot, the overall resistance of the system can be obtained. Both the electrode resistance and the solution resistance can influence the measured value of overall resistance. Since exact the same electrolyte has been used among all samples, with the distance between working and counter electrodes being kept similar, the measured changes in overall resistance provide information regarding the possibly increased ohmic resistance incurred with the insertion of TiO_xN_y layer. As shown for both pure Pt and PtNi samples, the overall resistance has increased by ~ 1.5 ohms when TiO_xN_y interlayer has been inserted. Considering the results of XPS, there is negligible change in the electronic structure near the surface of the catalyst for the high mass loaded Pt samples. We would therefore expect that the activity of Pt(0.15mg)/TiO_xN_y/CNTs to be worsened relative to the baseline Pt(0.15mg)/CNTs, due to additional electrical resistance of the oxynitride. Since the increase in electrical resistance is low with the oxynitride interlayer being atomically thin, it is expected that this detriment would be quite minor. This is exactly what was observed, with cathodic shift in the half wave potential (0.910 to 0.903 V), and a drop in the specific (0.474 to 0.371 $mA.cm^{-2}{}_{Pt}$) and mass activity (0.050 to 0.042 $A.mg_{Pt}{}^{-1}$) all being relatively small. Additionally, we applied the iR-correction to ORR data of samples with the high mass loading. By compensating for the ohmic losses, the TiO_xN_y-supported samples show comparable ORR activity relative to the CNTs-supported counterpart (see Table 6.2).

Table 6.2: Electrochemical surface area (ECSA), and iR-corrected ORR half-wave potentials, specific activities and Pt mass activities at 0.9 V and 0.95 V for high mass loading Pt/CNTs, $Pt/TiO_xN_y/CNTs$, PtNi/CNTs, and $PtNi/TiO_xN_y/CNTs$.

Precycling Sample	ECSA (cm^2)	Half-wave potential (V)	Specific activity (0.9V) ($mA.cm^{-2}{}_{Pt}$)	Mass activity (0.9V) ($A.mg_{Pt}{}^{-1}$)	Specific activity (0.95V) ($mA.cm^{-2}{}_{Pt}$)	Mass activity (0.95V) ($A.mg_{Pt}{}^{-1}$)
Pt(0.15mg)/CNTs	15.7	0.941	1.717	0.179	0.211	0.022
Pt(0.15mg)/TiO_xN_y/CNTs	17.0	0.942	1.782	0.201	0.223	0.025
PtNi(0.11mg)/CNTs	11.2	0.965	5.258	0.695	0.952	0.126
PtNi(0.11mg)/TiO_xN_y/CNTs	10.9	0.963	5.371	0.689	0.947	0.121

For the low Pt mass loading, there is a strong opposite trend: Upon the insertion of TiO_xN_y, there is an anodic shift in the half wave potential (0.861 to 0.884 V), and almost a doubling of the specific (0.314 to 0.522 $mA.cm^{-2}{}_{Pt}$) and mass activity (0.110 to 0.195 $A.mg_{Pt}{}^{-1}$). This finding differentiates our work from a recent study on wet-method synthesized Pt supported on anhydrous sol-gel synthesized TiO_xN_y, where the ORR activity was found to be lower than that of Pt/C baseline [78]. While it is likely that Pt on sol-gel TiO_xN_y also exhibited strong metal support interactions, the support's more "bulk like" thickness (particle size on the order of 50 nm) would degrade the electrical conductance relative to the C baseline. We attribute the activity improvement in our material to a direct manifestation of the favorable change in the electronic structure of the Pt surface overcoming the minute IR losses associated with the atomic scale oxynitride interlayer. A thicker interlayer would still be effective in changing the d-band structure of the Pt. However, ORR enhancement would be reduced or completely negated by the increased electrical resistance of the electrode.

It is known that there is a strong correlation between the d-band center of the metal surface and the oxygen chemisorption energy ΔE_0, which is a key parameter determining the ORR activity of a given catalyst surface [79]. The surface of Pt(0.02mg)/TiO_xN_y/CNTs sample should bind oxygen relatively weaker, given a downshifted d-band center with respect to the Fermi level. This is supported by the CV profiles shown in Figure 6.6A. Close inspection reveals that the onset of surface oxide (OH_{ad}) formation for Pt(0.02mg)/TiO_xN_y/CNTs has shifted to a higher potential relative to Pt(0.02mg)/CNTs, whereas such discernible positive potential shift is not observed for thicker Pt(0.15mg)/TiO_xN_y/CNTs sample (Figure 6.6B). The higher onset potential of surface oxide formation is indicative of lower surface coverage onto active sites by intermediate O_{ads} and OH_{ads} species [80 , 81]. As shown in Figure 6.6C, CO electrooxidation on a Pt(0.02mg)/TiO_xN_y/CNTs surface also proceeds at lower potentials than on a Pt(0.02mg)/CNTs surface. Such observation is consistent with the trend for surface oxide formation, considering CO_{ad} and OH_{ad} are competing for the same Pt adsorption sites [76].

As expected, the PtNi catalyst shows more anodic voltages and substantially higher specific and mass activities than the Pt. In fact, the measured specific activities of the four PtNi samples, in the range of 1.057 to 1.154 $mA.cm^{-2}{}_{Pt}$ (see Table 6.1), all meet the 2015 DOE’s target for specific activity of 0.7 $mA.cm^{-2}{}_{Pt}$ [1]. For PtNi alloy this effect has been well documented in literature, being attributed to both geometric and electronic effects associated with the development of a "Pt skeleton" at the alloy surface [46,54,74]. The interesting finding of this study, however, is that the oxynitride seems to have very little effect on the alloy's ORR activity, except the minor activity loss due to Ohmic drop. This makes good sense, considering that neither XPS nor TEM was able to detect meaningful bonding or microstructural changes incurred by the interlayer.

Finally it is important to consider the Pt particle size effects in considering the benefits of the oxynitride support. It has been demonstrated that for sub-5 nm Pt particles, size makes a profound impact on the ORR activity and stability, influencing the oxide binding energies and actually modifying the Pt dissolution path [69-71,82-84]. For instance authors in ref. [69] observed experimentally and confirmed through modeling that both mass activity and specific activity actually decreases when Pt particle sizes fall below 2.2 nm. Our group has also recently demonstrated that the specific activity of blanket Pt films sputtered onto planar oxide supports will increase up to a film thickness of 5 nm, and will remain constant at higher thicknesses [31]. Since to a first approximation the crystallite size of a thin film grown at high homologous temperatures is directly proportional to a fraction (e.g. 0.5) of its thickness [85], the two findings are in agreement. Judging from XRD and TEM analysis, the majority of Pt and the PtNi crystallites are larger than 5nm (Figure 6.4K and 6.5K). A notable number of the Pt particles in both systems are indeed below 2.5 nm, with their relative fraction being higher for Pt(0.02mg)/CNTs than for Pt(0.02mg)/TiO_xN_y/CNTs. Thus another contributor to the observed enhanced activity (and stability, as is demonstrated in the next section) due the oxynitride support is a lower fraction of these less active and less stable ultrafine Pt particles. Moreover the particle size distribution in the Pt(0.02mg)/CNTs specimen is bimodal. For this material there are enough large-diameter low-surface area Pt particles (e.g. > 20 nm diameter) to significantly reduce the mass activity of the electrode. The presence of large particles would not influence the specific activity of the system as their low surface area is accounted for in the calculation. Therefore the oxynitride support also improves the mass activity of the catalyst by reducing the "dead weight" of Pt from the right side of the size distribution.

6.3.3 Electrocatalyst Durability

The catalytic durabilities of the electrocatalysts were evaluated by an accelerated test involving 10,000 cycles between 0.6 V and 1.1 V at room temperature, using a sweep rate of 50 mV s^{-1}. Figure 6.9A and B show the CV profiles and the ORR polarization curves (1600 rpm), respectively, for low mass loaded samples, measured before and after 10,000 potential cycling. The same results for high mass loaded samples are shown in Figure 6.9C and D. Table 6.3 summarizes the results of durability tests, including the change of $E_{1/2}$, the % loss in ECSA, and the % loss in specific activity and in Pt mass activity. The Pt(0.02mg)/TiO_xN_y/CNTs sample shows approximate 2-fold enhancement in catalytic durability as compared to the Pt(0.02mg)/CNTs: The specific activity, mass activity and ECSA were degraded by 20.1%, 27.8% and 9.7%, respectively, as compared to 42.7%, 57.0% and 25.0%. Similarly, enhanced catalytic durability is observed for high mass loaded pure Pt. These findings demonstrate that inserting a 0.5nm TiO_xN_y between Pt and CNTs markedly improves the corrosion stability of the Pt electrocatalyst. In the case of PtNi, the oxynitride interlayer has minimal effect on the catalyst durability at either loading. PtNi(0.015mg)/CNTs and PtNi(0.015mg)/TiO$_x$N$_y$/CNTs demonstrate almost comparable degradation, as shown by the losses of their specific activity (41.7% vs. 40.9%), mass activity (45.0% vs. 44.8%) and in ECSA (5.7% vs. 6.6%). We attribute this to a lack of meaningful changes in the catalyst's electronic structure or morphology/wetting behavior with the introduction of the oxynitride. As Figure 6.10 demonstrates, the post-cycled PtNi/TiO$_x$N$_y$/CNTs and PtNi/CNTs electrodes possess comparable overall film morphology, a similar PtNi crystallite size distribution, and an almost identical electronic structure.

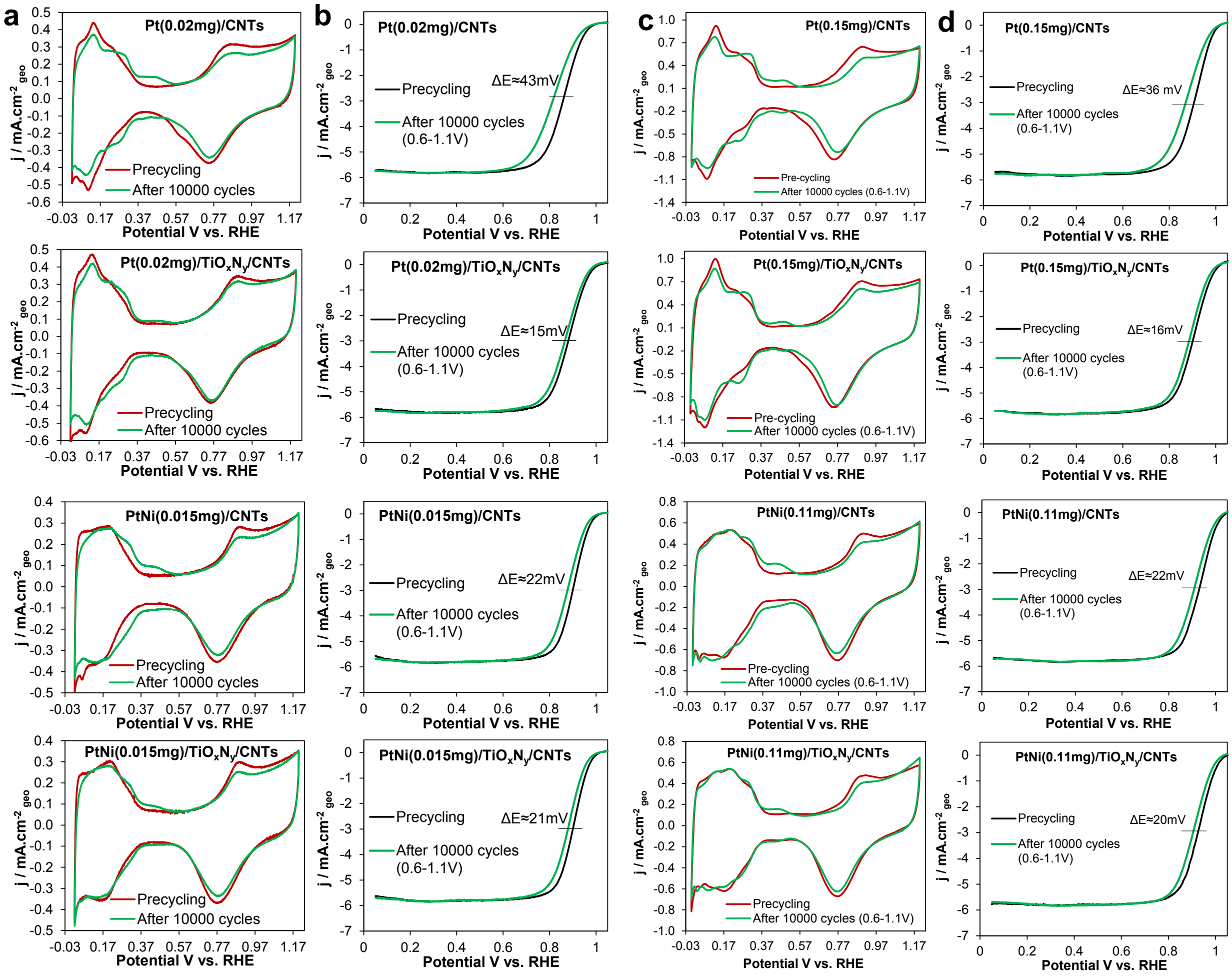

Figure 6.9: CV profiles and ORR polarization curves for (a, b) low and (c, d) high mass loaded samples, measured before and after 10,000 potential cycles between 0.6 V and 1.1 V at room temperature with a sweep rate of 50 mV s^{-1}.

Table 6.3: Comparison of the electrochemical durabilities for Pt/CNTs, Pt/TiO_xN_y/CNTs, PtNi/CNTs and PtNi/TiO_xN_y/CNTs. The durabilities were evaluated by 10000 potential cycling between 0.6 V and 1.1 V at 50 mV s^{-1}.

Sample	Change of half-wave Potential (mV)	% loss in ECSA after cycling	Specific activity ($mA.cm^{-2}{}_{Pt}$)			Mass activity ($A.mg_{Pt}{}^{-1}$)		
			Before cycling	After cycling	% loss	Before cycling	After cycling	% loss
Pt(0.02mg)/CNTs	43	-25.0%	0.314	0.180	-42.7%	0.110	0.047	-57.0%
Pt(0.02mg)/TiO_xN_y/CNTs	15	-9.7%	0.522	0.417	-20.1%	0.195	0.141	-27.8%
Pt(0.15mg)/CNTs	36	-16.2%	0.474	0.249	-47.5%	0.050	0.022	-56.0%
Pt(0.15mg)/TiO_xN_y/CNTs	16	-10.2%	0.371	0.280	-24.5%	0.042	0.028	-32.2%
PtNi(0.015mg)/CNTs	22	-5.7%	1.068	0.623	-41.7%	0.543	0.298	-45.0%
PtNi(0.015mg)/TiO_xN_y/CNTs	21	-6.6%	1.057	0.625	-40.9%	0.550	0.304	-44.8%
PtNi(0.11mg)/CNTs	22	-4.8%	1.154	0.713	-38.2%	0.153	0.090	-41.1%
PtNi(0.11mg)/TiO_xN_y/CNTs	20	-4.0%	1.097	0.676	-38.4%	0.141	0.083	-40.9%

For pure Pt, the oxynitride-induced changes in Pt electronic structure and crystallite/particle size distributions are strongly manifested in the measured corrosion stability. For Pt(0.02mg)/TiO_xN_y/CNTs, the downshift in d-band center with respect to the Fermi level indicates weaker oxide formation on the Pt surface. Assuming that Pt dissolution is an oxide-mediated process, as discussed in ref. [86,87], a reduced rate of Pt dissolution due to modified Pt electronic structure is surely one factor contributing to the lower catalytic loss. The TiO_xN_y support appears to be equally effective in enhancing the corrosion stability of both the low and the high mass loaded samples. This is fundamentally different from what we observed for the ORR activity data, and was initially unexpected since XPS showed no changes in the electronic structure of the high mass loaded Pt catalyst near its surface. As we mentioned earlier, however, the electronic structure of Pt near the oxynitride interface is very likely to still be affected. We therefore hypothesize that Pt-support interface plays a key role in determining the durability of both the high and the low mass loaded pure Pt. The strong chemical bonding between the metal and the oxynitride could be of tremendous benefit if the Pt dissolution actually initiates at the Pt-support-electrolyte triple boundary. We believe that this may indeed be the case, though more studies would be required to firmly confirm or negate this hypothesis.

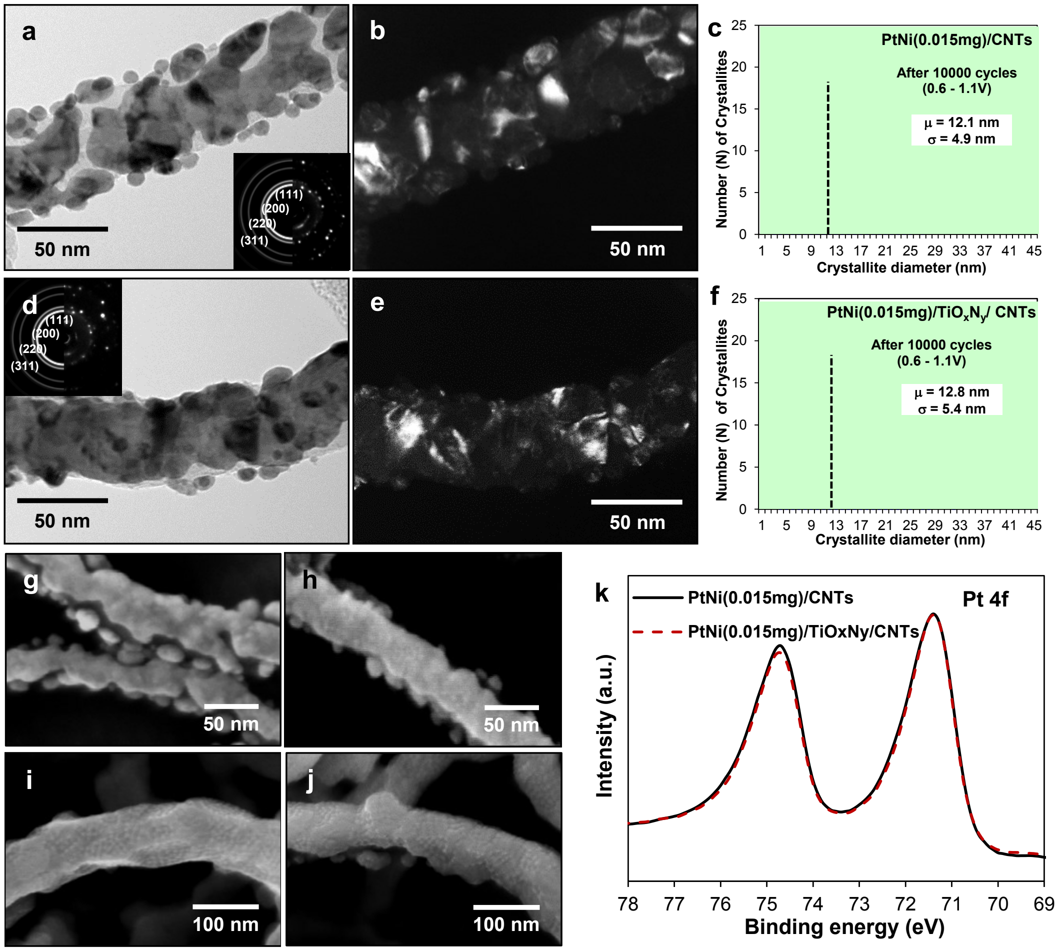

Figure 6.10: TEM analysis and the corresponding PtNi crystallite size distribution for post-cycling (a)-(c) PtNi(0.015mg)/CNTs, and (d)-(f) PtNi(0.015mg)/TiO$_x$N$_y$/CNTs, after 10,000 cycles between 0.6 V and 1.1 V at room temperature with a sweep rate of 50 mV s^{-1}. SEM analysis of post-cycling (g) PtNi(0.015mg)/CNTs, (h) PtNi(0.015mg)/TiO$_x$N$_y$/CNTs, (i) PtNi(0.11mg)/CNTs, and (j) PtNi(0.11mg)/TiO$_x$N$_y$/CNTs. (k) Pt 4f XPS spectra of post-cycling PtNi(0.015mg)/CNTs and PtNi(0.015mg)/TiO$_x$N$_y$/CNTs.

It is known that oxide mediated Pt dissolution is driven by the size-dependent surface excess energies of nanoparticles. Smaller particles, having larger surface energies, are more prone to oxidation and dissolution [86]. As Figure 6.4 demonstrated, the oxynitride interlayer strongly modifies the size distribution of Pt particles as compared to the baseline. It can be expected that a more uniform distribution of Pt particles supported on TiO$_x$N$_y$, with fewer of them being below 5 nm in diameter, would naturally lead to less Pt dissolution. This argument is supported by the results of post-cycling TEM analysis.

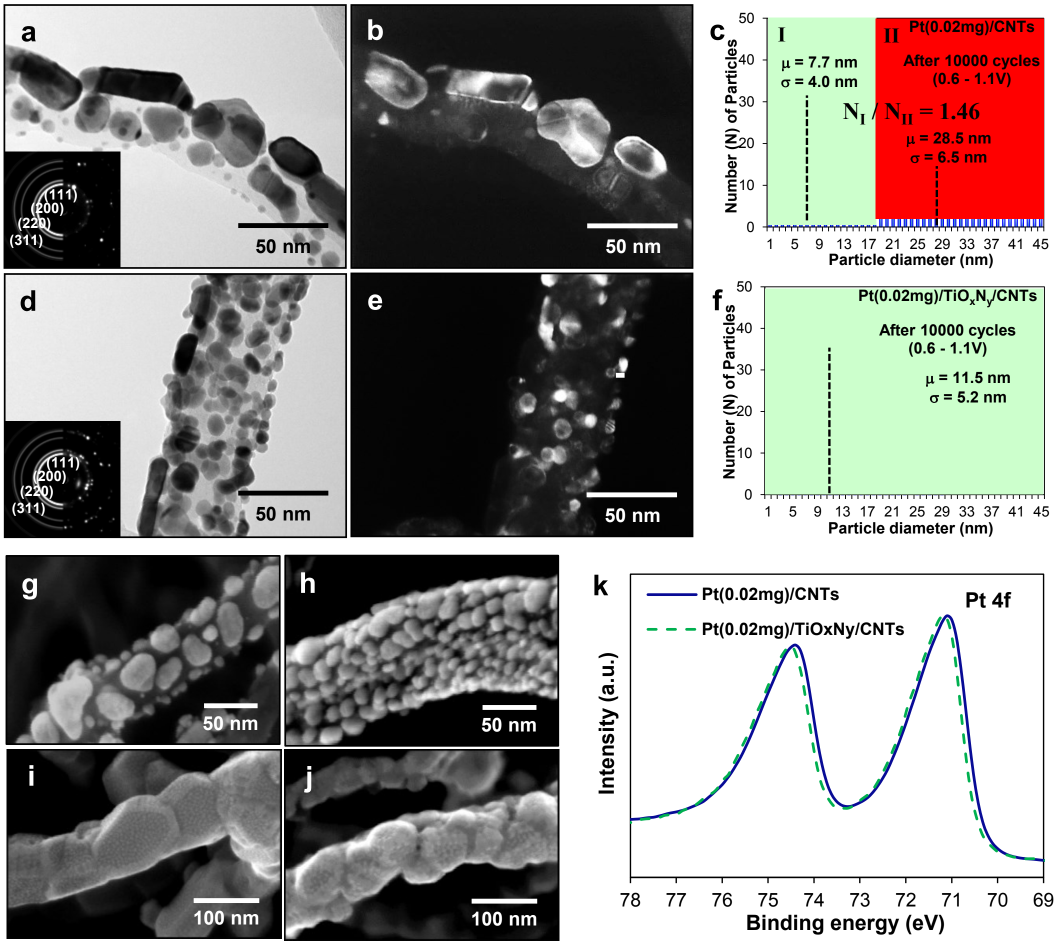

Figure 6.11: TEM analysis and the corresponding Pt particle size distribution for post-cycling (a)-(c) Pt(0.02mg)/CNTs, and (d)-(f) Pt(0.02mg)/TiO$_x$N$_y$/CNTs, after 10,000 cycles between 0.6 V and 1.1 V at room temperature with a sweep rate of 50 mV s^{-1}. SEM analysis of post-cycling (g) Pt(0.02mg)/CNTs, (h) Pt(0.02mg)/TiO$_x$N$_y$/CNTs, (i) Pt(0.15mg)/CNTs, and (j) Pt(0.15mg)/TiO$_x$N$_y$/CNTs. (k) Pt 4f XPS spectra of post-cycling Pt(0.02mg)/CNTs and Pt(0.02mg)/TiO$_x$N$_y$/CNTs.

Figure 6.11A-C and Figure 6.11D-F show representative TEM micrographs and the corresponding Pt particle size distributions for post-cycled Pt(0.02mg)/CNTs and Pt(0.02mg)/TiO$_x$N$_y$/CNTs, respectively. For CNTs-supported baseline, the bimodal size distribution of Pt particles retains after cycling. However, the ratio of the number of particles in distribution I over the number of particles in distribution II (N_I / N_{II}) decreased from 2.54 before cycling to 1.46 after cycling. A comparison with the distribution in the as-synthesized state (Figure 6.4K) demonstrates that the decrease in the number of Pt particles in distribution I is mainly due to the disappearance of the smallest of them, i.e. the ones in the sub-3 nm range. This indicates that the smaller Pt particles indeed suffer more from corrosion during the potential cycling, being preferentially dissolved into the electrolyte. It is possible that some dissolved Pt has redeposited onto the surfaces of larger particles due to electrochemical Ostwald ripening. This notion can be supported by the fact that the average particle diameters of distributions I and II have increased from 6.7 to 7.7 nm, and from 26.9 nm to 28.5 nm, respectively.

For TiO_xN_y-supported Pt sample, the originally narrower size distribution of the Pt particles is preserved after cycling, with the average particle diameter increasing negligibly from 11.2 nm to 11.5 nm. In contrast to the Pt(0.02mg)/CNTs baseline, the absence of bimodal size distribution may provide Pt(0.02mg)/TiO_xN_y/CNTs sample with further resistance to coarsening. According to Lifshitz-Slyozov-Wagner (LSW) theory, Ostwald ripening is less likely to happen for uniformly sized Pt particles [88]. Figure 6.11K shows the Pt 4f XPS spectra of low mass loaded Pt samples after 10,000 potential cycles. It is clear that the modification in the electronic structure of the Pt, introduced by the insertion of the TiO_xN_y, is retained after cycling. As any support effects must rely on the structural integrity of the support-catalyst interface, this is direct evidence that for the remaining Pt particles the TiO_xN_y-Pt interface is fully intact.

The conformal coating of a largely defect-free electrochemically stable TiO_xN_y on CNTs also isolates CNTs from the electrolyte, which prevents, or at least mitigates, the corrosion of the underlying CNTs. Comparing the CV before and after cycling (see Figure 6.9), all TiO_xN_y-coated samples exhibit smaller quinone-hydroquinone peaks (~ 0.6 V) relative to their corresponding non-TiO_xN_y-coated baselines. This highlights the beneficial additional role of the TiO_xN_y interlayer in protecting the underlying high surface area carbon support. As the Pt particles are physically dislodged from the electrode due to the corrosion of the underlying support, protecting the CNTs is also synergistic for promoting catalyst retention.

6.3.4 Computational Study

We employed DFT calculations to gain further insight regarding how the pure Pt and Pt-Ni alloy catalysts interact with the two types of supports. Overall the computational study emphasized the role of the titanium oxynitride layer. For reasons of computational viability, we made the following simplifications in model systems considered: i) Pt and PtNi particle structures are simplified as PtNi doublelayers with either homogeneous or phase-segregated configuration; ii) titanium oxynitride layers are included as two atomic layers with the nitrogen doping level similar to the experimentally measured composition; iii) the CNT support is replaced by a single layer of graphene. The experimentally measured diameter of the CNTs is quite large, being in the 50 nm - 100 nm range. While changes in the electronic structure of the carbon due to the CNT curvature may be important for much thinner CNTs (e.g. several nm's), they should not play a major role for such a coarse system.

We modeled a rutile Ti oxynitride (110) surface that is energetically most stable. A stoichiometric TiO_2 slab consists of three types of geometrically different O atoms on the (110) surface: bridging oxygen atoms above the uppermost Ti plane as labeled by O_{br}, single bonded oxygen atoms as labeled by O_s, and basal oxygen atoms at the same plane of the uppermost Ti plane as labeled by O_{ba}. These are illustrated in Figure 6.12A. We considered three different doping configurations by replacing an O_{br}, O_s, or O_{ba} atom by a nitrogen atom in each layer of the TiO_2 unit cell. After this replacement, each unit cell contains 16 Ti atoms, 28 O atoms and 4 N atoms, which represents a $TiO_{1.75}N_{0.25}$ slab, the same composition as the one determined by XPS analysis. Following the oxidation reaction of

$$Ti + \frac{x}{2}O_2 + \frac{y}{2}N_2 = TiO_xN_y \qquad \text{Eq. 6.3}$$

we calculated the formation energies of the oxynitride using [89]

$$E_f = E_{TiO_xN_y} - [\mu_{Ti} + \frac{x}{2}\mu_{O_2} + \frac{y}{2}\mu_{N_2}] \qquad \text{Eq. 6.4}$$

where E_{TiOxNy} is the total energy of a unit cell; μ_{N2} and μ_{O2} are the chemical potentials of O_2 and N_2 in vacuum, respectively. The calculated values of μ_{O2} and μ_{N2} are -9.61eV and -13.20eV, respectively. Based on the benchmark calculations, our calculations using a four-layer slab with a 2x2 unit cell provided E_f values of -14.63eV, -14.28eV and -14.65eV for $TiO_{1.75}N_{0.25}$ with N doped at O_{br}, O_s, and O_{ba} positions, respectively. Doping N at the O_{ba} position results in a structure with the most negative formation energy. This structure after geometric optimization is shown in Figure 6.12B.

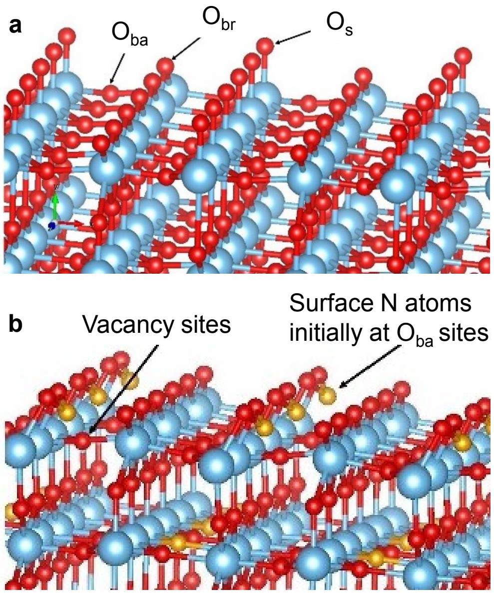

Figure 6.12: Optimized geometric structure of (a) TiO_2 and (b) $TiO_{1.75}N_{0.25}$ with N doping on O_{ba} sites. Blue, red and yellow balls denote Ti, O and N atoms, respectively.

In the ground state, surface nitrogen atoms initially occupying O_{ba} sites form bonds with two O_s atoms and create a vacancy sites at the O_{ba} plane. Such surface reconstruction is consistent with the results reported in literature [90,91]. On the stoichiometric surface of TiO_2, each Ti atom at the uppermost layer is coordinated with 6 O atoms. Each Ti atom possesses a charge of $2.5e_0$ while each O_s atom possessing a charge of $-0.8e_0$. After N-doping at the O_{ba} position, each Ti atom at the uppermost layer loses a Ti-O bond due to N-O bond formation. Each Ti atom now possesses a charge of $2.6e_0$ while each O_s atom possessing a charge of $-0.6e_0$. Comparing to the TiO_2 surface, O_s atoms in $TiO_{1.75}N_{0.25}$ exhibit higher electron affinity due to a reduced amount of electronic charge. This favors the adsorption of metal atoms on the surface of $TiO_{1.75}N_{0.25}$, considering the bond formation between metal atoms and surface oxygen atoms being accompanied by electronic charge transfer from metal atoms to surface oxygen atoms.

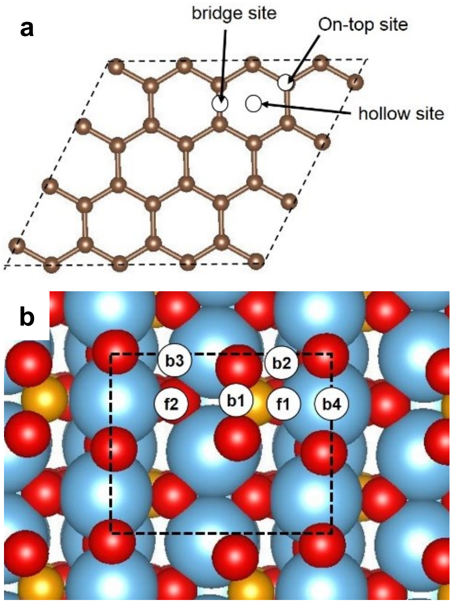

Figure 6.13: High symmetry adsorption sites on (a) graphene and (b) rutile $TiO_{1.75}N_{0.25}$ (110) surface. Black dashed line shows the boundary of the unit cell.

Before working with the relatively complex doublelayers, we examined the case for adsorption of single Pt and Ni atoms on the supports. Figure 6.13 illustrates the high symmetry adsorption sites on graphene and $TiO_{1.75}N_{0.25}$ (110) surface. As shown in Figure 6.13A, three high symmetry adsorption sites are distinguished on the graphene surface. They are the bridge site of two carbon atoms, the site on top of carbon atoms, and the hollow site at the center of carbon hexagon. As shown in Figure 6.13B, six high symmetry adsorption sites are distinguished on the (110) surface of $TiO_{1.75}N_{0.25}$ within one unit cell. b1 is the bridge site formed by two O_s atoms; b2 is the bridge site of O_{br} and O_s atoms that have a row of doped N atoms in between; b3 is the bridge site of O_{br} and O_s atoms that has no doped N atoms in between; b4 is the bridge site of two O_{br} atoms; f1 and f2 are both four fold site of two O_{br} and two O_s atoms, with f1 being closer to the N atoms than f2. For a specific adsorption site, we calculated the adsorption energy, E_{ad}, of a single Pt or Ni atom, by

$$E_{ad} = E_{Msub} - E_{sub} - \mu_M \qquad \text{Eq. 6.5}$$

where E_{Msub}, E_{sub} and μ_M are the energy of the system with adsorbed metal, the energy of the bare support and the chemical potential of the metal atom in vacuum, respectively.

Table 6.4: Calculated E_{ad} (eV per metal atom) values for a single Pt or Ni atom adsorbed at various high symmetry surface sites of graphene and $TiO_{1.75}N_{0.25}$ (110).

	E_{ad} (eV) Pt/graphene	E_{ad} (eV) Ni/graphene		E_{ad} (eV) Pt/$TiO_{1.75}N_{0.25}$	E_{ad} (eV) Ni/$TiO_{1.75}N_{0.25}$
bridge	-1.43	-0.93	b1	-0.97	-2.15
			b2	-1.67	-1.25
on-top	-1.26	-0.86	b3	-1.75	-1.27
			b4	-0.86	-1.73
hollow	-0.76	-1.26	f1	-1.37	-3.01
			f2	-2.11	-3.47

Table 6.4 lists the calculated E_{ad} values for a single Pt or Ni atom adsorbed at various surface sites of graphene and $TiO_{1.75}N_{0.25}$ (110). On graphene, E_{ad} values of Pt vs. Ni vary with the specific adsorption sites. At the bridge and the on-top sites, the adsorption of Pt is energetically more stable than the adsorption of Ni, given the E_{ad} values of Pt vs. Ni being -1.43 vs. -0.93 eV and -1.26 vs. -0.86 eV, respectively. At the hollow sites, the adsorption of Ni on the other hand becomes energetically more stable than Pt. The E_{ad} values of Pt vs. Ni are now -0.76 vs. -1.26 eV. Based on the calculated E_{ad} values, the bridge site is the most favorable surface site for Pt, while the hollow site is the most favorable one for Ni. These results of adsorption on graphene compare well with those in reference [92]. On $TiO_{1.75}N_{0.25}$, the E_{ad} values of Ni are generally more negative than those of Pt. At the surface sites of b1, b4, f1 and f2, the E_{ad} values of Pt vs. Ni are -0.97 vs. -2.15 eV, -0.86 vs. -1.73 eV, -1.37 vs. -3.01 eV and -2.11 vs. -3.47 eV, respectively. The stronger interaction between Ni atoms and the $TiO_{1.75}N_{0.25}$ surface implies that upon deposition of PtNi alloy, Ni atoms may segregate towards the $TiO_{1.75}N_{0.25}$ surface. Based on the calculated E_{ad} values, the f2 site is the most favorable surface adsorption site for both Pt and Ni atoms. In addition, it has been proposed that the formation of surface defects on TiO_2 is an important factor responsible for the strong metal-support interaction SMSI [93]. Therefore, we also calculated E_{ad} for Pt or Ni atom, inserted at the vacancy sites in the O_{ba} plane. After geometric optimization, E_{ad} for Pt and Ni atoms in the vacancy sites are +0.21 eV and -4.54 eV, respectively. The positive value of E_{ad} for Pt suggests that a Pt atom imbedded in a vacancy site with a defined unit cell size is

energetically unfavorable. Whereas, a Ni atom inserted at vacancy sites are even more stable than adsorbed on the other surface sites.

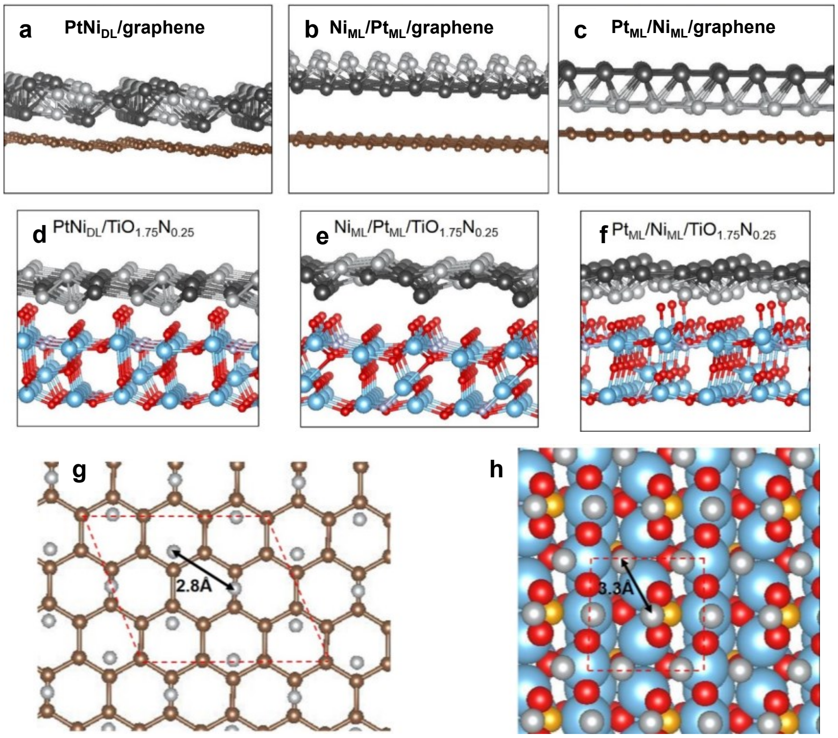

Figure 6.14: Side view showing the optimized configuration of the metal-support systems. (a) A (111) textured homogeneous PtNi doublelayer on graphene, (b) A (111) textured PtNi doublelayer on graphene, with Pt being segregated to the interface, (c) A (111) textured PtNi doublelayer on graphene, with Ni being segregated to the interface. (e) – (f) same metal configurations, but on $TiO_{1.75}N_{0.25}$ (110). Top view of initial atomic positions of the first-layer metal atoms (grey balls) on (g) graphene and on (h) $TiO_{1.75}N_{0.25}$ (110) surface. Red dash line denotes the unit cell in our calculations.

Figure 6.14A-F show the side view of three different PtNi doublelayer models on graphene and on $TiO_{1.75}N_{0.25}$ (110) surface after structural optimization. Specifically, the models include a (111) textured homogenous PtNi doublelayer (denoted as $PtNi_{DL}$), a (111) textured PtNi doublelayer with a monolayer of Pt (111) being segregated to the support interface (denoted as Ni_{ML}/Pt_{ML}), and a (111) textured PtNi doublelayer with a monolayer of Ni (111) being segregated to the interface (denoted as Pt_{ML}/Ni_{ML}). To retain the close packed atomic arrangement of (111) plane with a six-fold symmetry, the initial atomic positions for the metal layer at the support interface have been specified. As illustrated in Figure 6.14G, the metal layer at the graphene interface contains six atoms in each unit cell. Two of them are positioned on the bridge sites of graphene in order to form a (111) hexagon. As illustrated in Figure 6.14H, the metal layer at the $TiO_{1.75}N_{0.25}$ interface contains four atoms in each unit cell. They were positioned on the b1, b4, f1 and f2 sites of $TiO_{1.75}N_{0.25}$ (110) surface in order to form a (111) hexagon. For the second metal layer that is epitaxial along the [111] orientation, we assumed a stacking order of "AB" for close packed atomic planes. The metal atoms of the second layer are thus sitting on the 3-fold sites of the first metal layer. It is noted that by matching the atomic positions of the metal layer with the high symmetry adsorption sites on support surface, we imposed a substantial lattice strain within the unit cell due to the mismatch between the initially assumed lattice structure and the ones in bulk phase. As shown in Figure 6.14G and H, the M-M distances of PtNi doublelayer have been initially set as 2.8Å on graphene and 3.3Å on $TiO_{1.75}N_{0.25}$ (110). Considering the bulk values of 2.7Å, 2.8Å and 2.5Å for PtNi, Pt and Ni, respectively, metal layer on $TiO_{1.75}N_{0.25}$ surface experiences a stronger lattice strain than on graphene. This results in the lattice distortion after structural optimization as can be seen in Figure 6.14.

For the six combinations of metal-support interfaces, we calculated the adsorption energies, E_{ad}, by

$$E_{ad} = \frac{1}{N_M}(E_{tot} - E_{sub} - E_M) \qquad \text{Eq. 6.6}$$

where E_{tot} is the total energy of metal/support system per unit cell; E_M is the ground state cohesive energy of metal layers in vacuum; N_M is the number of metal atoms in a unit cell. The calculated values of E_{ad}, E_{tot} and E_M are summarized in Table 6.5. Comparing the E_{ad} values of the three PtNi doublelayer models, a fundamentally important result is that Pt_{ML}/Ni_{ML} doublelayer shows the most negative E_{ad} on either graphene or $TiO_{1.75}N_{0.25}$ (110) surface. In the case of graphene, the E_{ad} values of $PtNi_{DL}$, Ni_{ML}/Pt_{ML} and Pt_{ML}/Ni_{ML} are -0.10, -0.05 and -0.16 eV/unit cell, respectively. In the case of $TiO_{1.75}N_{0.25}$ (110), the E_{ad} values of $PtNi_{DL}$, Ni_{ML}/Pt_{ML} and Pt_{ML}/Ni_{ML} are -0.61, -0.93 and -1.02 eV/unit cell, respectively. For either graphene or $TiO_{1.75}N_{0.25}$ support, having Ni segregated at the support interface induces a stronger metal-support interaction than the other two doublelayer configurations. These results imply a universal tendency for Ni to segregate at the interfaces of both PtNi/graphene and PtNi/$TiO_{1.75}N_{0.25}$.

Table 6.5: E_{ad}, E_{tot} and E_M values of various metal-support systems.

	E_{tot} (eV per unit cell)	E_M (eV per unit cell)	E_{ad} (eV per metal atom)
$PtNi_{DL}$/graphene	-208.3	-59.6	-0.10
Ni_{ML}/Pt_{ML}/graphene	-207.2	-59.1	-0.05
Pt_{ML}/Ni_{ML}/graphene	-208.5	-59.1	-0.16
$PtNi_{DL}/TiO_{1.75}N_{0.25}$	-246.9	-37.7	-0.61
$Ni_{ML}/Pt_{ML}/TiO_{1.75}N_{0.25}$	-246.0	-34.2	-0.93
$Pt_{ML}/Ni_{ML}/TiO_{1.75}N_{0.25}$	-246.7	-34.2	-1.02

As indicated by our calculations, a segregated Ni layer should be present at the interface of either PtNi/graphene or PtNi/oxynitride. For this reason, we calculated the d-band structures of Pt_{ML}/Ni_{ML}/graphene and $Pt_{ML}/Ni_{ML}/TiO_{1.75}N_{0.25}$, with the results of Pt (bulk) and PtNi (bulk) being also included as the baseline. Table 6.6 lists the calculated values of d-band center, projected out for Pt atoms on the surface of metal slabs. While the variation of d-band center is correlated with the interfacial electronic charge transfer, the d-band center is certainly affected by the metal-metal bond distance $\bar{d}$ as also listed in Table 6.6. Comparing with bulk PtNi, Pt_{ML}/Ni_{ML} supported on either graphene or $TiO_{1.75}N_{0.25}$ exhibits larger $\bar{d}$ value. A larger metal-metal distance results in a lower overlap between the d-orbitals of metal atoms, leading to a narrowing of the d-band and an upward shift of the d-band center towards the Fermi level. It should be noted that such undesired change in d-band structure as a result of significant lattice expansion should be negligible in experimental condition, as confirmed by the results of XRD and XPS analysis. At the relatively high synthesis temperature of 700°C, Ni is expected to be much plastically softer than Pt, and may serve as a buffer layer that will allow the entire catalysts to relax. Earlier studies have demonstrated that interfacial dislocations in Ni would relieve some of the stress generated in a multilayer system (such as Ni on Cu), even at near atomic-scale dimensions of each layer, and even at room temperature [94-98]. We argue that this high temperature plasticity, dislocation mediated and/or purely diffusional, in the segregated Ni is responsible for the lack of an electronic enhancement of PtNi on the oxynitride versus on the CNTs. In both cases, the support-induced stresses (i.e. the strong chemical interactions) are relaxed during the initial synthesis process. This phenomenon is not captured by the current DFT analysis, which assumes zero temperature and cannot extend to treat long-range atomic flow.

Table 6.6: Comparison of the average metal-metal bond distance $\bar{d}$ and the d-band center for various systems.

	$\bar{d}$ (Å)	d-band center (eV)
Pt (bulk)	2.80	-2.40
PtNi (bulk)	2.64	-2.70
Pt_{ML}/Ni_{ML}/graphene	2.77	-2.37
$Pt_{ML}/Ni_{ML}/TiO_{1.75}N_{0.25}$	2.97	-2.50

Comparing the E_{ad} values of Ni_{ML}/Pt_{ML} and Pt_{ML}/Ni_{ML} provides insights regarding how differently pure Pt and PtNi alloy catalysts interact with each of the support. On graphene, the E_{ad} value of Pt_{ML}/Ni_{ML} is 3 times more negative than that of Ni_{ML}/Pt_{ML}. This suggests a relatively stronger chemical interaction between PtNi and graphene, agreeing very well with our experimental observation that PtNi wets much better on CNTs than pure Pt does. On $TiO_{1.75}N_{0.25}$, the E_{ad} values of both systems are quite negative, though their difference is much less (< 10%). This result again compares quite well with our experimental observation that both pure Pt and PtNi wet the surface of Ti oxynitride well. Our theoretical results demonstrate the stronger chemical interactions between metal electrocatalysts and Ti oxynitride, which is exactly what was observed for pure Pt.

6.4 Conclusions

We investigated the ORR activity and the corrosion stability of pure Pt or Pt-50at.%Ni electrocatalysts, supported on an ultra-thin (0.5 nm) titanium oxynitride film ALD coated onto an array of carbon nanotubes. For pure Pt, the oxynitride induces a downshift in the d-band center. The oxynitride also changes the catalyst particle size distribution, reducing the number of the less active and less stable ultrafine Pt particles and of the large ones that serve as "dead weight". This results in major enhancements in specific activity, mass activity and corrosion stability relative to the identically synthesized Pt deposited onto bare CNTs. Compared to this baseline, the Pt(0.02mg)/TiO_xN_y/CNTs system shows an anodic shift in the half wave potential (0.861 vs. 0.884 V), and an improvement in specific activity (0.314 vs. 0.522 $mA.cm^{-2}{}_{Pt}$) and mass activity (0.110 vs. 0.195 $A.mg_{Pt}^{-1}$). The insertion of TiO_xN_y layer also boosts the catalyst durability, with 9.7% vs. 25% loss in ECSA, 20.1% vs. 42.7% loss in specific activity, and 27.8% vs. 57% loss in mass activity, after 10,000 cycles of 0.6 to 1.1 V.

The PtNi alloy shows superior specific activity, mass activity and corrosion resistance to Pt. However neither its activity nor durability is affected by the insertion of TiO_xN_y. Both baseline and Pt(0.015mg)/TiO_xN_y/CNTs systems display a similar half wave potential (0.902 vs. 0.903 V), specific activity (1.068 vs. 1.057 $mA.cm^{-2}{}_{Pt}$) and mass activity (0.543 vs. 0.550 $A.mg_{Pt}^{-1}$). After 10,000 cycles of 0.6 to 1.1 V, the two systems have comparable losses in ECSA (-5.7% vs. -6.6%), in specific activity (-41.7% vs. -40.9%) and in mass activity (-45.0% vs. -44.8%). These results are attributed to the likeness of the metal-support interactions in PtNi-CNTs and PtNi-TiO_xN_y. By calculating the adsorption energies of three proposed doublelayer models, including $PtNi_{DL}$, Ni_{ML}/Pt_{ML} and Pt_{ML}/Ni_{ML}, on either graphene or on titanium oxynitride support, we found that a segregated Ni layer should be present at the interface of either PtNi/graphene or PtNi/oxynitride. Such Ni layer may serve as a buffer layer that is responsible for the minimal support effect of titanium oxynitride interlayer on the electronic structure or on the microstructure of PtNi alloy electrocatalyst.

6.5 Reference

[1] M. K. Debe, *Nature* **2012**, *486*, 43-51.

[2] F. T. Wagner, B. Lakshmanan, M. F. Mathias, *J. Phys. Chem. Lett.* **2010**, *1*, 2204-2219.

[3] S. Guo, S. Zhang, S. Sun, *Angew. Chem. Int. Ed.* **2013**, *52*, 8526-8544.

[4] a) Y. Liang, H. Wang, P. Diao, W. Chang, G. Hong, Y. Li, M. Gong, L. Xie, J. Zhou, J. Wang, T. Z. Regier, F. Wei, H. Dai, *J. Am. Chem. Soc.* **2012**, *134*, 15849-15857; b) Z. Yang, X. Zhou, Z. Jin, Z. Liu, H. Nie, X. Chen, S. Huang, *Adv. Mater.* **2014**, *26*, 3156-3161.

[5] T. Maiyalagan, K. A. Jarvis, S. Therese, P. J. Ferreira, A. Manthiram, *Nature Commun.* **2014**, *5*, 3949.

[6] a) D. Yu, Y. Xue, L. Dai, *J. Phys. Chem. Lett.* **2012**, *3*, 2863-2870; b) I-Y Jeon, H-J Choi, S-M Jung, J-M Seo, M-J Kim, L. Dai, J-B Baek, *J. Am. Chem. Soc.* **2013**, *135*, 1386-1393; c) H. Zhong, H. Zhang, Z. Xu, Y. Tang, J. Mao, *ChemSusChem*, **2012**, *5*, 1698-1702.

[7] Y. Dong, Y. Wu, M. Liu, J. Li, *ChemSusChem* **2013**, *6*, 2016-2021.

[8] N. Danilovic, A. Vincent, J-L Luo, K. T. Chuang, R. Hui, A. R. Sanger, *Chem. Mater.* **2010**, *22*, 957-965.

[9] a) A. Serov, K. Artyushkova, P. Atanassov, *Adv. Energy Mater.* **2014**, *4*, 1301735; b) A. Serov, U. Tylus, K. Artyushkova, S. Mukerjee, P. Atanassov, *Appl. Catal., B: Environ.* **2014**, *150*, 179-186.

[10] A. M. Gomez-Marin, J. M. Feliu, *ChemSusChem* **2013**, *6*, 1091-1100.

[11] P. Strasser, S. Koh, T. Anniyev, J. Greeley, K. More, C. Yu, Z. Liu, S. Kaya, D. Nordlund, H. Ogasawara, M. F. Toney, A. Nilsson, *Nature Chem.* **2010**, *2*, 454-460.

[12] I. E. L. Stephens, A. S. Bondarenko, U. Gronbjerg, J. Rossmeisl, I. Chorkendorff, *Energy Environ. Sci.* **2012**, *5*, 6744-6762.

[13] J. Kibsgaard, Y. Gorlin, Z. Chen, T. F. Jaramillo, *J. Am. Chem. Soc.* **2012**, *134*, 7758-7765.

[14] V. D. Noto, E. Negro, S. Polizzi, F. Agresti, G. A. Giffin, *ChemSusChem* **2012**, *5*, 2451-2459.

[15] K. A. Kuttiyiel, K. Sasaki, Y. Choi, D. Su, P. Liu, R. R. Adzic, *Energy Environ. Sci.* **2012**, *5*, 5297-5304.

[16] a) B. Kinkead, J. van Drunen, M. T. Y. Paul, K. Dowling, G. Jerkiewicz, B. D. Gates, *Electrocatal.* **2013**, *4*, 179-186; b) G. Jerkiewicz, *Electrocatal.* **2010**, *1*, 179-199.

[17] U. Martinez, A. Serov, M. Padilla, P. Atanassov, *ChemSusChem* **2014**, *7*, 2351 – 2357.

[18] N. Danilovic, R. Subbaraman, K-C Chang, S. H. Chang, Y. Kang, J. D. Snyder, A. P. Paulikas, D. Strmcnik, Y-T Kim, D. J. Myers, V. R. Stamenkovic, N. M. Markovic, *J. Phys. Chem. Lett.* **2014**, *5*, 2474−2478.

[19] L. Su, W. Jia, C-M Li, Y. Lei, *ChemSusChem* **2014**, *7*, 361-378.

[20] S. Ye, M. Hall, P. He, *ECS Trans.* **2008**, *16 (2)*, 2101-2113.

[21] B. Fang, M-S Kim, J. H. Kim, M. Y. Song, Y-J Wang, H. Wang, D. P. Wilkinson, J-S Yu, *J. Mater. Chem.* **2011**, *21*, 8066-8073.

[22] J. van Drunen, B. K. Pilapil, Y. Makonnen, D. Beauchemin, B. D. Gates, G. Jerkiewicz, *ACS Appl. Mater. Interfaces* **2014**, *6*, 12046–12061.

[23] S. Pylypenko, A. Borisevich, K. L. More, A. R. Corpuz, T. Holme, A. A. Dameron, T. S. Olson, H. N. Dinh, T. Gennett, R. O'Hayre, *Energy Environ. Sci.* **2013**, *6*, 2957-2964.

[24] Y. Shao, G. Yin, Y. Gao, *J. Power Sources,* **2007**, *171*, 558-566.

[25] J. C. Meier, C. Galeano, I. Katsounaros, A. A. Topalov, A. Kostka, F. Schuth, K. J. J. Mayrhofer, *ACS Catal.* **2012**, *2*, 832-843.

[26] K. J. J. Mayrhofer, J. C. Meier, S. J. Ashton, G. K. H. Wiberg, F. Kraus, M. Hanzlik, M. Arenz, *Electrochem. Commun.* **2008**, *10*, 1144-1147.

[27] J. Masa, A. Bordoloi, M. Muhler, W. Schuhmann, W. Xia, *ChemSusChem* **2012**, *5*, 523-525.

[28] X. Zhao, J. Zhu, L. Liang, J. Liao, C. Liu, W. Xing, *J. Mater. Chem.* **2012**, *22*, 19718-19725.

[29] A. G. Scheuermann, J. D. Prange, M. Gunji, C. E. D. Chidsey, P. C. Mclntyre, *Energy Environ. Sci.* **2013**, *6*, 2487-2496.

[30] K. Sasaki, L. Zhang, R. R. Adzic, *Phys. Chem. Chem. Phys.* **2008**, *10*, 159-167.

[31] L. Zhang, L. Wang, C. M. B. Holt, T. Navessin, K. Malek, M. H. Eikerling, D. Mitlin, *J. Phys. Chem. C* **2010**, *114*, 16463-16474.

[32] L. Zhang, L. Wang, C. M. B. Holt, B. Zahiri, Z. Li, K. Malek, T. Navessin, M. H. Eikerling, D. Mitlin, *Energy Environ. Sci.* **2012**, *5*, 6156-6172.

[33] A. Bonakdarpour, R. T. Tucker, M. D. Fleischauer, N. A. Beckers, M. J. Brett, D. P. Wilkinson, *Electrochim. Acta* **2012**, *85*, 492-500.

[34] M. Dou, M. Hou, H. Zhang, G. Li, W. Lu, Z. Wei, Z. Shao, B. Yi, *ChemSusChem* **2012**, *5*, 945-951.

[35] Y. Liu, W. E. Mustain, *J. Am. Chem. Soc.* **2013**, *135*, 530-533.

[36]Y. Luo, A. Habrioux, L. Calvillo, G. Granozzi, N. Alonso-Vante, *ChemPhysChem* **2014**, *15*, 2136 – 2144.

[37] D. C. Higgins, J-Y Choi, J. Wu, A. Lopez, Z. Chen, *J. Mater. Chem.* **2012**, *22*, 3727-3732.

[38] S. Dong, X. Chen, S. Wang, L. Gu, L. Zhang, X. Wang, X. Zhou, Z. Liu, P. Han, Y. Duan, H. Xu, J. Yao, C. Zhang, K. Zhang, G. Cui, L. Chen, *ChemSusChem* **2012**, *5*, 1712-1715.

[39] K. A. Kuttiyiel, K. Sasaki, Y. Choi, D. Su, P. Liu, R. R. Adzic, *Nano Lett.* **2012**, *12*, 6266-6271.

[40] J. Yin, L. Wang, C. Tian, T. Tan, G. Mu, L. Zhao, H. Fu, *Chem. Eur. J.* **2013**, *19*, 13979-13986.

[41] Y-J Wang, D. P. Wilkinson, J. Zhang, *Dalton Trans.* **2012**, *41*, 1187-1194.

[42] Y. P. Yu, W. Liu, S. X. Wu, S. W. Li, *J. Phys. Chem. C* **2012**, *116*, 19625−19629.

[43] Y. Qiu, K. Yan, S. Yang, L. Jin, H. Deng, W. Li, *ACS Nano*, **2010**, *4*, 6515-6526.

[44] X. Cui, M. Ma, W. Zhang, Y. Yang, Z. Zhang, *Electrochem. Commun.* **2008**, *10*, 367-371.

[45] N. C. Saha, H. G. Tompkins, *J. Appl. Phys.* **1992**, *72*, 3073-3079.

[46] S-I Choi, S. Xie, M. Shao, N. Lu, S. Guerrero, J. H. Odell, J. Park, J. Wang, M. J. Kim, Y. Xia, *ChemSusChem* **2014**, *7*, 1476-1483.

[47] J. Greeley, I. E. L. Stephens, A. S. Bondarenko, T. P. Johansson, H. A. Hansen, T. F. Jaramillo, J. Rossmeisl, I. Chorkendorff, J. K. Norskov, *Nature Chem.* **2009**, *1*, 552-556.

[48] a) C. Wang, N. M. Markovic, V. R. Stamenkovic, *ACS Catal.* **2012**, *2*, 891-898; b) C. Wang, D. Li, M. Chi, J. Pearson, R. B. Rankin, J. Greeley, Z. Duan, G. Wang, D. van der Vliet, K. L. More, N. M. Markovic, V. R. Stamenkovic, *J. Phys. Chem. Lett.* **2012**, *3*, 1668-1673.

[49] C. Chen, Y. Kang, Z. Huo, Z. Zhu, W. Huang, H. L. Xin, J. D. Snyder, D. Li, J. A. Herron, M. Mavrikakis, M. Chi, K. L. More, Y. Li, N. M. Markovic, G. A. Somorjai, P. Yang, V. R. Stamenkovic, *Science* **2014**, *343*, 1339-1343.

[50] D. Wang, H. L. Xin, R. Hovden, H. Wang, Y. Yu, D. A. Muller, F. J. DiSalvo, H. D. Abruna, *Nature Mater.* **2013**, *12*, 81-87.

[51] S. Prabhudev, M. Bugnet, C. Bock, G. A. Botton, *ACS Nano*, **2013**, *7*, 6103-6110.

[52] S. Guo, D. Li, H. Zhu, S. Zhang, N. M. Markovic, V. R. Stamenkovic, S. Sun, *Angew. Chem. Int. Ed.* **2013**, *52*, 3465-3468.

[53] M. K. Carpenter, T. E. Moylan, R. S. Kukreja, M. H. Atwan, M. M. Tessema, *J. Am. Chem. Soc.* **2012**, *134*, 8535-8542.

[54] C. Wang, M. Chi, G. Wang, D. van der Vliet, D. Li, K. More, H-H Wang, J. A. Schlueter, N. M. Markovic, V. R. Stamenkovic, *Adv. Funct. Mater.* **2011**, *21*, 147-152.

[55] Y. Liu, C. M. Hangarter, U. Bertocci, T. P. Moffat, *J. Phys. Chem. C* **2012**, *116*, 7848-7862.

[56] L. Yang, S. Shan, R. Loukrakpam, V. Petkov, Y. Ren, B. N. Wanjala, M. H. Engelhard, J. Luo, J. Yin, Y. Chen, C-J Zhong, *J. Am. Chem. Soc.* **2012**, *134*, 15048−15060.

[57] T. Wang, G. Mpourmpakis, W. W. Lonergan, D. G. Vlachos, J. G. Chen, *Phys. Chem. Chem. Phys.* **2013**, *15*, 12156-12164.

[58] a) S. H. Kang, Y-E Sung, W. H. Smyrl, *J. Electrochem. Society* **2008**, *155*, B1128-B1135; b) S. H. Kang, T-Y Jeon, H-S Kim, Y-E Sung, W. H. Smyrl, *J. Electrochem. Society* **2008**, *155*, B1058-B1065.

[59] M. Wojdyr, *J. Appl. Cryst.* **2010**, *43*, 1126-1128.

[60] L. Zhang, C. M. B. Holt, E. J. Luber, B. C. Olsen, H. Wang, M. Danaie, X. Cui, X. Tan, V. W. Lui, W. P. Kalisvaart, D. Mitlin, *J. Phys. Chem. C* **2011**, *115*, 24381-24393.

[61] G. Kresse, J. Hafner. *Phys. Rev. B* **1994**, *49*, 14251-14269.

[62] G. Kresse, J. Furthmüller, *Comput. Mat. Sci.* **1996**, *6*, 15-50.

[63] P. E. Blochl. *Phys. Rev. B* **1994**, *50*, 17953-17978.

[64] J. P. Perdew, J. A. Chevary, S. H. Vosko, K. A. Jackson, M. R. Pederson, D.J. Singh, and C. Fiolhais. *Phys. Rev. B* **1992**, 46, 6671.

[65] J. P. Perdew, J. A. Chevary, S. H. Vosko, K. A. Jackson, M. R. Pederson, D. J. Singh, and C. Fiolhais. *Phys. Rev. B* **1993**, 48, 4978.

[66] M. Wakisaka, S. Mitsui, Y. Hirose, K. Kawashima, H. Uchida, M. Watanabe, *J. Phys. Chem. B* **2006**, *110*, 23489-23496.

[67] T. Toda,H. Igarashi,H. Uchida, M. Watanabe, J. Electrochem. Soc. **1999**, *146*, 3750 – 3756.

[68] C. Ophus, E. Luber, D. Mitlin, *Acta Mater.* **2009**, *57*, 1327-1336.

[69] M. Shao, A. Peles, K. Shoemaker, *Nano Lett.* **2011**, *11*, 3714-3719.

[70] R. Jinnouchi, E. Toyoda, T. Hatanaka, Y. Morimoto, *J. Phys. Chem. C* **2010**, *114*, 17557-17568.

[71] L. Tang, B. Han, K. Persson, C. Friesen, T. He, K. Sieradzki, G. Ceder, *J. Am. Chem. Soc.* **2010**, *132*, 596-600.

[72] C. Cui, L. Gan, M. Heggen, S. Rudi, P. Strasser, *Nature Mater.* **2013**, *12*, 765-771.

[73] J. Solla-Gullon, P. Rodriguez, E. Herrero, A. Aldaz, J. M. Feliu, *Phys. Chem. Chem. Phys.* **2008**, *10*, 1359-1373.

[74] C. Wang, M. Chi, D. Li, D. Strmcnik, D. van der Vliet, G. Wang, V. Komanicky, K-C Chang, A. P. Paulikas, D. Tripkovic, J. Pearson, K. L. More, N. M. Markovic, V. R. Stamenkovic, *J. Am.Chem. Soc.* **2011**, *133*, 14396-14403.

[75] D. F. van der Vliet, C. Wang, D. Tripkovic, D. Strmcnik, X. F. Zhang, M. K. Debe, R. T. Atanasoski, N. M. Markovic, V. R. Stamenkovic, *Nature Mater.* **2012**, *11,* 1051-1058.

[76] D. F. van der Vliet, C. Wang, D. Li, A. P. Paulikas, J. Greeley, R. B. Rankin, D. Strmcnik, D. Tripkovic, N. M. Markovic, V. R. Stamenkovic, *Angew. Chem. Int. Ed.* **2012**, *51*, 3139-3142.

[77] V. Stamenkovic, T. J. Schmidt, P. N. Ross, N. M. Markovic, *J. Electroanal. Chem.* **2003**, *554-555,* 191-199.

[78] W. Wang, O. Savadogo, Z-F. Ma, *J. Appl. Electrochem*. **2012**, *4*2, 857-866.

[79] V. R. Stamenkovic, B. S. Mun, K. J. J. Mayrhofer, P. N. Ross, N. M. Markovic, J. Rossmeisl, J. Greeley, J. K. Norskov, *Angew. Chem. Int. Ed.* **2006**, *45*, 2897-2901.

[80] H. S. Casalongue, S. Kaya, V. Viswanathan, D. J. Miller, D. Friebel, H. A. Hansen, J. K. Norskov, A. Nilsson, H. Ogasawara, *Nature Commun.* **2014**, *4*, 2817.

[81] N. Danilovic, R. Subbaraman, D. Strmcnik, A. P. Paulikas, D. Myers, V. R. Stamenkovic, N. M. Markovic, *Electrocatal.* **2012**, *3*, 221-229.

[82] M. Nesselberger, S. Ashton, J. C. Meier, I. Katsounaros, K. J. J. Mayrhofer, M. Arenz, *J. Am. Chem. Soc.* **2011**, *133*, 17428-17433.

[83] F. J. Perez-Alonso, D. N. McCarthy, A. Nierhoff, P. Hernandez-Fernan-dez, C. Strebel, I. E. L. Stephens, J. H. Nielsen, Ib Chorkendorff, *Angew. Chem. Int. Ed.* **2012**, *51*, 4641-4643.

[84] A. Anasasopoulos, J. C. Davies, L. Hannah, B. E. Hayden, C. E. Lee, C. Milhano, C. Mormiche, L. Offin, *ChemSusChem* **2013**, *6*, 1973-1982.

[85] C. Ophus, T. Ewalds, E. J. Luber, D. Mitlin, *Acta Mater.* **2010**, *58*, 5150-5159.

[86] S. G. Rinaldo, J. Stumper, M. Eikerling, *J. Phys. Chem. C* **2010**, *114*, 5773-5785.

[87] L. Xing, G. Jerkiewicz, D. Beauchemin, *Analyt. Chim. Acta* **2013**, *785*, 16-21.

[88] P. W. Voorhees, *J. Statist. Phys.* **1985**, *38*, 231-252.

[89] K. Yang, Y. Dai, B. Huang, S. Han, *J. Phy. Chem. B* **2006**, *110*, 24011-24014.

[90] C. Di Valentin, G. Pacchioni, A. Selloni, s. Livraghi, E. Giamello, *J. Phys. Chem. B* **2005**, *109*, 11414-11419.

[91] S. Livraghi, M. C. Paganini, E. Giamello, A. Selloni, C. Di Valentin, G. Pacchioni, *J. Am. Chem. Soc*. **2006**, *128*, 15666-15671.

[92] L. Hu, X. Hu, X. Wu, C. Du, Y. Dai, J. Deng, *Physica B* **2010**, *405*, 3337-3341.

[93] S. J. Tauster, S. C. Fung, R. T. K. Baker, J. A. Horsley, *Science* **1981**, *211*, 1121-1125.

[94] D. Mitlin, A. Misra, V. Radmilovic, M. Nastasi, R. Hoagland, D. J. Embury, J. P. Hirth, T. E. Mitchell, *Philos. Mag.* **2004**, *84*, 719-736.

[95] D. Mitlin, A. Misra, T. E. Mitchell, R. G. Hoagland, J. P. Hirth, *Appl. Phys. Lett.* **2004**, *85*, 1686-1688.

[96] D. Mitlin, A. Misra, T. E. Mitchell, J. P. Hirth, R. G. Hoagland, *Philos. Mag.* **2005**, *85*, 3379-3392.

[97] C. B. Carter, R. Q Hwang, *Phys. Rev. B* **1995**, *51*, 4730-4733.

[98] C. B. Carter, S. M. Holmes, *Philos. Mag.* **1977**, *35*, 1161-1172.

Chapter 7

Pt-Au-Co Alloy Electrocatalysts Demonstrate Enhanced Activity and Durability towards Oxygen Reduction Reaction*

7.1 Introduction

The development of proton exchange membrane fuel cells (PEMFCs) that are commercially more competitive demands more efficient electrocatalysts for the cathodic oxygen reduction reaction (ORR) [1]. Despite the progress in the development of non-noble electrocatalysts [2,3], platinum-based electrocatalysts continue to remain at the center of intensive research [4-7]. Many efforts are directed toward enhancing the catalytic activity by developing advanced catalyst supports [8-11], by alloying Pt with transition metals (TM) [12-18], or by catalyst surface design at the atomic level [19-21]. The latter includes the well-known strategies such as dealloying of binary/ternary alloys [22-24], monolayer coating of Pt on suitable metal substrate [25,26], and creating the "Pt skin" electrocatalysts through thermal annealing Pt alloys in a reduced environment [27-29].

The enhanced catalytic activities of the Pt-based alloy electrocatalysts and their derivatives, relative to pure Pt, originate from the compressed lattice [30-32] and the

---

[*] Materials in this chapter has been submitted to:

- XueHai Tan, Sagar Prabhudev, Alireza Kohandehghan, Dimitre Karpuzov, Gianluigi A. Botton, Michael H. Eikerling, David Mitlin, ACS Catalysis 2015, doi:.

modified electronic structures [33,34] of Pt. Such catalyst surface exhibits a slightly weaker binding than Pt to the intermediate oxygenated spectator species (e.g., O*, OH* and OOH*), and thus an increasing number of active sites accessible to molecular oxygen [33]. It is however important to note that further weakening of the oxygen binding induces a change in the rate-limiting step of the ORR, from $OH^* + H^+ + e^- \rightarrow H_2O(l)$ on the strong-binding side, to $O_2(g) + H^+ + e^- \rightarrow OOH^*$ on the weak-binding side [12,34]. This volcano-type dependence of catalytic efficacy on the surface oxygen binding energy is essentially another application of traditional Sabatier's principle [35], which is typical for heterogeneous catalysis involving multiple reaction intermediates. The linearly scaling relations between the binding energies of O*, OH* and OOH* on the active sites of close-packed and stepped metal surfaces [36] make the oxygen binding energy a determinant parameter for ORR activity on Pt-based electrocatalyst surfaces [33]. Previous studies suggest that a surface that binds O* 0 to 0.4 eV more weakly than Pt(111) should exhibit an ORR activity better than Pt, with the optimum being theoretically predicted at a binding energy of roughly 0.2 eV weaker than that of Pt [5,12].

Binary Pt-based electrocatalysts have been extensively studied for ORR. Based on the reported results, Pt-Co binary alloy catalysts, for example Pt_3Co, are highly active [37-40]. The catalysts however suffer from rapid catalytic decaying due to the preferred leaching of the non-noble solute during electrode potential cycling in an acid medium [41-44]. This is so far the biggest limitation for disordered Pt-based alloys with early or late transition metals [5-7,32]. Platinum group metal (PGM) alloys have thus been proposed aiming at improving electrochemical stability. Considering the standard electrode potential, only Au and Ir (besides Pt) are thermodynamically stable in the bulk metallic form at potentials greater than 0.9V. Unfortunately, binary Pt-PGM alloys are usually lacking of ORR catalytic activities. Pt/Au(111) has been reported to bind oxygen even more strongly than Pt (111) resulting in a sluggish ORR catalytic efficacy [45]. On the other hand, Pt-Ir and Pt-Ru binaries are known to bind oxygen too weakly, positioning on far end of the other side of volcano [45]. Guided by the reported properties of the individual binary systems, we hypothesize that fine-tuning of ORR catalytic activity is possible by adding Au or Ir into a Pt-3d TM binary system. We understand that

Au or Ir should be chosen based on where the binary Pt-3d TM system already position on the ORR volcano. For example, a binary system that positions on the weak-binding side should be tuned towards a stronger binding of O*, in order to reach the possible maximum on the ORR volcano. Such hypothesis is consistent with the conclusion of a recent theoretical modeling [46].

In the present work, we report a detailed study on the ORR electrocatalytic activities and the corrosion stabilities for Pt-Au-Co and Pt-Ir-Co alloys. By keeping the atomic ratio of PGM over Co fixed at 3:1, we systematically evaluated the ORR catalytic performance as a function of Au or Ir substitution, using binary Pt–25 at.% Co and pure Pt as the baseline. Based on authors' best knowledge, Pt-Au-Co alloy systems have never been studied for ORR. Such ternary system should however be highly promising, given the increasing attention on ternary Pt-Au-X (X = Fe, Cu, Pd and Ni) alloy catalysts recently [47-51]. It is noted that Pt-Ir-Co alloy systems have already been reported [52-54], though the trend of catalytic activity is not entirely established for such multimetallic systems. Herein, one of the main objectives of this study is to establish the trend of catalytic activity and corrosion stability for the ternary alloy catalysts. For that reason, we performed a systematic investigation on well-defined extended surfaces of thin-film model systems.

7.2 Experimental

Film synthesis: The atomic ratio of platinum group metals (Pt + Au) or (Pt + Ir) versus Co was fixed at 3:1. As baselines we synthesized and tested pure Pt and a known state-of-the-art binary alloy ORR catalyst Pt-25at.%Co, i.e. Pt_3Co. For simplicity, we denote samples as Pt-xAu-25Co and Pt-xIr-25Co, which indicates a stoichiometry of (75-x)at.%Pt-(x)at.%Au-25at.%Co and (75-x)at.%Pt-(x)at.%Ir-25at.%Co. All depositions were conducted with the substrate temperature being maintained near ambient, resulting in a range of single-phase solid solution alloys. The thicknesses of all catalyst films were fixed at 20 nm, unless otherwise stated.

The catalyst thin films were magnetron sputtered (AJA International, Orion) onto a mirror-polished glassy carbon (GC) disk with 11.32 mm in diameter, which was then directly employed as an electrode for the electrochemical measurements. The geometrical area of the active Pt surfaces was ~ 1 cm^2. Prior to catalyst deposition, the glassy carbon surface was further treated with a mild Ar plasma procedure inside the sputtering chamber to promote better surface adhesion for the catalyst film. Deposition was performed in a sputter-up configuration with continuous substrate rotation. The details of deposition condition are similar to those described in previous chapters. The deposition rate of Pt was kept at 1 Å s^{-1}. The deposition rates of Au, Ir and Co were varied accordingly to adjust for different alloy stoichiometries.

Electrochemical testing: Electrochemical measurements were carried out using a standard rotating disk electrode (RDE) system (Princeton applied research model 616), a Solartron 1470 multistat test station and a three-electrode electrochemical cell. A helical Pt wire and a Cl^- free Hg/Hg_2SO_4 with a taper joint were used as the counter and reference electrode, respectively. Perchloric acid ($HClO_4$ optima grade, Fisher Scientific) diluted with Milli-Q water to 0.1M was the electrolyte solution in all cases. All electrochemical measurements were carried out at room temperature using research grade gases (99.999%, Praxair). The reported potentials are specified relative to the reversible hydrogen electrode (RHE) scale. The cyclic voltammetry (CV) was recorded in Ar-saturated electrolyte between 0 V and 1.0 V with a scan rate of 100 mV s^{-1}. The electrochemical surface area (ECSA) of the catalyst was estimated by averaging the integral charges of the hydrogen adsorption and desorption areas of the CV profiles, including a correction for double layer charging [55]. To avoid the underestimation of the ECSA owing to a possible suppression of hydrogen adsorption, the ECSA was confirmed by CO-stripping [56]. Before CO-stripping, the electrode was immersed in a CO-saturated electrolyte for 10 minutes. After that, the electrolyte was purged with Ar and the CO-stripping voltammetry was then recorded. Anodic linear sweep voltammetry (LSV) from 0.05 V to 1.05 V was conducted in oxygen-saturated electrolyte to measure the ORR at different rotational speeds (100, 225, 400, 625, 900, 1225, 1600, 2025 and 2500 rpm) using a scan rate of 20 mV s^{-1}. The kinetic current was extracted from measured ORR polarization curve according to the Koutecky-Levich equation:

$$\frac{1}{I}=\frac{1}{I_k}+\frac{1}{I_L}=\frac{1}{I_k}+\frac{1}{B\omega^{1/2}}=\frac{1}{I_k}+\frac{1}{0.62nFA_{geo}D^{2/3}\omega^{1/2}v^{-1/6}C_{O_2}} \qquad \text{Eq. 7.1}$$

where I is the measured ORR current, I_k and I_L are the kinetic and the diffusion limited currents, respectively, B is the Levich slope, F is the Faraday constant, n is the number of electron transferred per O_2 molecule, D is the diffusion coefficient of oxygen, C_{O2} is the concentration of oxygen in the bulk solution, ω is the angular velocity and ν is the kinematic viscosity of the solution. The electrocatalyst stability test involved 100,000 potential cycles between 0.6 V and 1.0 V using a sweep rate of 50 mV s^{-1}. CV and LSV were recorded after 1st, 2nd, 5th, 10th, 50th, 100th, 200th, 300th, 400th, 500th, 5,000th, 10,000th, 20,000th, 50,000th and 100,000th cycles during the stability test. Prior to measuring the post-cycling ECSA and ORR activities, the electrolyte was replaced with fresh solution. For the electrochemical impedance spectroscopy (EIS) measurements, we applied an alternating current in the frequency range from 20 kHz to 1 Hz with 10 mV amplitude at 0 V vs. open circuit potential.

Microstructural characterization: X-ray photoelectron spectroscopy (XPS) measurements were performed on an ULTRA (Kratos Analytical) spectrometer under ultrahigh vacuum (10^{-9} Torr) using monochromatic Al-Kα radiation (*h*ν = 1486.6 eV) operated at 210 W. All XPS spectra were calibrated using the universal hydrocarbon contamination C1s peak at 284.8 eV. Angle resolved XPS (ARXPS) analysis was conducted with an electron emission angle of 60° measured from the surface normal, denoted as ARXPS-60°. Such technique was used to enhance surface selectivity, sampling photoelectrons emitted from the very surface of catalyst films. While the ordinary XPS analysis, denoted as XPS-0°, collects photoelectrons from up to 5 nm depth of a metal surface, the ARXPS-60° analysis is expected to sample signals from a surface depth of only ~ 2 nm. We hereafter take the quantification results of XPS-0° analysis as the near-surface chemical composition, while taking the results of ARXPS-60° analysis as the surface chemical composition. Ultraviolet photoelectron spectroscopy (UPS) measurements were performed using a Kratos Ultra spectrometer with He I light (*h*ν = 21.2 eV). The analyser pass energy was 5 eV and the aperture was set at 110 μm. X-ray diffraction (XRD) analysis was performed on a Bruker AXS diffractometer (Bruker

Discover 8) using a Cu-K$_\alpha$ radiation (λ = 1.5406 Å). The details of XRD instrumentation are similar to those described in previous chapters. Given the same thicknesses for all catalyst films deposited on GC, the XRD patterns were calibrated using the universal GC (101) peak. Conventional bright-field and dark-field imaging and selected area electron diffraction (SAD) analysis were performed on a JEOL 2100 transmission electron microscope (TEM) operated at 200 kV accelerating voltage. Atomically-resolved high angle annular dark field (HAADF) and electron energy loss spectroscopy (EELS) analysis were conducted on a FEI-Titan cubed TEM using scanning mode (STEM). The microscope is operated at 300 kV accelerating voltage and is equipped with two hexapole-design spherical aberration correctors of the probe and image forming lenses. Given the fact that deconvolution of Pt and Au signals is difficult due to their similar energies, we acquired (Pt+Au) combined and Co maps by integrating over the core-loss edges of Pt $M_{4,5}$ at 2120 eV, Au $M_{4,5}$ at 2206 eV, and Co $L_{2,3}$ at 779 eV, respectively. TEM analysis of the as-synthesis microstructures were performed on catalyst films directly deposited onto the ultra-thin carbon film on TEM grids. For post-cycling analysis, the TEM specimens were mechanically removed from the electrodes and dry dispersed on the grids. Commercial software Crystal Maker ^{TM} and TEM diffraction ring profiler [57] were used to simulate electron diffraction patterns. Based on dark-field TEM images, we determined the catalyst crystallite size distribution. For each sample, a total of 500 crystallites that displayed strong Bragg contrast have been measured. Scanning electron microscopy (SEM) analysis was performed on a Hitachi S-4800 field emission SEM operated at 15 kV accelerating voltage.

7.3 Results and Discussion

The 20 nm thick Pt-Au-Co and Pt-Ir-Co, binary Pt-Co and pure Pt baseline catalyst films were deposited at ambient temperature onto mirror polished glassy carbon substrates. As shown by bright-field transmission electron microscopy (TEM) analysis (selected results are shown in Figure 7.1), all as-synthesis catalyst films are continuous. This is an important catalyst electrode property for systematic evaluation on ORR activities. Nesselberger et al. have demonstrated that the catalyst interparticle distance on flat electrode will decisively influence the measured catalytic activity [58]. As the result a continuous catalyst film with the closely packed assemblies of catalyst particles will minimize such undesired effect. It has been well documented that the catalyst particle/crystallite size also has a profound impact on the ORR activity [59]. By sputtering at room temperature using almost identical deposition rates, i.e. ensuring analogous kinetic energies of the sputtering fluxes, very similar mean crystallite sizes of ~ 8 nm have been achieved for all systems, as demonstrated by extensive dark-field TEM analysis along with statistically determined crystallite size distribution (selected results are shown in Figure 7.1). The above-mentioned experimental designs provided us a platform of model study to establish the trend of catalytic performance as a function of alloy compositions.

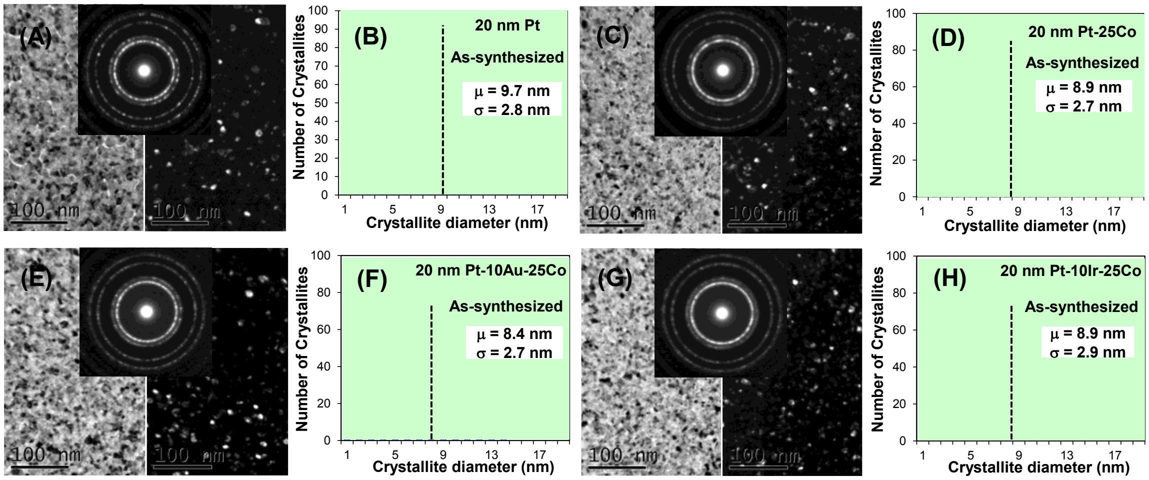

Figure 7.1: TEM bight field, dark field and selected area electron diffraction (SAD) micrographs and the corresponding catalyst crystallite size distributions of as-synthesized (A, B) pure Pt baseline, (C, D) Pt-25Co, (E, F) Pt-10Au-25Co and (G, H) Pt-10Ir-25Co. Identical analysis for the other samples is presented in the supplemental.

Typical selected area electron diffraction (SAD) patterns are shown in the insets of Figure 7.1. All catalyst films are random solid solution with face-centered cubic (fcc) crystal structure. As shown by the results of the X-ray diffraction (XRD) analysis (Figure 7.2A and B), the fcc (111) peak of Pt-Au-Co alloys shifted towards lower angles with increasing Au content. This observation is in accordance with the Vegard's Law, since

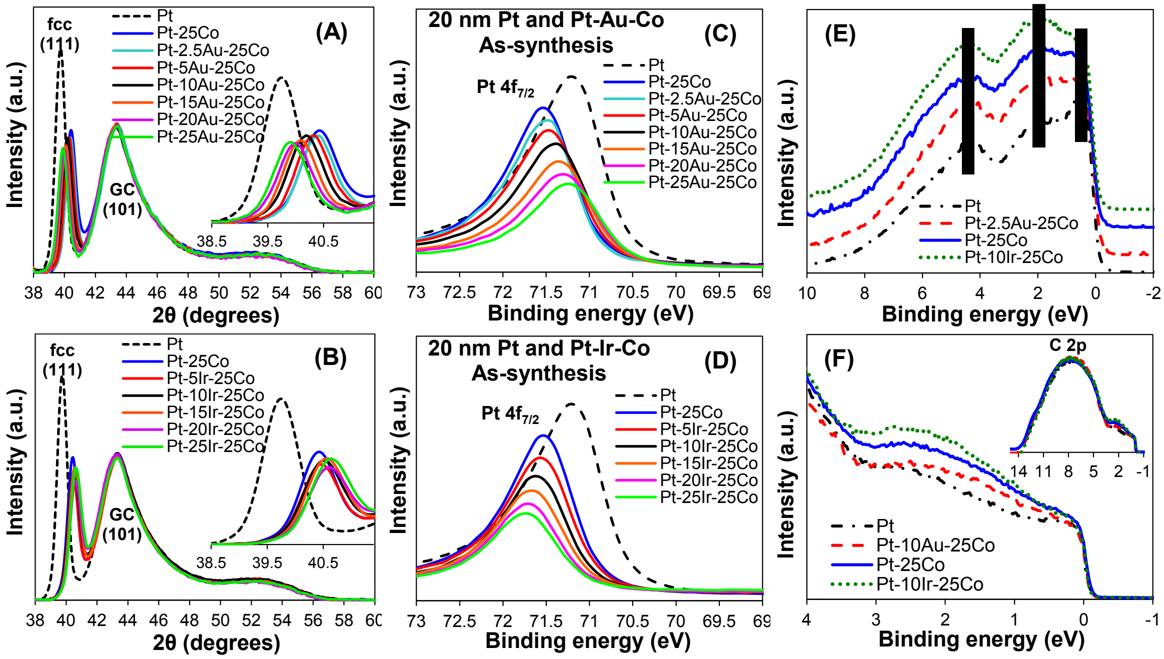

Figure 7.2: (A, B) XRD patterns and (C, D) Pt 4f$_{7/2}$ XPS spectra of 20 nm Pt-Au-Co and Pt-Ir-Co alloy films, with Pt-25Co and pure Pt being included as the baselines. (E, F) Valence band spectra of selected samples, measured by (E) XPS and (F) UPS. As shown in the inserts of (F), the UPS spectra have been normalized with respect to C 2p peak at binding energy of 8 eV.

Au substitution with larger crystal lattice parameter than Pt will gradually compensate the lattice compression as induced by alloying with Co. Meanwhile, the (111) peak of Pt-Ir-Co alloys remains essentially unchanged. This is as expected given the similar lattice parameters between the Pt and Ir crystal structures. For each sample, we have used energy-dispersive x-ray spectroscopy (EDS) to confirm the bulk composition. In parallel, we carried out X-ray photoelectron spectroscopy (XPS-0°) analysis to examine the near-surface composition. It is noted that the alloy composition near the surface starts to deviate from the bulk value with increasing Au content. There, the relatively higher concentration of Au on the surface indicates preferred segregation. This could be explained by the differences in surface segregation energies of Au, Pt and Co [47,60]. The results of the microstructural characterizations for all samples' initial microstructure are summarized in Table 7.1.

Figures 7.2C and D show the Pt 4f$_{7/2}$ X-ray photoelectron spectroscopy (XPS) spectra of the as-synthesis Pt-Au-Co and Pt-Ir-Co alloy films, respectively. The XPS

Table 7.1: Results of XRD, EDS, XPS-0° and dark field TEM analysis of the as-synthesized catalyst films, summarizing the measured lattice parameters, the bulk and the near-surface chemical compositions and the mean crystallite diameters.

	X-ray analysis		EDS analysis			XPS-0° analysis			TEM analysis
	2θ fcc (111)	fcc lattice parameter (Å)	bulk composition (at.%)			near-surface composition (at.%)			crystallite diameter distribution (nm)
			Pt	Ir/Au	Co	Pt	Ir/Au	Co	
Pt	39.75	3.924	100%	-	-	100%	-	-	9.7 ± 2.8
Pt-25Au-25Co	39.91	3.909	54%	23%	24%	49%	29%	22%	8.6 ± 2.6
Pt-20Au-25Co	39.98	3.902	58%	19%	23%	55%	23%	22%	8.7 ± 2.7
Pt-15Au-25Co	40.09	3.892	60%	16%	25%	60%	17%	23%	8.1 ± 2.2
Pt-10Au-25Co	40.19	3.882	66%	10%	24%	65%	11%	24%	8.4 ± 2.7
Pt-5Au-25Co	40.32	3.870	70%	6%	24%	70%	6%	24%	7.8 ± 2.4
Pt-2.5Au-25Co	40.40	3.863	72%	4%	25%	73%	3%	24%	7.8 ± 2.3
Pt-25Co	40.43	3.860	74%	-	26%	74%	-	26%	8.9 ± 2.7
Pt-5Ir-25Co	40.47	3.857	70%	5%	25%	69%	5%	25%	8.4 ± 2.7
Pt-10Ir-25Co	40.52	3.852	64%	12%	24%	65%	11%	24%	8.9 ± 2.9
Pt-15Ir-25Co	40.57	3.848	59%	16%	25%	60%	17%	24%	8.8 ± 2.3
Pt-20Ir-25Co	40.61	3.844	57%	19%	24%	54%	21%	26%	8.5 ± 2.2
Pt-25Ir-25Co	40.64	3.841	52%	25%	23%	49%	26%	25%	8.3 ± 2.1

spectra of the Pt-25Co and pure Pt baselines are included for reference. There is a clear shift in the Pt $4f_{7/2}$ core level (CL) as a function of Au or Ir alloying compositions. While the surface CL of Pt-Au-Co alloys shifts to lower binding energies as compared to Pt-25Co, the surface CL of Pt-Ir-Co alloys shifts to higher binding energies. The shift in CL is associated with a shift in the center of gravity of the d-bands [61,62]. It has been previously shown that a CL shift to a higher binding energy indicates a downshift in d-band center with respect to the Fermi level [63,64], and thus vice versa for a CL shift to a lower binding energy. Additionally, we carried out XPS and Ultraviolet photoelectron spectroscopy (UPS) analysis to directly probe the changes in valence band for selected samples. The results, as shown in Figure 7.2E and F, respectively, support our arguments based on CL shift. As Pt d-band character dominates the band structures of alloy surfaces, it may be seen that the 5d-band center of Pt is shifting downwards in following order: Pt > Pt-Au-Co > Pt-25Co > Pt-Ir-Co. Considering the strong correlation between the d-band center of a given catalyst surface and the oxygen binding energy [33], we anticipate a predictable variation in the ORR activity of the alloys with the level of Au or Ir substitution for Pt.

Cyclic voltammetry (CV) and rotating-disk electrode (RDE) linear sweep voltammetry (LSV) were used to investigate the electrochemical adsorption and catalytic properties of the catalyst electrodes. Figure 7.3A-B compare the CV profiles of Pt-Au-Co and Pt-Ir-Co, respectively. These CV tests were performed in argon-saturated 0.1 M $HClO_4$ solution using a scan rate of 100 mV s^{-1}. Close inspection of the CV profiles reveals that by varying the substitution level of Au or Ir, the electrochemical adsorption properties of the resulting surfaces are significantly altered. Using binary Pt-25Co and pure Pt as the reference, the reduction of surface oxide species (OH*) on Pt-Au-Co alloy surfaces are observed to fall in between the two. With increasing level of Au substitution, the oxide reduction peak gradually shifts towards that of pure Pt, i.e. a more negative potential. This observation confirms stronger oxygen binding on Pt-Au-Co alloy surfaces relative to Pt-25Co, which can be attributed to the expanding lattice and the upward shift of d-band center towards the Fermi level that is observed with increasing Au content. For Pt-Ir-Co alloy surfaces, there is an opposite trend. With increasing level of Ir substitution, the ternary alloy surfaces exhibit anodic shifts for the reduction of surface oxide species relative to binary Pt-25Co. This indicates further weakening of the electrochemically adsorbed oxygenated species on Pt-Ir-Co alloy surfaces in comparison to Pt-25Co.

Figure 7.3C shows the CO stripping curves for Pt-10Au-25Co, Pt-10Ir-25Co, Pt-25Co and pure Pt. Considering CO and OH* are competing for the same Pt adsorption sites, the trend observed for CO electro-oxidation is consistent with the above trend for surface oxide reduction. While the electro-oxidation of adsorbed CO proceeds at lower potentials on the surfaces of Pt-10Ir-25Co and other Pt-Ir-Co alloys comparing to binary Pt-25Co, higher potentials are required to strip the CO from the surfaces of Pt-10Au-25Co and other Pt-Au-Co alloys. Our results of CO stripping and XPS analysis demonstrate a correlation between the changes in CO chemisorption energy and the relative shifts in surface CL binding energy. These trends agree well with an earlier study of CO thermal adsorption on Pd, Ni and Cu overlayers on various supports, where the CO desorption temperature was found to be lower with a relative shift in surface CL to higher binding energies [65]. To summarize the effects of Au or Ir substitution on chemical interactions of alloy catalyst surfaces with OH* or CO: Adding Au stabilizes the adsorbates, and adding Ir destabilizes the adsorbates.

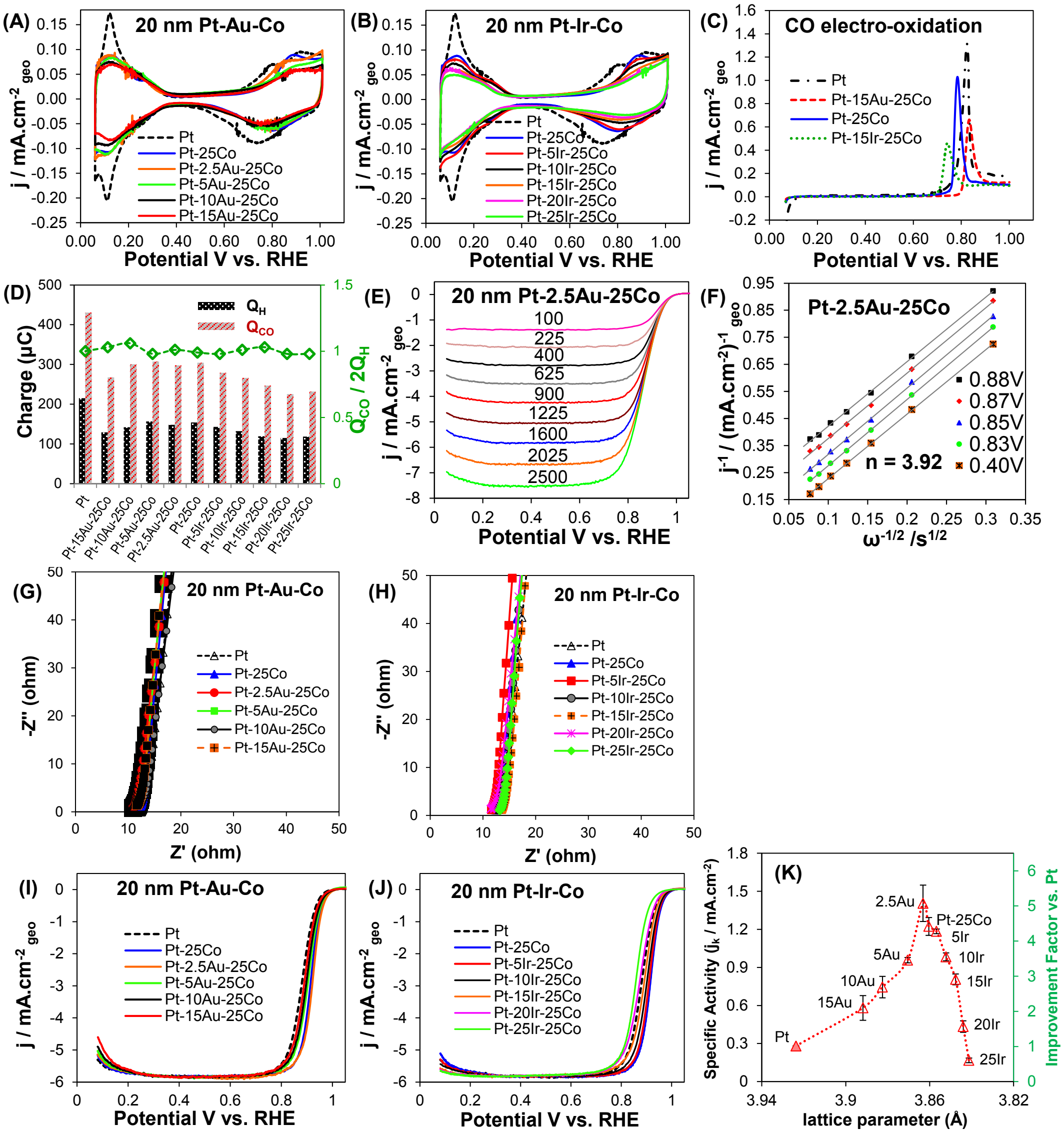

Figure 7.3: (A, B) Cycling voltammetry (CV) of Pt-Au-Co, Pt-Ir-Co, Pt-25Co and pure Pt in argon-saturated 0.1 M $HClO_4$ solution using a scan rate of 100 mV s^{-1}. (C) CO stripping curves for selected samples. (D) Integral charges of underpotentially deposited hydrogen (Q_H) and CO stripping (Q_{CO}) with the ratio of Q_{CO} / $2Q_H$ included. (E, F) ORR polarization curves at different rotation speeds (100 to 2500 rpm) in oxygen-saturated electrolyte with the corresponding K-L plot shown for Pt-2.5Au-25Co. (G, H) Nyquist plots for Pt-Au-Co and Pt-Ir-Co with binary Pt-25Co and pure Pt being included as baseline. (I, J) Master plots comparing the iR-corrected ORR polarization curves at 1600 rpm using a scan rate of 20 mV s^{-1}. All electrochemical tests were conducted at room temperature. (K) Specific activities measured at 0.95 V versus RHE, and the improvement factors relative to pure Pt are plotted as a function of lattice parameters that were experimentally determined by XRD analysis. The triangular data points represent the experimental results, averaging from 2 independent measurements. The error bars show the deviation from the mean.

We estimated the electrochemical surface area (ECSA) by both integral charges of underpotentially deposited hydrogen (H_{upd}) and CO electro-oxidation. As shown in Figure 7.3D, the ratio between the two integral charges remains close to 1 for all investigated samples. This rules out the formation of a thermally segregated Pt-skin structure with its characteristic ratio of close to 1.5, and agrees with the homogenous structure expected from near-ambient substrate temperatures during deposition. During the initial potential cycling, a leached-type "Pt skeleton" will most likely develop on the surface of a random solid solution alloy [66]. It has been reported that non-annealed alloy surface does not show discrepancy between the ECSA based on H_{upd} and CO stripping [12,67], and therefore the surface area estimation based on integral charge of H_{upd} is reasonable. Table 7.2 provides the list of ECSA estimation based on H_{upd}.

Table 7.2: The initial electrochemical surface area (ECSA), ORR half-wave potentials ($E_{1/2}$) for Pt-Au-Co, Pt-Ir-Co, Pt-25Co and pure Pt electrocatalysts.

	ECSA		$E_{1/2}$
	[cm^2]	[$m^2.g^{-1}{}_{Pt}$]	[V]
Pt	1.03	2.57	0.880
Pt-15Au-25Co	0.61	2.43	0.884
Pt-10Au-25Co	0.66	2.41	0.898
Pt-5Au-25Co	0.71	2.37	0.904
Pt-2.5Au-25Co	0.73	2.36	0.922
Pt-25Co	0.74	2.30	0.915
Pt-5Ir-25Co	0.66	2.20	0.910
Pt-10Ir-25Co	0.62	2.21	0.901
Pt-15Ir-25Co	0.52	2.00	0.891
Pt-20Ir-25Co	0.51	2.13	0.872
Pt-25Ir-25Co	0.50	2.28	0.857

Figure 7.3E-F present the ORR polarizations curves for Pt-2.5Au-25co electrocatalyst, tested between 100 to 2500 rpm at room temperature. These LSV measurements were conducted in oxygen-saturated 0.1 M $HClO_4$ solution using a scan rate of 20 mV s^{-1}. The RDE data was analyzed with the Koutecky-Levich (K-L) approach to extract the kinetic currents from the polarization curves. The number of electrons transferred (n) per O_2 molecule calculated from the slope of K-L plot supports the complete 4 electron reduction of O_2 to H_2O for potential above 0.4V. The complete set of ORR curves and the corresponding K-L plots for other electrocatalysts are not shown

here. However, similar conclusion regarding the 4 electron reduction mechanism was obtained for all investigated systems.

Figures 7.3G and H show the results of electrochemical impedance spectroscopy (EIS) for all catalyst electrodes. From the real component value of the impedance at the minimum of Nyquist plot, the overall resistance of the electrochemical cell was obtained. The investigated catalyst electrodes show similar resistances of ~ 12 ohms. These values were used to correct the ohmic loss (iR correction) for the measured ORR polarization curves. Figure 7.3I and J provide the master plots of iR-corrected ORR polarization curves at 1600 rpm, comparing the initial catalytic efficacies of different electrocatalysts. As shown in Figure 7.3I, the polarizations curves of Pt-Au-Co alloys show first an increase in half-wave potential ($E_{1/2}$) from binary Pt-25Co to Pt-2.5Au-25Co, and then a quick decrease in $E_{1/2}$ with further increasing levels of Au substitution. As shown in Figure 7.3J, the polarization curves of Pt-Ir-Co alloys show a monotonic decreasing in $E_{1/2}$ with increasing Ir substitution. Table 7.2 also provides the list of $E_{1/2}$ for all investigated samples.

The ORR specific activities that represent the intrinsic properties of the electrocatalysts were calculated through normalization by ECSA. Figure 7.3K plots the initial specific activities measured at 0.95 V vs. RHE as a function of the measured bulk lattice constants. For initial catalytic performance, the bulk lattice constant of a homogeneous solid solution represents a reasonable estimate of the surface lattice strain. The volcano plot of the catalytic activities versus lattice constants is clearly uneven across the composition range. This suggests that the observed trend of ORR activities versus Au or Ir substitution level is not solely due to the strain effect, but likely caused by a combination of strain and ligand effects. This argument is in line with the general understanding for Pt alloy catalysts that the strain and ligand effects are usually inseparable [13].

The outcome of a combination of strain and ligand effects is the changing of oxygen binding energy on catalyst surface [13,33,45]. Based on the results of XRD and XPS analysis, combined with the measured properties of electrochemical adsorption, we herein describe the volcano of ORR activities as a function of oxygen binding energies.

From high to low level of Au substitution (sample Pt-15Au-25Co to sample Pt-2.5Au-25Co), the Pt-Au-Co alloy surfaces exhibit increasing ORR catalytic activities with gradually decreasing oxygen binding energies relative to pure Pt. This is indicative of lower activation barriers for electro-reduction of OH* and thus higher availability of active surface sites that are accessible to oxygen. For Au substitution level of 10 at.%, the Pt-10Au-25C alloy shows a specific activity of 0.75 mA cm^{-2} at 0.95 V. This represents an improvement factor of 2.7 compared to the identically synthesized Pt baseline. For Au substitution level of 2.5 at.%, we have achieved fine-tuning of the ORR electrocatalytic activity towards the volcano peak by discovering a Pt-Au-Co alloy surface that binds oxygen weaker than Pt but slightly stronger than Pt-25Co. The Pt-2.5Au-25Co shows an ORR specific activity of 1.41 mA cm^{-2} at 0.95 V, even higher than that of the state-of-the-art binary Pt-25Co. This represents an improvement factor of 5 compared to the Pt baseline. The result makes good sense, considering that binary Pt-25Co alloy surface was previously found to position just to the weak-binding side of ORR volcano [5,12]. Alternatively, Ir substitution to binary Pt-25Co is not effective for enhancing the ORR catalytic activity. From low to high level of Ir substitution (sample Pt-5Ir-25Co to sample Pt-25Ir-25Co), Pt-Ir-Co alloy surfaces exhibit further weakening in oxygen binding as compared to binary Pt-25Co. This induces a change in the rate-limiting step, with the ORR being limited by an increased activation barrier for oxygen dissociation or the hydrogenation of oxygen.

Table 7.3 compares some of our best-performing Pt-Au-Co alloy electrocatalysts with the state-of-the-art previously published in scientific literature. We employ a measure termed specific activity Improvement Factor (IF) to compare the performance of alloy catalysts to identically synthesized pure Pt. IF is defined as the ratio of the two specific activities at the same voltage. We target a comparison to the results reported for a range of alloy and bilayer systems, including work based on thin film polycrystalline surfaces, single crystalline surfaces, monolayer Pt deposited on single crystalline substrates, and also a few nanoparticulate materials. In these works, the authors avoided using commercial Pt/C as the baseline, because commercial Pt/C catalysts usually have significantly lower specific activity than the extended Pt surfaces [68]. It is noteworthy that our alloy Pt-2.5Au-25Co alloy in fact exhibits the highest IF (a factor of 5) ever

Table 7.3: Comparison of the achieved Improvement Factor of our best-performing Pt-Au-Co alloys with previously published state-of-the-art ORR electrocatalysts.

* TF = thin films, NP = nanoparticles, NSA = near surface alloy, AL = Atomic layer, ML = Monolayer, SC = single crystal, PC = polycrystalline

Electrocatalysts	Catalyst type	Surface type	Improvement Factor	SA (mA.cm^{-2})	Measured @ (V vs. RHE)	T (C°)
PtNi [28]	TF	Pt-skin	13.2	5.6	0.95	60
$Pt_{2\text{-}3L}$ / intermetallic Pt_3Co[39]	NP	Pt-skin / core-shell	11.2	1.25	0.90	RT
Pt_3Ni(111) [68]	bulk SC	Pt-skin	10.0	18	0.90	60
Cu / Pt(111) NSA [34]	AL on Pt SC	NSA	8.0	10.1	0.90	60
Pt_3Y [13]	bulk PC	Pt-skin	6.0	11	0.90	RT
this study: Pt-2.5Au-25Co	**TF**	**Pt-skeleton**	**5.0**	**1.41**	**0.95**	**RT**
$Pt_{45}Ni_{55}$ ~ $Pt_{55}Ni_{45}$ [15]	TF	Pt-skeleton	4.7	2.8	0.90	RT
$Pt_3(CoNi)_1$ [12]	TF	Pt-skin	3.9	1.75	0.95	60
PtCu dealloyed [30]	NP	core-shell	3.8	0.75	0.90	RT
PtNi [28]	TF	Pt-skeleton	3.4	1.5	0.95	60
$Pt_3(FeNi)_1$ [12]	TF	Pt-skin	3.3	1.47	0.95	60
Pt_3Co [33]	TF	Pt-skin	3	4.3	0.90	60
this study: Pt-10Au-25Co	**TF**	**Pt-skeleton**	**2.7**	**0.75**	**0.95**	**RT**
Pt_{ML} / Pd_9Au_1 [72]	NP	Pt-monolayer	2.7	0.38	0.90	80
Pt_3Fe / Au(111) [47]	TF	Pt-skeleton/core-shell	2.6	6.7	0.90	60
Pt_3Fe [33]	TF	Pt-skin	2.6	3.75	0.90	60
$Pt_3(CoNi)_1$ [12]	TF	Pt-skeleton	2.5	1.12	0.95	60
$Pt_3(FeCo)_1$ [12]	TF	Pt-skin	2.4	1.1	0.95	60
$Pt_3(FeNi)_1$ [12]	TF	Pt-skeleton	2.3	1.03	0.95	60
Pt_3Ni [33]	TF	Pt-skin	2.25	3.25	0.90	60
Pt_3Co [66]	TF	Pt-skeleton	2	2.8	0.90	60
$Pt_3(FeCo)_1$ [12]	TF	Pt-skeleton	1.9	0.85	0.95	60
Pt_3Ni [66]	TF	Pt-skeleton	1.8	2.7	0.90	60
Pt_3V [33]	TF	Pt-skin	1.7	2.5	0.90	60
Pt_3Fe [66]	TF	Pt-skeleton	1.63	2.25	0.90	60
$Pt_{2\text{-}3L}$ / Pd [20]	NP	core-shell	1.6	0.48	0.90	RT
Pt_3Ti [33]	TF	Pt-skin	1.4	2	0.90	60
Pt_{ML} / Pd(111) [45]	ML on SC	Pt monolayer	1.34	16.5	0.80	RT
Pt_3V [66]	TF	Pt-skeleton	1.3	1.85	0.90	60
Pt_3Ti [66]	TF	Pt-skeleton	1.05	1.5	0.90	60
Pt_{ML} / Au(111) [45]	ML on SC	Pt monolayer	0.85	10.4	0.80	RT
Pt_{ML} / Rh(111) [45]	ML on SC	Pt monolayer	0.55	6.8	0.80	RT
Pt_3Sc [13]	bulk PC	Pt-skin	0.5	2.38	0.90	RT
Pt_{ML} / Ir(111) [45]	ML on SC	Pt monolayer	0.45	5.5	0.80	RT
Pt_{ML} / Ru(111) [45]	ML on SC	Pt monolayer	0.11	1.4	0.80	RT

reported for a skeleton-type Pt alloy electrocatalysts. The few materials with higher IF are either Pt-skin systems or in one case a near surface alloy, both of which are expected to possess greatly enhanced activity at the expense of long-term cycling durability. For Pt-10Au-25Co, the obtained catalytic enhancement, an IF of 2.7, is still highly promising.

The durability of the electrocatalysts was evaluated by 100,000 potential cycles between 0.6 V and 1.0 V, at room temperature, using a sweep rate of 50 mV s^{-1}. Figure 7.4A to D depict the results of stability test for Pt-Au-Co, Pt-Ir-Co, binary Pt-25Co and pure Pt, plotting the ORR specific activities at 0.95 V as a function of potential cycle number. The results during the initial 500 cycles are detailed in Figure 7.4A and B. Interestingly, while Pt-Au-Co and pure Pt show monotonic degradation in ORR specific activities during the initial 500 cycles, Pt-Ir-Co and Pt-25Co alloys first show an increase in ORR activity before their activities starting to degrade with higher cycle numbers. We term this temporary increase as an "activation period". The length of this activation period varies with the sample compositions. While for Pt-25Co the activation is 2 cycles, the activation period of Pt-Ir-Co lasts for more cycles within creasing Ir content. For Pt-5Ir-25Co, Pt-10Ir-25Co, Pt-15Ir-25Co and Pt-25Ir-25Co, the activation period lasts for ~ 10, 50, 100, 150 and as long as 300 cycles, respectively. We hypothesize that this ORR activation behavior for Pt-Ir-Co and Pt-25Co systems is related to the early-stage Co dissolution that actually results in favorable changes in lattice and electronic structures of the alloy surface. As discussed for Figure 7.3K, the Pt-Ir-Co alloys with high Ir content should bind oxygen too weakly, exhibiting sluggish initial ORR activities. With progressive Co dissolution, the partial relaxation of surface lattice strain and electronic effect would first initiate an increase in ORR activity, as moving from the right side of activity volcano towards the peak. We argue that our hypothesis may indeed be the case, though a more complex early-stage activation behavior may be associated with Pt-Ir-Co systems.

Figure 7.4C and D show the results in the course of 100,000 potential cycles. For Pt-25Co, such extended stability test results in a substantial degradation in ORR activity, which happens particularly fast at the early stage of potential cycles. Although the specific activity of Pt-25Co was initially as high as 1.294 mA cm^{-2} at 0.95 V, it is degraded by 43 % after 100 cycles, by 62 % after 500 cycles and by nearly 80% after 100,000 potential cycles. The specific activity of the ternary alloys shows progressively less cycling degradation with increasing levels of Au or Ir substitution. After 100,000 cycles the specific activity degradation in Pt-2.5Au-25Co, Pt-5Au-25Co, Pt-10Au-25Co and Pt-15Au-25Co is 70%, 56%, 25% and 22%, respectively. For Pt-5Ir-25Co, Pt-10Ir-25Co, Pt-15Ir-25Co and Pt-20Ir-25Co these values are 71%, 55%, 43% and 33%, respectively. All the Pt-Au-Co and Pt-Ir-Co alloys possess higher activities than Pt-Co after 100,000 cycles. Here, we highlight the catalytic stability for Pt-10Au-25Co alloy. Despite the lower initial ORR activity, its specific activity after 100,000 cycles is actually 2.4 times higher than that of Pt-25Co.

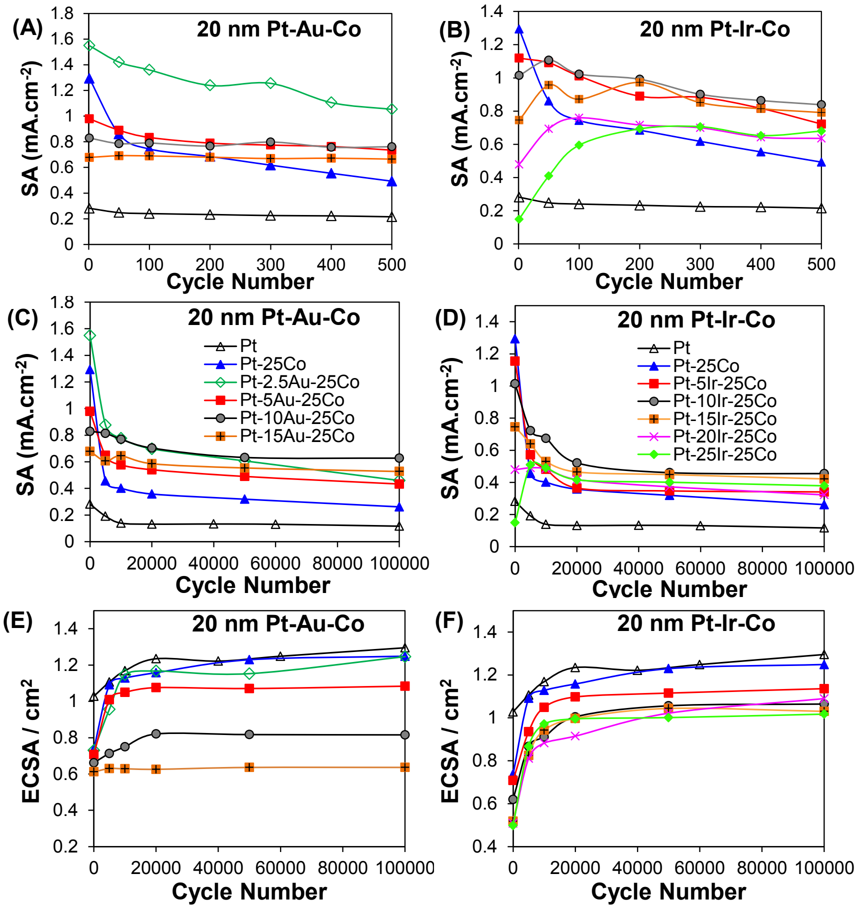

Figure 7.4: Catalysts stability test with 100,000 potential cycles between 0.6 and 1.0 V at a sweep rate of 50 mV s^{-1} at room temperature. The ORR specific activities (SA) at 0.95 V versus RHE for Pt-Au-Co, Pt-Ir-Co, Pt-25Co and pure Pt are plotted as a function of potential cycle number. (A, B) SA during the initial 500 cycles. (C, D) SA in the course of 100,000 cycles. (E, F) ECSA in the course of 100,000 cycles.

Figure 7.4E and F show the evolution of ECSA for Pt-Au-Co, Pt-Ir-Co, Pt-25Co and pure Pt in the course of 100,000 potential cycles. Unlike other supported electrocatalyst particulates, continuous catalyst thin films with sufficient thickness do not show loss in ECSA, at least for a certain range cycling number. Instead, the ECSA of all investigated catalyst films actually increase over cycling, with higher gains in ECSA for samples having more degradation in activity. We would like to point out that such behavior makes sense for polycrystalline catalyst films that were initially continuous. Driven by higher free energy, low-coordinated atoms at grain boundaries are more prone to oxidation and dissolution. As shown by the high magnification scanning electron microscopy (SEM) images of 20 nm Pt film after cycling (see Figure 7.5), rapid dissolution at grain boundaries has turned the continuous polycrystalline film into Pt crystallites that are isolated or partially interconnected. This process increases the film surface roughness, exposing more electrochemical active surface to the electrolyte. The process that turns a continuous Pt film into isolated crystallites also changes the proportion of the Pt crystal facets that are exposed to the electrolyte (see Figure 7.6A). It is well documented that the ORR activities on the low-index Pt single-crystal surfaces in perchloric acid increase in following order: Pt(100) << Pt(111) < Pt (110), being attributed to the structure-sensitive adsorption of reaction intermediates on different facets [7,69]. A decreasing ratio of Pt (110) to Pt (100) over cycling would explain the decaying ORR specific activity for pure Pt.

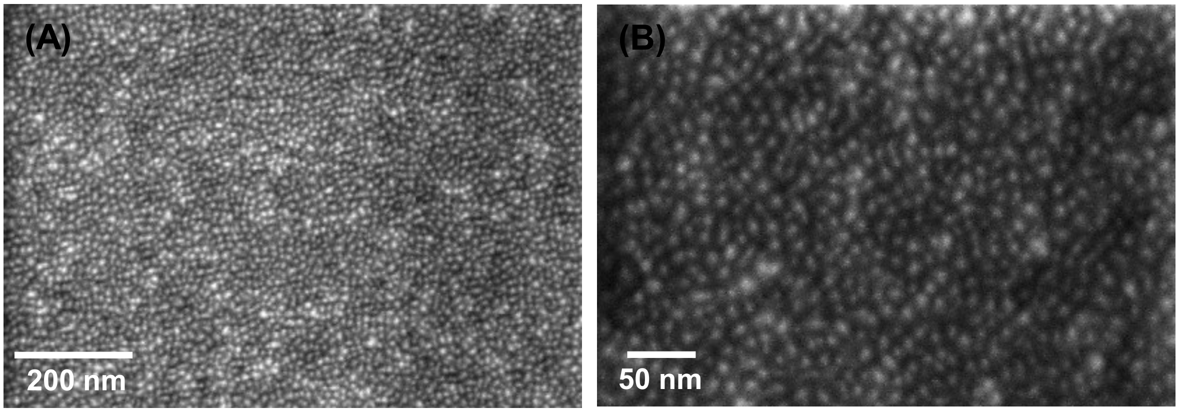

Figure 7.5: (A) Low and (B) High magnification SEM micrographs for 20 nm pure Pt film after 100,000 potential cycles between 0.6 V and 1.0 V.

For the alloy catalysts, the dealloying of the solute component is another key factor for the increasing ECSA. The preferred leaching of Co atoms, which are known for having no affinity to H, will create a catalyst surface that is atomically corrugated. The dealloyed surfaces may also contain higher fraction of H adsorbing elements than their original state. Consequently, any loss in real surface area due to Pt dissolution could be covered by an increasing H adsorption on surfaces that are depleted of the solute component. The ECSA of Pt-based alloy catalysts gradually increase to a stage where a steady-state value is achieved. This implies that the dealloyed Pt-rich or PGM-rich catalyst surface has rearranged to form a continuous overlayer, which should provide kinetic stability against further dissolution of the less noble solute component [70,71]. Figure 7.6B to D compare the CV profiles of Pt-10Au-25Co and Pt-15Au-25Co to that of Pt-25Co baseline, in the course of 100,000 potential cycles. For the Pt-Au-Co that have sufficient levels of Au substitution (≥ 10 at.%), their essentially unchanged CV coupled with minimal changes in activity and ECSA during cycling signal a tremendously enhanced resistance to degradation.

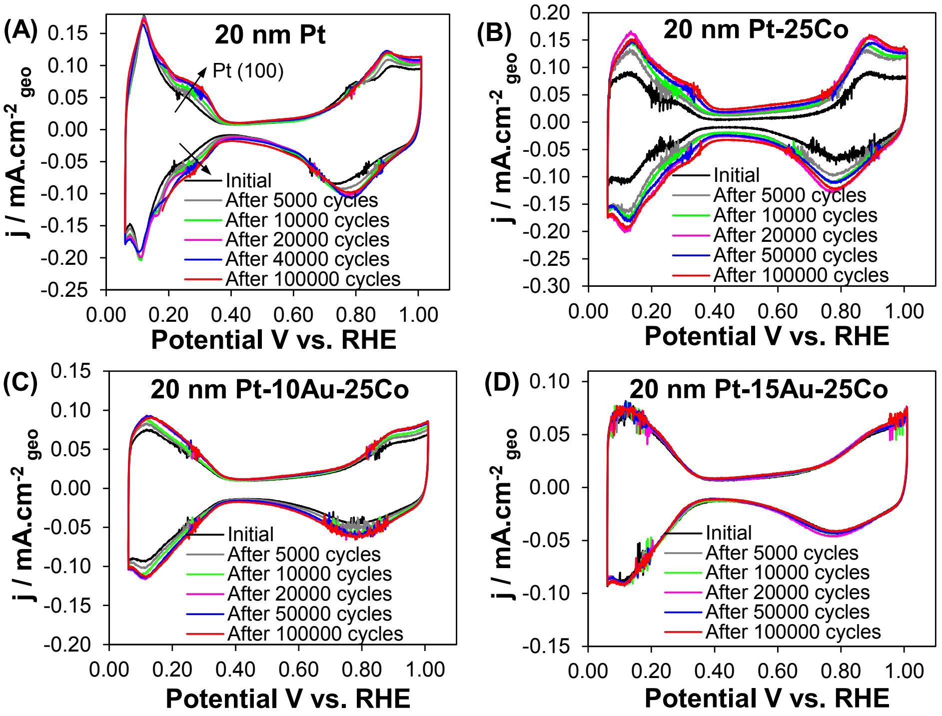

Figure 7.6: Cyclic Voltammetry (CV) of (A) pure Pt, (B) Pt-25Co, (C) Pt-10Au-25Co and (D) Pt-15Au-25Co during 100,000 potential cycles between 0.6 V and 1.0 V.

Figures 7.7A to C compare the surface ~ 2 nm sampling depth (ARXPS-60°) versus the near-surface ~ 5 nm sampling depth (XPS-0°) chemical compositions of the electrocatalysts after 100,000 potential cycles. For Pt-Au-Co alloys, with increasing Au additions the near-surface Co content is progressively stabilized relative to Pt-Ir-Co and to Pt-Co alloys. This indicates that the initial structure of Pt-Au-Co alloys is better maintained as compared to the other systems. The Pt-Au-rich surface layer acts as a protective layer for the alloy structure underneath, resulting in an enhanced preservation of the useful strain and ligand effects from the sub-surface Co solute.

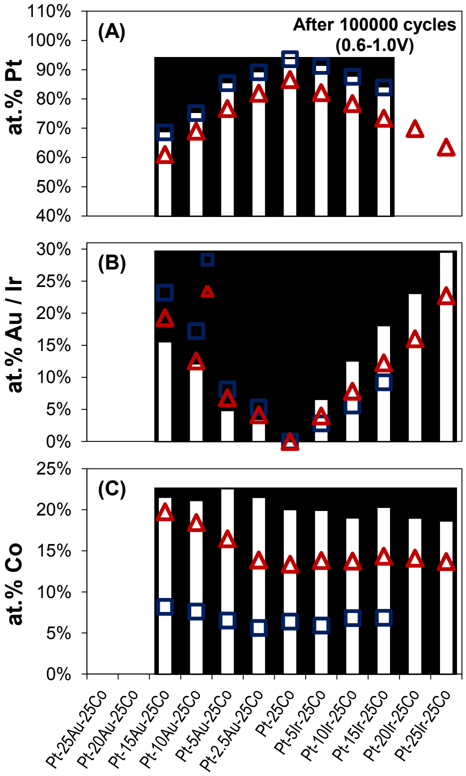

Figure 7.7: The comparisons of surface (penetration ~ 2 nm) and near surface (penetration ~ 5 nm) chemical compositions for (A) Pt, (B) Au or Ir and (C) Co, respectively, after 100,000 potential cycles between 0.6 V and 1.0 V.

The catalyst surface structure of Pt-10Au-25Co alloy was further characterized using HRTEM HAADF and EELS elemental mapping, conducted on a thinner 5 nm sample. As may be seen in the map of the as-synthesized alloy (Figure 7.8A), the material is overall quite homogenous on the atomic scale. However there does appear to be a sub-nanometer thick Pt-Au-rich surface layer in this specimen. Based on the aberration-corrected HR EELS elemental maps, the Pt-Au-rich surface layer is about 0.5 nm, which corresponds to 2 – 3 atomic layers. Such fine segregation would be driven by the differences in surface segregation energies of Au, Pt and Co, with the diffusion distances being small enough for it to occur even at ambient. As shown in Figure 7.8B, a similar scale Pt-Au-rich surface layer also exists after 5000 potential cycles between 0.6 V and 1.0 V. Figure 7.9 shows same analysis for another region in the specimen that was cycled 5000 times. A sub-nanometer thick Pt-Au-rich surface layer is again observed. These results highlight the structural stability of Pt-Au-Co alloy surface during extended electrochemical cycling.

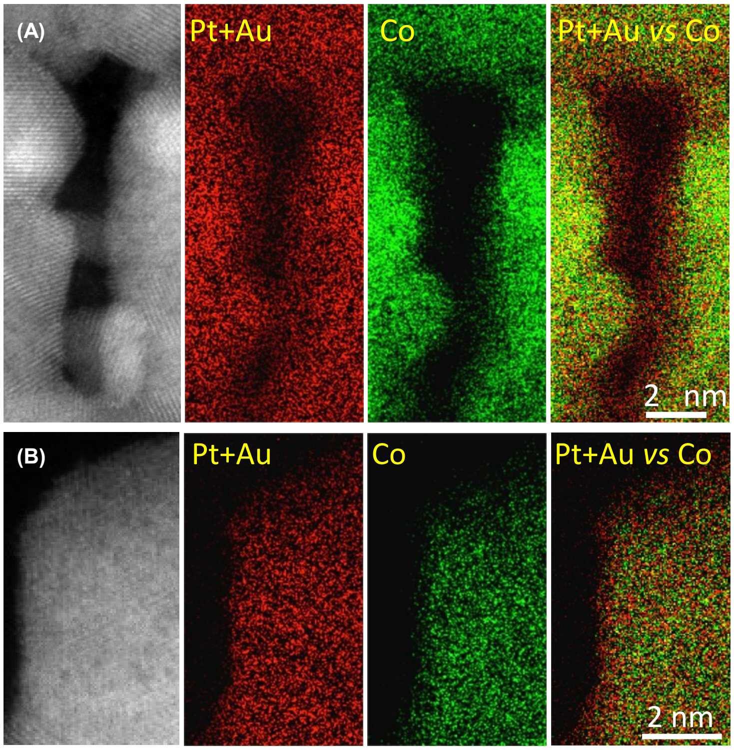

Figure 7.8: High resolution high angle annular dark field (HAADF) micrographs and electron energy loss spectroscopy (EELS) elemental maps of Pt+Au and Co for 5 nm Pt-10Au-25Co alloy film (A) before and (B) after 5000 potential cycles between 0.6 V and 1.0V.

The role of Au on structural/compositional stabilization can be attributed to the "self-healing" mechanism of Au that has been previously proposed for PdAu - Pt monolayer core-shell nanoparticle [72] Driven by the lower surface energy of Au, the segregated Au atoms on the surface and at the low-coordinated sites could potentially stabilize the Pt-Au surface layer, which in turn suppresses the dissolution of Co from the ternary core. This process should be effective for electrochemical cycling potentials that are lower than the standard electrode potential of Au. It should be note that the Au atoms at the surface contribute little to the measured ECSA, as hydrogen adsorption on Au atoms is negligible relative to Pt [47,73]. For Pt-Ir-Co, adding Ir is not as efficient as Au in suppressing the dissolution of Co due to the lower standard electrode potential for Ir as compared to Au. However Ir is also useful for stabilizing the activity of Pt-Co. Assuming surface-oxide formation and its subsequent chemical dissolution is the mechanism for Pt dissolution, as discussed in reference [74], a reduced rate of Pt dissolution is plausible if the coverage of surface oxide species could be decreased. As demonstrated in Figures 7.2 and 7.3, the Pt-Ir-Co alloy surfaces show weaker binding to oxygen with increasing levels of Ir substitution. Such alloy surfaces are therefore less susceptible to surface-oxide formation, leading to a higher resistance to Pt dissolution despite the loss of some Ir with cycling.

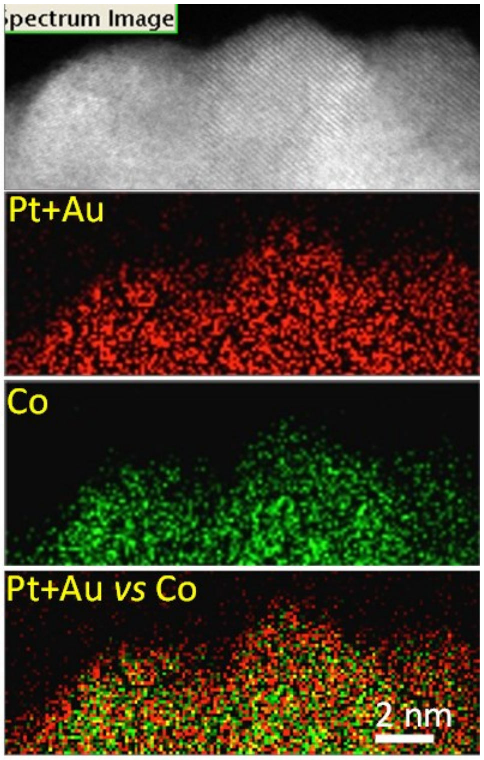

Figure 7.9: High resolution HAADF micrographs and EELS elemental mapping of another sample region for 5 nm Pt-10Au-25Co alloy film after 5000 potential cycles between 0.6 V and 1.0 V.

7.4 Conclusion

In this study we systematically investigated the ORR activity and the corrosion stability for Pt-Au-Co and Pt-Ir-Co thin film alloys, employing binary Pt-25Co and pure Pt as the baseline. The Pt–2.5at.%Au–25at.%Co alloy reaches the peak of the activity volcano with a specific activity of 1.41 mA cm^{-2} at 0.95 V, representing an improvement factor of 5 as compared to the identically synthesized Pt baseline and beating the state-of-the-art Pt–25at.%Co by 16%. Moreover the alloys exhibit dramatically improved corrosion stability with increasing levels of Au or Ir substitution. For instance, Pt–10 at.%Au–25at.%Co shows an initial specific activity of 0.75 mA cm^{-2}, which is still 2.7 times better than pure Pt. Following 100,000 potential cycles (0.6 - 1.0 V) this alloy has only a 25% loss in specific activity, while Pt–25at.%Co shows a 80% loss. Thus after 100,000 cycles the activity of Pt–10at.%Au–25at.%Co is actually 140% higher than that of Pt–25at.%Co.

7.5 Reference

[1] F. T. Wagner, B. Lakshmanan, M. F. Mathias, *J. Phys. Chem. Lett.* **2010**, *1*, 2204-2219.

[2] T. Xing, Y. Zheng, L. H. Li, B. C. C. Cowie, D. Gunzelmann, S. Z. Qiao, S. Huang, Y. Chen, *ACS Nano*, **2014**, *8*, 6856-6862.

[3] Y. Wang, X. Jiang, *ACS Appl. Mater. Interfaces* **2013**, *5*, 11597-11602.

[4] J. Snyder, N. Danilovic, A. P. Paulikas, D. Tripkovic, D. Strmcnik, N. M. Markovic, V. R. Stamenkovic, *J. Phys. Chem. C* **2013**, *117*, 23790-23796.

[5] I. E. L. Stephens, A. S. Bondarenko, U. Gronbjerg, J. Rossmeisl, I. Chorkendorff, *Energy Environ. Sci.* **2012**, *5*, 6744-6762.

[6] G-Z Zhu, S. Prabhudev, J. Yang, C. M. Gabardo, G. A. Botton, L. Soleymani, *J. Phys. Chem. C* **2014**, *118*, 22111-22119.

[7] L. Su, W. Jia, C-M Li, Y. Lei, *ChemSusChem* **2014**, *7*, 361-378.

[8] K. W. Kim, S. M. Kim, S. Choi, J. Kim, I. S. Lee, *ACS Nano*, **2012**, *6*, 5122-5129.

[9] J. Xie, X. Yang, B. Han, S-H Yang, D. Wang, *ACS Nano*, **2013**, *7*, 6337-6345.

[10] C. Kok Poh, S. Hua Lim, Z. Tian, L. Lai, Y. P. Feng, Z. Shen, J. Lin, *Nano Energy,* **2013**, *2*, 28-39.

[11] J. van Drunen, B. K. Pilapil, Y. Makonnen, D. Beauchemin, B. D. Gates, G. Jerkiewicz, *ACS Appl. Mater. Interfaces* **2014**, *6*, 12046-12061.

[12] C. Wang, D. Li, M. Chi, J. Pearson, R. B. Rankin, J. Greeley, Z. Duan, G. Wang, D. van der Vliet, K. L. More, N. M. Markovic, V. R. Stamenkovic, *J. Phys. Chem. Lett.* **2012**, *3*, 1668-1673.

[13] J. Greeley, I. E. L. Stephens, A. S. Bondarenko, T. P. Johansson, H. A. Hansen, T. F. Jaramillo, J. Rossmeisl, I. Chorkendorff, J. K. Norskov, *Nat. Chem.* **2009**, *1*, 552-556.

[14] B. N. Wanjala, B. Fang, S. Shan, V. Petkov, P. Zhu, R. Loukrakpam, Y. Chen, J. Luo, J. Yin, L. Yang, M. Shao, C-J Zhong, *Chem. Mater.* **2012**, *24*, 4283-4293.

[15] Y. Liu, C. M. Hangarter, U. Bertocci, T. P. Moffat, *J. Phys. Chem. C* **2012**, *116*, 7848-7862.

[16] C. Wang, N. M. Markovic, V. R. Stamenkovic, *ACS Catal.* **2012**, *2*, 891-898.

[17] L. Su, S. Shrestha, Z. Zhang, W. Mustain, Y. Lei, *J. Mater. Chem. A*, **2013**, *1*, 12293-12301.

[18] S-I Choi, M. Shao, N. Lu, A. Ruditskiy, H-C Peng, J. Park, S. Guerrero, J. Wang, M. J. Kim, Y. Xia, *ACS Nano*, **2014**, DOI: 10.1021/nn5036894

[19] S. Zhang, X. Zhang, G. Jiang, H. Zhu, S. Guo, D. Su, G. Lu, S. Sun, *J. Am. Chem. Soc.* **2014**, *136*, 7734-7739.

[20] S. Xie, S-I Choi, N. Lu, L. T. Roling, J. A. Herron, L. Zhang, J. Park, J. Wang, M. J. Kim, Z. Xie, M. Mavrikakis, Y. Xia, *Nano Lett.* **2014**, *14*, 3570-3576.

[21] J. B. Henry, A. Maljusch, M. Huang, W. Schuhmann, A. S. Bondarenko, *ACS Catal.* **2012**, *2*, 1457-1460.

[22] L. Gan, M. Heggen, S. Rudi, P. Strasser, *Nano Lett.* **2012**, *12*, 5423-5430.

[23] L. Gan, M. Heggen, R. O'Malley, B. Theobald, P. Strasser, *Nano Lett.* **2013**, *13*, 1131-1138.

[24] D. Wang, Y. Yu, H. L. Xin, R. Hovden, P. Ercius, J. A. Mundy, H. Chen, J. H. Richard, D. A. Muller, F. J. DiSalvo, H. D. Abruna, *Nano Lett.* **2012**, *12*, 5230-5238.

[25] K. A. Kuttiyiel, K. Sasaki, Y. choi, D. Su, P. Liu, R. R. Adzic, *Energ. Environ. Sci.* **2012**, *5*, 5297-5304.

[26] Y. Choi, K. A. Kuttiyiel, J. P. Labis, K. Sasaki, G-G Park, T-H Yang, R. R. Adzic, *Top Catal.* **2013**, *56*, 1059-1064.

[27] C. Chen, Y. Kang, Z. Huo, Z. Zhu, W. Huang, H. L. Xin, J. D. Snyder, D. Li, J. A. Herron, M. Mavrikakis, M. Chi, K. L. More, Y. Li, N. M. Markovic, G. A. Somorjai, P. Yang, V. R. Stamenkovic, *Science* **2014**, *343*, 1339-1343.

[28] D. F. van der Vliet, C. Wang, D. Tripkovic, D. Strmcnik, X. F. Zhang, M. K. Debe, R. T. Atanasoski, N. M. Markovic, V. R. Stamenkovic, *Nat. Mater.* **2012**, *11*, 1051-1058.

[29] C-H Cui, H-H Li, X-J Liu, M-R Gao, S-H Yu, *ACS Catal.* **2012**, *2*, 916-924.

[30] P. Strasser, S. Koh, T. Anniyev, J. Greeley, K. More, C. Yu, Z. Liu, S. Kaya, D. Nordlund, H. Ogasawara, M. F. Toney, A. Nilsson, *Nat. Chem.* **2010**, *2*, 454-460.

[31] J. Yang, J. Yang, J. Y. Ying, *ACS Nano*, **2012**, *6*, 9373-9382.

[32] S. Prabhudev, M. Bugnet, C. Bock, G. A. Botton, *ACS Nano*, **2013**, *7*, 6103-6110.

[33] V. R. Stamenkovic, B. S. Mun, K. J. J. Mayrhofer, P. N. Ross, N. M. Markovic, J. Rossmeisl, J. Greeley, J. K. Norskov, *Angew. Chem. Int. Ed.* **2006**, *45*, 2897-2901.

[34] I. E. L. Stephens, A. S. Bondarenko, F. J. Perez-Alonso, F. Calle-Vallejo, L. Bech, T. P. Johansson, A. K. Jepsen, R. Frydendal, B. P. Knudsen, J. Rossmeisl, I. Chorkendorff, *J. Am. Chem. Soc.* **2011**, *133*, 5485-5491.

[35] G. Rothenberg, *Catalysis: Concepts and Green Applications,* **2008**, Wiley-VCH, pp. 65

[36] F. Abild-pedersen, J. Greeley, F. Studt, J. Rossmeisl, T. R. Munter, P. G. Moses, E. Skulason, T. Bligaard, J. K. Norskov, *Phys. Rev. Lett.* **2007**, *99*, 016105.

[37] S. Guo, D. Li, H. Zhu, S. Zhang, N. M. Markovic, V. R. Stamenkovic, S. Sun, *Angew. Chem. Int. Ed.* **2013**, *52*, 3465-3468.

[38] B. Patrick, H. C. Ham, Y. Shao-Horn, L. F. Allard, G. S. Hwang, P. J. Ferreira, *Chem. Mater.* **2013**, *25*, 530-535.

[39] D. Wang, H. L. Xin, R. Hovden, H. Wang, Y. Yu, D. A. Muller, F. J. DiSalvo, H. D. Abruna, *Nat. Mater.* **2013**, *12*, 81-87.

[40] D. A. Cantane, F. E. R. Oliveira, S. F. Santos, F. H. B. Lima, *Appl. Catal. B-Environ.* **2013**, *136*, 351-360.

[41] K. D. Beard, D. Borrelli, A. M. Cramer, D. Blom, J. W. Van Zee, J. R. Monnier, *ACS Nano*, **2009**, *3*, 2841-2853.

[42] F. Maillard, L. Dubau, J. Durst, M. Chatenet, J. Andre, E. Rossionot, *Electrochem. Commun.* **2010**, *12*, 1161-1164.

[43] L. Dubau, M. Lopez-Haro, L. Castanheira, J. Durst, M. Chatenet, P. Bayle-Guillemaud, L. Guetaz, N. Caque, E. Rossinot, F. Maillard, *Appl. Catal. B-Environ.* **2013**, *142*, 801-808.

[44] M. Lopez-Haro, L. Dubau, L. Guetaz, P. Bayle-Guillemaud, M. Chatenet, J. Andre, N. Caque, E. Rossinot, F. Maillard, *Appl. Catal. B-Environ.* **2014**, *152*, 300-308.

[45] J. Zhang, M. B. Vukmirovic, Y. Xu, M. Mavrikakis, R. R. Adzic, *Angew. Chem. Int. Ed.* **2005**, *44*, 2132-2135.

[46] L. Zhang, R. Iyyamperumal, D. F. Yancey, R. M. Crooks, G. Henkelman, *ACS Nano*, **2013**, *7*, 9168-9172.

[47] C. Wang, D. van der Vliet, K. L. More, N. J. Zaluzec, S. Peng, S. Sun, H. Daimon, G. Wang, J. Greeley, J. Pearson, A. P. Paulikas, G. Karapetrov, D. Strmcnik, N. M. Markovic, V. R. Stamenkovic, *Nano Lett.* **2011**, *11*, 919-926.

[48] J. Yang, X. Chen, X. Yang, J. Y. Ying, *Energy Environ. Sci.* **2012**, *5*, 8976-8981.

[49] X. Sun, D. Li, Y. Ding, W. Zhu, S. Guo, Z. L. Wang, S. Sun, *J. Am. Chem. Soc.* **2014**, *136*, 5745-5749.

[50] G. Wang, B. Huang, L. Xiao, Z. Ren, H. Chen, D. Wang, H. D. Abruna, J. Lu, L. Zhuang, *J. Am. Chem. Soc.* **2014**, *136*, 9643-9649.

[51] Y. Kang, J. Snyder, M. Chi, D. Li, K. L. More, N. M. Markovic, V. R. Stamenkovic, *Nano Lett.* **2014**, DOI: 10.1021/nl5028205

[52] R. Loukrakpam, B. N. Wanjala, J. Yin, B. Fang, J. Luo, M. Shao, L. Protsailo, T. Kawamura, Y. Chen, V. Petkov, C-J Zhong, *ACS Catal.* **2011**, *1*, 562-572.

[53] R. Loukrakpam, S. Shan, V. Petkov, L. Yang, J. Luo, C-J Zhong, *J. Phys. Chem. C* **2013**, *117*, 20715-20721.

[54] Y. Ma, P. B. Balbuena, *J. Phys. Chem. C* **2013**, *117*, 23224-23234.

[55] G. Jerkiewicz, *Electrocatal.* **2010**, *1*, 179-199.

[56] P. Urchaga, S. Baranton, C. Coutanceau, G. Jerkiewicz, *Langmuir,* **2012**, *28*, 3658-3663.

[57] L. Zhang, C. M. B. Holt, E. J. Luber, B. C. Olsen, H. Wang, M. Danaie, X. Cui, X. Tan, V. W. Lui, W. P. Kalisvaart, D. Mitlin, *J. Phys. Chem. C* **2011**, *115*, 24381-24393.

[58] M. Nesselberger, M. Roefzaad, R. F. Hamou, P. U. Biedermann, F. F. Schweinberger, S. Kunz, K. Schloegl, G. K. H. Wiberg, S. Ashton, U. Heiz, K. J. J. Mayrhofer, M. Arenz, *Nat. Mater.* **2013**, *12*, 919-924.

[59] M. Shao, A. Peles, K. Shoemaker, *Nano Lett.* **2011**, *11*, 3714-3719.

[60] A. V. Ruban, H. L. Skriver, J. K. Norskov, *Phys. Rev. B* **1999**, *59*, 15990-16000.

[61] M. Weinert, R. E. Watson, *Phys. Rev. B* **199**5, *51*, 17168-17180.

[62] B. Hammer, Y. Morikawa, J. K. Norskov, *Phys. Rev. Lett.* **1996**, *76*, 2141-2144.

[63] M. Wakisaka, S. Mitsui, Y. Hirose, K. Kawashima, H. Uchida, M. Watanabe, *J. Phys. Chem. B* **2006**, *110*, 23489-23496.

[64]T. Toda, H. Igarashi, H. Uchida, M. Watanabe, *J. Electrochem. Soc.* **1999**, *146*, 3750-3756.

[65] J. A. Rodriguez, D. W. Goodman, *Science* **1992**, *257*, 897-903.

[66] V. R. Stamenkovic, B. S. Mum, M. Arenz, K. J. J. Mayrhofer, C. A. Lucas, G. Wang, P. N. Ross, N. M. Markovic, *Nat. Mater.* **2007**, *6*, 241-247.

[67] D. F. van der Vliet, C. Wang, D. Li, A. P. Paulikas, J. Greeley, R. B. Rankin, D. Strmcnik, D. Tripkovic, N. M. Markovic, V. R. Stamenkovic, *Angew. Chem. Int. Ed.* **2012**, *51*, 3139-3142.

[68] V. R. Stamenkovic, B. Fowler, B. S. Mum, G. Wang, P. N. Ross, C. A. Lucas, N. M Markovic, *Science* **2007**, *315*, 493-497.

[69] N. M. Markovic, P. N. Ross, Surf. Sci. Rep. **2002**, 45, 121–229.

[70] C. Cui, L. Gan, M. Heggen, S. Rudi, P. Strasser, *Nat. Mater.* **2013**, *12*, 765-771.

[71] H. C. Ham, D. Manogaran, K. H. Lee, K. Kwon, S. Jin, D. J. You, C. Pak, G. S. Hwang, *J. Chem. Phys.* **2013**, *139*, 201104.

[72] K. Sasaki, H. Naohara, Y. Choi, Y. Cai, W-F Chen, P. Liu, R. R. Adzic, *Nat. Commun.* **2012**, *3*, 1115.

[73] M. Hu, D. P. Linder, M. B. Nardelli, A. Striolo, *J. Phys. Chem. C* **2013**, *117*, 15050-15060.

[74] S. G. Rinaldo, J. Stumper, M. Eikerling, *J. Phys. Chem. C* **2010**, *114*, 5773-5785.

Summary

Nowadays, the increasing concerns of the limited traditional energy sources e.g. fossil fuels and the associated environmentally unfriendly emission demand the adoption of renewable energy sources and clean energy carriers. The use of hydrogen produced in a sustainable manner, such as from solar or wind power, has been proposed as a promising energy carrier. To realize the future energy system based on hydrogen requires both reliable mechanisms for storage of the hydrogen and high efficient energy conversion to electricity. To this end, we utilized thin films as model systems to develop various alloys and composites for application of solid-state hydrogen storage and proton exchange membrane fuel cell (PEMFCs) cathode electrocatalysts. This thesis therefore encompasses aspects of alloy design, fabrication and characterization of thin films to enhance hydrogen storage kinetics and thermodynamics in magnesium hydride and to enhance the catalytic efficacy and corrosion stability of platinum-based electrocatalysts towards oxygen reduction reaction.

Chapter 2 describes the development of various bilayer Pd/X (X = Ti, Nb, Ta) surface catalysts that have been used for all films of Mg-based alloys and composites in this thesis. The selected interlayer, which forms stable hydride both during absorption and during desorption, reduces the rate of intermetallic formation between Mg and Pd, allowing the Pd to stay catalytically active. The Pd coating is also effective to prevent the underlying alloy film from oxidation during the transfer/storage before the hydrogen sorption measurement.

Chapter 3 describes a new bimetallic Nb-V catalyst for enhancing the hydrogen storage kinetics of magnesium hydride. Magnesium hydride combined with bimetallic Nb-V catalyst displays remarkably rapid and stable low temperature (200 °C) hydrogen storage kinetics even after 500 full volumetric absorption/desorption cycles. The system is also able to fairly rapidly absorb hydrogen at room temperature at a pressure of 1 bar. This unprecedented absorption behavior was demonstrated for 20 cycles. We employed extensive cryo-stage TEM analysis on fully and partially sorbed materials to provide insight into the rapid Mg to MgH_2 phase transformation. After extended cycling of what

was initially a 1.5 μm thick fully dense alloy film, the sample structure becomes analogous to that of a weakly agglomerated nanocomposite powder. The cycled Mg-V-Nb structure consists of a dense distribution of catalytic Nb-V nanocrystallites covering the surfaces of larger Mg and MgH_2 particles. The partially absorbed 20 °C and 200 °C microstructures both show this morphology. TEM results combined with Johnson-Mehl-Avrami-type kinetic analysis point to the surface catalyst distribution and stability against coarsening as being a key influence on the two-stage hydriding kinetics. Remarkably, the mean size of the $Nb_{0.5}V_{0.5}H$ nanocrystallites stays essentially invariant throughout cycling; it is 3 nm after 45 cycles and 4 nm after 500 cycles. A mechanistic description is provided for the cycling-induced microstructural evolution in the ternary alloy as well as in the binary baselines.

Chapter 4 describes the hydrogen storage properties of Mg rich ternary Mg-Ni-Cu films using binary Mg-Ni and Mg-Cu as baselines, and aims to elucidate the precise influences of alloying element Cu on the hydrogen sorption kinetics, thermodynamics and cycleability. Mg-rich Mg-Ni-(Cu) alloys show two stages during absorption. The first stage due to the absorption of Mg not alloyed in the form of Mg_2Ni and Mg_2Cu is very quick, but the second one due to the absorption of intermetallic Mg_2Ni and/or Mg_2Cu is significantly slower. This sequence is confirmed by XRD characterizations at different absorption stages. The rapid first stage absorption is mainly catalyzed by the intermetallic phase Mg_2Ni. Cu substitution improves the desorption kinetics, but severely decreases the kinetics of the second absorption stage. Failure to completely absorb Mg_2Cu to MgH_2 and $MgCu_2$ in consecutive absorption cycles leads to complete loss of desorption-ability in binary Mg-15at.%Cu. XRD combined with TEM shows that segregation of Mg_2Cu towards the grain boundaries is responsible for this. Pressure-Composition Isotherms are used to examine the thermodynamic properties of the alloys. It is found that the Cu substitution has no influence on the plateau pressure of MgH_2 from free-Mg phase, but slightly increases the plateau pressure of LT-Mg_2NiH_4.

Chapter 5 describes a new metastable metal hydride with promising hydrogen storage properties. Body centered cubic (bcc) magnesium niobium hydride $(Mg_{0.75}Nb_{0.25})H_2$ possesses 4.5 wt.% hydrogen gravimetric density, with 4 wt.% being reversible. Volumetric hydrogen absorption measurements yield an enthalpy of hydride formation of -53 kJ mol^{-1} H_2, which indicates a significant thermodynamic destabilization relative to the baseline -77 kJ mol^{-1} H_2 for rutile MgH_2. The hydrogenation cycling kinetics are remarkable: At room temperature and 1 bar hydrogen it takes 30 minutes to absorb a 1.5 µm thick film at sorption cycle 1, and 1 minute at cycle 5. Reversible desorption is achieved in about 60 minutes at 175 °C. Using ab initio calculations we have examined the thermodynamic stability of metallic alloys with hexagonal close packed (hcp) versus bcc crystal structure. Moreover we have analyzed the formation energies of the alloy hydrides that are bcc, rutile or fluorite.

A key advancement target for PEMFCs cathode electrocatalysts is to simultaneously improve both their electrochemical activity and durability towards ORR. To this end, Chapter 6 describes the efficacy of a new highly electrically conductive support that comprises of a 0.5 nm titanium oxynitride film atomic layer deposition coated onto an array of carbon nanotubes. We consider support effects for pure Pt and for a Pt-50at.%Ni alloy, and demonstrate that the performance of pure Pt is tremendously enhanced by the interlayer while the performance of PtNi is not impacted. Upon the insertion of TiO_xN_y between Pt and CNTs there is a marked increase in the specific (0.314 to 0.522 $mA.cm^{-2}_{Pt}$) and mass activity (0.110 to 0.195 $A.mg_{Pt}^{-1}$). The interlayer also dramatically improves the durability of pure Pt, going from 25% to 9.7% loss in electrochemical surface area, and 42.7% to 20.1% loss in specific activity, following 10,000 cycles of 0.6 to 1.1 V. We utilize XPS and TEM to demonstrate that the catalyst - support chemical interaction is much stronger for Pt on oxynitride versus on carbon, but remains on par for PtNi on either support. For pure Pt, the oxynitride induces a downshift in the d-band center. The oxynitride also changes the catalyst particle size distribution, reducing the number of the less active and less stable ultrafine Pt particles and of the large ones that serve as "dead weight" for mass activity. Calculations based on density functional (DFT) theory add complementary insight regarding the compositional segregation occurring at the alloy catalyst – support interface.

Chapter 7 describes the oxygen reduction reaction electrocatalytic activity and the corrosion stability of several ternary Pt-Au-Co and Pt-Ir-Co alloys, with Pt-Au-Co having never been previously studied for ORR. The addition of Au fine-tunes the lattice strain and the surface electronic structure to enable activity and cycling stability that is unachievable in Pt–25at.%Co (state-of-the-art binary baseline). The ternary alloys exhibit a volcano-type dependence of catalytic efficacy on the content of Au or Ir. Pt–2.5at.%Au–25at.%Co alloy shows a specific activity of 1.41 mA cm^{-2} at 0.95 V, which is 16% and 404% higher than identically synthesized Pt-Co and pure Pt, respectively. This enhancement is promising as compared to a range of previously published Pt "skeleton" and Pt "skin" alloys, and is in fact the most optimum reported for a skeleton-type system. The catalysts exhibit dramatically improved corrosion stability with increasing levels of Au or Ir substitution, with the specific activity of all the ternary alloys being superior to that of Pt–Co after 100,000 potential cycles of 0.6 - 1.0 V. For instance, post-cycled Pt–10at.%Au–25at.%Co shows a specific activity of 0.63 mA cm^{-2}, which is 140% higher than Pt-Co and 439% higher than Pt. HRTEM and XPS shows that Au alloying promotes the formation of an atomically thin Pt-Au-rich surface layer, which imparts kinetic stabilization against the dissolution of the less noble solute component.

Bibliography

[1] F. Barbir, PEM fuel cells: theory and practice, Elsevier Academic Press, London, 2005.

[2] P. H. L. Notten, Rechargeable nickel-metal hydride batteries: a successful new concept, in: F. Grandjean, G. J. Long, K. H. J. Buschow (Editors), Interstitial Intermetallic Alloys, NATO ASI Series E, vol. 281, 1995.

[3] R. F. Nelson, J. Power Sources, 2000, 91, 2-26.

[4] The US Department of Energy (DOE), Office of Energy Efficiency & Renewable Energy, http://energy.gov/eere/fuelcells/hydrogen-storage-current-technology.

[5] The US Department of Energy (DOE), Office of Energy Efficiency & Renewable Energy, http://energy.gov/eere/fuelcells/gaseous-and-liquid-hydrogen-storage.

[6] The US Department of Energy (DOE), Office of Energy Efficiency & Renewable Energy, http://energy.gov/eere/fuelcells/materials-based-hydrogen-storage.

[7] J. Graetz, Chem. Soc. Rev. 2009, 38, 73-82.

[8] T. Graham, Phil. Trans. R. Soc. 1866, 156, 399-439.

[9] W. M. Müller, J. P. Blackledge, J. J. Libowitz, Metal hydrides, Academic press, New York, 1968.

[10] The US Department of Energy (DOE), Office of Energy Efficiency & Renewable Energy, http://energy.gov/eere/fuelcells/chemical-hydrogen-storage.

[11] The US Department of Energy (DOE), Office of Energy Efficiency & Renewable Energy, http://energy.gov/eere/fuelcells/carbon-based-materials-high-surface-area-sorbents-and-new-materials-and-concepts.

[12] D. Pukazhselvan, V. Kumar, S. K. Singh, Nano Energy 2012, 1, 566-589.

[13] X. Tan, L. Wang, C. M. B. Holt, B. Zahiri, M. H. Eikerling, D. Mitlin, Phys. Chem. Chem. Phys. 2012, 14, 10904-10909.

[14] P. P. Edwards, V. L. Kuznetsov, W. I. F. David, Phil. Trans. R. Soc. A 2007, 365, 1043-1056.

[15] A. J. Du, S. C. Smith, X. D. Yao, G. Q. Lu, J. Phys. Chem. B 2005, 109, 18037-18041.

[16] G. Wu, J. Zhang, Q. Li, Y. Wu, K. Chou, X. Bao, Comput.Mater.Sci. 2010, 49, S144-S149.

[17] S. Hao, D. S. Sholl, Appl. Phys. Lett. 2008, 93, 251901.

[18] H. G. Schimmel, G. J. Kearley, J. Huot, F. M. Mulder, J. Alloy. Compd. 2005, 404-406, 235-237.

[19] M. Danaie, S. X. Tao, P. Kalisvaart, D. Mitlin, Acta Mater. 2010, 58, 3162-3172.

[20] X. Tan, B. Zahiri, C. M. B. Holt, A. Kubis, D Mitlin, Acta Mater. 2012, 60, 5646-5661

[21] W. P. Kalisvaart, C. T. Harrower, J. Haagsma, B. Zahiri, E. J. Luber, C. Ophus, E. Poirier, H. Fritzsche, D. Mitlin, Int. J. Hydrogen Energ. 2010, 35, 2091-2103.

[22] W. P. Kalisvaart, A. Kubis, M. Danaie, B. S. Amirkhiz, D. Mitlin, Acta Mater. 2011, 59, 2083-2095.

[23] A. Borgschulte, R. Gremaud, Phys. Rev. B 2008, 78, 094106.

[24] M. Dornheim, N. Eigen, G. barkhordarian, T. Klassen, R. Bormann, Adv. Eng. Mater. 2006, 8, 377-385.

[25] B. Sakintuna, F. Lamari-Darkrim, M. Hirscher, Int. J. Hydrogen Energm 2007, 32, 1121-1140.

[26] R. Gremaud, C. P. Broedersz, A. Borgschulte, M. J. van Setten, H. Schreuders, M. Slaman, B. Dam, R. Griessen, Acta Mater. 2010, 58, 658-668.

[27] S. X. Tao, P. H. L. Notten, R. A. van Santen, A. P. J. Jansen, Phy.s Rev. B 2010, 82, 125448.

[28] M. G. Shelyapina, D. Fruchart, Solid State Phenom. 2011, 170, 227-231.

[29] M. Dornheim, S. Doppiu, G. Barkhordarian, U. Boesenberg, T. Klassen, O. Gutfleisch, R. Bormann, Scripta Mater. 2007, 56, 841-846.

[30] A. Baldi, M. Gonzalez-Silveira, V. Palmisano, B. Dam, R. Griessen, Phys. Rev. Lett. 2009, 102, 226102.

[31] L. P. A. Mooij, A. Baldi, C. Boelsma, K. Shen, M. Wagemaker, Y. Pivak, H. Schreuders, R. Griessen, B. Dam, Adv. Energy Mater. 2011, 1, 754-758.

[32] http://www.fueleconomy.gov

[33] F. T. Wagner, B. Lakshmanan, M. F. Mathias, J. Phys. Chem. Lett. 2010, 1, 2204-2219.

[34] M. K. Debe, Nature 2012, 486, 43-51.

[35] T. Maiyalagan, K. A. Jarvis, S. Therese, P. J. Ferreira, A. Manthiram, Nature Commun. 2014, 5, 3949.

[36] a) D. Yu, Y. Xue, L. Dai, J. Phys. Chem. Lett. 2012, 3, 2863-2870; b) I-Y Jeon, H-J Choi, S-M Jung, J-M Seo, M-J Kim, L. Dai, J-B Baek, J. Am. Chem. Soc. 2013, 135, 1386-1393; c) H. Zhong, H. Zhang, Z. Xu, Y. Tang, J. Mao, ChemSusChem, 2012, 5, 1698-1702.

[37] a) Y. Liang, H. Wang, P. Diao, W. Chang, G. Hong, Y. Li, M. Gong, L. Xie, J. Zhou, J. Wang, T. Z. Regier, F. Wei, H. Dai, J. Am. Chem. Soc. 2012, 134, 15849-15857; b) Z. Yang, X. Zhou, Z. Jin, Z. Liu, H. Nie, X. Chen, S. Huang, Adv. Mater. 2014, 26, 3156-3161.

[38] P. Strasser, S. Koh, T. Anniyev, J. Greeley, K. More, C. Yu, Z. Liu, S. Kaya, D. Nordlund, H. Ogasawara, M. F. Toney, A. Nilsson, Nature Chem. 2010, 2, 454-460.

[39] U. Martinez, A. Serov, M. Padilla, P. Atanassov, ChemSusChem 2014, 7, 2351 – 2357.

[40] I. E. L. Stephens, A. S. Bondarenko, U. Gronbjerg, J. Rossmeisl, I. Chorkendorff, Energy Environ. Sci. 2012, 5, 6744-6762.

[41] J. C. Meier, C. Galeano, I. Katsounaros, A. A. Topalov, A. Kostka, F. Schuth, K. J. J. Mayrhofer, ACS Catal. 2012, 2, 832-843.

[42] Y. Shao, G. Yin, Y. Gao, J. Power Sources, 2007, 171, 558-566.

[43] A. Baldi, R. Gremaud, D. M. Borsa, C. P. Balde, A. M. J. van der Eerden, G. L. Kruijtzer, et al. Int. J. Hydrogen Energ. 2009, 34, 1450-1457.

[44] Y. Wang, W. Hua, J. Qu, X. Li, Int. J. Hydrogen Energ. 2008, 33, 7207-7213.

[45] J. Qu, Y. Wang, L. Xie, J. Zheng, Y. Liu, X. Li, Int. J. Hydrogen Energ. 2009, 34, 1910-1915.

[46] P. Vermeulen, P. C. J. Graat, H. J. Wondergem, P. H. L. Notten, Int. J. Hydrogen Energ. 2008, 33, 5646-5650.

[47] H. Fritzsche, M. Saoudi, J. Haagsma, C. Ophus, E. Luber, C. T. Harrower, et al. Appl. Phys. Lett. 2008, 92, 12917.

[48] A. Baldi, R. Gremaud, D. M. Borsa, C. P. Balde, A. M. J. van der Eerden, G. L. Kruijtzer, et al. Int. J. Hydrogen Energ. 2008, 33, 3188-3192.

[49] A. Sepulveda, A. F. Lopeandia, R. Domenech-Ferrer, G. Garcia, F. Pi, J. Rodriguez-Viejo, et al. Int. J. Hydrogen Energ. 2008, 33, 2729-2737.

[50] J. L. Slack, J. C. W. Locke, S. W. Song, J. Ona, T. J. Richardson, Sol. Energ. Mat. Sol. C 2006, 90, 485-490.

[51] J. Greely, M. Mavrikakis, Nat. Mater. 2004, 3, 810-815.

[52] A. Remhof, G. Song, K. Theis-Brohl, H. Zabel, Phys. Rev. B 1997, 56, R2897.

[53] S. J. van der Molen, J. W. J. Kerssemakers, J. H. Rector, N. J. Koeman, B. Dam, R. Griessen, J Appl. Phys. 1999, 86, 6107.

[54] A. T. M. van Gogh, S. J. van der Molen, J. W. J. Kerssemakers, N. J. Koeman, R. Griessen, Appl. Phys. Lett. 2000, 77, 815-817.

[55] T. J. Richardson, J. L. Slack, R. D. Armitage, R. Kostecki, B. Farangis, M. D. Rubin, Appl. Phys. Lett. 2001, 78, 3047-3049.

[56] A. Borgschulte, R. J. Westerwaal, J. H. Rector, B. Dam, R. Griessen, J. Schoenes, Phys. Rev. B 2004, 70, 155414.

[57] M. Pasturel, M. Slaman, D. M. Borsa, H. Schreuders, B. Dam, R. Griessen, et al. Appl. Phys. Lett. 2006, 89, 021913.

[58] A. Borgschulte, R. Gremaud, S. de Man, R. J. Westerwaal, J. H. Rector, B. Dam, et al. Appl. Surf. Sci. 2006, 253, 1417-1423.

[59] D. M. Borsa, A. Baldi, M. Pasturel, H. Schreuders, B. Dam, R. Griessen, et al. Appl. Phys. Lett. 2006, 88, 241910.

[60] G. Garcia, R. Domenech-Ferrer, F. Pi, J. Santiso, J. Rodriguez-Viejo, J Comb. Chem. 2007, 9, 230-236.

[61] M. Pasturel, R. J. Wijngaarden, W. Lohstroh, H. Schreuders, M. Slaman, B. Dam, et al. Chem. Mater. 2007, 19, 624-633.

[62] R. Hoogeveen, M. Moske, H. Geisler, K. Samwer, Thin Solid Films 1996, 275, 203-206.

[63] N. W. Ockwig, T. M. Nenoff, Chem. Rev. 2007, 107, 4078-4110.

[64] T. B. Massalski, editor. Binary alloy phase diagrams, 2nd ed. Materials Park, Ohio: ASM International; 1990.

[65] B. S. Amirkhiz, M. Danaie, D. Mitlin, Nanotechnology 2009, 20, 204016.

[66] M. Danaie, D. Mitlin, J. Alloy. Compd. 2009, 476, 590-598.

[67] J. Huot, J. F. Pelletier, G. Liang, M. Sutton, R. Schulz, J. Alloy. Compd. 2002, 330–332, 727-731.

[68] G. Alefeld, J. Volkl, editors. Hydrogen in metals I (Topics in applied physics). Berlin: Springer-Verlag; 1978. p. 266–9.

[69] H. Fritzsche, C. Ophus, C. T. Harrower, E. Luber, D. Mitlin, Appl. Phys. Lett. 2009, 94, 241901.

[70] K. F. Aguey-Zinsou, J. R. Ares-Fernandez, Energ. Environ. Sci. 2010, 3, 526-543.

[71] T. K. Nielsen, F. Besenbacher, T. R. Jensen, Nanoscale 2011, 3, 2086-2098.

[72] R. Bardhan, A. M. Ruminski, A. Brand, J. J. Urban, Energ. Environ. Sci. 2011, 4, 4882-4895.

[73] H. Shao, G. Xin, J. Zheng, X. Li, E. Akiba, Nano Energy 2012, 1, 590-601.

[74] I. P. Jain, C. Lal, A. Jain, Int. J. Hydrogen Energ. 2010, 35, 5133-5144.

[75] R. Gosalawit-Utke, T. K. Nielsen, I. Saldan, D. Laipple, Y. Cerenius, T. R. Jensen, T. Klassen, M. Dornheim, J. Phys. Chem. C 2011, 115, 10903-10910.

[76] R. V. Denys, A. B. Riabov, J. P. Maehlen, M. V. Lototsky, J. K. Solberg, V. A. Yartys, Acta Mater. 2009, 57, 3989-4000.

[77] S. D. Beattie, U. Setthanan, G. S. McGrady, Int. J. Hydrogen Energ. 2011, 36, 6014-6021.

[78] D. L. Croston, D. M. Grant, G. S. Walker, J. Alloy. Compd. 2010, 492, 251-258.

[79] B. S. Amirkhiz, M. Danaie, D. Mitlin, Nanotechnology 2009, 20, 204016.

[80] S. X. Tao, W. P. Kalisvaart, M. Danaie, D. Mitlin, P. H. L. Notten, R. A. Van Santen, A. P. J. Jansen, Int. J. Hydrogen Energ. 2011, 36, 11802-11809.

[81] P. K. Pranzas, U. Bosenberg, F. Karimi, M. Munning, O. Metz, C. B. Minella, H. W. Schmitz, F. Beckmann, U. Vainio, D. Zajac, E. Welter, T. R. Jensen, Y. Cerenius, R. Bormann, T. Klassen, M. Dornheim, A. Schreyer, Adv. Eng. Mater. 2011, 13, 730-736.

[82] H. Fritzsche, C. Ophus, C. T. Harrower, E. Luber, D. Mitlin, Appl. Phys. Lett. 2009, 94, 241901.

[83] T. E. C. Price, D. M. Grant, V. Legrand, G. S. Walker, Int. J. Hydrogen Energ. 2010, 35, 4154-4161.

[84] R. Gremaud, C. P. Broedersz, A. Borgschulte, M. J. van Setten, H. Schreuders, M. Slaman, B. Dam, R. Griessen, Acta Mater. 2010, 58, 658-668.

[85] S. X. Tao, P. H. L. Notten, R. A. van Santen, A. P. J. Jansen, Phy.s Rev. B 2010, 82, 125448.

[86] M. G. Shelyapina, D. Fruchart, Solid State Phenom. 2011, 170, 227-231.

[87] A. Baldi, M. Gonzalez-Silveira, V. Palmisano, B. Dam, R. Griessen, Phys. Rev. Lett. 2009, 102, 226102.

[88] L. P. A. Mooij, A. Baldi, C. Boelsma, K. Shen, M. Wagemaker, Y. Pivak, H. Schreuders, R. Griessen, B. Dam, Adv. Energy Mater. 2011, 1, 754-758.

[89] X. F. Liu, G. S. McGrady, H. W. Langmi, C. M. Jensen, J. Am. Chem. Soc. 2009, 131, 5032-5033.

[90] W. P. Kalisvaart, C. T. Harrower, J. Haagsma, B. Zahiri, E. J. Luber, C. Ophus, E. Poirier, H. Fritzsche, D. Mitlin, Int. J. Hydrogen Energ. 2010, 35, 2091-2103.

[91] H. Shao, M. Felderhoff, F. Schuth, C. Weidenthaler, Nanotechnology 2011, 22, 235401.

[92] A. Fernandez, E. Deprez, O. Friedrichs, Int. J. Hydrogen Energ. 2011, 36, 3932-3940.

[93] Z. Zlatanova, T. Spassov, G. Eggeler, M. Spassova, Int. J. Hydrogen Energ. 2011, 36, 7559-7566.

[94] H. W. Langmi, G. S. McGrady, X. F. Liu, C. M. Jensen, J. Phys. Chem. C 2010, 114, 10666-10669.

[95] K. J. Jeon, H. R. Moon, A. M. Ruminski, B. Jiang, C. Kisielowski, R. Bardhan, J. J. Urban, Nat. Mater. 2011, 10, 286-290.

[96] W. P. Kalisvaart, A. Kubis, M. Danaie, B. S. Amirkhiz, D. Mitlin, Acta Mater. 2011, 59, 2083-2095.

[97] V. A. Vons, A. Anastasopol, W. J. Legerstee, F. M. Mulder, S. W. H. Eijt, A. Schmidt-Ott, Acta Mater. 2011, 59, 3070-3080.

[98] Y. Liu, G. C. Wang, Nanotechnology 2012, 23, 025401.

[99] C. Zlotea, C. Chevalier-Cesar, E. Leonel, E. Leroy, F. Cuevas, P. Dibandjo, C. Vix-Guterl, T. Martens, M. Latroche, Faraday Discuss 2011, 151, 117-131.

[100] A. Anastasopol, T. V. Pfeiffer, A. Schmidt-Ott F. M. Mulder, S. W. H. Eijt, Appl. Phys. Lett. 2011, 99, 194103.

[101] M. Danaie, C. Mauer, D. Mitlin, J. Huot, Int. J. Hydrogen Energ. 2011, 36, 3022-3036.

[102] J. Lang, J. Huot, J. Alloy. Compd. 2011, 509, L18-L22.

[103] A. Revesz, A. Kis-Toth, L. K. Varga, E. Schafler, I. Bakonyi, T. Spassov, Int. J. Hydrogen Energ. 2012, 37, 5769.

[104] A. Baldi, B. Dam, J. Mater. Chem. 2011, 21, 4021-4026.

[105] Z. P. Tan, C. Chiu, E. J. Heilweil, L. A. Bendersky, Int. J. Hydrogen Energ. 2011, 36, 9702-9713..

[106] H. Oguchi, Z. Tan, E. J. Heilweil, L. A. Bendersky, Int. J. Hydrogen Energ. 2010, 35, 1296-1299.

[107] B. Zahiri, B. S. Amirkhiz, M. Danaie, D. Mitlin, Appl. Phys. Lett. 2010, 96, 013108.

[108] B. Zahiri, B. S. Amirkhiz, D. Mitlin, Appl. Phys. Lett. 2010, 97, 083106.

[109] H. Fritzsche, W. P. Kalisvaart, B. Zahiri, R. Flacau, D. Mitlin, Int. J. Hydrogen Energ. 2012, 37, 3540-3547.

[110] P. Kalisvaart, E. Luber, H. Fritzsche, D. Mitlin, Chem Commun 2011, 47, 4294-4296.

[111] J. F. Pelletier, J. Huot, M. Sutton, R. Schulz, A. R. Sandy, L. B. Lurio, S. G. J. Mochrie, Phys. Rev. B 2001, 63, 052103.

[112] G. Liang, J. Huot, S. Boily, A. Van Neste, R. Schulz, J. Alloy. Compd. 1999, 291, 295-299.

[113] S. A. Jin, J. H. Shim, J. P. Ahn, Y. W. Cho, K .W. Yi, Acta Mater 2007, 55, 5073-5079.

[114] H. Wipf, R. G. Barnes, Hydrogen in metals III; Springer: Berlin ; New York, 1997.

[115] H. G. Schimmel, J. Huot, L. C. Chapon, F. D. Tichelaar, F. M. Mulder, J. Am. Chem. Soc. 2005, 127, 14348-14354.

[116] X. H. Tan, C. T. Harrower, B. S. Amirkhiz, D. Mitlin, Int. J. Hydrogen Energ. 2009, 34, 7741-7748.

[117] M. Wojdyr, J. Appl. Crystallogr. 2010, 43, 1126-1128.

[118] M. Danaie, D. Mitlin, J. Alloy. Compd. 2009, 476, 590-598.

[119] M. Gonzalez-Silveira, R. Gremaud, A. Baldi, H. Schreuders, B. Dam, R. Griessen, Int. J. Hydrogen Energ. 2010, 35, 6959-6979.

[120] M. Avrami, J. Chem. Phys. 1941, 9, 177-184.

[121] J. W. Christian, The theory of transformations in metals and alloys; 2nd ed.; Pergamon Press: Oxford ; New York, 1975.

[122] B. Zahiri, M. Danaie, X. Tan, B. S. Amirkhiz, G. A. Botton, D. Mitlin, J. Phys. Chem. C 2012, 116, 3188-3199.

[123] P. S. Rudman, J. Appl. Phys. 1979, 50, 7195-7199.

[124] R. Griessen, T. Riesterer, Hydrogen in Intermetallic Compounds I; Springer-Verlag: Berlin Heidelberg NewYork London Paris Tokyo, 1988.

[125] T. Schober, Hydrogen Metal Systems I; Zurich: Trans Tech Publications, Ltd., 1996.

[126] H. Muller, K. Weymann, J. Less-Common Met. 1986, 119, 115-126.

[127] P. Vermeulen, A. Ledovskikh, D. Danilov, P. H. L Notten, Acta Mater. 2009, 57, 4967-4973.

[128] M. S. Conradi, M. P. Mendenhall, T. M. Ivancic, E. A. Carl, C. D. Browning, P. H. L. Notten, W. P. Kalisvaart, P. C. M. M. Magusin, R. C. Bowman, S. J. Hwang, N. L. Adolphi, J. Alloy. Compd. 2007, 446, 499-503.

[129] H. Fritzsche, M. Saoudi, J. Haagsma, C. Ophus, E. Luber, C. T. Harrower, et al. Appl. Phys. Lett. 2008, 92, 12917.

[130] T. Schober, Metallurgical Transactions A 1981, 12A, 951

[131] R. W. Hertzberg, Deformation and fracture mechanics of engineering materials; 4th ed.; J. Wiley & Sons: New York, 1996

[132] M. F. Ashby, L. M. Brown, Philos Mag 1963, 8, 1083-1103.

[133] M. F. Ashby, L. M. Brown, Philos Mag 1963, 8, 1649-1676.

[134] C. Zener, Tran. Amer. Inst. Min. Metall. Engrs. 175, 15.

[135] T. Gladman, Proc R Soc Lon Ser-A 1966, 294, 298-309.

[136] F. M. Mulder, S. Singh, S. Bolhuis, S. W. H. Eijt, J. Phys. Chem. C 2012, 116, 2001-2012.

[137] B. S. Amirkhiz, B. Zahiri, P. Kalisvaart, D. Mitlin, Int. J. Hydrogen Energ. 2011, 36, 6711-6722.

[138] M. Danaie, S. X. Tao, P. Kalisvaart, D. Mitlin, Acta Mater. 2010, 58, 3162-3172.

[139] M. Vittori Antisari, A. Aurora, D. Mirabile Gattia, A. Montone, Scripta Materialia 2009, 61, 1064-1067.

[140] C. Nishimura, M. Komaki, M. Amano, J. Alloy. Compd. 1999, 293, 329-333.

[141] H. G. Schimmel, G. J. Kearley, J. Huot, F. M. Mulder, J. Alloy. Compd. 2005, 404, 235-237.

[142] R. L. Corey, T. M. Ivancic, D. T. Shane, E. A. Carl, R. C. Bowman, J. M. B. von Colbe, M. Dornheim, R. Bormann, J. Huot, R. Zidan, A. C. Stowe, M. S. Conradi, J. Phys. Chem. C 2008, 112, 19784-19790.

[143] S. Q. Hao, D. S. Sholl, Appl. Phys. Lett. 2008, 93, 251901.

[144] J. Cermak, L. Kral, Acta Mater. 2008, 56, 2677-2686.

[145] W. P. Kalisvaart, C. T. Harrower, J. Haagsma, B. Zahiri, E. J. Luber, C. Ophus, E. Poirier, H. Fritzsche, D. Mitlin, Int. J. Hydrogen Energ. 2010, 35, 2091-2103.

[146] B. Zahiri, B. S. Amirkhiz, M. Danaie, D. Mitlin, Appl. Phys. Lett. 2010, 96, 013108.

[147] B. Zahiri, C. T. Harrower, B. S. Amirkhiz, D. Mitlin, Appl. Phys. Lett. 2009, 95, 013114.

[148] C. X. Shang, M. Bououdina, Y. Song, Z. X. Guo, Int. J. Hydrogen Energ. 2004, 29, 73-80.

[149] J. J. Reilly, R. H. Wiswall, Inorg. Chem. 1968, 7, 2254-2256.

[150] W. R. Myers, L. W. Wang, T. J. Richardson, M. D. Rubin, J. Appl. Phys. 2002, 91, 4879-4885.

[151] H. Y. Shao, K. Asano, H. Enoki, E. Akiba, J. Alloys Compd. 2009, 477, 301-306.

[152] J. Zhang, D. W. Zhou, L. P. He, P. Peng, J. S. Liu, J. Phys. Chem. Solids 2009, 70, 32-39.

[153] G. Liang, S. Boily, J. Huot, A. Van Neste, R. Schulz, J. Alloys Compd. 1998, 267, 302-306.

[154] K. Tanaka, Y. Kanda, M. Furuhashi, K. Saito, K. Kuroda, H. Saka, J. Alloys Compd. 1999, 295, 521-525.

[155] S. E. Guthrie, G. J. Thomas, D. Noreus, E. Ronnebro, Mat. Res. Soc. Symp. Proc. Materials Research Society, 1998

[156] J. J. Reilly, R. H. Wiswall, Inorg. Chem. 1967, 6, 2220-2223.

[157] A. Andreasen, M. B. Sorensen, R. Burkarl, B. Moller, A. M. Molenbroek, A. S. Pedersen, T. Vegge, T. R. Jensen, Appl. Phys. A-Mater. 2006, 82, 515-521.

[158] A. Zaluska, L. Zaluski, J. O. Strom-Olsen, J. Alloys Compd. 1999, 289, 197-206.

[159] H. Gu, Y. F. Zhu, L. Q. Li, Int. J. Hydrogen Energ. 2009, 34, 2654-2660.

[160] C. Milanese, A. Girella, G. Bruni, P. Cofrancesco, V. Berbenni, M. Villa, P. Matteazzi, A. Marini, Int. J. Hydrogen Energ. 2008, 33, 4593-4606.

[161] C. Milanese, A. Girella, G. Bruni, P. Cofrancesco, V. Berbenni, P. Matteazzi, A. Marini, Intermetallics 2010, 18, 203-211.

[162] X. H. Tan, C. T. Harrower, B. S. Amirkhiz, D. Mitlin, Int. J. Hydrogen Energ. 2009, 34, 7741-7748.

[163] H. P. Klug, L. E. Alexander, X-ray Diffraction Procedures; John Wiley and Sons, New York, 1974.

[164] A. T. W. Kempen, H. Nitsche, F. Sommer, E. J. Mittemeijer, Metal Mater. Trans. A 2002, 33, 1041-1050.

[165] F. Cuevas, J. F. Fernandez, J. R. Ares, F. Leardini, C. Sanchez, J. Phys. Chem. Solids 2010, 71, 1259-1263.

[166] L. Zaluski, A. Zaluska, J. O. Stromolsen, J. Alloys Compd. 1995, 217, 245-249.

[167] J. H. Woo, K. S. Lee, J. Electrochem. Soc. 1999, 146, 819-823.

[168] Y. Takahashi, H. Yukawa, M. Morinaga, J. Alloys Compd. 1996, 242, 98-107.

[169] S. Gorsse, G. J. Shiflet, Calphad-Computer Coupling of Phase Diagrams and Thermochemistry 2002, 26, 63-83.

[170] A. Karty, J. Grunzweiggenossar, P. S. Rudman, J. Appl. Phys. 1979, 50, 7200-7209.

[171] M. Pasturel, R. J. Wijngaarden, W. Lohstroh, H. Schreuders, M. Slaman, B. Dam, R. Griessen, Chem. Mater. 2007, 19, 624-633.

[172] D. Noreus, P. E. Werner, Acta Chem Scand A 1982, 36, 847-851.

[173] K-F Aguey-Zinsou, J-R Ares-Fernandez, Energy Environ. Sci. 2010, 3, 526-543.

[174] C. Weidenthaler, M. Felderhoff, Energy Environ. Sci. 2011, 4, 2495-2502.

[175] S. X. Tao, W. P. Kalisvaart, M. Danaie, D. Mitlin, P. H. L. Notten, R. A. van Santen, A. P. J. Jansen, Int. J. Hydrogen Energ. 2011, 36, 11802-11809.

[176] B. Zahiri, M. Danaie, X. H. Tan, B. S. Amirkhiz, G. A. Botton, D. Mitlin, J. Phys. Chem. C 2012, 116, 3188–3199.

[177] F. M. Mulder, S. Singh, S. Bolhuis, S. W. H. Eijt, J. Phys. Chem. C 2012, 116 2001–2012.

[178] R. Bardhan, A. M. Ruminski, A. Brand, J. J. Urban, Energy Environ. Sci. 2011, 4, 4882-4895.

[179] T. K. Nielsen, F. Besenbacher, T. R. Jensen, Nanoscale 2011, 3, 2086-2098.

[180] W. P. Kalisvaart, E. J. Luber, E. Poirier, C. T. Harrower, A. Teichert, D. Wallacher, N. Grimm, R. Steitz, H. Fritzsche, D. Mitlin, J. Phys. Chem. C 2012, 116, 5868−5880.

[181] V.A. Vons, A. Anastasopol, W.J. Legerstee, F.M. Mulder, S.W.H. Eijt, A. Schmidt-Ott, Acta Mater., 2011, 59, 3070-3080.

[182] F. Cuevas, D. Korablov, M. Latroche, Phys. Chem. Chem. Phys. 2012, 14, 1200-1211.

[183] H. Reardon, J. M. Hanlon, R. W. Hughes, A. Godula-Jopek, T. K. Mandal, D. H. Gregory, Energy Environ. Sci. 2012, 5, 5951-5979

[184] KJ Jeon, H. R. Moon, A. M. Ruminski, B. Jiang, C. Kisielowski, R. Bardhan, J. J. Urban, Nat. Mater. 2011, 10, 286-290.

[185] G. S. Walker, M. Abbas, D. M. Grant, C. Udeh, Chem. Commun. 2011, 47, 8001-8003.

[186] A. Baldi, M. Gonzalez-Silveira, V. Palmisano, B. Dam, R. Griessen, Phys. Rev. Lett. 2009, 102, 226102.

[187] C-J Chung, S-C Lee, J. R. Groves, E. N. Brower, R. Sinclair, B. M. Clemens, Phys. Rev. Lett. 2012, 108, 106102.

[188] S. X. Tao, P. H. L. Notten, R. A. van Santen, A. P. J. Jansen, Phys. Rev. B 2010, 82, 125448.

[189] L. P. A. Mooij, A. Baldi, C. Boelsma, K. Shen, M. Wagemaker, Y. Pivak, H. Schreuders, R. Griessen, B. Dam, Adv. Energy Mater. 2011, 1, 754-758.

[190] M. G. Shelyapina, D. Fruchart, Solid state Phenom. 2011, 170, 227-231.

[191] D. M. Borsa, R. Gremaud, A. Baldi, H. Schreuders, J. H. Rector, B. Kooi, P. Vermeulen, P. H. L. Notten, B. Dam, R. Griessen, Phys. Rev. B 2007, 75, 205408.

[192] T. Takasaki, D. Kyoi, N. Kitamura, S. Tanase, T. Sakai, J. Phys. Chem. B 2007, 111, 14102-14106.

[193] D. Moser, D. J. Bull, T. Sato, D. Noreus, D. Kyoi, T. Sakai, N. Kitamura, H. Yusa, T. Taniguchi, W. P. Kalisvaart, P. H. L. Notten, J. Mater. Chem. 2009, 19, 8150-8161.

[194] S. X. Tao, P. H. L. Notten, R. A. van Santen, A. P. J. Jansen, J. Alloy. Compd. 2011, 509, 210-216.

[195] D. Kyoi, N. Kitamura, H. Tanaka, A. Ueda, S. Tanase, T. Sakai, J. Alloy. Compd. 2007, 428, 268-273.

[196] S. Bao, Y. Yamada, K.Tajima, M. Okada, K. Yoshimura, Japanese J. Appl. Phys. 2007, 46, L13-L15.

[197] X. H. Tan, C. T. Harrower, B. S. Amirkhiz, D. Mitlin, Int. J. Hydrogen Energ. 2009, 34, 7741-7748.

[198] G. Kresse, D. Joubert, Phys. Rev. B 1999, 59, 1758–1775.

[199] P. E. Blöchl, O. Jepsen, O. K. Andersen, Phys. Rev. B 1994, 49, 16223–16233.

[200] F. R. de Boer, R. Boom, W. C. M. Mattens, A. R. Miedema, A. K. Niessen, Cohesion in metals: Transition metal alloys, Elsevier Science Publishers B.V., North-Holland, Amsterdam, 1988.

[201] K. Klyukin, M. G. Shelyapina, D. Fruchart, Solid State Phenom. 2011, 170, 298-301.

[202] Y. Fukai, The Metal-Hydrogen System, Springer Series in Materials Science, 2nd Ed., vol. 21, Springer Verlag, Berln, 2005.

[203] N. Novakovic, L Matovic, J. G. Novakovic, M. Manasijevic and N. Ivanovic, Mater. Sci. Eng. B. Solid., 2009, 165, 235-238.

[204] M. Danaie, S.X. Tao, W.P. Kalisvaart and D. Mitlin, Acta Mater. 2010, 58, 3162-3172.

[205] R. Zahiri, B. Zahiri, A. kubis, W. P. Kalisvaart, B. S. Amirkhiz, D. Mitlin, Int. J. Hydrogen Energ. 2012, 37, 4215-4226.

[206] J. Matsuda, H. Shao, Y. Nakamura, E. Akiba, Nanotechnology 2009, 20, 204015.

[207] H. Kim, J. Nakamura, H. Shao, Y. Nakamura, E. Akiba, K. W. Chapman, P. J. Chupas, T. Proffen, J. Phys. Chem. C 2011, 115, 20335-20341.

[208] M. K. Debe, Nature 2012, 486, 43-51.

[209] F. T. Wagner, B. Lakshmanan, M. F. Mathias, J. Phys. Chem. Lett. 2010, 1, 2204-2219.

[210] S. Guo, S. Zhang, S. Sun, Angew. Chem. Int. Ed. 2013, 52, 8526-8544.

[211] a) Y. Liang, H. Wang, P. Diao, W. Chang, G. Hong, Y. Li, M. Gong, L. Xie, J. Zhou, J. Wang, T. Z. Regier, F. Wei, H. Dai, J. Am. Chem. Soc. 2012, 134, 15849-15857; b) Z. Yang, X. Zhou, Z. Jin, Z. Liu, H. Nie, X. Chen, S. Huang, Adv. Mater. 2014, 26, 3156-3161.

[212] T. Maiyalagan, K. A. Jarvis, S. Therese, P. J. Ferreira, A. Manthiram, Nature Commun. 2014, 5, 3949.

[213] a) D. Yu, Y. Xue, L. Dai, J. Phys. Chem. Lett. 2012, 3, 2863-2870; b) I-Y Jeon, H-J Choi, S-M Jung, J-M Seo, M-J Kim, L. Dai, J-B Baek, J. Am. Chem. Soc. 2013, 135, 1386-1393; c) H. Zhong, H. Zhang, Z. Xu, Y. Tang, J. Mao, ChemSusChem, 2012, 5, 1698-1702.

[214] Y. Dong, Y. Wu, M. Liu, J. Li, ChemSusChem 2013, 6, 2016-2021.

[215] N. Danilovic, A. Vincent, J-L Luo, K. T. Chuang, R. Hui, A. R. Sanger, Chem. Mater. 2010, 22, 957-965.

[216] a) A. Serov, K. Artyushkova, P. Atanassov, Adv. Energy Mater. 2014, 4, 1301735; b) A. Serov, U. Tylus, K. Artyushkova, S. Mukerjee, P. Atanassov, Appl. Catal., B: Environ. 2014, 150, 179-186.

[217] A. M. Gomez-Marin, J. M. Feliu, ChemSusChem 2013, 6, 1091-1100.

[218] P. Strasser, S. Koh, T. Anniyev, J. Greeley, K. More, C. Yu, Z. Liu, S. Kaya, D. Nordlund, H. Ogasawara, M. F. Toney, A. Nilsson, Nature Chem. 2010, 2, 454-460.

[219] I. E. L. Stephens, A. S. Bondarenko, U. Gronbjerg, J. Rossmeisl, I. Chorkendorff, Energy Environ. Sci. 2012, 5, 6744-6762.

[220] J. Kibsgaard, Y. Gorlin, Z. Chen, T. F. Jaramillo, J. Am. Chem. Soc. 2012, 134, 7758-7765.

[221] V. D. Noto, E. Negro, S. Polizzi, F. Agresti, G. A. Giffin, ChemSusChem 2012, 5, 2451-2459.

[222] K. A. Kuttiyiel, K. Sasaki, Y. Choi, D. Su, P. Liu, R. R. Adzic, Energy Environ. Sci. 2012, 5, 5297-5304.

[223] a) B. Kinkead, J. van Drunen, M. T. Y. Paul, K. Dowling, G. Jerkiewicz, B. D. Gates, Electrocatal. 2013, 4, 179-186; b) G. Jerkiewicz, Electrocatal. 2010, 1, 179-199.

[224] U. Martinez, A. Serov, M. Padilla, P. Atanassov, ChemSusChem 2014, 7, 2351 – 2357.

[225] N. Danilovic, R. Subbaraman, K-C Chang, S. H. Chang, Y. Kang, J. D. Snyder, A. P. Paulikas, D. Strmcnik, Y-T Kim, D. J. Myers, V. R. Stamenkovic, N. M. Markovic, J. Phys. Chem. Lett. 2014, 5, 2474−2478.

[226] L. Su, W. Jia, C-M Li, Y. Lei, ChemSusChem 2014, 7, 361-378.

[227] S. Ye, M. Hall, P. He, ECS Trans. 2008, 16 (2), 2101-2113.

[228] B. Fang, M-S Kim, J. H. Kim, M. Y. Song, Y-J Wang, H. Wang, D. P. Wilkinson, J-S Yu, J. Mater. Chem. 2011, 21, 8066-8073.

[229] J. van Drunen, B. K. Pilapil, Y. Makonnen, D. Beauchemin, B. D. Gates, G. Jerkiewicz, ACS Appl. Mater. Interfaces 2014, 6, 12046–12061.

[230] S. Pylypenko, A. Borisevich, K. L. More, A. R. Corpuz, T. Holme, A. A. Dameron, T. S. Olson, H. N. Dinh, T. Gennett, R. O'Hayre, Energy Environ. Sci. 2013, 6, 2957-2964.

[231] Y. Shao, G. Yin, Y. Gao, J. Power Sources, 2007, 171, 558-566.

[232] J. C. Meier, C. Galeano, I. Katsounaros, A. A. Topalov, A. Kostka, F. Schuth, K. J. J. Mayrhofer, ACS Catal. 2012, 2, 832-843.

[233] K. J. J. Mayrhofer, J. C. Meier, S. J. Ashton, G. K. H. Wiberg, F. Kraus, M. Hanzlik, M. Arenz, Electrochem. Commun. 2008, 10, 1144-1147.

[234] J. Masa, A. Bordoloi, M. Muhler, W. Schuhmann, W. Xia, ChemSusChem 2012, 5, 523-525.

[235] X. Zhao, J. Zhu, L. Liang, J. Liao, C. Liu, W. Xing, J. Mater. Chem. 2012, 22, 19718-19725.

[236] A. G. Scheuermann, J. D. Prange, M. Gunji, C. E. D. Chidsey, P. C. Mclntyre, Energy Environ. Sci. 2013, 6, 2487-2496.

[237] K. Sasaki, L. Zhang, R. R. Adzic, Phys. Chem. Chem. Phys. 2008, 10, 159-167.

[238] L. Zhang, L. Wang, C. M. B. Holt, T. Navessin, K. Malek, M. H. Eikerling, D. Mitlin, J. Phys. Chem. C 2010, 114, 16463-16474.

[239] L. Zhang, L. Wang, C. M. B. Holt, B. Zahiri, Z. Li, K. Malek, T. Navessin, M. H. Eikerling, D. Mitlin, Energy Environ. Sci. 2012, 5, 6156-6172.

[240] A. Bonakdarpour, R. T. Tucker, M. D. Fleischauer, N. A. Beckers, M. J. Brett, D. P. Wilkinson, Electrochim. Acta 2012, 85, 492-500.

[241] M. Dou, M. Hou, H. Zhang, G. Li, W. Lu, Z. Wei, Z. Shao, B. Yi, ChemSusChem 2012, 5, 945-951.

[242] Y. Liu, W. E. Mustain, J. Am. Chem. Soc. 2013, 135, 530-533.

[243]Y. Luo, A. Habrioux, L. Calvillo, G. Granozzi, N. Alonso-Vante, ChemPhysChem 2014, 15, 2136 – 2144.

[244] D. C. Higgins, J-Y Choi, J. Wu, A. Lopez, Z. Chen, J. Mater. Chem. 2012, 22, 3727-3732.

[245] S. Dong, X. Chen, S. Wang, L. Gu, L. Zhang, X. Wang, X. Zhou, Z. Liu, P. Han, Y. Duan, H. Xu, J. Yao, C. Zhang, K. Zhang, G. Cui, L. Chen, ChemSusChem 2012, 5, 1712-1715.

[246] K. A. Kuttiyiel, K. Sasaki, Y. Choi, D. Su, P. Liu, R. R. Adzic, Nano Lett. 2012, 12, 6266-6271.

[247] J. Yin, L. Wang, C. Tian, T. Tan, G. Mu, L. Zhao, H. Fu, Chem. Eur. J. 2013, 19, 13979-13986.

[248] Y-J Wang, D. P. Wilkinson, J. Zhang, Dalton Trans. 2012, 41, 1187-1194.

[249] Y. P. Yu, W. Liu, S. X. Wu, S. W. Li, J. Phys. Chem. C 2012, 116, 19625−19629.

[250] Y. Qiu, K. Yan, S. Yang, L. Jin, H. Deng, W. Li, ACS Nano, 2010, 4, 6515-6526.

[251] X. Cui, M. Ma, W. Zhang, Y. Yang, Z. Zhang, Electrochem. Commun. 2008, 10, 367-371.

[252] N. C. Saha, H. G. Tompkins, J. Appl. Phys. 1992, 72, 3073-3079.

[253] S-I Choi, S. Xie, M. Shao, N. Lu, S. Guerrero, J. H. Odell, J. Park, J. Wang, M. J. Kim, Y. Xia, ChemSusChem 2014, 7, 1476-1483.

[254] J. Greeley, I. E. L. Stephens, A. S. Bondarenko, T. P. Johansson, H. A. Hansen, T. F. Jaramillo, J. Rossmeisl, I. Chorkendorff, J. K. Norskov, Nature Chem. 2009, 1, 552-556.

[255] a) C. Wang, N. M. Markovic, V. R. Stamenkovic, ACS Catal. 2012, 2, 891-898; b) C. Wang, D. Li, M. Chi, J. Pearson, R. B. Rankin, J. Greeley, Z. Duan, G. Wang, D. van der Vliet, K. L. More, N. M. Markovic, V. R. Stamenkovic, J. Phys. Chem. Lett. 2012, 3, 1668-1673.

[256] C. Chen, Y. Kang, Z. Huo, Z. Zhu, W. Huang, H. L. Xin, J. D. Snyder, D. Li, J. A. Herron, M. Mavrikakis, M. Chi, K. L. More, Y. Li, N. M. Markovic, G. A. Somorjai, P. Yang, V. R. Stamenkovic, Science 2014, 343, 1339-1343.

[257] D. Wang, H. L. Xin, R. Hovden, H. Wang, Y. Yu, D. A. Muller, F. J. DiSalvo, H. D. Abruna, Nature Mater. 2013, 12, 81-87.

[258] S. Prabhudev, M. Bugnet, C. Bock, G. A. Botton, ACS Nano, 2013, 7, 6103-6110.

[259] S. Guo, D. Li, H. Zhu, S. Zhang, N. M. Markovic, V. R. Stamenkovic, S. Sun, Angew. Chem. Int. Ed. 2013, 52, 3465-3468.

[260] M. K. Carpenter, T. E. Moylan, R. S. Kukreja, M. H. Atwan, M. M. Tessema, J. Am. Chem. Soc. 2012, 134, 8535-8542.

[261] C. Wang, M. Chi, G. Wang, D. van der Vliet, D. Li, K. More, H-H Wang, J. A. Schlueter, N. M. Markovic, V. R. Stamenkovic, Adv. Funct. Mater. 2011, 21, 147-152.

[262] Y. Liu, C. M. Hangarter, U. Bertocci, T. P. Moffat, J. Phys. Chem. C 2012, 116, 7848-7862.

[263] L. Yang, S. Shan, R. Loukrakpam, V. Petkov, Y. Ren, B. N. Wanjala, M. H. Engelhard, J. Luo, J. Yin, Y. Chen, C-J Zhong, J. Am. Chem. Soc. 2012, 134, 15048−15060.

[264] T. Wang, G. Mpourmpakis, W. W. Lonergan, D. G. Vlachos, J. G. Chen, Phys. Chem. Chem. Phys. 2013, 15, 12156-12164.

[265] a) S. H. Kang, Y-E Sung, W. H. Smyrl, J. Electrochem. Society 2008, 155, B1128-B1135; b) S. H. Kang, T-Y Jeon, H-S Kim, Y-E Sung, W. H. Smyrl, J. Electrochem. Society 2008, 155, B1058-B1065.

[266] M. Wojdyr, J. Appl. Cryst. 2010, 43, 1126-1128.

[267] L. Zhang, C. M. B. Holt, E. J. Luber, B. C. Olsen, H. Wang, M. Danaie, X. Cui, X. Tan, V. W. Lui, W. P. Kalisvaart, D. Mitlin, J. Phys. Chem. C 2011, 115, 24381-24393.

[268] G. Kresse, J. Hafner. Phys. Rev. B 1994, 49, 14251-14269.

[269] G. Kresse, J. Furthmüller, Comput. Mat. Sci. 1996, 6, 15-50.

[270] P. E. Blochl. Phys. Rev. B 1994, 50, 17953-17978.

[271] J. P. Perdew, J. A. Chevary, S. H. Vosko, K. A. Jackson, M. R. Pederson, D.J. Singh, and C. Fiolhais. Phys. Rev. B 1992, 46, 6671.

[272] J. P. Perdew, J. A. Chevary, S. H. Vosko, K. A. Jackson, M. R. Pederson, D. J. Singh, and C. Fiolhais. Phys. Rev. B 1993, 48, 4978.

[273] M. Wakisaka, S. Mitsui, Y. Hirose, K. Kawashima, H. Uchida, M. Watanabe, J. Phys. Chem. B 2006, 110, 23489-23496.

[274] T. Toda,H. Igarashi,H. Uchida, M. Watanabe, J. Electrochem. Soc. 1999, 146, 3750 – 3756.

[275] C. Ophus, E. Luber, D. Mitlin, Acta Mater. 2009, 57, 1327-1336.

[276] M. Shao, A. Peles, K. Shoemaker, Nano Lett. 2011, 11, 3714-3719.

[277] R. Jinnouchi, E. Toyoda, T. Hatanaka, Y. Morimoto, J. Phys. Chem. C 2010, 114, 17557-17568.

[278] L. Tang, B. Han, K. Persson, C. Friesen, T. He, K. Sieradzki, G. Ceder, J. Am. Chem. Soc. 2010, 132, 596-600.

[279] C. Cui, L. Gan, M. Heggen, S. Rudi, P. Strasser, Nature Mater. 2013, 12, 765-771.

[280] J. Solla-Gullon, P. Rodriguez, E. Herrero, A. Aldaz, J. M. Feliu, Phys. Chem. Chem. Phys. 2008, 10, 1359-1373.

[281] C. Wang, M. Chi, D. Li, D. Strmcnik, D. van der Vliet, G. Wang, V. Komanicky, K-C Chang, A. P. Paulikas, D. Tripkovic, J. Pearson, K. L. More, N. M. Markovic, V. R. Stamenkovic, J. Am.Chem. Soc. 2011, 133, 14396-14403.

[282] D. F. van der Vliet, C. Wang, D. Tripkovic, D. Strmcnik, X. F. Zhang, M. K. Debe, R. T. Atanasoski, N. M. Markovic, V. R. Stamenkovic, Nature Mater. 2012, 11, 1051-1058.

[283] D. F. van der Vliet, C. Wang, D. Li, A. P. Paulikas, J. Greeley, R. B. Rankin, D. Strmcnik, D. Tripkovic, N. M. Markovic, V. R. Stamenkovic, Angew. Chem. Int. Ed. 2012, 51, 3139-3142.

[284] V. Stamenkovic, T. J. Schmidt, P. N. Ross, N. M. Markovic, J. Electroanal. Chem. 2003, 554-555, 191-199.

[285] W. Wang, O. Savadogo, Z-F. Ma, J. Appl. Electrochem. 2012, 42, 857-866.

[286] V. R. Stamenkovic, B. S. Mun, K. J. J. Mayrhofer, P. N. Ross, N. M. Markovic, J. Rossmeisl, J. Greeley, J. K. Norskov, Angew. Chem. Int. Ed. 2006, 45, 2897-2901.

[287] H. S. Casalongue, S. Kaya, V. Viswanathan, D. J. Miller, D. Friebel, H. A. Hansen, J. K. Norskov, A. Nilsson, H. Ogasawara, Nature Commun. 2014, 4, 2817.

[288] N. Danilovic, R. Subbaraman, D. Strmcnik, A. P. Paulikas, D. Myers, V. R. Stamenkovic, N. M. Markovic, Electrocatal. 2012, 3, 221-229.

[289] M. Nesselberger, S. Ashton, J. C. Meier, I. Katsounaros, K. J. J. Mayrhofer, M. Arenz, J. Am. Chem. Soc. 2011, 133, 17428-17433.

[290] F. J. Perez-Alonso, D. N. McCarthy, A. Nierhoff, P. Hernandez-Fernan-dez, C. Strebel, I. E. L. Stephens, J. H. Nielsen, Ib Chorkendorff, Angew. Chem. Int. Ed. 2012, 51, 4641-4643.

[291] A. Anasasopoulos, J. C. Davies, L. Hannah, B. E. Hayden, C. E. Lee, C. Milhano, C. Mormiche, L. Offin, ChemSusChem 2013, 6, 1973-1982.

[292] C. Ophus, T. Ewalds, E. J. Luber, D. Mitlin, Acta Mater. 2010, 58, 5150-5159.

[293] S. G. Rinaldo, J. Stumper, M. Eikerling, J. Phys. Chem. C 2010, 114, 5773-5785.

[294] L. Xing, G. Jerkiewicz, D. Beauchemin, Analyt. Chim. Acta 2013, 785, 16-21.

[295] P. W. Voorhees, J. Statist. Phys. 1985, 38, 231-252.

[296] K. Yang, Y. Dai, B. Huang, S. Han, J. Phy. Chem. B 2006, 110, 24011-24014.

[297] C. Di Valentin, G. Pacchioni, A. Selloni, s. Livraghi, E. Giamello, J. Phys. Chem. B 2005, 109, 11414-11419.

[298] S. Livraghi, M. C. Paganini, E. Giamello, A. Selloni, C. Di Valentin, G. Pacchioni, J. Am. Chem. Soc. 2006, 128, 15666-15671.

[299] L. Hu, X. Hu, X. Wu, C. Du, Y. Dai, J. Deng, Physica B 2010, 405, 3337-3341.

[300] S. J. Tauster, S. C. Fung, R. T. K. Baker, J. A. Horsley, Science 1981, 211, 1121-1125.

[301] D. Mitlin, A. Misra, V. Radmilovic, M. Nastasi, R. Hoagland, D. J. Embury, J. P. Hirth, T. E. Mitchell, Philos. Mag. 2004, 84, 719-736.

[302] D. Mitlin, A. Misra, T. E. Mitchell, R. G. Hoagland, J. P. Hirth, Appl. Phys. Lett. 2004, 85, 1686-1688.

[303] D. Mitlin, A. Misra, T. E. Mitchell, J. P. Hirth, R. G. Hoagland, Philos. Mag. 2005, 85, 3379-3392.

[304] C. B. Carter, R. Q Hwang, Phys. Rev. B 1995, 51, 4730-4733.

[305] C. B. Carter, S. M. Holmes, Philos. Mag. 1977, 35, 1161-1172.

[306] F. T. Wagner, B. Lakshmanan, M. F. Mathias, J. Phys. Chem. Lett. 2010, 1, 2204-2219.

[307] T. Xing, Y. Zheng, L. H. Li, B. C. C. Cowie, D. Gunzelmann, S. Z. Qiao, S. Huang, Y. Chen, ACS Nano, 2014, 8, 6856-6862.

[308] Y. Wang, X. Jiang, ACS Appl. Mater. Interfaces 2013, 5, 11597-11602.

[309] J. Snyder, N. Danilovic, A. P. Paulikas, D. Tripkovic, D. Strmcnik, N. M. Markovic, V. R. Stamenkovic, J. Phys. Chem. C 2013, 117, 23790-23796.

[310] I. E. L. Stephens, A. S. Bondarenko, U. Gronbjerg, J. Rossmeisl, I. Chorkendorff, Energy Environ. Sci. 2012, 5, 6744-6762.

[311] G-Z Zhu, S. Prabhudev, J. Yang, C. M. Gabardo, G. A. Botton, L. Soleymani, J. Phys. Chem. C 2014, 118, 22111-22119.

[312] L. Su, W. Jia, C-M Li, Y. Lei, ChemSusChem 2014, 7, 361-378.

[313] K. W. Kim, S. M. Kim, S. Choi, J. Kim, I. S. Lee, ACS Nano, 2012, 6, 5122-5129.

[314] J. Xie, X. Yang, B. Han, S-H Yang, D. Wang, ACS Nano, 2013, 7, 6337-6345.

[315] C. Kok Poh, S. Hua Lim, Z. Tian, L. Lai, Y. P. Feng, Z. Shen, J. Lin, Nano Energy, 2013, 2, 28-39.

[316] J. van Drunen, B. K. Pilapil, Y. Makonnen, D. Beauchemin, B. D. Gates, G. Jerkiewicz, ACS Appl. Mater. Interfaces 2014, 6, 12046-12061.

[317] C. Wang, D. Li, M. Chi, J. Pearson, R. B. Rankin, J. Greeley, Z. Duan, G. Wang, D. van der Vliet, K. L. More, N. M. Markovic, V. R. Stamenkovic, J. Phys. Chem. Lett. 2012, 3, 1668-1673.

[318] J. Greeley, I. E. L. Stephens, A. S. Bondarenko, T. P. Johansson, H. A. Hansen, T. F. Jaramillo, J. Rossmeisl, I. Chorkendorff, J. K. Norskov, Nat. Chem. 2009, 1, 552-556.

[319] B. N. Wanjala, B. Fang, S. Shan, V. Petkov, P. Zhu, R. Loukrakpam, Y. Chen, J. Luo, J. Yin, L. Yang, M. Shao, C-J Zhong, Chem. Mater. 2012, 24, 4283-4293.

[320] Y. Liu, C. M. Hangarter, U. Bertocci, T. P. Moffat, J. Phys. Chem. C 2012, 116, 7848-7862.

[321] C. Wang, N. M. Markovic, V. R. Stamenkovic, ACS Catal. 2012, 2, 891-898.

[322] L. Su, S. Shrestha, Z. Zhang, W. Mustain, Y. Lei, J. Mater. Chem. A, 2013, 1, 12293-12301.

[323] S-I Choi, M. Shao, N. Lu, A. Ruditskiy, H-C Peng, J. Park, S. Guerrero, J. Wang, M. J. Kim, Y. Xia, ACS Nano, 2014, DOI: 10.1021/nn5036894

[324] S. Zhang, X. Zhang, G. Jiang, H. Zhu, S. Guo, D. Su, G. Lu, S. Sun, J. Am. Chem. Soc. 2014, 136, 7734-7739.

[325] S. Xie, S-I Choi, N. Lu, L. T. Roling, J. A. Herron, L. Zhang, J. Park, J. Wang, M. J. Kim, Z. Xie, M. Mavrikakis, Y. Xia, Nano Lett. 2014, 14, 3570-3576.

[326] J. B. Henry, A. Maljusch, M. Huang, W. Schuhmann, A. S. Bondarenko, ACS Catal. 2012, 2, 1457-1460.

[327] L. Gan, M. Heggen, S. Rudi, P. Strasser, Nano Lett. 2012, 12, 5423-5430.

[328] L. Gan, M. Heggen, R. O'Malley, B. Theobald, P. Strasser, Nano Lett. 2013, 13, 1131-1138.

[329] D. Wang, Y. Yu, H. L. Xin, R. Hovden, P. Ercius, J. A. Mundy, H. Chen, J. H. Richard, D. A. Muller, F. J. DiSalvo, H. D. Abruna, Nano Lett. 2012, 12, 5230-5238.

[330] K. A. Kuttiyiel, K. Sasaki, Y. choi, D. Su, P. Liu, R. R. Adzic, Energ. Environ. Sci. 2012, 5, 5297-5304.

[331] Y. Choi, K. A. Kuttiyiel, J. P. Labis, K. Sasaki, G-G Park, T-H Yang, R. R. Adzic, Top Catal. 2013, 56, 1059-1064.

[332] C. Chen, Y. Kang, Z. Huo, Z. Zhu, W. Huang, H. L. Xin, J. D. Snyder, D. Li, J. A. Herron, M. Mavrikakis, M. Chi, K. L. More, Y. Li, N. M. Markovic, G. A. Somorjai, P. Yang, V. R. Stamenkovic, Science 2014, 343, 1339-1343.

[333] D. F. van der Vliet, C. Wang, D. Tripkovic, D. Strmcnik, X. F. Zhang, M. K. Debe, R. T. Atanasoski, N. M. Markovic, V. R. Stamenkovic, Nat. Mater. 2012, 11, 1051-1058.

[334] C-H Cui, H-H Li, X-J Liu, M-R Gao, S-H Yu, ACS Catal. 2012, 2, 916-924.

[335] P. Strasser, S. Koh, T. Anniyev, J. Greeley, K. More, C. Yu, Z. Liu, S. Kaya, D. Nordlund, H. Ogasawara, M. F. Toney, A. Nilsson, Nat. Chem. 2010, 2, 454-460.

[336] J. Yang, J. Yang, J. Y. Ying, ACS Nano, 2012, 6, 9373-9382.

[337] S. Prabhudev, M. Bugnet, C. Bock, G. A. Botton, ACS Nano, 2013, 7, 6103-6110.

[338] V. R. Stamenkovic, B. S. Mun, K. J. J. Mayrhofer, P. N. Ross, N. M. Markovic, J. Rossmeisl, J. Greeley, J. K. Norskov, Angew. Chem. Int. Ed. 2006, 45, 2897-2901.

[339] I. E. L. Stephens, A. S. Bondarenko, F. J. Perez-Alonso, F. Calle-Vallejo, L. Bech, T. P. Johansson, A. K. Jepsen, R. Frydendal, B. P. Knudsen, J. Rossmeisl, I. Chorkendorff, J. Am. Chem. Soc. 2011, 133, 5485-5491.

[340] G. Rothenberg, Catalysis: Concepts and Green Applications, 2008, Wiley-VCH, pp. 65

[341] F. Abild-pedersen, J. Greeley, F. Studt, J. Rossmeisl, T. R. Munter, P. G. Moses, E. Skulason, T. Bligaard, J. K. Norskov, Phys. Rev. Lett. 2007, 99, 016105.

[342] S. Guo, D. Li, H. Zhu, S. Zhang, N. M. Markovic, V. R. Stamenkovic, S. Sun, Angew. Chem. Int. Ed. 2013, 52, 3465-3468.

[343] B. Patrick, H. C. Ham, Y. Shao-Horn, L. F. Allard, G. S. Hwang, P. J. Ferreira, Chem. Mater. 2013, 25, 530-535.

[344] D. Wang, H. L. Xin, R. Hovden, H. Wang, Y. Yu, D. A. Muller, F. J. DiSalvo, H. D. Abruna, Nat. Mater. 2013, 12, 81-87.

[345] D. A. Cantane, F. E. R. Oliveira, S. F. Santos, F. H. B. Lima, Appl. Catal. B-Environ. 2013, 136, 351-360.

[346] K. D. Beard, D. Borrelli, A. M. Cramer, D. Blom, J. W. Van Zee, J. R. Monnier, ACS Nano, 2009, 3, 2841-2853.

[347] F. Maillard, L. Dubau, J. Durst, M. Chatenet, J. Andre, E. Rossionot, Electrochem. Commun. 2010, 12, 1161-1164.

[348] L. Dubau, M. Lopez-Haro, L. Castanheira, J. Durst, M. Chatenet, P. Bayle-Guillemaud, L. Guetaz, N. Caque, E. Rossinot, F. Maillard, Appl. Catal. B-Environ. 2013, 142, 801-808.

[349] M. Lopez-Haro, L. Dubau, L. Guetaz, P. Bayle-Guillemaud, M. Chatenet, J. Andre, N. Caque, E. Rossinot, F. Maillard, Appl. Catal. B-Environ. 2014, 152, 300-308.

[350] J. Zhang, M. B. Vukmirovic, Y. Xu, M. Mavrikakis, R. R. Adzic, Angew. Chem. Int. Ed. 2005, 44, 2132-2135.

[351] L. Zhang, R. Iyyamperumal, D. F. Yancey, R. M. Crooks, G. Henkelman, ACS Nano, 2013, 7, 9168-9172.

[352] C. Wang, D. van der Vliet, K. L. More, N. J. Zaluzec, S. Peng, S. Sun, H. Daimon, G. Wang, J. Greeley, J. Pearson, A. P. Paulikas, G. Karapetrov, D. Strmcnik, N. M. Markovic, V. R. Stamenkovic, Nano Lett. 2011, 11, 919-926.

[353] J. Yang, X. Chen, X. Yang, J. Y. Ying, Energy Environ. Sci. 2012, 5, 8976-8981.

[354] X. Sun, D. Li, Y. Ding, W. Zhu, S. Guo, Z. L. Wang, S. Sun, J. Am. Chem. Soc. 2014, 136, 5745-5749.

[355] G. Wang, B. Huang, L. Xiao, Z. Ren, H. Chen, D. Wang, H. D. Abruna, J. Lu, L. Zhuang, J. Am. Chem. Soc. 2014, 136, 9643-9649.

[356] Y. Kang, J. Snyder, M. Chi, D. Li, K. L. More, N. M. Markovic, V. R. Stamenkovic, Nano Lett. 2014, DOI: 10.1021/nl5028205

[357] R. Loukrakpam, B. N. Wanjala, J. Yin, B. Fang, J. Luo, M. Shao, L. Protsailo, T. Kawamura, Y. Chen, V. Petkov, C-J Zhong, ACS Catal. 2011, 1, 562-572.

[358] R. Loukrakpam, S. Shan, V. Petkov, L. Yang, J. Luo, C-J Zhong, J. Phys. Chem. C 2013, 117, 20715-20721.

[359] Y. Ma, P. B. Balbuena, J. Phys. Chem. C 2013, 117, 23224-23234.

[360] G. Jerkiewicz, Electrocatal. 2010, 1, 179-199.

[361] P. Urchaga, S. Baranton, C. Coutanceau, G. Jerkiewicz, Langmuir, 2012, 28, 3658-3663.

[362] L. Zhang, C. M. B. Holt, E. J. Luber, B. C. Olsen, H. Wang, M. Danaie, X. Cui, X. Tan, V. W. Lui, W. P. Kalisvaart, D. Mitlin, J. Phys. Chem. C 2011, 115, 24381-24393.

[363] M. Nesselberger, M. Roefzaad, R. F. Hamou, P. U. Biedermann, F. F. Schweinberger, S. Kunz, K. Schloegl, G. K. H. Wiberg, S. Ashton, U. Heiz, K. J. J. Mayrhofer, M. Arenz, Nat. Mater. 2013, 12, 919-924.

[364] M. Shao, A. Peles, K. Shoemaker, Nano Lett. 2011, 11, 3714-3719.

[365] A. V. Ruban, H. L. Skriver, J. K. Norskov, Phys. Rev. B 1999, 59, 15990-16000.

[366] M. Weinert, R. E. Watson, Phys. Rev. B 1995, 51, 17168-17180.

[367] B. Hammer, Y. Morikawa, J. K. Norskov, Phys. Rev. Lett. 1996, 76, 2141-2144.

[368] M. Wakisaka, S. Mitsui, Y. Hirose, K. Kawashima, H. Uchida, M. Watanabe, J. Phys. Chem. B 2006, 110, 23489-23496.

[369] T. Toda, H. Igarashi, H. Uchida, M. Watanabe, J. Electrochem. Soc. 1999, 146, 3750-3756.

[370] J. A. Rodriguez, D. W. Goodman, Science 1992, 257, 897-903.

[371] V. R. Stamenkovic, B. S. Mum, M. Arenz, K. J. J. Mayrhofer, C. A. Lucas, G. Wang, P. N. Ross, N. M. Markovic, Nat. Mater. 2007, 6, 241-247.

[372] D. F. van der Vliet, C. Wang, D. Li, A. P. Paulikas, J. Greeley, R. B. Rankin, D. Strmcnik, D. Tripkovic, N. M. Markovic, V. R. Stamenkovic, Angew. Chem. Int. Ed. 2012, 51, 3139-3142.

[373] V. R. Stamenkovic, B. Fowler, B. S. Mum, G. Wang, P. N. Ross, C. A. Lucas, N. M Markovic, Science 2007, 315, 493-497.

[374] N. M. Markovic, P. N. Ross, Surf. Sci. Rep. 2002, 45, 121–229.

[375] C. Cui, L. Gan, M. Heggen, S. Rudi, P. Strasser, Nat. Mater. 2013, 12, 765-771.

[376] H. C. Ham, D. Manogaran, K. H. Lee, K. Kwon, S. Jin, D. J. You, C. Pak, G. S. Hwang, J. Chem. Phys. 2013, 139, 201104.

[377] K. Sasaki, H. Naohara, Y. Choi, Y. Cai, W-F Chen, P. Liu, R. R. Adzic, Nat. Commun. 2012, 3, 1115.

[378] M. Hu, D. P. Linder, M. B. Nardelli, A. Striolo, J. Phys. Chem. C 2013, 117, 15050-15060.

[379] S. G. Rinaldo, J. Stumper, M. Eikerling, J. Phys. Chem. C 2010, 114, 5773-5785.